**Springer Theses**
Recognizing Outstanding Ph.D. Research

Michaela Laupheimer

# Gelled Bicontinuous Microemulsions

## A New Type of Orthogonal Self-Assembled Systems

Springer

# Springer Theses

Recognizing Outstanding Ph.D. Research

For further volumes:
http://www.springer.com/series/8790

## Aims and Scope

The series "Springer Theses" brings together a selection of the very best Ph.D. theses from around the world and across the physical sciences. Nominated and endorsed by two recognized specialists, each published volume has been selected for its scientific excellence and the high impact of its contents for the pertinent field of research. For greater accessibility to non-specialists, the published versions include an extended introduction, as well as a foreword by the student's supervisor explaining the special relevance of the work for the field. As a whole, the series will provide a valuable resource both for newcomers to the research fields described, and for other scientists seeking detailed background information on special questions. Finally, it provides an accredited documentation of the valuable contributions made by today's younger generation of scientists.

## Theses are accepted into the series by invited nomination only and must fulfill all of the following criteria

- They must be written in good English.
- The topic should fall within the confines of Chemistry, Physics, Earth Sciences, Engineering and related interdisciplinary fields such as Materials, Nanoscience, Chemical Engineering, Complex Systems and Biophysics.
- The work reported in the thesis must represent a significant scientific advance.
- If the thesis includes previously published material, permission to reproduce this must be gained from the respective copyright holder.
- They must have been examined and passed during the 12 months prior to nomination.
- Each thesis should include a foreword by the supervisor outlining the significance of its content.
- The theses should have a clearly defined structure including an introduction accessible to scientists not expert in that particular field.

Michaela Laupheimer

# Gelled Bicontinuous Microemulsions

## A New Type of Orthogonal Self-Assembled Systems

Doctoral Thesis accepted by
the University of Stuttgart, Germany

Springer

*Author*
Dr. Michaela Laupheimer
Institute of Physical Chemistry
University of Stuttgart
Stuttgart
Germany

*Supervisor*
Prof. Dr. Cosima Stubenrauch
Institute of Physical Chemistry
University of Stuttgart
Stuttgart
Germany

ISSN 2190-5053 ISSN 2190-5061 (electronic)
ISBN 978-3-319-07718-5 ISBN 978-3-319-07719-2 (eBook)
DOI 10.1007/978-3-319-07719-2
Springer Cham Heidelberg New York Dordrecht London

Library of Congress Control Number: 2014941290



Printed on acid-free paper

Springer is part of Springer Science+Business Media (www.springer.com)

**Parts of this thesis have been published in the following journal articles:**

1. M. Laupheimer, K. Jovic, F.E. Antunes, M. da Graça Martins Miguel, C. Stubenrauch, Soft Matter **9**, 3661–3670 (2013)
2. M. Laupheimer, C. Stubenrauch, Tenside Surf. Det. **51**, 17–25 (2014)

*For my family*

# Supervisor's Foreword

Orthogonal self-assembly is the independent but simultaneous formation of two coexisting self-assembled structures within a single system. Nature knows well how to make use of orthogonal self-assembly, the most prominent example of which is the structure of the cell. In the cell phospholipid bilayers are needed for the functioning of the cell, while self-assembled proteins give the cell the required mechanical resistance. Colloidal and interfacial science deals with self-assembly on a broad variety of length scales and the idea of copying nature by combining two different self-assembled systems is straightforward. Pioneering work in this area combined the structure of a gel with the structure of aqueous surfactant solutions resulting in gelled complex fluids. Using a microemulsion instead of an aqueous surfactant solution leads to the formation of a gelled microemulsion.

Gelled microemulsions are very promising for all those applications in which the microstructure of the microemulsion is needed and low viscosity is undesirable. An example could be the administration of a drug-delivering microemulsion to a certain spot of the skin. However, using the concept of orthogonal self-assembly to gel microemulsions has never been tried because gelling a microemulsion means that different length and timescales have to be dealt with at the same time. Moreover, finding an appropriate gelator is like "looking for a needle in a haystack" since gelators typically either gel oil or water! This is where Michaela Laupheimer's work steps in. Based on preliminary results from one of my former Ph.D. students, Michaela Laupheimer's task was to formulate and to characterize a gelled bicontinuous microemulsion. Her systematic and multifaceted approach indeed allowed us to learn a lot about these novel orthogonal self-assembled systems. Comparing gelled bicontinuous microemulsions with respective non-gelled bicontinuous microemulsions and binary gels, Michaela showed that bicontinuous microemulsion domains indeed coexist with a gelator network.

Her huge contribution was to identify gelled bicontinuous microemulsions as a new type of orthogonal self-assembled systems, which will have an enormous impact on future work in this area.

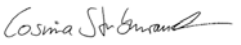

Stuttgart, April 2014 Prof. Dr. Cosima Stubenrauch

# Acknowledgments

I wish to thank, first and foremost, *Prof. Dr. Cosima Stubenrauch* for giving me the opportunity to do my diploma and, in particular, my Ph.D. thesis in her group. Thank you so much for your help and guidance, for supporting and challenging me, for the possibility to attend national and international conferences, for all the productive discussions we had and especially for countless times encouraging me the way only you managed to.

I would also like to thank *Prof. Dr. Thomas Hellweg* for reviewing my thesis as a second referee and *Prof. Dr. Sabine Laschat* for taking over the chairwoman position during my defense.

A special thanks goes to *PD Dr. Thomas Sottmann* for his invaluable help concerning all scattering issues. Thank you for contributing with your know-how and assistance when we carried out the SANS measurements, for all explanations and the numerous discussions we had in Cologne, Stuttgart and on the telephone as well as for proofreading the SANS chapters.

Furthermore, I wish to thank several other people for their practical, theoretical, and moral help with the measurements carried out for this thesis, namely *Kristina Jovic* and *Erna Muks* who worked with me on the phase studies during a bachelor thesis and 'Hiwi' employment and during a 'Forschungspraktikum', respectively, *Dr. Filipe Antunes* for sharing with me his expertise in rheometry during my STSM in Coimbra, *Prof. Dr. Michael Hunger* for giving helpful advice regarding the NMR measurements, *Diana Zauser* who stayed with me in the NMR lab and assisted in various situations, *Mireia Subinyà Albrich* for her help with the NMR data treatment in Matlab and during the SANS measuring times, *Helge Klemmer* for also helping with the SANS measurements and subsequently with treating the raw data, and last but not least *Dr. Natalie Preisig* for taking the FFEM pictures.

Moreover, thank you, all *group members of the AK Stubenrauch* and in particular my roommates in 2009–2013, for the good time, conversations, laughter, lunch breaks, and movie sessions we had together. I will never forget.

Finally, I want to thank all friends who were by my side during all these university years and especially *Petra Michelfelder*, my sister *Sabrina* and my parents *Hans-Peter* and *Maria Laupheimer* for their love and continuous support.

# Contents

# Abbreviations

In the following the most important abbreviations and symbols used in this thesis are listed.

## Numerical

1 One-phase microemulsion
$\underline{2}$ Oil-in-water (o/w) microemulsion coexisting with an excess oil phase
$\overline{2}$ Water-in-oil (w/o) microemulsion coexisting with an excess water phase
3 Three-phase bicontinuous microemulsion coexisting with an excess water and an excess oil phase

## Latin

| | |
|---|---|
| $A$ | Area; e.g. of a gelator fiber node in a gelator network |
| $A(\boldsymbol{q})$ | Amplitude of a scattered neutron wave (cp. Eqs. (2.49) and (2.51)) |
| $a_{\text{surfactant}}$ | Area which one surfactant molecule occupies in the surfactant monolayer at the water–oil interface |
| $\boldsymbol{B}$ | Magnetic field |
| $b_{\text{i}}$ | Scattering length of an atom $i$ |
| $C_{10}E_4$ | Tetraethylene glycol monodecyl ether |
| $C_iE_j$ | Polyethylene glycol monoalkyl ether ($i$ = number of carbon atoms in the $n$-alkyl chain, $j$ = number of ethylene glycol units) |
| $c_{\text{12-HOA,mon.}}$ | Concentration of monomerically dissolved 12-HOA in a gel sample |
| $D$ | Self-diffusion coefficient |
| $D_0$ | Self-diffusion coefficient of a pure compound |
| $D_{\text{rel}}$ | Relative (normalized) self-diffusion coefficient (cp. Eq. (2.34)), "obstruction factor" |
| DSC | **D**ifferential **s**canning **c**alorimetry |

| | |
|---|---|
| $d$ | Distance between two deflection sites (cp. Eq. (2.41)) or length scale of the microstructure (cp. Eq. (2.42)), i.e. in bicontinuous microemulsions the domain size |
| $d_{TS}$ | Repetition distance in the scattering length density profile of a bicontinuous microemulsion in bulk contrast characterizing its local quasi-periodicity, parameter in the **T**eubner-**S**trey model (cp. Eq. (4.6)) |
| $d_{sample}$ | Sample layer thickness |
| $d_{s\text{-}d}$ | Sample-detector distance |
| $d\sigma/d\Omega$ | Differential scattering cross-section |
| $d\Sigma/d\Omega$ | Normalized scattering intensity (cp. Eq. (2.47)) |
| $E$ | Spin-echo attenuation in FT-PGSE NMR experiments |
| $\boldsymbol{F}$ | Force vector |
| FFEM | **F**reeze-**f**racture transmission **e**lectron **m**icroscopy |
| FID | **F**ree **i**nduction **d**ecay |
| FRM II | Research Neutron Source Heinz Maier-Leibnitz in Garching near Munich, Germany |
| FT | **F**ourier **t**ransformation |
| FT-PGSE | **F**ourier **T**ransform **P**ulsed-**G**radient **S**pin-**E**cho |
| $f$ | In rheology: frequency; in SANS: length fraction of "free" gelator fibers in a gelator network (cp. Eq. (4.19)) |
| $G$ | Shear modulus (cp. Eq. (2.10)) |
| $G'$ | Storage modulus |
| $G'_0$ | Fit parameter in Eq. (3.3) (corresponding to $G'$ at 1 Hz) |
| $G''$ | Loss modulus |
| $\lvert G^* \rvert$ | Complex modulus (cp. Eq. (2.16)) |
| $g$ | In PGSE NMR: strength of the magnetic field gradient pulses; in SANS: mole fraction of gelator which is monomerically dissolved in the solvent of a gel |
| $g_{max}$ | Maximum gradient strength in a PGSE NMR experiment |
| $H$ | Mean curvature of the surfactant film (cp. Eq. (2.5)) |
| $H_0$ | Spontaneous curvature of the surfactant film which would be adopted in the absence of external forces, thermal fluctuations and conservation constrains |
| $\Delta_{sol\text{-}gel}H$ | Sol-gel transition enthalpy |
| 12-HOA | **12-H**ydroxy**o**ctadecanoic **a**cid (12-hydroxystearic acid) |
| $\boldsymbol{I}$ | Nuclear spin |
| $I$ | Scattering intensity |
| $I_{bg}$ | Intensity of the incoherent **b**ack**g**round scattering |
| $I_{sc}$ | Scattering function of a **sc**atterer, e.g. $I_{gel}$ as scattering function of a binary gel |

| | |
|---|---|
| ILL | **I**nstitute **L**aue-**L**angevin in Grenoble, France |
| $\boldsymbol{k}_{\mathrm{in}}$ | Wave-vector of incident neutron wave |
| $\boldsymbol{k}_{\mathrm{sc}}$ | Wave-vector of scattered neutron wave |
| $k$ | Magnitude of the wave-vector (cp. Eq. (2.38)) |
| KJ | Measurement carried out by **K**ristina **J**ovic during her bachelor thesis and her 'Hiwi' employment under my supervision |
| $L$ | Length of a cylinder or rod; length of a "free" gelator fiber in a gelator network (cp. Eq. (4.23)) |
| $L_{\mathrm{fibers}}$ | Total length of all "free" gelator fibers in a gelator network (cp. Eq. (4.20)) |
| $L_{\mathrm{nodes}}$ | Total length of all gelator fibers in a gelator network which are involved in nodes (cp. Eq. (4.26)) |
| $L_{\mathrm{total}}$ | Total length of all gelator fibers in a gelator network (cp. Eqs. (4.18) and (4.21)) |
| LC | **L**iquid **c**rystalline |
| LMG | **L**ow **m**olecular weight **g**elator |
| LMOG | **L**ow **m**olecular weight **o**rganic **g**elator |
| LVE | **L**inear **v**isco**e**lastic |
| $\boldsymbol{M}$ | In rheology: momentum of force, torque; in NMR: magnetization |
| $M_{\mathrm{k}}$ | Molar mass of substance $k$ |
| ME | **M**icro**e**mulsion |
| $m$ | Mass |
| $N_{\mathrm{i}}$ | Number of elements $i$, e.g. $N_{\mathrm{nodes}}$ as number of the nodes in a gelator network |
| NMR | **N**uclear **m**agnetic **r**esonance |
| $n$ | Number density of the scatterers |
| $P(q)$ | Form factor |
| $\overline{P(q)}$ | Average form factor (cp. Eq. (2.54)) |
| $P_{\mathrm{sc}}$ | Form factor of a single **sc**atterer, e.g. $P_{\mathrm{fiber}}$ as form factor of a cylindrical gelator fiber |
| PGSE | **P**ulsed-**G**radient **S**pin-**E**cho |
| $\boldsymbol{q}$ | Momentum transfer vector, 'scattering vector' (cp. Eq. (2.39) and Fig. 2.20) |
| $q$ | Magnitude of the 'scattering vector' (cp. Eq. (2.40)) |
| $q_{\mathrm{max}}$ | $q$ value for which the scattering intensity of a bicontinuous microemulsion in bulk contrast possesses its maximum in the characteristic "Teubner-Strey peak" |
| $q_{\mathrm{shoulder}}$ | $q$ value of the characteristic shoulder in the scattering curve of a bicontinuous microemulsion in film contrast |
| $R$ | Radius; in particular cross-sectional radius of a gelator fiber which is modeled as cylindrical rod with circular cross-section |

| | |
|---|---|
| $R_0$ | Mean cross-sectional radius of the cylindrical gelator fibers |
| $\boldsymbol{r}$ | Position vector |
| $S(q)$ | Structure factor (cp. Eq. (2.61)) |
| $S_{\text{eff}}(q)$ | Effective structure factor (cp. Eq. (2.58)) |
| $S/V$ | Surface to volume ratio, specific internal interface |
| SAFIN | **S**elf-**a**ssembled **fi**brillar **n**etwork |
| SANS | **S**mall **a**ngle **n**eutron **s**cattering |
| $T$ | Temperature; in SANS: thickness of a gelator fiber node in a gelator network |
| $\widetilde{T}$ | Temperature coordinate of a microemulsion's characteristic $\widetilde{X}$ point (phase inversion temperature) |
| $T_0$ | Mean thickness of the gelator fiber nodes in a gelator network |
| $T_{1-\overline{2}}$ | Upper phase transition temperature of a microemulsion |
| $T_{\underline{2}-1}$ | Lower phase transition temperature of a microemulsion |
| $T_{\text{1-LC}}$ | Lower phase transition temperature between the one-phase microemulsion and a liquid crystalline phase |
| $T_{\text{LC-1}}$ | Upper phase transition temperature between the one-phase microemulsion and a liquid crystalline phase |
| $T_{\text{sol-gel}}$ | Sol-gel transition temperature |
| $Tr$ | Sample transmission |
| $t$ | Time; diffusivity of the amphiphilic film in Eq. (4.28) |
| $V$ | (Sample) volume |
| V-SANS | **V**ery **s**mall **a**ngle **n**eutron **s**cattering |
| $v$ | Shear velocity; velocity of neutrons (cp. Eq. (2.36)) |
| $v_{\text{surfactant}}$ | Volume of a single surfactant molecule |
| $W(X, X_0)$ | Distribution function for the distribution of a characteristic dimension $X$ around a mean value $X_0$, e.g., Gaussian distribution (cp. Eq. (4.11)) |
| $\widetilde{X}$ | Characteristic point of a microemulsion |
| $x_{\text{k}}$ | Mole fraction of the substance $k$ |
| $z$ | Plate–plate distance in a rheometry experiment |

## Greek

| | |
|---|---|
| $\alpha$ | Mass fraction of the hydrophobic component in the mixture of the hydrophobic and the hydrophilic component (cp. Eq. (2.1)) |
| $\gamma$ | Mass fraction of the surfactant in the total mixture (cp. Eq. (2.3)); in rheology: shear strain (cp. Eq. (2.8)) |

| | |
|---|---|
| $\widetilde{\gamma}$ | Composition coordinate of a microemulsion's characteristic $\widetilde{X}$ point, denotes the efficiency of the system |
| $\gamma_g$ | Gyromagnetic ratio |
| $\gamma_{g,pr.}$ | Gyromagnetic ratio of the proton ($2.675\ 10^8\ s^{-1}\ T^{-1}$)[1] |
| $\gamma_{max}$ | Maximum shear strain amplitude |
| $\dot{\gamma}$ | Shear rate (cp. Eq. (2.9)) |
| $\Delta$ | Diffusion time in FT-PGSE NMR experiments |
| $\delta$ | In PGSE NMR: (effective) duration of the magnetic field gradient pulses; in rheology: phase shift (cp. Eq. (2.20)) |
| $\eta$ | Mass fraction of the gelator in the total mixture (cp. Eq. (2.4)) |
| $\theta$ | Scattering angle |
| $\kappa$ | Exponent of the frequency in Eq. (3.3) |
| $\lambda$ | Wave length (for neutrons cp. Eq. (2.37)) |
| $\xi_{TS}$ | Correlation length of the bicontinuous microemulsion structure, parameter in the **T**eubner-**S**trey model (cp. Eq. (4.7)) |
| $\rho$ | Scattering length density (cp. Eqs. (2.44) and (2.45)) |
| $\bar{\rho}$ | Mean value of the scattering length density |
| $\rho_k^0$ | Macroscopic density of substance $k$ |
| $\Delta\rho$ | Scattering contrast (cp. Eq. (2.52)) |
| $\sigma_i$ | Scattering cross-section of an atom $i$ (cp. Eq. (2.43)) |
| $\sigma_R$ | Distribution coefficient of the fiber radius $R$ (half width of a Gaussian curve) |
| $\sigma_T$ | Distribution coefficient of the node thickness $T$ (half width of a Gaussian curve) |
| $\tau$ | In NMR: duration of the dephasing (rephasing) period in spin-echo experiments; in rheology: shear stress (cp. Eq. (2.7)) |
| $\tau_{max}$ | Maximum shear stress amplitude |
| $\tau_{\text{“drop”}}$ | Shear stress for which $G'$ and $G''$ intersect, i.e., the stress which causes a break-down of the gel's microstructure |
| $\phi$ | Volume fraction of the hydrophobic component in the mixture of the hydrophobic and the hydrophilic component (cp. Eq. (2.2)) |
| $\phi_d$ | Volume fraction of the deuterated component in a bulk contrast microemulsion |
| $\phi_{surf.,int.}$ | Volume fraction of surfactant at the water–oil interface (cp. Eq. (4.31)) |
| $\varphi_i$ | Initial phase angle of oscillating shear stress ($i = \tau$) and strain ($i = \gamma$) |
| $\psi$ | Exponent of the gelator mass fraction in Eq. (3.4) |
| $\omega$ | Angular frequency |
| $\Omega$ | Solid angle in SANS measurements |

[1] P.W. Atkins, *Physikalische Chemie—Dritte, korrigierte Auflage* (Wiley-VCH, Weinheim, 2002).

# Chapter 1
# Introduction

## 1.1 Motivation

Orthogonal self-assembly is the independent but simultaneous formation of two coexisting self-assembled structures within a single system. Laibinis et al. introduced the term "orthogonal self-assembled" in 1989 for monolayers of alkane thiols and alkane carboxylic acids which form in an ordered manner at differently treated regions of a surface exposed to a common solution of both adsorbates (Fig. 1.1, left top) [1]. This behaviour is explained by the different coordination chemistry involved in the two self-assembling processes. However, bulk systems can also comprise structures that form due to non-covalent interactions which are selective and non-interfering. Hence, orthogonal self-assembly is by no means limited to surface chemistry. Hofmeier and Schubert, for instance, described that polymers which possess different non-covalent binding sites can, in a defined and controlled way, be multifunctionalized in single-step reactions due to orthogonal self-assembly (Fig. 1.1, left bottom) [2]. This is desirable regarding the design of new functional and "smart" materials. Moreover, nature has always used in parallel a variety of non-covalent interactions to build up complex structures like DNA molecules, proteins and cells. The latter are confined by a bilayered membrane of amphiphilic phospholipids which coexists with a variety of other self-assembled architectures such as protein assemblies that form scaffolding filaments in the cell, i.e. the cytoskeleton [3] (Fig. 1.1, right). These examples demonstrate the huge prospects of studying orthogonal self-assembled systems a special type of which, namely **gelled complex fluids**, is currently of increasing interest in the field of soft matter science.

As this work examines gelled complex fluids in general and gelled bicontinuous microemulsions in particular, 'complex fluids' and 'gels' are briefly explained at the outset before known examples of gelled complex fluids are discussed and the specific tasks of this thesis are described.

M. Laupheimer, *Gelled Bicontinuous Microemulsions*,
Springer Theses, DOI: 10.1007/978-3-319-07719-2_1,

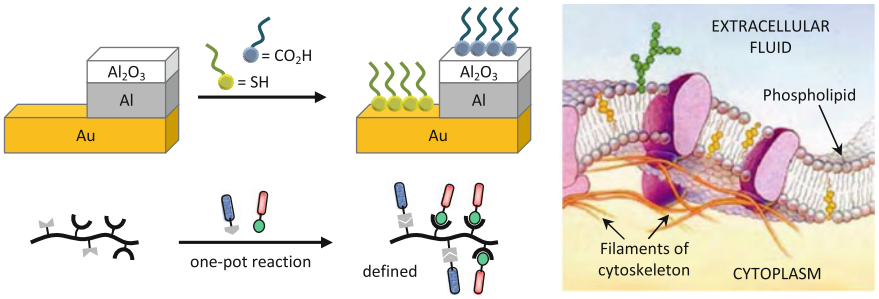


**Fig. 1.1** (*Left top*) Orthogonal self-assembled monolayers according to [1]. (*Left bottom*) Multifunctionalizing a polymer via orthogonal self-assembly (adapted from [2] with permission of The Royal Society of Chemistry). (*Right*) Orthogonal self-assembled structures in a cell (modified from [4])

### *1.1.1 Complex Fluids*

Complex fluids may be defined as fluids possessing a microstructure on a mesoscopic length scale which determines the characteristic properties of the system [5]. All complex fluids consist of 'particles' (or rather structural motifs) which are either dynamic aggregates or of a fixed molecular weight. Particles of a fixed molecular weight can be polymers or solid colloids while dynamic aggregates consist of self-assembled monomers. In all cases the 'particles' are mesoscopic, i.e. their size is between the molecular and the macroscopical level (Greek *mesos*: middle). One example of complex fluids is liquid crystals in which anisometric molecules assemble in a structure on a mesoscopic length scale. Thus they possess an orientational but not necessarily a long-range positional order. Other complex fluids are micellar or vesicular solutions, in which amphiphiles self-assemble to spherical, cylindrical or worm-like aggregates. Those aggregates constitute discrete units of a bended surfactant layer, which is a monolayer in the case of micelles and a bilayer for vesicles, respectively. Moreover, the presence of a second liquid, immiscible in the first one, can account for the microstructure of a complex fluid. This is the case in emulsions and microemulsions in which one finds oil-in-water or water-in-oil droplets as well as, exclusively in microemulsions, bicontinuous sponge-like formations. These structures are stabilized by surfactant molecules. In the case of microemulsions the surfactant molecules cover the entire water–oil interface and account for thermodynamic stability [5].

### *1.1.2 Gels*

From a rheological point of view gels are viscoelastic systems with self-supporting properties which prevents them from flowing on the timescale of observation.

They consist of a solvent and a gelator, which builds up a three-dimensional network. Thus gels can also be seen as complex fluids since their properties arise from the microstructure; however, it is arguable whether or not the three-dimensional network is mesoscopic. Common gel classifications refer to the type of solvent, the type of gelator or the type of the cross-links in the network. In the first case one distinguishes 'organogels' (in which an organic solvent is gelled by an 'organogelator') from 'hydrogels' (in which a hydrophilic solvent is gelled by a 'hydrogelator'). Regarding the type of gelator, the term 'polymer gels' is used when the gelator network is built up of a polymer like polyacrylamide or gelatin. On the other hand, there are 'low molecular weight gelators' (LMGs) which self-assemble to form the gelator fibers. If non-covalent interactions stabilize the gelator network, which is the case for LMGs, one speaks of 'physical gels'. Their formation is reversible with temperature variations, i.e. at high temperatures the system is a liquid 'sol' which gelifies when the temperature falls below the sol-gel boundary. On the other hand, there are 'chemical gels' in which the gelator network is cross-linked via covalent bonds [6].

### *1.1.3 Gelled Complex Fluids*

Gelled complex fluids can be looked at from different points of view. One can either see them as a combination of two 'base systems', i.e. the complex fluid and the gel, or as a modification of one or the other base system. Consequently, to "make" a gelled complex fluid one either adds a gelator to a complex fluid or replaces the solvent in a gel by a complex fluid. Different examples of such gelled complex fluids have been described in the literature and three important ones will be presented here, namely 'microemulsion-based organogels', 'microemulsion elastomers' and gelled surfactant solutions.

**Microemulsion-based organogels** are gelled water-in-oil droplet microemulsions which are transparent and thermoreversible [7]. The famous system reported in the literature consists of water, *n*-heptane and the ionic surfactant Aerosol-OT and is gelled by the biopolymer gelatin [7]. Interestingly, gelatin is a hydrogelator which is normally used to gel aqueous systems. Hence, according to the gel definition given above, it seems counterintuitive to speak of microemulsion-based *organo*gels. However, this name is in fact justified with regard to the microstructure of these systems. Based on small angle neutron scattering (SANS) data and electrical conductivity measurements Atkinson et al. proposed that microemulsion-based organogels have a continuous oil phase throughout which spans a rigid network of gelatin/water rods [7]. Thus the gelled bulk phase is indeed organic. Besides the network, gelatin-free water droplets are present (see Fig. 1.2, left) which, just like the rods, are covered by a surfactant monolayer [7]. When gelatin is added to the water-in-oil microemulsion the hydrophilic polymer gelatin is first entrapped in the water droplets which, with increasing gelatin concentration, begin to interact until a rigid infinite network is formed at a critical gelatin

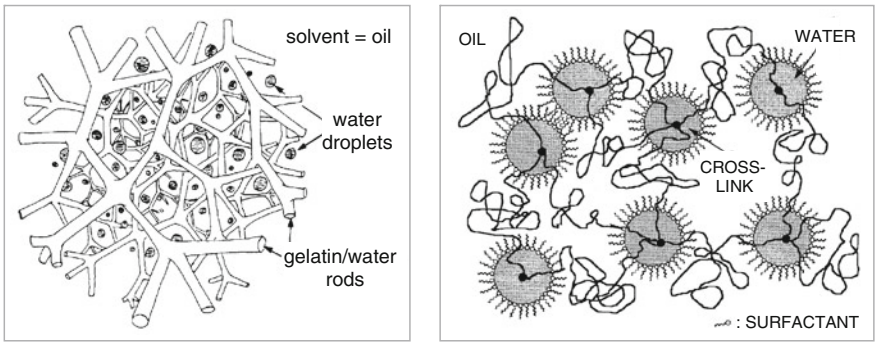


**Fig. 1.2** (*Left*) Schematic drawing of a microemulsion-based organogel (reproduced from [7] with permission of The Royal Society of Chemistry). (*Right*) Microemulsion elastomer cross-linked in water-in-oil microemulsion droplets (adapted from [11])

concentration [8]. From the viewpoint of the microemulsion the water and surfactant content are reduced when the gel is formed because gelatin needs water to form the rods, which, in turn, are covered by a surfactant monolayer to prevent direct contact with the solvent. However, the size of the remaining water droplets that coexist with the gelatin/water network is unaffected [7]. Thus microemulsion-based organogels can be classified as orthogonal self-assembled systems, even though this expression has never been used in this context. A context in which microemulsion-based organogels have been mentioned is transdermal drug delivery [9]. Microemulsions are effective drug carrier systems, and gelled formulations are renowned for easy handling, for directed administration and for enhanced residence times of the drug [10].

**Microemulsion elastomers** are also polymer gels which are based on water-in-oil droplet microemulsions [11, 12]. However, in contrast to the reversibly formed microemulsion-based organogels, microemulsion elastomers are chemical gels with covalently linked junctions in the polymer network [11, 12]. In the preparation process ABA-triblock copolymers with polymerizable end groups are added to a droplet microemulsion. In the case of water-in-oil microemulsions triblock copolymers with a hydrophobic middle and hydrophilic end blocks are used while the opposite is true for oil-in-water microemulsions [11]. The triblock co-polymer end blocks dissolve in the microemulsion droplets and bridge them such that a transient network is formed [13, 14]. In a subsequent step the end blocks of the spacially arranged triblock copolymers are photopolymerized and thus chemically cross-linked within the microemulsion droplets [11, 12] (see Fig. 1.2, right). The resulting microemulsion elastomers possess a stability of shape as well as elastic properties. Moreover, just like the intermediate transient network, they qualitatively retain the microemulsion phase behaviour [11, 12, 13]. However, since the polymer network in the systems described is intrinsically tied to the microstructure of the microemulsion and does not coexist with it independently, microemulsion elastomers are not regarded as orthogonal self-assembled systems.

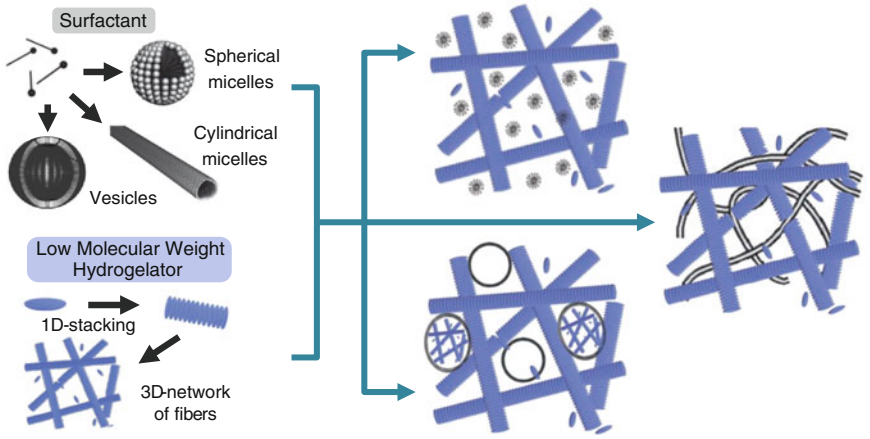


**Fig. 1.3** Surfactant assemblies (*left top*) and network of low molecular weight hydrogelator (*left bottom*) which make up gelled solutions of spherical micelles (*right top*), worm-like micelles (*right middle*) and vesicles (*right bottom*) (in part from [18] with permission of The Royal Society of Chemistry and from [16] with permission of John Wiley and Sons)

**Gelled surfactant solutions** have been studied extensively in the group of van Esch, who, in 2003, were the first who applied the expression "orthogonal self-assembly" to a gelled complex fluid [15]. They described how low molecular weight hydrogelators form a three-dimensional network in aqueous solutions of anionic, cationic or non-ionic surfactants [15]. The latter self-assemble to micelles, cylindrical micelles or vesicles which coexist independently with the gelator network (see Fig. 1.3) [16]. Such systems are interesting, for example, as simple models for cell architectures because vesicles have been prepared which incorporate gelator fibers in the same way as the bilayered cell membrane encapsulates the cytoskeleton [17]. Furthermore, worm-like micelles coexisting with the gelator network form two 'interpenetrating networks', which gives rise to synergistic effects. For example, new rheological properties are attained [18].

### *1.1.4 Gelled Bicontinuous Microemulsions*

This thesis evolved from a project in which bicontinuous microemulsions were gelled with a view to finding a new templating route for nanomaterials [19, 20, 21, 22] which are in great demand due to the universal trend towards miniaturization. Due to their characteristic domain sizes in the nanometer range microemulsions are interesting templates for such nanomaterials. Several groups have already succeeded in synthesizing nanoparticles of well-defined size in droplet microemulsions (see [23, 24, 25, 26] and references therein). However, for the reproduction of a bicontinuous microemulsion retaining the characteristic length only one successful but

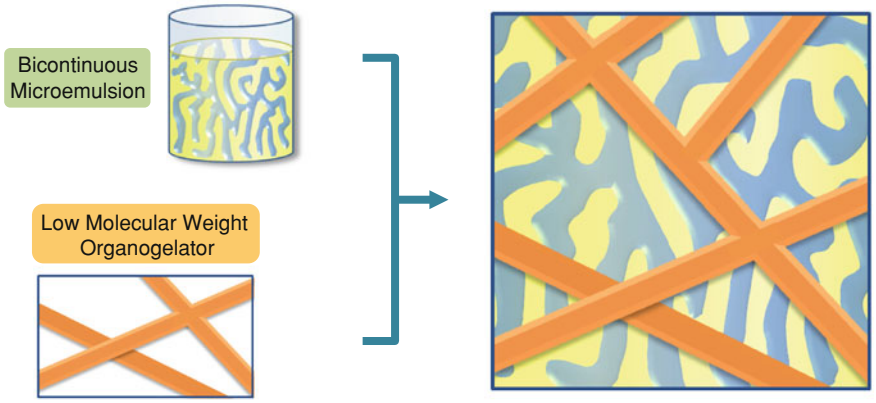


**Fig. 1.4** Schematic representation of a gelled bicontinuous microemulsion

extremely laborious attempt has been described to date [27]. Gao et al. photopolymerized the hydrophobic divinylbenzene phase in a bicontinuous microemulsion in which the hydrophilic phase consisted of a concentrated sugar solution. The dehydration of the latter made it possible to 'freeze' the structure in the form of a sugar glass, thus yielding a polymer with a pore size of about 25 nm [27]. However, although the sugar can easily be washed out of the resulting polymer, studying the phase behaviour of the glass-like system is very time-consuming. Hence, a new templating route has been developed with a view to finding a more feasible method for replicating bicontinuous microemulsions [22]. This route comprises four steps, the first of which is to gel one of the subphases (e.g. the oil phase) of the bicontinuous microemulsion. In other words, the original motivation for adding a gelator to a bicontinuous microemulsion was to 'freeze' its microstructure by arresting one of the two subphases. The next steps included adding a suitable monomer to the other subphase and UV-polymerizing it in order to 'copy' the bicontinuous structure. In a final washing step one gets rid of the gel and yields the pure nanostructured polymer. Indeed, the first step of the described route, i.e. the gelation of a bicontinuous microemulsion, was performed successfully [19, 20, 21, 22]. The low molecular-weight organogelator 12-hydroxyoctadecanoic acid (12-HOA) was used to gel bicontinuous microemulsions consisting of *n*-dodecane, a water phase with N-isopropylacrylamide and N,N'-methylene bisacrylamide as monomer and cross-linker, respectively, and a technical-grade non-ionic surfactant. However, it turned out to be very difficult to fully characterize the resulting polymer so that it is still unclear whether or not a nanostructured material with the same domain size as the templating microemulsion has been obtained.

In any case, the idea of how a gelled bicontinuous microemulsion is structured changed during the course of the previous project. The gel network apparently does not arrest any of the subphases of a bicontinuous microemulsion but the investigations carried out by Tessendorf suggest that in a gelled bicontinuous

**Table 1.1** Overview of common features and differences of gelled complex fluids

| Gelled complex fluid | Complex fluid | Microstructure | Gelator | Physical/ chemical gel | Orthogonal self-assembly |
|---|---|---|---|---|---|
| Gelled bicontinuous microemulsion | Microemulsion | Bicontinuous water and oil domains | Low molecular weight organogelator | Physical gel | Yes? |
| Gelled surfactant solution | Binary surfactant solution | Micelles, worm-like micelles, vesicles | Low molecular weight hydrogelator | Physical gel | Yes |
| Microemulsion elastomer | Microemulsion | Water-in-oil or oil-in-water droplets | Polymerized ABA-block copolymers | Chemical gel | No |
| Microemulsion-based organogel | Microemulsion | Water-in-oil droplets | Gelatin (biopolymer) | Physical gel | Yes |

microemulsion there are two three-dimensional structures on different length scales, i.e. the gelator network and the microemulsion, which coexist independently of each other [22]. This assumption is corroborated, for example, by preliminary freeze-fracture transmission electron microscopy (FFEM) pictures and small angle neutron scattering (SANS) data which show practically unaltered microemulsion structures in the presence of the gelator 12-HOA [22]. Hence, it was suggested that bicontinuous microemulsions gelled by a low molecular weight gelator are a new type of orthogonal self-assembled systems (Fig. 1.4). In fact, these new systems can directly be compared with the gelled surfactant solutions studied in the group of van Esch [15–17]. Instead of adding a low molecular weight *hydro*gelator to the aqueous surfactant solutions, a low molecular weight *organo*gelator has been used to gel the bicontinuous microemulsions. Thus there is a self-assembled fibrillar network of LMGs in both cases. However, the type of the complex fluid which is gelled differs significantly. Aqueous surfactant solutions are binary systems, while bicontinuous microemulsions consist of at least three components, namely water, oil and surfactant, which increases the complexity of the gelled system. Gelled bicontinuous microemulsions also differ from the above-mentioned microemulsion-based organogels and microemulsion elastomers which consist of microemulsion droplets rather than of a bicontinuous structure (cp. overview in Table 1.1). Finally, apart from gelled solutions of worm-like micelles gelled bicontinuous microemulsions are the only example of orthogonal-self assembled 'interpenetrating networks', i.e. systems in which both the gelator network and the microstructure of the complex fluid three-dimensionally span the whole sample volume.

## 1.2 Task Description

Bicontinuous microemulsions gelled by a low molecular weight gelator are believed to be a new type of orthogonal self-assembled systems, i.e. systems in which a bicontinuous microemulsion and a self-assembled fibrillar network of LMGs coexist independently. To prove this hypothesis a model system was to be comprehensively studied and compared with its two 'base systems', i.e. the respective non-gelled bicontinuous microemulsion and the corresponding binary gel. The characteristic features and properties of these base systems, which should be retained in an orthogonal self-assembled system, are described in Sects. 2.1 and 2.2, respectively.

The model system of choice was the microemulsion $H_2O$–*n*-decane–tetraethylene glycol monodecyl ether ($C_{10}E_4$) which should be gelled with the low molecular weight organogelator 12-HOA. The chosen gelator has proved to successfully gel similar microemulsions [19, 20, 21, 22]; regarding the choice of *n*-decane and $C_{10}E_4$ the following was considered. Firstly, the previously used technical-grade surfactant [19, 20, 21, 22] should be replaced by a pure surfactant to ensure the maximum reproducibility and to keep the model system as simple

and well-defined as possible. Secondly, the gelled bicontinuous microemulsion should form at temperatures around 25 °C in order to allow studies with various methods without the need for extensive heating or cooling. A non-gelled microemulsion consisting of $H_2O$, *n*-decane and $C_{10}E_4$ has a $\widetilde{T}$ of 30.15 °C at which it is bicontinuous [28]. However, the gelator 12-HOA lowers the phase boundaries [20] such that its addition to the system $H_2O$–*n*-decane–$C_{10}E_4$ was supposed to shift $\widetilde{T}$ close to room temperature.

At first, appropriate conditions, i.e. composition and temperature, for preparing gelled one-phase microemulsions of the type $H_2O$–*n*-decane/12-HOA–$C_{10}E_4$ had to be identified. Hence, temperature versus surfactant mass fraction phase diagrams at a constant 1:1 water-to-oil volume ratio were to be recorded for the system with three different gelator concentrations, namely 1.5, 2.5 and 5.0 wt% (Sect. 3.1). To be able to assess whether or not the characteristic phase behaviour of the non-gelled base microemulsion $H_2O$–*n*-decane–$C_{10}E_4$ is retained, the latter had to be studied in comparison. Furthermore, the sol-gel transition temperature of the gelled microemulsions was to be investigated using two complementary techniques, namely differential scanning calorimetry (DSC) and temperature-dependent oscillating shear rheometry (Sect. 3.2). This should ensure proper gelation in the one-phase state and reveal similarities with the binary organogel *n*-decane/12-HOA, which served as the reference system in this case. After identifying compositions and temperatures at which the system $H_2O$–*n*-decane/12-HOA–$C_{10}E_4$ is gelled and in the one-phase state, its rheological properties were to be examined. Again samples with three different gelator concentrations should be studied and compared with the respective binary gels (Sect. 3.3).

Subsequently, the focus turned to the microstructure. To begin with, it was to be verified that the gelled one-phase microemulsion at its $\widetilde{T}$ temperature is indeed bicontinuous as it is known for the non-gelled base microemulsion [29]. For this purpose Fourier transform pulsed-gradient spin-echo (FT-PGSE) $^1$H-NMR measurements were to be carried out for both the non-gelled and the gelled microemulsion because these measurements yield the self-diffusion coefficients of the microemulsion components which correlate with the microstructure (Sect. 4.1). Eventually, further structure investigations were intended to show the independent coexistence of the bicontinuous microemulsion domains and the gelator network. Thus small angle neutron scattering (SANS) experiments should be performed (Sect. 4.2) and freeze-fracture transmission electron microscopy (FFEM) pictures taken (Sect. 4.3) for the gelled bicontinuous microemulsion as well as for both base systems.

Altogether these investigations aimed at creating a comprehensive picture of gelled bicontinuous microemulsions, their properties and structure in comparison to those of the base systems, which allows verifying the claim of their orthogonal self-assembly.

## References


1. P.E. Laibinis, J.J. Hickman, M.S. Wrighton, G.M. Whitesides, Science **245**, 845–847 (1989)
2. H. Hofmeier, U.S. Schubert, Chem. Commun. **19**, 2423–2432 (2005)
3. J.M. Berg, J.L. Tymoczko, L. Stryer, *Stryer Biochemie 7 Auflage* (Springer Spektrum, Heidelberg, 2013)
4. C.V.D. Kelly, *Perturbations of Cellular Membranes with Synthetic Polymers and Ultrafast Lasers*, dissertation, University of Michigan, 2009 and ref. 12 therein
5. W.M. Gelbart, J. Phys. Chem. **100**, 13169–13189 (1996)
6. K. Nishinari, Progr Colloid Polym. Sci. **136**, 87–94 (2009)
7. P.J. Atkinson, M.J. Grimson, R.K. Heenan, A.M. Howe, B.H. Robinson, J. Chem. Soc. Chem. Commun. (1989) 1807–1809
8. F. Aliotta, V. Arcoleo, G. La Manna, V. Turco Liveri, Colloid Polym. Sci. **274**, 989–994 (1996)
9. S. Kantaria, G.D. Rees, M.J. Lawrence, J. Control. Release **60**, 355–365 (1999)
10. S. Heuschkel, A. Goebel, R.H.H. Neubert, J. Pharm. Sci. **97**, 603–631 (2008)
11. W. Meier, A. Falk, M. Odenwald, F. Stieber, Colloid Polym. Sci. **274**, 218–226 (1996)
12. W. Meier, Langmuir **12**, 6341–6345 (1996)
13. M. Odenwald, H.-F. Eicke, W. Meier, Macromolecules **28**, 5069–5074 (1995)
14. F.E. Antunes, K. Thuresson, B. Lindman, M.G. Miguel, Colloids Surf. A **215**, 87–100 (2003)
15. A. Heeres, C. van der Pol, M. Stuart, A. Friggeri, B.L. Feringa, J. van Esch, J. Am. Chem. Soc. **125**, 14252–14253 (2003)
16. A.M. Brizard, M. Stuart, K. van Bommel, A. Friggeri, M. de Jong, J.H. van Esch, Angew. Chem. Int. Ed. **47**, 2063–2066 (2008)
17. A.M. Brizard, J.H. van Esch, Soft Matter **5**, 1320–1327 (2009)
18. A.M. Brizard, M.C.A. Stuart, J.H. van Esch, Faraday Discuss. **143**, 345–357 (2009)
19. C. Stubenrauch, R. Tessendorf, R. Strey, I. Lynch, K.A. Dawson, Langmuir **23**, 7730–7737 (2007)
20. C. Stubenrauch, R. Tessendorf, A. Salvati, D. Topgaard, T. Sottmann, R. Strey, I. Lynch, Langmuir **24**, 8473–8482 (2008)
21. M. Magno, R. Tessendorf, B. Medronho, M. da Graça, Martins Miguel, C. Stubenrauch, Soft Matter **5**, 4763–4772 (2009)
22. R. Tessendorf, *Microemulsions as Templates for High Surface Area Polymers* (WiKu-Wissenschaftsverlag Dr. Stein, Köln, 2009)
23. C. Stubenrauch, T. Wielpütz, T. Sottmann, C. Roychowdhury, F.J. DiSalvo, Colloids and surfaces A: physicochem. Eng. Aspects **317**, 328–338 (2008)
24. N.M. Huang, C.S. Kan, P.S. Khiew, S. Radiman, J. Mater. Sci. **39**, 2411–2415 (2004)
25. J.-P. Roman, P. Hoornaert, D. Faure, C. Biver, F. Jacquet, J.-M. Martin, J. Colloid Interface Sci. **144**, 324–339 (1991)
26. J. He, T. Ma, Y. Huang, J. Yang, Key Eng. Mater. **280–283**, 977–980 (2005)
27. F. Gao, C.-C. Ho, C.C. Co, Macromolecules **39**, 9467–9472 (2006)
28. S. Burauer, T. Sachert, T. Sottmann, R. Strey, Phys. Chem. Chem. Phys. **1**, 4299–4306 (1999)
29. T. Sottmann, C. Stubenrauch, in *Microemulsions Background, New Concepts, Applications, Perspectives*, ed. by C. Stubenrauch, (Wiley, Oxford 2009), 1–83

# Chapter 2
# Theoretical Background

This chapter gives an overview of the two base systems of gelled bicontinuous microemulsions, namely bicontinuous microemulsions (Sect. 2.1) and binary gels (Sect. 2.2). Moreover, the basics of the three techniques which were used extensively for studying the systems' characteristic properties and their microstructure are introduced. Thus Sect. 2.3 deals with rheology, Sect. 2.4 with Fourier transform pulsed-gradient spin-echo NMR spectroscopy and Sect. 2.5 with small angle neutron scattering.

## 2.1 Base System 1: Bicontinuous Microemulsion

Quite intuitively, the first base system of a gelled bicontinuous microemulsion is the respective non-gelled, low viscous bicontinuous microemulsion without any gelator. Nevertheless, the system contains at least three components, namely a polar, a non-polar and an amphiphilic one. These are self-assembled in a way that the polar and the non-polar component form continuous, interpenetrating domains which are separated by a monolayer of the amphiphile. In fact, this is why one calls the system 'bicontinuous'. One distinguishes bicontinuous microemulsions from so-called 'droplet microemulsions' in which discrete droplets of the polar component are dispersed in a continuous non-polar phase or vice versa. The characteristic features of all microemulsions are that their microstructure is nanometer-sized and that they are formed via spontaneous self-assembly, which is why they are thermodynamically stable [1]. The name 'microemulsion' is thus counterintuitive, however, it dates back to times when these interesting systems were far from being understood. Schulman and Winsor initiated the research on microemulsions when they described the systems' composition and exceptional properties, such as their transparency and ultra-low interfacial tension, in 1943 and 1954, respectively [2, 3]. In the following Friberg, Shinoda and their co-workers investigated the phase behaviour of microemulsions [4–6], on which further extensive studies were carried out by Kahlweit and Strey [7–10]. It turned out that close relations exist between the systems' properties, microstructure and phase

M. Laupheimer, *Gelled Bicontinuous Microemulsions*,
Springer Theses, DOI: 10.1007/978-3-319-07719-2_2,

behaviour [11]. Up to today an in-depth knowledge has been acquired in the field, particularly about "simple" microemulsions like, e.g., ternary systems consisting of water, *n*-alkane and a non-ionic surfactant. Thus scientists are now exploring various fields of applications for microemulsions, including their use as reaction media [12], templating materials [13], detergents [14], drug delivery systems [15] and much more. This of course requires an understanding of the complex interplay of the classical microemulsion system with the components which are added for the specific application. The work at hand contributes a piece to this understanding by investigating the mutual effects of a bicontinuous microemulsion and an added gelator. This combination could, for example, be interesting for gelled microemulsion skin care formulations which would be easy to administer and feature enhanced residence times of the active ingredients.

### *2.1.1 Composition of Microemulsions*

As mentioned before, microemulsions are liquid systems comprising at least three components two of which are intrinsically immiscible due to different polarity and a third one which mediates between the first two such that macroscopically homogeneous mixtures are formed. The polar component in a microemulsion is usually **water**, just as it is the case in this thesis. In principle it is of course also possible to employ other polar substances such as formamide [16] or ionic liquids [17]. However, rather than that one finds microemulsions comprising aqueous solutions of salts [9] or other polar additives. The second, non-polar component is commonly referred to as '**oil**'. It is often an aromatic or aliphatic (cyclic or non-cyclic) hydrocarbon but also vegetable oils (e.g. soybean oil [18]) or other non-polar substances, like supercritical $CO_2$ [19], are used. If people work with mixtures of different oils they call the minor component the 'co-oil'. In the work at hand the used oil is *n*-decane, i.e. a linear hydrocarbon with a boiling point of 174 °C and a density of 0.730 g $cm^{-3}$ [20]. When it comes to the **amphiphile** the variety of possible substances is even more extended than is the case for the oil component. One usually classifies surface active compounds on the basis of their polar 'head group' which is bound to a non-polar moiety, usually a long hydrocarbon chain. One distinguishes ionic from non-ionic surfactants whose head groups are charged and non-charged, respectively. Moreover one can specify the chemical structure of the head group, which can, e.g., be a carbohydrate as it is the case in 'sugar surfactants' or a polyethylene glycol unit like in the here used tetraethylene glycol monodecyl ether ($C_{10}E_4$). The latter is from the group of the non-ionic '$C_iE_j$ surfactants' which possess *j* ethylene glycol units in their head group and an *n*-alkyl chain with *i* carbon atoms. $C_iE_j$ surfactants have been used, together with water and *n*-alkanes, for comprehensive and systematic studies of the phase behaviour and properties of microemulsions, e.g. [8, 10, 21]. These systems

are convenient for this purpose because they form microemulsions without 'co-surfactants' which are needed with many other mixtures. The possibility to work with a minimum number of simple substances is always advantageous for systematic studies, hence also in the thesis at hand. This explains the choice of the used microemulsion components water, *n*-decane and $C_{10}E_4$ and also the decision to work with a pure instead of a much cheaper technical-grade surfactant, which constitutes a mixture of amphiphiles whose head groups and chain lengths possess a certain distribution.

According to the conventional nomenclature one simply lists the polar, the non-polar and the amphiphilic component separated by dashes to name a microemulsion and separates additives by a slash from the respective main component, i.e. water/polar additive–oil/co-oil–surfactant/co-surfactant. Hence the here described base microemulsion is $H_2O$–*n*-decane–$C_{10}E_4$ while the gelled microemulsion is $H_2O$–*n*-decane/12-HOA–$C_{10}E_4$, where 12-HOA is denoted as "co-oil" because it is an organogelator notwithstanding the claimed coexistence of the gelator network with the entire microemulsion.

To specify the quantitative composition of a microemulsion several variables are introduced. First, one states the ratio of water to oil either as mass fraction

$$\alpha = \frac{m_{\text{oil}}}{m_{\text{water}} + m_{\text{oil}}} \tag{2.1}$$

or as volume fraction

$$\phi = \frac{V_{\text{oil}}}{V_{\text{water}} + V_{\text{oil}}} \tag{2.2}$$

where $m$ and $V$ are the masses and volumes of the components, respectively. For reasons which will be explained below all microemulsions in this work were prepared with equal volumes of water and *n*-decane, thus $\phi = 0.5$ which corresponds to $\alpha = 0.422$. Secondly, the surfactant concentration is quoted, generally as its mass fraction in the total mixture and thus here as

$$\gamma = \frac{m_{\text{surfactant}}}{m_{\text{water}} + m_{\text{oil}} + m_{\text{surfactant}} + m_{\text{gelator}}}. \tag{2.3}$$

The concentration of the gelator is defined in this thesis by

$$\eta = \frac{m_{\text{gelator}}}{m_{\text{water}} + m_{\text{oil}} + m_{\text{surfactant}} + m_{\text{gelator}}}, \tag{2.4}$$

which is the last parameter needed to fully quantify the composition of a $H_2O$–*n*-decane/12-HOA–$C_{10}E_4$ microemulsion.

### 2.1.2 Phase Behaviour

When water, oil and a surfactant are mixed it depends on the composition of the mixture whether a microemulsion is formed or not. Moreover, one often finds the microemulsion coexisting with a water or/and an oil excess phase in a macroscopically two-phase or three-phase system, respectively [1]. Which situation is encountered can be read from a 'phase diagram' of the system. Given that the system comprises three different components, a suitable phase diagram is a Gibbs triangle the three corners of which stand for water, oil and the surfactant, respectively. However, since the formation of a microemulsion often also depends on additional parameters, like the concentration of a co-surfactant or the temperature, most phase diagrams need to be expanded in a third dimension. In the case of the here discussed ternary water–*n*-alkane–non-ionic surfactant microemulsions the temperature-dependent phase behaviour is fully mapped by a phase prism [22] like the one schematically shown in Fig. 2.1. It can be seen as a stack of isothermal Gibbs triangles as the ordinate axis represents the temperature. The three vertical sides of the prism are the temperature-composition phase diagrams of the binary systems water–oil, water–surfactant and oil–surfactant, respectively. The interplay of their miscibility gaps determines the location of the multi-phase regions within the phase prism. Accordingly, one can also imagine that the prism results from "folding" the three binary phase diagrams together.

To understand the quite complex phase prism it is reasonable to first "unfold" it and look at the binary phase diagrams separately (see Fig. 2.2). The water–oil mixture possesses, as expected, a large miscibility gap which expands for all accessible temperatures over nearly the whole composition range. Water and surfactant, by contrast, mix at low temperatures but with increasing temperature one runs into a (closed) upper miscibility gap with a lower critical point $cp_\beta$ at a critical temperature $T_\beta$, which is usually between 0 and 100 °C. Note that for long-chain surfactants the water–surfactant phase behaviour is much more complex since one also finds liquid crystalline regions; however, this is neglected in the simple representation of Fig. 2.2. The third binary system, oil–surfactant, possess a critical point $cp_\alpha$ which belongs to a lower miscibility gap. The corresponding upper critical temperature $T_\alpha$ normally lies around or somewhat below 0 °C. In a nutshell, the descriptions of the binary systems reveal that the water solubility of the surfactant decreases with increasing temperature while its solubility in oil increases.

The isothermal Gibbs triangles certainly reflect the described behaviour as well (cp. Fig. 2.1). They show at high temperatures two-phase regions with tie-lines sloped in the direction of the water corner indicating the coexistence of a surfactant-rich oil phase with a water excess phase. At low temperatures the situation is inversed and one finds a surfactant-rich water phase coexisting with an excess oil phase. Note that the temperature-dependence of the surfactant's head group hydration, which is high at low and low at high temperatures, essentially influences the described behaviour in the three component mixture because the most part of

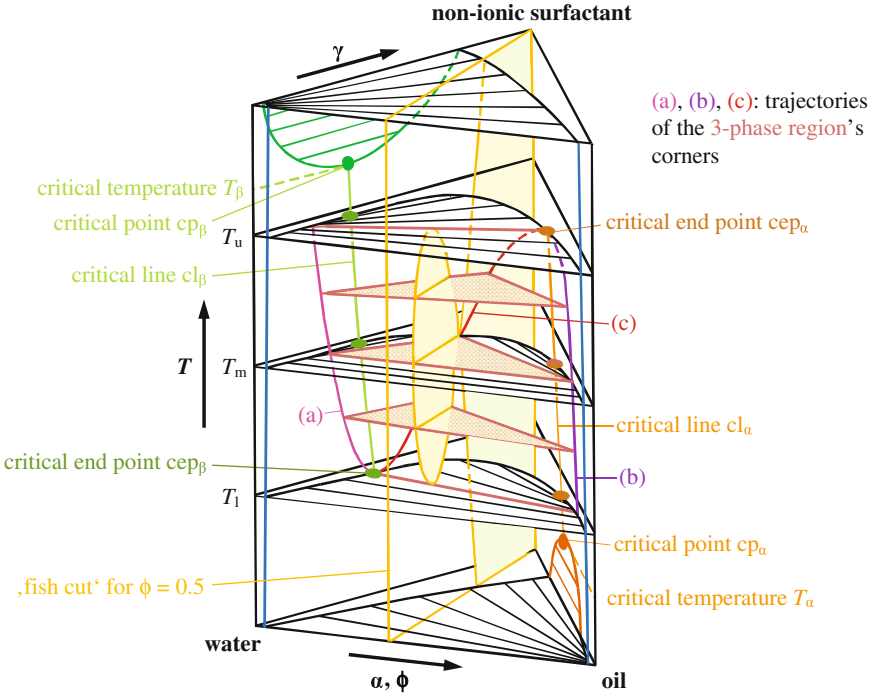


**Fig. 2.1** Schematic phase prism describing the temperature-dependence of a ternary water–oil–non-ionic surfactant microemulsion system (adapted from [89] with permission of the Bunsen Society)

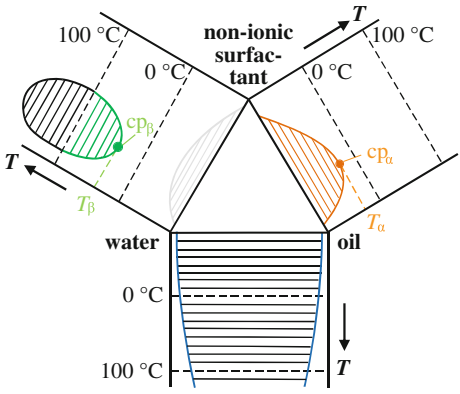


**Fig. 2.2** Unfolded phase prism showing the miscibility gaps in the temperature-composition phase diagrams of the binary systems (adapted from [10] with permission of John Wiley and Sons)

the surfactant is not dissolved in the oil or the water bulk phase as will be explained below. In any case, the gradual inversion from a surfactant-rich water phase at low to a surfactant-rich oil phase at high temperatures results in the formation of a distinct surfactant phase at intermediate temperatures. The latter

coexists with both an oil and a water excess phase in a temperature range between $T_l$ ("$T$ lower") and $T_u$ ("$T$ upper") where a three-phase region is formed. The temperature in the middle of the three-phase range, i.e. the mean temperature $T_m = (T_l + T_u)/2$, is called the 'phase inversion temperature' (PIT). Interestingly, it is exactly at $T_m$ where a minimum amount of surfactant is needed to form a one-phase ternary mixture with equal volumes of water and oil. This follows from geometrical considerations taking into account different trajectories in the phase prism such as the critical lines $cl_\alpha$ and $cl_\beta$ (cp. Fig. 2.1).

Since the three-dimensional phase prism is pretty complex it is hardly possible to fully determine it for every microemulsion system under investigation. Hence one usually limits oneself to studying a "cut" through the prism, like for example an isothermal Gibbs triangle for a certain temperature. This is often sufficient to extract the required information about the system. The cut which was used throughout this work is a $T$-$\gamma$ cut for which the temperature and the surfactant concentration are varied while the water-to-oil ratio is held constant. With the equal volumes of water and oil that were used the $T$-$\gamma$ diagram possesses phase boundaries which are in the ideal case symmetric with respect to the $T_m$ temperature. Furthermore they resemble the contour of a schematic fish such that one also speaks of a 'fish cut diagram' (see Figs. 2.1 and 2.3). On the left hand side of the $T$-$\gamma$ diagram, i.e. for small surfactant mass fractions $\gamma$, the water–oil–non-ionic surfactant mixture consists of two immiscible phases of water and oil. The comprised surfactant self-assembles at the interfacial area and dissolves in part monomerically in the two bulk phases, in particular in the oil. With increasing $\gamma$ one reaches a surfactant concentration $\gamma_0$ at which the bulk phases are saturated and the water–oil-interface is fully occupied by a surfactant monolayer. Thus beyond $\gamma_0$ the surfactant concentration is high enough to solubilize water and oil into one another, i.e. a microemulsion is formed. According to the explanations given above it depends on the temperature whether oil is solubilized in water or vice versa. In any case the surfactant-rich phase constitutes the microemulsion which coexists with so-called 'excess phases'. While an oil excess phase is present at low and a water excess phase at high temperatures one finds both excess phases coexisting with a newly formed microemulsion phase at medium temperatures. Note that the two-phase regions are named $\underline{2}$ and $\overline{2}$; the dash indicating the location of the microemulsion phase. Since with the addition of surfactant more and more volumes of water and oil can be solubilized into one another the excess phases shrink with increasing $\gamma$ until the water–oil–surfactant mixture is one-phase. The smallest amount of surfactant needed to reach the one-phase region is $\widetilde{\gamma}$, which is therefore referred to as the microemulsion's 'efficiency'. Together with the temperature $\widetilde{T}$, which in an ideal system is just the phase inversion temperature $T_m$, $\widetilde{\gamma}$ determines the so-called $\widetilde{X}$ point which is an important and often stated parameter characterizing the microemulsion system.

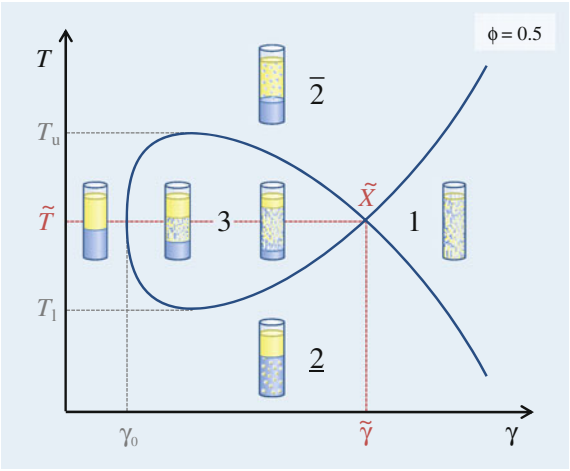


**Fig. 2.3** Schematic $T$-γ ('fish cut') diagram of a water–oil–non-ionic surfactant microemulsion with test tubes illustrating the different phases

## 2.1.3 Microstructure

Very characteristic for microemulsions is, besides the just discussed phase behaviour, their microstructure which is nanometer-sized [1]. Note that the wavelength of visible light is just somewhat larger than the microstructure which explains why microemulsions often appear transparent and show the Tyndall effect. What type of microstructure is formed depends on the local curvature of the amphiphilic film [23] which is determined by the structure and conformation of the surfactant molecules at the water–oil interface. Depending on whether the surfactant's hydrophilic (and hydrated) head groups or their lipophilic chains are sterically more demanding the surfactant monolayer either bends around the oil or around the water, respectively. To quantify this behaviour one specifies the 'mean curvature' of the surfactant film as

$$H = \frac{c_1 + c_2}{2} \tag{2.5}$$

where $c_1$ and $c_2$ are the film's principal curvatures, i.e. the reciprocal radii $R_1$ and $R_2$ of two orthogonal osculating circles at a certain point on the film (cp. Fig. 2.4, right).

Generally, curvature around oil is defined positive and curvature around water negative. If the surfactant film is in an 'optimal shape' $c_1$ and $c_2$ adopt values for which the Helfrich bending energy per unit film area [24]

$$f = 2\kappa(H - H_0)^2 + \overline{\kappa}\, c_1\, c_2 \tag{2.6}$$

becomes minimal. In this equation κ and $\overline{\kappa}$ are elasticity moduli which are measures for the film rigidity and the energy cost to form structures with connected

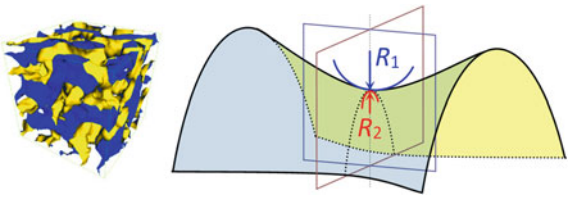


**Fig. 2.4** Three-dimensional model of a bicontinuous structure (*left*, modified from [90]) and its local saddle-like conformation (*right*)

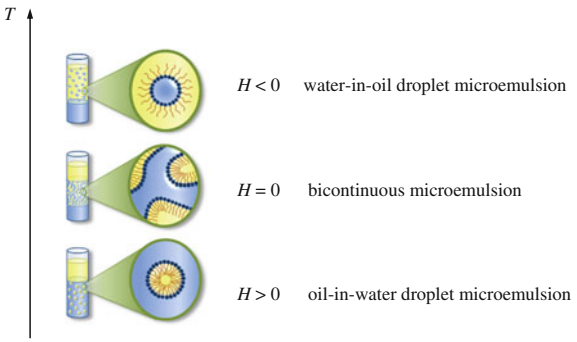


**Fig. 2.5** Schematic representation of the different microstructures which occur in water–oil–non-ionic surfactant microemulsions as a function of temperature

topology (like bicontinuous structures, Fig. 2.4), respectively. $H_0$ is the spontaneous curvature which the interfacial layer would adopt if there were no external forces, thermal fluctuations or conservation constrains.

Due to the very low interfacial tensions in microemulsions the spontaneous curvature is usually quite low, i.e. the curvature radius is much bigger than the thickness of the surfactant layer ($\sim$1 nm). Therefore the surfactant film is very flexible and fluctuates permanently. The most flexible surfactant layer with the strongest fluctuations, along with an ultra-low interfacial tension between the water and the oil phase (down to about $10^{-4}$ N m$^{-1}$ [25]), is found in bicontinuous microemulsions. Here water and oil domains interpenetrate such that a "sponge-like" microstructure with local saddle-like conformations is formed (cp. Fig. 2.4). Thus the interfacial layer is locally planar and for the mean curvature it holds $H = 0$. One also speaks of a "balanced" state since the surfactant head group and chain have effectively the same space requirements. If the latter is not the case the mean curvature deviates from zero and in the extreme cases spherical droplets of water or oil are formed. The mean curvature $H$ is then the reciprocal droplet radius with a positive sign for oil and a negative sign for water droplets. A descriptive reason for the droplet formation is increased repulsive forces which act between the head groups or between the alkyl chains of the surfactant, respectively. In the case of non-ionic surfactants these forces are governed by temperature (cp. Fig. 2.5). When the temperature is low the surfactant head groups are strongly solvated and thus bulky. Hence oil droplets are formed which are dispersed in a continuous water phase ('oil-in-water droplet microemulsion'). At high

temperatures, in contrast, the hydration shell around the head groups is considerably reduced while the alkyl chains are in increased thermal motion. Accordingly one finds a 'water-in-oil (w/o) droplet microemulsion'.

One can conclude that the microemulsion which coexists at high temperatures with an excess water phase is a water-in-oil-droplet microemulsion while at low temperatures it is an oil-in-water-droplet microemulsion that coexists with the oil excess phase. Furthermore, it is self-evident that the microemulsion's microstructure does not change all of a sudden but continuously with the temperature. When the temperature increases the mean curvature $H$ changes from positive to negative values and runs through zero, notably, just at the temperature $\widetilde{T}$. Consequently, microemulsions are bicontinuous at (and, a little less ideally, also around) their $\widetilde{T}$ temperature. This fact was made use of throughout this work. To investigate the microemulsions in the bicontinuous state and in the absence of excess phases samples were prepared with a surfactant mass fraction $\gamma$ slightly above $\widetilde{\gamma}$, then they were studied at or close to $\widetilde{T}$. To facilitate the measurements, i.e. to avoid phase separation upon small temperature fluctuations during the sample handling, the surfactant mass fraction was usually chosen about 2–5 wt% above $\widetilde{\gamma}$. There the one-phase temperature region between $T_{\underline{2}-1}$ and $T_{1-\overline{2}}$ is wider than close to the $\widetilde{X}$ point. However, one must be aware that the bicontinuous microstructure which is ideal at $\widetilde{\gamma}$ is altered the stronger the more the surfactant mass fraction is increased above $\widetilde{\gamma}$. The additional surfactant leads to a stiffening of the surfactant film which is thus less curved such that the water and oil domains are enlarged. Eventually the surfactant film is so rigid that a lamellar liquid crystalline structure is formed. Such high surfactant mass fractions, however, were obviated for the measurements in this thesis.

## 2.2 Base System 2: Binary Gel

The second base system of the gelled bicontinuous microemulsion $H_2O$–*n*-decane/12-HOA–$C_{10}E_4$, which is studied in this thesis, is a "simple" gel of the gelator 12-HOA in which the solvent is not a complex fluid like the bicontinuous microemulsion but an ordinary liquid. Which type of liquid is suitable follows from the chemical structure of 12-HOA (see Fig. 2.6). The latter is a hydroxylated fatty acid, also called 12-hydroxystearic acid, which is a hydrogenation derivative of castor oil and industrially used, e.g., as thickener in lubrication greases [26, 27]. Its "thickening effect" is based on a spontaneous aggregation (self-assembly) of the 12-HOA molecules in solution which can be seen as micro-phase separation of the gelator from the solvent [28]. This micro-phase separation competes with the gelator's solubility in the liquid. Given that both effects are balanced a gel is formed [29, 30]. In the case of 12-HOA this is normally found when the solvent is a non-polar "oil" like, e.g., an *n*-alkane, cyclohexane or benzene. Therefore one classifies 12-HOA as 'organogelator', as opposed to 'hydrogelators' which gel aqueous solutions [31].

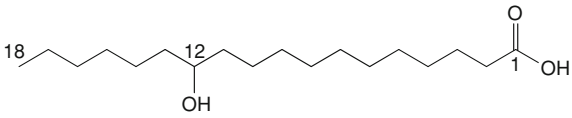


**Fig. 2.6** Molecular structure of 12-hydroxyoctadecanoic acid (12-HOA)

For the thesis at hand it was reasonable to work with *n*-decane as solvent in the 12-HOA gel since this substance was also contained in the investigated microemulsion. Further components were not needed for gel formation, hence the system *n*-decane/12-HOA is often referred to as the "binary gel" in this work. Since the major constituent of a gel is always the solvent [32] the gelator concentration in the studied gels was 1.5, 2.5 wt% and at the most 5.0 wt%. Note that 12-HOA is a chiral molecule due to the hydroxy group at C-atom 12 (see Fig. 2.6).

### *2.2.1 12-HOA as Low Molecular Weight Organic Gelator Building Physical Gels*

As a carbon compound with a molecular weight of 330.48 g $mol^{-1}$ 12-HOA is reckoned among the so-called 'low molecular weight organic gelators' (LMOGs) which make up 'molecular gels' [31]. LMOGs are "gelators that are primarily organic in composition and whose molecular mass is usually less than 2,000 Da" [29]. They can be distinguished from polymeric gelators, like gelatin or polyacrylamide, which are much bigger building blocks for the formation of the three-dimensional gelator network that is found in every gelled system. Thus, another classification for gels is based on the nature of the bonds between the building blocks and in the junctions of the gelator network. When these bonds are covalent one speaks of 'chemical gels' [32]. In 'physical gels', by contrast, those bonds are non-covalent, like, e.g., van-der-Waals interactions, hydrogen or ionic bonds. As a consequence physical gels show a thermoreversible phase-behaviour [28, 29, 32–34]. When they are heated up above a certain temperature they 'melt' and a low-viscous 'sol', i.e. an isotropic solution of freely diffusing gelator molecules, is formed. Cooled down below the 'sol-gel transition temperature' $T_{\text{sol-gel}}$, the gelator molecules self-assemble (again) and the mixture (re-)gels. The temperature of the 'sol-gel boundary' is the higher the higher the gelator concentration, however, it levels off at some point [29] as can be seen in the schematic temperature-composition phase diagram shown in Fig. 2.7. Note that due to the different interactions which stabilize the gelator network in a physical gel the sol-gel transition happens not at a certain point but within a certain temperature range, thus one also speaks of a sol-gel "transition zone".

In chemical gels the situation is different. Their strong covalent bonds do not loosen at elevated temperatures like the non-covalent bonds in physical gels. Hence chemical gels undergo irreversible degradation when they are overheated. Moreover, chemical gels possess a special swelling behaviour due to their

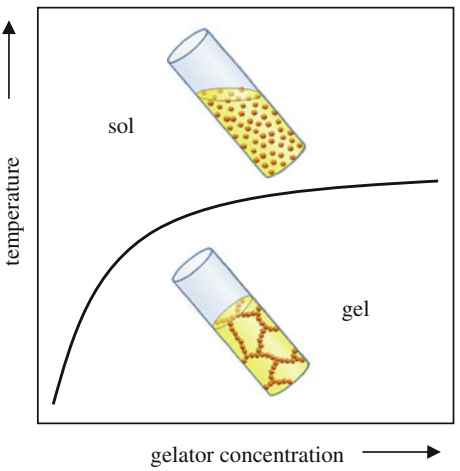


**Fig. 2.7** Schematic representation of a temperature versus gelator concentration phase diagram of a physical gel. The test tubes above and below the sol-gel boundary illustrate the respective states of the solvent/gelator mixture

permanent bonds which is even used for a gel definition in the Dictionary of Polymers [35]. There it is stated that a covalently linked polymer gel "swells in a solvent to a certain finite extend, but does not dissolve even in a good solvent". Physical gels, in contrast, can dissolve or rather do not form if the solvent concentration is too high or the gelator concentration too low, respectively [32].

### *2.2.2 Structure of 12-HOA Gels*

From a topological point of view gels consist of a three-dimensional network which is infinitely extended throughout the whole system and swollen by an embodied solvent [36]. While chemical gels possess discrete connection points in the gelator network one finds in physical gels rather extended 'junction zones' of the gelator strands [37]. In molecular gels the latter are the primary structures formed when the low molecular weight gelator (LMG) molecules self-assemble [31]. This happens upon cooling of the sol which yields a supersaturated mixture wherein a nucleation process initiates. The formed microcrystallites grow preferentially in one dimension such that elongated structures like, e.g., rods or tubes develop [31]. These eventually branch and/or associate building the secondary three-dimensional so-called 'self-assembled fibrillar network' (SAFIN). In the case of 12-HOA one finds dimers of the gelator molecules (pairing their carboxylic acid groups) across the fiber section while hydrogen bonds between the hydroxy groups are the dominating interactions in the direction of the fiber axis [34, 38] (see Fig. 2.8). Moreover, hydrogen bonds can be formed between two neighbouring gelator fibers which expose their hydroxy groups to the fiber surface [39]. This happens in the so-called 'non-permanent' or 'transient junction zones' of 12-HOA networks while the 'permanent junction zones' are branch points of the fibers which arise because of crystallographic mismatches during fiber growth [40].

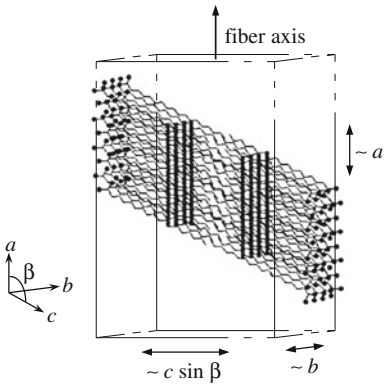


**Fig. 2.8** Structural model of 12-HOA molecules in a gelator fiber wherein the crystal symmetry is monoclinic ($a \neq b \neq c$, $\alpha = \gamma = 90°$, $\beta \neq 90°$). The *dark bands* indicate the hydrogen bonds in the direction of the fiber axis and the *spheres* are the carboxylic acid groups. (Reprinted with permission from [28]. Copyright 1997 American Chemical Society)

Notably the shape and size of the gelator fibers and junction zones is very much dependent on the molecular structure of the gelator [29, 41], on the type of the solvent in the gel [29, 30, 38, 42], on the presence of additives [43] and on the cooling rate upon gel formation [42, 44, 45]. In 12-HOA gels one finds gelator fibers whose cross-section is, e.g., square when the solvent is benzene and rectangular in nitrobenzene where the 12-HOA strands are ribbon-shaped [38]. As regards dimensions, the thickness of gelator fibers is usually in the nanometer range while their length can be of several micrometers. Note that the crystalline packing of the gelator molecules within the gelator fibers differs from the packing in a neat gelator crystal [37, 46]. Another difference between neat gelator crystals and gels is that the former are thermodynamically stable systems while the latter are, though they are long-lived, not in an equilibrium state [47].

### 2.2.3 Mechanical Properties of Gels

When it comes to properties, it is remarkable that though consisting predominantly of a liquid a gel shows a solid-like behaviour [32]. This can be ascribed to the rather rigid (in SAFINs crystalline) gelator fibers and their cross-linking, especially in the permanent junction zones or connection points. The gelator network thus "arrests" the solvent molecules and gives rise to the gel's mechanical stability. The latter is the basis for phenomenological gel definitions like the claimed "self-supporting ability" of gels and the statement that "a gel does not flow" [32]. However, attempting to experimentally test this for a system under investigation one directly faces the questions which environmental conditions to use and how long to wait for a flow of the potential gel. Unfortunately there are no definite answers to these questions—in principle one should observe the sample forever. Yet in practice there is of course always a limit for the timescale of observation. Thus it becomes evident that a gel is "easier to recognize than to define" as Dr. Dorothy Jordan Lloyd already realized in 1926 [48]. An approach to quantify

the solid-like behaviour of gels is to study their rheological properties. Gelled systems are viscoelastic, i.e. they show both characteristics of Hookean solids (elasticity) and of Newtonian liquids (viscosity) [32]. Therefore gels are in an intermediate state in between a solid and a liquid. The rheological parameters representing elasticity and viscosity are the storage modulus $G'(\omega)$ and the loss modulus $G''(\omega)$, respectively, as will be explained in detail in the following Sect. 2.3. These parameters are measureable, however, there is again a limit of observation which is in this case the lowest (angular) frequencies $\omega$ that are accessible by a state-of-the-art rheometer. With the aim to give another, applicable gel definition Almdal et al. specified that "solid-like gels are characterized by the absence of an equilibrium modulus, by a storage modulus, $G'(\omega)$, which exhibits a pronounced plateau extending to times at least of the order of seconds, and by a loss modulus, $G''(\omega)$, which is considerably smaller than the storage modulus in the plateau region" [49].

## 2.3 Rheology

Rheology comes from the Greek word 'rheos' which means 'flow'. Flow, which is nothing but the continuous deformation of a material, occurs as a reaction to experienced stress. Thus, rheology deals with the deformation behaviour of materials which reveals characteristic properties of the latter. For example, squeezing a rubber ball and a piece of dough causes completely different 'responses' from the probed materials and it is indeed these responses that are described, measured and interpreted in rheometrical studies. The basics of rheology have been described in numerous textbooks, like Refs. [50–55], of which the theory relevant for the thesis at hand is explained in this chapter.

### *2.3.1 Basic Definitions*

All rheometry experiments carried out for this work were oscillating shear rheometry measurements. **Shear** deformation of an object is associated to a **shear stress** $\tau$ which results from a force $\boldsymbol{F}$ (of magnitude $F$) directed parallel to one of the object's surfaces $A$

$$\tau = \frac{F}{A}. \tag{2.7}$$

This is illustrated in Fig. 2.9 where a sample is sheared between two plates of distance $z$ the lower of which remains stationary while the upper plate is moved by a distance $x$.

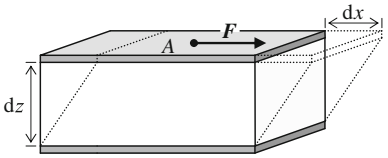


**Fig. 2.9** Shearing a sample between two plates of distance $z$ by moving the upper plate of area $A$ with a force $\boldsymbol{F}$ by the distance $x$

The **shear strain** experienced by the sample is defined as

$$\gamma = \frac{\mathrm{d}x}{\mathrm{d}z}. \tag{2.8}$$

Also important is the **shear rate**, i.e. the shear strain per time unit d$t$, which is equivalent to the shear velocity $v$ (i.e. the shear displacement d$x$ per time unit) at gap width d$z$

$$\dot{\gamma} = \frac{\gamma}{\mathrm{d}t} = \frac{\mathrm{d}x/\mathrm{d}z}{\mathrm{d}t} = \frac{\mathrm{d}x/\mathrm{d}t}{\mathrm{d}z} = \frac{v}{\mathrm{d}z}. \tag{2.9}$$

### *2.3.2 Elastic, Viscous and Viscoelastic Materials and Their Rheologic Behaviour*

Different materials react differently when exposed to a (shear) stress. In general, one distinguishes between **elastic** solids and **viscous** liquids. If an elastic solid is deformed an internal restoring force arises which brings the material back to its initial shape once the external force is released. Thus the deformation is reversible like, e.g., in a spring. According to Hooke, there is a linear proportion between the deformation of the object and the magnitude of the force. Applying this to shear deformations one introduces the shear modulus

$$G = \frac{\mathrm{d}\tau}{\mathrm{d}\gamma} \tag{2.10}$$

as proportionality constant between the shear stress $\tau$ and the shear strain $\gamma$.

If one, by contrast, deforms a viscous liquid the deformation is irreversible since the counterforce to the external force is not a restoring but a frictional force between the particles in the fluid. This is the case, e.g., in a dashpot. The friction is the greater the faster the fluid is deformed. Thus, according to Newton, the shear stress $\tau$ in a shear deformation is linearly proportional to the shear rate $\dot{\gamma}$. The proportionality constant

$$\eta = \frac{d\tau}{d\dot{\gamma}} \tag{2.11}$$

is called the dynamic viscosity of the fluid. This characteristic property can be measured in **stationary**, i.e. **time-independent**, **rheometry** experiments like rotational measurements. One shears the sample with a certain shear rate and determines the respective shear stress. For an ideal Newtonian liquid one single measurement would be enough since its $\tau - \dot{\gamma}$ curve is linear. However, for real liquids Newtonian behaviour is usually found for small shear rates only, i.e. for slow shearing or thick sample layers. At higher shear rates one often observes shear-thinning or shear-thickening behaviour like, e.g., in 'solid paint' and starch suspensions, respectively. Accordingly, one measures non-linear flow curves for such "non-Newtonian" liquids which are described by different more complex models as Newton's simple model is not valid any more. Also temperature has an effect on the dynamic viscosity of a fluid. One finds that $\eta$ decreases for liquid samples with increasing temperature while it increases for gases.

Some, so-called 'plastic' materials appear as solids below a certain yield stress $\tau_B$ while above they are liquid-like and flow. This is described by the Bingham model

$$\tau = \eta_B \, \dot{\gamma} + \tau_B \tag{2.12}$$

in which $\eta_B$ is the plastic viscosity.

Note that a material in a stationary rheometry experiment behaves either as an elastic solid, which reversibly deforms up to a certain point under the experienced stress, or as a viscous fluid, which continuously flows and thus deforms irreversibly under the stress. Many materials, however, do possess both elastic and viscous properties. They are called **viscoelastic** and can be represented by a connection of a spring and a dashpot as, e.g., in the **Kelvin-Voigt model** (connection in parallel; Fig. 2.10, left top) or in the **Maxwell model** (connection in series; Fig. 2.10, left bottom). When a continuous stress is applied these models exhibit solid-like (Kelvin-Voigt model) or liquid-like (Maxwell model) behaviour. However, if stress is applied only temporarily the models' behaviour is more complex. For example, when stress is applied on the Maxwell model between a time $t_0$ and a time $t_1$ (Fig. 2.10, right top) this leads initially to a deformation $\Delta\gamma$ of the spring and between $t_0$ and $t_1$ to a continuous deformation of the dashpot with a rate $\dot{\gamma}$ (Fig. 2.10, right bottom). The dashpot deformation immediately stops once the stress is released at $t_1$ where furthermore the spring resets by $-\Delta\gamma$ to its undeformed state. This leaves the system with a total deformation of $\gamma_1 = \dot{\gamma}(t_1 - t_0)$. Note that it is possible to deduce both the spring constant (from $\Delta\gamma$) and the viscosity of the dashpot fluid (from $\dot{\gamma}$) from the obtained $\gamma$–$t$ curve. Thus, this example demonstrates that when the applied stress in a rheometry experiment is varied as a function of time it is possible to simultaneously yield information on the solid-like and the liquid-like properties of the probed material. Therefore, **non-stationary**, i.e. **time-dependent**, **rheometry** experiments are normally used to study viscoelastic samples like the gelled microemulsions in this thesis.

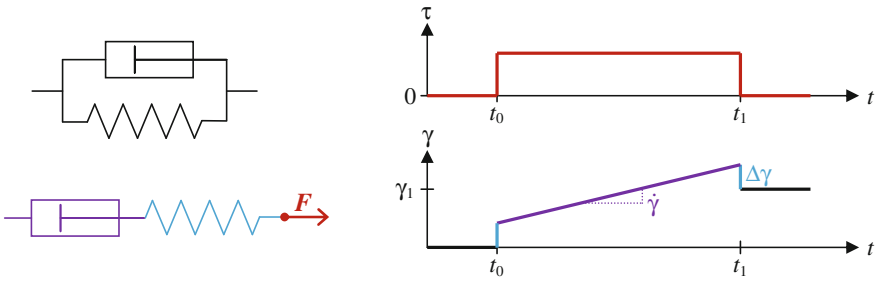


**Fig. 2.10** Kelvin-Voigt model (*left top*) and Maxwell model (*left bottom*) for viscoelastic materials. (*Right*) Stress τ and strain γ versus time *t* curves for the described experiment with the Maxwell model

### 2.3.3 *Studying Viscoelastic Materials with Non-Stationary Rheometry*

If one investigates a viscoelastic material with time-dependent rheometry it is important to be aware of the great impact of (a) the applied stresses and (b) the timescale of observation. This shall be illustrated on the basis of the experiment with the Maxwell model described above (see Fig. 2.11, cp. Fig. 2.10, bottom right).

As it is shown in Fig. 2.11 (left) an increase of the stress τ, which is applied at $t_0$ and released at $t_1$, linearly increases the spring deformation Δγ. Since the spring deformation allows characterizing the solid-like properties of the studied material a sufficiently high stress should be chosen to yield a significant Δγ value. However, if the applied stress is too high the spring is damaged and loses its linear Hookean elasticity which precludes obtaining reasonable results. In a complex fluid this corresponds to an alteration of the system's microstructure by the high stresses which, aiming to probe the original system, one normally seeks to avoid. Therefore, the so-called "**linear viscoelastic (LVE) range**" is usually determined within the first experiments.

To be able to characterize the liquid-like properties of a material, which in the described experiment requires the reliable determination of the slope $\dot{\gamma} = \Delta_{\text{flow}}\gamma/\Delta t = \gamma_1/\Delta t$, it is important to observe the sample deformation over a sufficiently long time span $\Delta t = t_1 - t_0$ (cp. Fig. 2.11, right). Especially when the slope is very small, i.e. when the viscosity of the dashpot fluid is high and it takes a long time for the dashpot to deform, it is the more difficult to notice that $\gamma_1$ differs from zero the shorter the observation time $\Delta t$. However, if no slope and, respectively, no flow are observed this misleadingly implies that the probed model does not consist of a spring and a dashpot but of a spring only. In other words, recognizing the liquid-like properties of a viscoelastic material and thus distinguishing it from a solid material can take a very long time. At this point rheology can even become philosophic. The saying "panta rhei" (Greek) which is ascribed to Heraclitus who

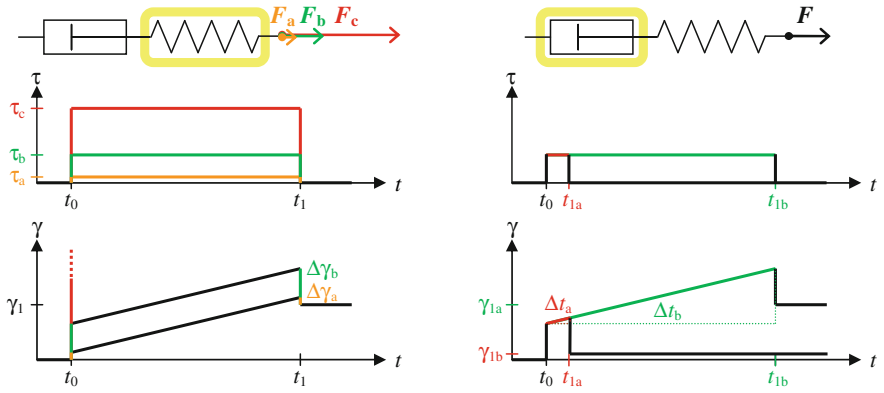


**Fig. 2.11** Impact of the applied stress (*left*) and the timescale of observation (*right*) on the described non-stationary rheometry experiment with the Maxwell model

lived around 500 BC means "**everything flows**"; from a rheological point of view one might complement: it is just a matter of time [51]. An example of a very slowly flowing material which appears solid when observed at room temperature for just a minute, an hour or even a day is the resin pitch. However, the famous pitch drop experiment demonstrates that pitch does possess liquid-like properties: it drops out of a funnel, but only once every 7–12 years (observation period: 1930–2013) [56–58]. In short, while fast (instantaneous) stress variations expose the elastic properties of viscoelastic materials long observation times are preferable to reveal the viscous behaviour. Accordingly, it is beneficial to study a sample on both short and long timescales in a rheometry experiment, being aware that there is always a practical limit of observation as regards the long timescales.

### *2.3.4 Oscillating Shear Rheometry*

A non-stationary method with which one can probe a sample on different timescales is oscillating shear rheometry. In such experiments one applies an alternating shear stress the maximum amplitude of which is within the LVE region. The frequency of the stress variation and thus of the shear deformation corresponds to the inverse timescale of observation. At low frequencies where the sample is sheared slowly the viscoelastic material has enough time to flow while it behaves predominantly elastic when sheared fast at high frequencies. If the shear strain $\gamma$ is sinusoidal and oscillates as a function of time $t$ with the frequency $f$—or, respectively, with the angular frequency $\omega = 2\pi f$—and the maximum amplitude $\gamma_{max}$

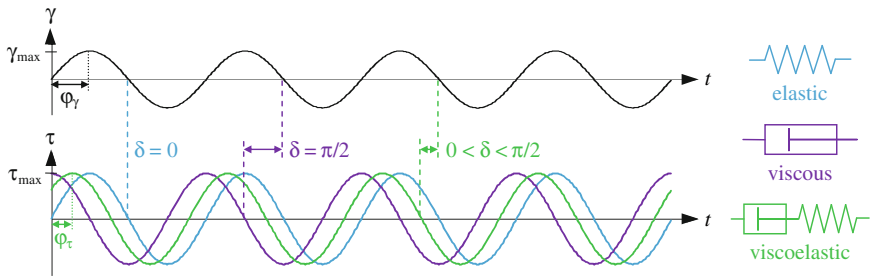


**Fig. 2.12** Sinusoidal shear strain (*top*) and stress responses of different materials (*bottom*)

$$\gamma(t) = \gamma_{max} \sin(\omega t) \tag{2.13}$$

the shear stress $\tau_{elastic}$ in an ideal elastic solid is, according to Hooke, completely in phase with this deformation (phase shift $\delta = 0$) and thus

$$\tau_{elastic}(t) = \tau_{max}\ \gamma(t) = \tau_{max}\ \sin(\omega t) \tag{2.14}$$

with the maximum amplitude $\tau_{max}$ (cp. Fig. 2.12, blue). In an ideal viscous fluid, by contrast, the shear stress $\tau_{viscous}$ is, according to Newton, proportional to the shear rate, i.e. to the shear strain differentiated with respect to the time. Thus it is not in phase with $\gamma(t)$ but cosinusoidal

$$\tau_{viscous}(t) = \tau'_{max}\ \dot{\gamma}(t) = \tau'_{max}\ \frac{d(\gamma_{max} \sin(\omega t))}{dt} = \tau'_{max}\ \omega\ \cos(\omega t) = \tau_{max}\ \cos(\omega t) \tag{2.15}$$

which means phase shifted by $\delta = \pi/2$ (cp. Figure 2.12, purple). When a material is viscoelastic the combination of the elastic and the viscous contributions leads to a phase shift between $\gamma(t)$ and $\tau(t)$ of $0 \leq \delta \leq \pi/2$ (cp. Fig. 2.12, green). This phase shift can be measured and is characteristic for the studied material. The second parameter which is needed to fully characterize the relationship between the shear stress and the strain response of a sample is the ratio between the amplitudes $\tau_{max}$ and $\gamma_{max}$. This ratio is called the **complex modulus**

$$|G^*| = \frac{\tau_{max}}{\gamma_{max}} \tag{2.16}$$

and interpreted as the absolute value of a complex number $G^*$ which is by definition [50]

$$G^*(\omega) \equiv \frac{\tau^*(\omega)}{\gamma^*(\omega)}. \tag{2.17}$$

Thus, $G^*$ can be seen as proportionality constant between $\tau^*$ and $\gamma^*$ at the angular frequency $\omega$, in analogy to the shear modulus definition in Eq. (2.10). The introduction of complex numbers for the description of shear oscillations is simply for reasons of mathematical handiness. The complex numbers allow, e.g., the separation of $G^*$ in a real and an imaginary component called the **storage modulus** $G'$ and the **loss modulus** $G''$

$$G^*(\omega) = G'(\omega) + i\, G''(\omega). \tag{2.17a}$$

As will shortly be evidenced these moduli represent the elastic and the viscous contribution to a viscoelastic material's behaviour (elastic solids *store* applied energy through restoring forces while the energy is *lost* in viscous fluids due to friction). To understand how $G'$ and $G''$ can be determined it is convenient to express the complex number $G^*$ in Euler's notation for which also the shear stress and the shear strain must be expressed as complex functions according to Euler. Thus instead of using sinus or cosine one writes for the oscillating shear stress

$$\tau^*(\omega) = \tau_{max}(\cos(\omega t + \varphi_\tau) + i\ \sin(\omega t + \varphi_\tau)) = \tau_{max}\ e^{i(\omega t + \varphi_\tau)} = \tau_{max}\ e^{i\omega t}\ e^{i\varphi_\tau} \tag{2.18}$$

and for the oscillating shear strain

$$\gamma^*(\omega) = \gamma_{max}\big(\cos(\omega t + \varphi_\gamma) + i\ \sin(\omega t + \varphi_\gamma)\big) = \gamma_{max}\ e^{i(\omega t + \varphi_\gamma)} = \gamma_{max}\ e^{i\omega t}\ e^{i\varphi_\gamma} \tag{2.19}$$

in which $\omega$ is the angular frequency and $\varphi_\tau$ and $\varphi_\gamma$ are the initial phase angles the difference of which yields the phase shift

$$\delta = \left|\varphi_\tau - \varphi_\gamma\right|. \tag{2.20}$$

Note that the imaginary parts of $\tau^*(\omega)$ and $\gamma^*(\omega)$ are irrelevant in practice while the real parts correspond to the time-dependent equations specified above, e.g. Eq. (2.13) which is yielded as real part of Eq. (2.19) if $\varphi_\gamma = -\pi/2$

$$\mathrm{Re}(\gamma^*(\omega)) = \gamma_{max}\ \cos(\omega t + \varphi_\gamma) = \gamma_{max}\ \cos(\omega t - \pi/2) = \gamma_{max}\ \sin(\omega t) = \gamma(t). \tag{2.13a}$$

If one now puts the expressions (2.18) and (2.19) in Eq. (2.17) one can calculate $G^*$ as

$$G^*(\omega) = \frac{\tau_{max}\ e^{i\omega}\ e^{i\varphi_\tau}}{\gamma_{max}\ e^{i\omega}\ e^{i\varphi_\gamma}} = \frac{\tau_{max}}{\gamma_{max}}\ \frac{e^{i\varphi_\tau}}{e^{i\varphi_\gamma}} = |G^*|\ e^{i\delta}. \tag{2.17b}$$

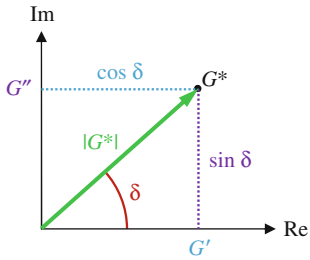


**Fig. 2.13** Visualization of $G^*$ in the complex plane where Im is imaginary and Re the real axis

To eventually clarify the relationship between the complex modulus $|G^*|$, the phase shift δ, which is determined in the measurement, and the storage and loss moduli $G'$ and $G''$, which represent a viscoelastic material's solid-like and liquid-like properties, respectively, one can visualize $G^*$ in the complex plane (Fig. 2.13) [51, 54].

Trigonometrical laws now directly reveal the equations

$$G'(\omega) = |G^*| \cos\delta \tag{2.21}$$

and

$$G''(\omega) = |G^*| \sin\delta \tag{2.22}$$

according to which the storage modulus $G'$ and the loss modulus $G''$ are calculated in a rheometry experiment. Note that $G'$ and $G''$ have the same unit as the complex modulus $|G^*|$ which originates from $\tau_{max}$ as one can see in Eq. (2.16) and is thus pascals. The assignment of these two moduli to elastic and viscous behaviour, respectively, becomes obvious when one puts into the Eqs. (2.21) and (2.22) the two possible boundary values for the phase shift between the stress and the strain oscillation, i.e. $\delta = 0$ and $\delta = \pi/2$. As explained above, stress and strain are in phase for an elastic solid. Thus with $\delta = 0$ one obtains $[G'(\omega)]_{\text{elastic},\delta=0} = |G^*|$ and $[G''(\omega)]_{\text{elastic},\delta=0} = 0$ which shows that the loss modulus vanishes for perfect elasticity. The opposite is true for perfectly viscous fluids in which stress and strain are out of phase by $\delta = \pi/2$. Here one obtains $[G'(\omega)]_{\text{viscous},\delta=\pi/2} = 0$ and $[G''(\omega)]_{\text{viscous},\delta=\pi/2} = |G^*|$, respectively. In general, it holds for viscoelastic materials that they behave the more solid-like the bigger the storage modulus in comparison to the loss modulus, i.e. the smaller the 'loss factor'

$$\frac{G''}{G'} = \tan\delta. \tag{2.23}$$

Note that for defined models such as the Maxwell or the Kelvin-Voigt model one can form constitutive equations which unequivocally relate stress and strain. Based on such an equation it is possible to find explicit expressions for $G'(\omega)$ and

$G''(\omega)$ which depend on characteristic parameters of the sample like the shear modulus and the dynamic viscosity. Thus, data measured in a rheometry experiment can be fitted to these expressions in order to yield the characteristic quantities as fit parameters. Moreover, the quality of the fit indicates whether the applied model is appropriate for the studied sample. Many viscoelastic materials, however, possess an intricate rheological behaviour and cannot be described by simple models. Thus complex models have been developed which are, e.g., based on different interconnections of numerous Hookean springs and Newtonian dashpots.

### 2.3.5 Stress-Controlled Shear Rheometer

In non-stationary rheometry experiments one usually determines the storage modulus $G'$ and the loss modulus $G''$ as a function of the frequency. For the thesis at hand this was accomplished through oscillation measurements on a stress-controlled shear rheometer with a plate–plate geometry. In such a rheometer the sample is placed between two circular plates of distance $z$ the lower of which is stationary while the upper plate, which has a radius $R$, is moved via an electric motor (Fig. 2.14). The generated movement is rotative around the plate's center axis, in contrast to the linear displacement assumed above where the basic parameters of shear deformation were introduced. Therefore, shear stress and shear strain must be translated to parameters which are used for describing circular motion.

Shear stress, according to Eq. (2.7), is the force $F$ applied on an area $A$. In circular motion a force of magnitude $F$ which takes effect at a distance $r$ from the axis gives rise to a momentum of force (torque) $\boldsymbol{M}$ of magnitude

$$M = F\, r. \tag{2.24}$$

On the moving plate of the rheometer force affects each area element $\mathrm{d}A$, which, through differentiation of a circular area of radius $r$, can be expressed as

$$\mathrm{d}A = 2\pi\, r\, \mathrm{d}r. \tag{2.25}$$

Thus, if one applies the torque $M$ on a circular rheometer plate of radius $R$ the sample experiences the shear stress

$$\tau = \frac{F}{\mathrm{d}A} = \frac{M}{2\pi\, r^2\, \mathrm{d}r} = \frac{M}{2\pi \int_0^R r^2\, \mathrm{d}r} = \frac{3\, M}{2\pi\, R^3}. \tag{2.7a}$$

Inversely, a converted form of Eq. (2.7a) can be use to determine the torque $M(\omega, t)$ that an electromotor must produce in order to exert a specified oscillating shear stress $\tau(\omega, t)$ of angular frequency $\omega$ on a sample between the rheometer plates.

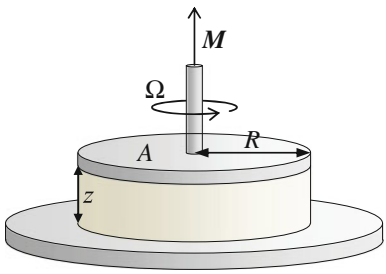


**Fig. 2.14** Plate–plate geometry of a shear rheometer (the parameters are explained in the text)

The measured quantity in a stress-controlled rheometer is the shear strain which is the ratio of the shear deformation to the gap width (cp. Eq. 2.8). The shear deformation is specified as the circular arc, which is of course different for different radii; however, it is the convention to quote the arc for the plate radius $R$. To calculate the arc one needs the angle of rotation $\alpha$ which is measured by a displacement sensor. Thus one yields the shear strain as

$$\gamma = \frac{\mathrm{d}x}{\mathrm{d}z} = \frac{R\,\alpha}{z}. \tag{2.8a}$$

Note that besides stress-controlled there are also strain-controlled shear rheometers which work according to the inverse concept: a certain shear strain $\gamma(\omega, t)$ is applied and the resulting shear stress $\tau(\omega, t)$ is measured. As regards the measurement geometry apart from plate–plate assemblies one also uses cone–plate systems in which the moving element is not an even plate but a shallow cone (angle $\leq 4°$). The advantage of using a cone is that the shear rate at an angular velocity $\Omega$ is uniform across the gap while in a plate–plate system $\dot{\gamma}$ depends also on the radius $r$

$$\dot{\gamma} = \frac{\gamma}{\mathrm{d}t} = \frac{r\,\mathrm{d}\alpha/\mathrm{d}t}{\mathrm{d}z} = \frac{r\,\Omega}{\mathrm{d}z}. \tag{2.9a}$$

An even shear velocity distribution is desirable particularly in stationary rotational shear rheometry experiments. However, for the present study with non-stationary oscillating shear rheometry experiments the plate–plate assembly was preferable since it allows adjusting the gap width to the needs of the sample which is not possible in a cone–plate system.

## 2.4 Fourier Transform Pulsed-Gradient Spin-Echo NMR Spectroscopy

Fourier transform pulsed-gradient spin-echo (FT-PGSE) nuclear magnetic resonance spectroscopy, also known as pulsed field gradient NMR or PFG-NMR, is a sophisticated technique for studying translational diffusion processes. The basic

principle is to measure the attenuation of the spin-echo signal in an NMR spin-echo experiment, during which pulses of a defined magnetic field gradient are applied. As the echo attenuation is induced by the displacement of the spin in the direction of the gradient the self-diffusion coefficient of the corresponding molecule can be computed. A great benefit of the Fourier transform variant of the PGSE NMR method is that it allows determining simultaneously self-diffusion coefficients of different components in one sample. This is possible since Fourier transforming the generated echo signal yields multiple signals in the frequency domain which can be assigned to the different species in the sample according to their chemical shifts. Consequently, one can follow the attenuation of each signal separately and obtains the individual self-diffusion coefficients $D$, e.g. of water and oil in a microemulsion. Another advantage of the FT-PGSE NMR technique is that it is non-invasive and non-destructive, i.e. neither the sample composition needs to be changed (e.g. by adding tracer molecules) nor is the sample destroyed by the measurement [59].

### 2.4.1 Fundamentals of Self-Diffusion and NMR Spectroscopy

Self-diffusion is the most fundamental transport mechanism of molecules and particles in fluid systems [60]. It results from random-walk processes due to thermal motion and leads to a radial Gaussian distribution of particles which all started at time $t = 0$ in the position $\boldsymbol{r_0}$ of an infinitely large, isotropic, homogeneous system. The probability to find one of the particles at time $t$ in the position $\boldsymbol{r}$ is thus [61]

$$P(\mathbf{r}_0, \mathbf{r}, t) = (4\pi Dt)^{-3/2}\, e^{-\frac{(\mathbf{r}-\mathbf{r}_0)^2}{4Dt}}. \tag{2.26}$$

This equation reveals that the self-diffusion process is fully described by the parameter $D$, i.e. the self-diffusion coefficient which is measured in the PGSE NMR experiment. The average displacement of particles via self-diffusion is zero. However, for the mean square displacement it holds

$$\left\langle |\boldsymbol{r} - \boldsymbol{r_0}|^2 \right\rangle = \left\langle r^2 \right\rangle = nDt \tag{2.27}$$

and the root mean square displacement is

$$\sqrt{\langle r^2 \rangle} = \sqrt{nDt} \tag{2.28}$$

in which $n = 2$, 4 or 6 for one-, two- or three-dimensional displacement, respectively. Equation (2.27) states that the mean square displacement of a self-diffusing molecule scales linearly with time which is what one finds in samples of

neat substances. The self-diffusion coefficient measured in the case of free self-diffusion is denoted $D_0$ and for low viscous solvents (e.g. water, alkanes) it lies in the order of $10^{-9}$ m$^2$ s$^{-1}$. However, when the self-diffusing molecules encounter obstruction within the observation time the situation is different. If, for example, an additional compound is present which forms aggregates or encloses itself in a solvation shell this can slow down the effective motion of the investigated molecules. Consequently, a reduced self-diffusion coefficient $D$ is measured which therefore contains structural information about the sample. Note that studying the microstructure of microemulsions via FT-PGSE NMR spectroscopy is possible particularly for this reason as will later be explained in detail.

If a sample is placed in a static and homogeneous magnetic field $\boldsymbol{B}$, as it is the case in an NMR spectrometer, the magnetic moments $\boldsymbol{\mu}$ associated to nuclear spins $\boldsymbol{I} \neq 0$ account for a net magnetisation $\boldsymbol{M}$ which is aligned parallel to the field. This happens due to the quantization of spin states which allows for a spin only $2I + 1$ orientations (specified as $m_\mathrm{I} = -I, -I + 1, \ldots, I$) with respect to an arbitrary axis, i.e. the direction of the magnetic field, usually referred to as the $z$-direction. The magnetic field causes energy level splitting for the different spin orientations which in case of protons ($I_\mathrm{proton} = ½$) results in slightly more low-energy 'α-spins' ($m_\mathrm{I} = ½$) than high-energy 'β-spins' ($m_\mathrm{I} = -½$). According to Boltzmann the ratio of the populations of the different energy levels in thermodynamical equilibrium is given by

$$\frac{N_\beta}{N_\alpha} = e^{-\frac{\Delta E}{k_\mathrm{B} T}} \tag{2.29}$$

where $N_\alpha$ and $N_\beta$ are the numbers of α-spins and β-spins, respectively, $k_\mathrm{B}$ is the Boltzmann constant, $T$ the absolute temperature and $\Delta E$ the energy difference between the two spin states. The latter is directly proportional to the strength of the magnetic field $B$ and can be overcome, i.e. spin reorientation can be induced, by irradiation of the resonance frequency $\nu_\mathrm{L}$, the so-called Larmor frequency. It holds

$$\Delta E = \hbar\, \gamma_\mathrm{g}\, B = h\, \nu_\mathrm{L} \tag{2.30}$$

where $h$ is the Planck constant ($h = 2\pi\hbar$) and the coefficient $\gamma_\mathrm{g}$ is the gyromagnetic ratio which is characteristic for the respective nucleus (e.g. proton: $\gamma_\mathrm{g,pr.} = 2.675 \times 10^8$ s$^{-1}$ T$^{-1}$ [62]). For example, in a magnetic field of 9.4 Tesla the Larmor frequency of protons is 400.2 MHz (hence, an NMR instrument with such a magnetic field is called a '400 MHz spectrometer'). To picture the energy difference between the spin states the spins are usually described as precessing with their Larmor frequency around the direction of the magnetic field. Therefore, the $x$- and $y$-components $\mu_\mathrm{x}$ and $\mu_\mathrm{y}$ of all magnetic moments in the sample cancel out while the $z$-components $\mu_\mathrm{z}$ sum up to the net magnetisation $\boldsymbol{M}$ in the direction of the magnetic field $\boldsymbol{B}$. By irradiating radio frequency pulses the sample can be excited which generates oscillating $x$- and $y$-components of the magnetisation $M_\mathrm{x}(t)$ and $M_\mathrm{y}(t)$. These magnetisation components, in turn, induce the measured

signal in the detector coil which is located in the *xy*-plane. As the spins relax to thermodynamic equilibrium the detected signal decays exponentially for which it is referred to as 'free induction decay' or 'FID signal'. In general, two relaxation processes are distinguished. Firstly, the spins flip their orientations and re-establish the equilibrium populations of the α- and β-energy levels (see Eq. 2.29) with a time constant $T_1$ which is called the longitudinal or spin–lattice relaxation. Secondly, the spins lose their phase coherence with a time constant $T_2$ due to different precession velocities induced by fluctuating fields which is referred to as transversal or spin–spin relaxation.

### 2.4.2 Principle of the PGSE NMR Experiment

In general, PGSE NMR experiments are based on radio frequency pulse sequences which induce a so-called 'spin-echo' signal. The easiest example is the $[\pi_x/2 - \tau - \pi_x - \tau]$ sequence, commonly referred to as 'Hahn echo' [63], which is depicted in Fig. 2.15.

The first $\pi_x/2$-pulse in the Hahn spin-echo experiment rotates the magnetisation in the *xy*-plane after which an FID signal is observed as the spins dephase because they possess different Larmor frequencies. This is predominantly due to inhomogeneities of the magnetic field $\boldsymbol{B}$ of the spectrometer. In order to eliminate this experimental effect and to follow the pure spin–spin relaxation process, a second radio frequency pulse ($\pi_x$-pulse) is irradiated after a time period τ. This pulse is twice as long as the first one and inverts the spin positions. Now the ongoing precession of the spins refocuses them which leads to an echo signal of the FID at time 2τ. Comparing the intensity of the echo to that of the original FID one can deduce the characteristic spin–spin relaxation time $T_2$. In PGSE NMR, however, one is not interested in $T_2$ but in the self-diffusion velocity of the studied molecules. Therefore, rather than correcting for magnetic field inhomogeneities an inhomogeneous field is created on purpose. This happens in a well-defined manner by applying a magnetic field gradient of strength $g$ along the sample tube, i.e. along the $z$-axis. Now different positions in the sample correspond to different Larmor frequencies which, in turn, are like spacial labels for the spins [64]. Consequently, if a molecule does not reside in the same position during the dephasing ($0 < t < \tau$) and the rephasing ($\tau < t < 2\tau$) period, which is the case when the molecule self-diffuses, the spin-echo signal is reduced. The observed echo attenuation is the stronger the bigger the gradient or the larger the molecule's displacement. The latter depends on the self-diffusion velocity, characterized by the self-diffusion coefficient $D$, as well as on the probed time span which in PGSE NMR experiments is conventionally called the 'diffusion time' Δ. Concerning the magnetic field gradient it was found that pulsed rather than static gradients are more convenient [59] (actually this is where the name PGSE NMR comes from). Accordingly, the impact of the gradient depends both on the strength $g$ and the

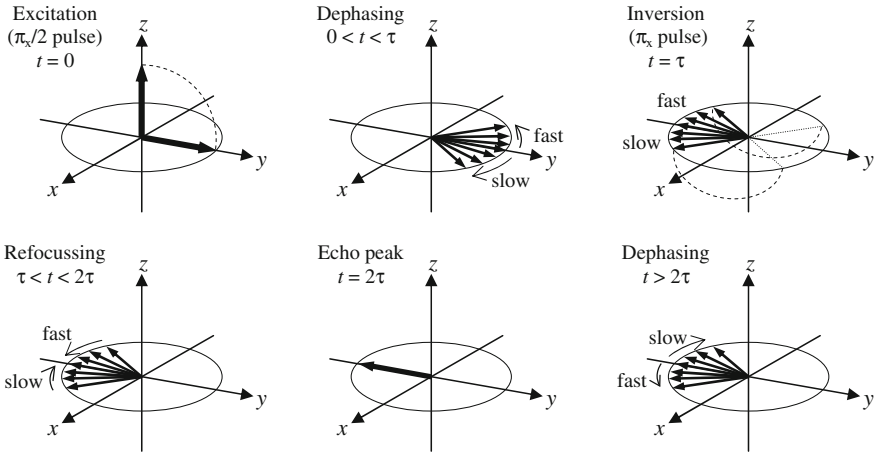


**Fig. 2.15** The $[\pi_x/2 - \tau - \pi_x - \tau]$ pulse sequence of the Hahn spin-echo experiment. (Reprinted from *Progress in NMR Spectroscopy*, Vol. 19, P. Stilbs, Fourier Transform Pulsed-Gradient Spin-Echo Studies of Molecular Diffusion, 1–45, Copyright 1987, with permission from Elsevier)

duration δ of these pulses. It holds for the influence of the parameters $D$, Δ, $g$ and δ on the intensity $S$ of the echo signal at time $t = 2\tau$ [59]

$$S(2\tau) = S(0)\, e^{-2\tau/T_2}\, e^{-\gamma_g^2\, g^2\, D\delta^2\, (\Delta - \delta/3)} \tag{2.31}$$

where $S(0)$ is the FID intensity directly after the first $\pi_x/2$-pulse and $\gamma_g$ is the gyromagnetic ratio of the observed nucleus. The equation is specific for the so-called Stejskal Tanner PGSE NMR experiment [59], which is based on the Hahn spin-echo pulse sequence [63] explained above. Thus the first exponential term accounts for spin–spin relaxation with the transversal relaxation time $T_2$. The second exponential term, however, is determined exclusively by self-diffusion. If Eq. (2.31) is normalized with respect to the echo intensity observed in the absence of a magnetic field gradient, i.e.

$$S(2\tau)_{g=0} = S(0)\, e^{-2\tau/T_2}, \tag{2.32}$$

the universal Stejskal Tanner equation [59] for the echo signal attenuation $E$ due to self-diffusion in PGSE NMR experiments is obtained for which it holds

$$E = \frac{S(2\tau)}{S(2\tau)_{g=0}} = e^{-\gamma^2\, g^2\, D\delta^2(\Delta - \delta/3)}. \tag{2.33}$$

The Stejskal Tanner pulse sequence is depicted in Fig. 2.16 where the gradient strength $g$, the gradient duration δ, the diffusion time Δ as well as the defocusing and the refocusing time periods τ are shown.

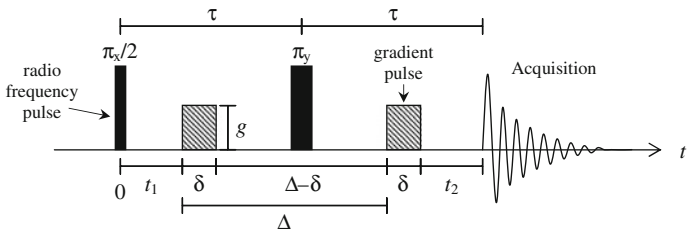


**Fig. 2.16** Pulse sequence of the Stejskal Tanner experiment (redrawn from [91] with permission of John Wiley and Sons)

When a molecule with the self-diffusion coefficient $D$ is studied in a Stejskal Tanner experiment with constant time period τ, an increase of any of the parameters $g$, δ or Δ results in a stronger attenuation of the echo signal. Thus, if a series of measurements is performed in which one of these values is varied, $D$ can easily be obtained by fitting the experimental data to Eq. (2.33). In a semi-logarithmic plot of the echo attenuation $E$ versus the varied parameter or, respectively, versus the term $\left\{\gamma_g^2 g^2 \delta^2 (\Delta - \delta/3)\right\}$, the self-diffusion coefficient $D$ can directly be extracted from the slope of the curve. Experimentally it is most convenient to change the gradient strength $g$ while keeping constant all times of the pulse sequence. Hence, the contribution of spin relaxation to the echo attenuation remains unaltered and simply cancels out. But also other practical issues have to be considered. For example, the diffusion time Δ as well as the gradient strength $g$ and duration δ must be chosen such that an echo signal with a reasonable signal-to-noise ratio is obtained. In this regard one must keep in mind that the echo attenuation in PGSE NMR experiments originates not only from self-diffusion but also from spin relaxation processes. In case of the standard $\left[\pi_x/2 - \tau - \pi_y - \tau\right]$ Stejskal Tanner sequence (cp. Fig. 2.16), for example, it depends directly on the spin–spin relaxation time $T_2$. However, various sequences for specific situations have been developed (e.g. [65–67]). A well-established one is based on the stimulated spin-echo method by Hahn which comprises three $\pi_x/2$ radiofrequency pulses [63]. The corresponding PGSE NMR sequence with two additional magnetic field gradient pulses was first described by Tanner in 1970 [68] and is depicted in Fig. 2.17.

Tanner's stimulated echo sequence, just like the Stejskal Tanner experiment, comprises a first $\pi_x/2$-radiofrequency pulse which rotates the magnetisation in the $xy$-plane whereupon the spins start to dephase. Then, however, instead of a $\pi_x$-pulse a second $\pi_x/2$-pulse is applied which aligns the magnetisation again along the $z$-axis while the system memorizes the experienced loss of phase coherence. In this state the magnetisation is only subjected to spin–lattice relaxation which, as can be seen Fig. 2.17, holds true during most of the diffusion time Δ. Hence, when longitudinal relaxation is slower than spin–spin relaxation, i.e. $T_1 \gg T_2$, which is true for many species, especially large molecules, the stimulated spin-echo method

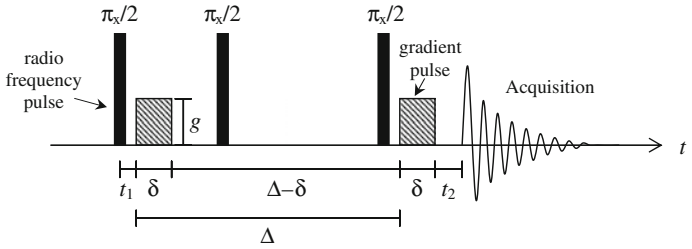


**Fig. 2.17** Pulse sequence of the Tanner pulsed-gradient stimulated spin-echo experiment (redrawn from [91] with permission of John Wiley and Sons)

by Tanner is often superior to the ordinary Stejskal Tanner experiment. As explained above, it allows under these circumstances to probe longer diffusion times Δ, which gives the molecules enough time to move significant distances such that a measurable self-diffusion effect on the attenuation of the echo signal is obtained. The latter is finally stimulated by a third $\pi_x/2$ pulse which returns the magnetisation in the *xy*-plane restoring the spin's phase angles with reversed signs. One has to be aware that in this sequence the maximum amplitude of the stimulated echo detected after spin refocusing is intrinsically only 50 % of the original signal [68]. However, due to the explained advantages, the experiment is still often superior to other techniques and therefore frequently applied—just as in the work at hand. Further relevant experimental details like strategies to prevent convective flow in the sample due to temperature gradients and the application of magnetic field gradient pulses of non-rectangular shape are covered in the Experimental Methods (Sect. 6.7).

### *2.4.3 General Strategy for Studying Microemulsions via FT-PGSE NMR Spectroscopy*

As mentioned above, the basic fact which allows studying the microstructure of microemulsions by PGSE NMR spectroscopy is that self-diffusion coefficients contain structural information about a sample if free self-diffusion in the latter is confined on a length scale probed in the experiment [64]. A detailed explanation of how this principle applies to microemulsions will be given below. Furthermore, the Fourier transform (FT) extension of the PGSE method opens up the possibility to simultaneously measure the self-diffusion coefficients *D* of several components in one sample [69], e.g. water, the oil compound as well as the surfactant in a microemulsion.

A typical diffusion time applied in a PGSE NMR experiment is $\Delta = 10$ ms. Thus, according to Eq. (2.28), after this period the average one-dimensional displacement of an $H_2O$ molecule in a pure water sample with $D_{0,H_2O} = 2.3 \times 10^{-9}$ m$^2$ s$^{-1}$ at 25 °C [70] is 6.8 µm. (Note that due to the simple magnetic field gradient along the

$z$-axis only the self-diffusional motion in this single direction is monitored, i.e. $n = 2$ in Eq. (2.28)). A microemulsion, however, possesses a microstructure with domain sizes in the nanometer range. Hence, travelling over micrometer distances a water molecule in the microemulsion encounters obstruction which hinders its motion. In detail, what is observed is the following: In the case of a water-in-oil droplet microemulsion a water molecule reaches numerous times the confining surfactant layer at the water–oil interface during the investigated time span $\Delta$. Therefore, the effective displacement of the water molecule is just as big as the displacement of the droplet it resides in. Because the latter moves relatively slow, a quite small $D_{H_2O}$ value results. In a bicontinuous microemulsion the situation is different. Here the self-diffusion of the $H_2O$ molecule in the water domains is only restricted in two dimensions. Accordingly, one measures a larger self-diffusion coefficient $D_{H_2O}$ than in the water-in-oil droplet microemulsion. Eventually, when an oil-in-water droplet microemulsion is formed, $D_{H_2O}$ approaches the value $D_{0,H_2O}$ for unrestricted self-diffusion since water is the continuous phase of the system. The presence of the oil droplets gives rise to only minor obstructive effects determined by the droplet volume fraction and shape. This discussion demonstrates how measuring the self-diffusion coefficient of water one can monitor the change of the microstructure in a microemulsion [71–74]. Of course, exactly the same observations as for $D_{H_2O}$, albeit inversed, are made for the self-diffusion coefficient of the oil component $D_{oil}$. The surfactant molecules at the water–oil interface, by contrast, travel in both water-in-oil and oil-in-water microemulsions effectively just as fast as the microemulsion droplets. However, in bicontinuous microemulsions one observes lateral self-diffusion of the surfactant molecules along the interfacial layer and therefore in principle a maximum of $D_{surfactant}$ [73].

In this thesis microemulsions with non-ionic surfactants are studied which change their microstructure as a function of temperature. Hence, when this change is followed with the FT-PGSE NMR method it is important to keep in mind that self-diffusion is a temperature-dependent process itself. Originating in the thermal motion of the molecules, which increases with increasing temperature, the self-diffusion coefficients are naturally the bigger the higher temperature. This is directly found for $D_0$ of pure substances. The self-diffusion coefficients $D$ measured in structured systems, however, combine the temperature and the microstructure effects. In order to interpret the self-diffusion coefficients measured in a microemulsion in terms of the microstructure it is therefore advisable to normalize them with respect to the self-diffusion coefficients $D_0$ of the pure solvents [75]

$$D_{rel} = \frac{D}{D_0}. \tag{2.34}$$

If the relative self-diffusion coefficients of water and oil are then plotted versus the temperature, i.e. the tuning parameter for the microstructure, one finds the values changing as shown schematically in Fig. 2.18.

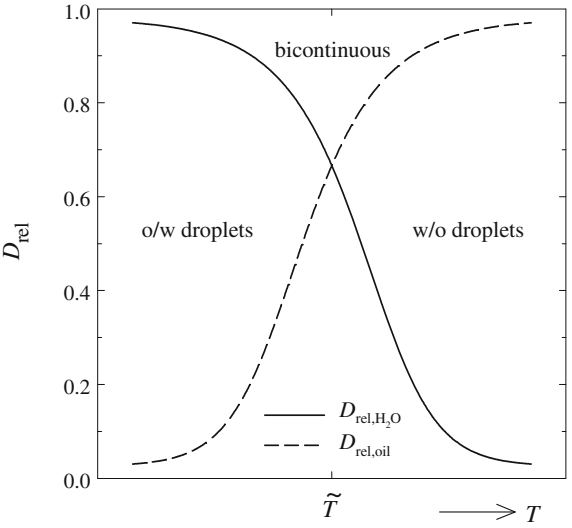


**Fig. 2.18** Schematic diagram of the normalized self-diffusion coefficients $D_{rel}$ of water and oil in a non-ionic microemulsion plotted versus the temperature $T$ [92]. For an ideal structure and equal volume fractions of water and oil the intersection of the two curves is located at $D_{rel} = 2/3$ [75] and $T = \widetilde{T}$

According to the explanation given above, the parameter $D_{rel}$, which is also referred to as "obstruction factor", is in droplet microemulsions high for the molecules of the continuous phase and small for the species enclosed in the droplets [73]. Thus, within the transition from a oil-in-water droplet microemulsion at low temperatures to a water-in-oil droplet microemulsion at high temperatures $D_{rel,H_2O}$ continuously decreases while $D_{rel,oil}$ continuously increases, respectively (see Fig. 2.18). In the intermediate bicontinuous regime where the microstructure inverts as the mean curvature of the surfactant layer runs through zero at $T = \widetilde{T}$ the relative self-diffusion coefficients of water and oil are equal. Hence $D_{rel,H_2O}(T)$ and $D_{rel,oil}(T)$ intersect for which it holds [75]

$$D_{rel,H_2O}(\widetilde{T}) = D_{rel,oil}(\widetilde{T}) = \frac{2}{3}, \tag{2.35}$$

given that the volume ratio of water and oil in the microemulsion is 1:1 and the structure is without any defects.

## 2.5 Small Angle Neutron Scattering

Small angle neutron scattering (SANS) is a powerful method for studying the microstructure of soft matter materials in size ranges from a few Ångströms up to hundreds of nanometers [76]. The underlying basic scattering theory is the same as for other small angle scattering experiments like small angle X-ray scattering (SAXS) or small angle light scattering (SALS). In fact, while Guinier's pioneering

work on SAXS dates to the late 1930s [77] the development of SANS started about 30–40 years later [76, 78]. This is because only then suitable techniques for the generation of free neutrons and their detection became available. Free neutrons can only be generated in large-scale facilities such as the research reactor of the Institute Laue-Langevin (ILL) in Grenoble, France, or the Research Neutron Source Heinz Maier-Leibnitz (FRM II) in Garching near Munich, Germany. Therefore beam time for SANS experiments is usually limited. However, applying for beam time and spending nights in the neutron guide hall is well worth the effort because of the inherent advantages of the SANS method. First of all it is completely non-destructive, i.e. the neutron radiation does not alter the sample. Secondly, SANS offers the unique possibility to vary and adjust the scattering contrast by selectively deuterating different sample components [76, 78, 79]. This allows masking or, respectively, highlighting different parts of the microstructure.

### 2.5.1 The SANS Experiment

When free neutrons are generated in a nuclear reactor in a controlled fission reaction of, e.g., uranium ($^{235}$U) this happens at extremely high temperatures which means that the free neutrons move very fast. Due to the thermal energy of the order of $k_B\ T$ a neutron has the velocity

$$v = \sqrt{\frac{2\ k_B\ T}{m_{neutron}}} \tag{2.36}$$

in which $k_B$ is the Boltzmann constant, $T$ the absolute temperature and $m_{neutron} = 1.675 \times 10^{-27}$ kg [62] the mass of the particle. Moreover, one can ascribe a certain wavelength $\lambda$ to the moving neutron according to the de Broglie formalism. With the Planck constant $h$ one yields

$$\lambda = \frac{h}{v\ m_{neutron}}. \tag{2.37}$$

The idea of the wave-particle duality is important for the SANS experiment because the scattering pattern is understood as the result of superimposed neutron waves, as will shortly be explained, while one records it by counting the number of neutrons encountering the detector plane [76]. However, before the generated neutrons are guided to the sample they are slowed down in a so-called moderator. The latter transforms the initially "hot" neutrons, moving with more than 4,000 m s$^{-1}$, to "thermal" and "cold" neutrons which are used for the SANS experiment [76]. Typically one works with neutron beams with wavelengths in the order of 10 Å which, according to Eqs. (2.36) and (2.37), corresponds to cold neutrons ($T \approx 10$ K) moving with a velocity of about 400 m s$^{-1}$. The moderated neutron beam is monochromized by a mechanical velocity selector, i.e. a rotating

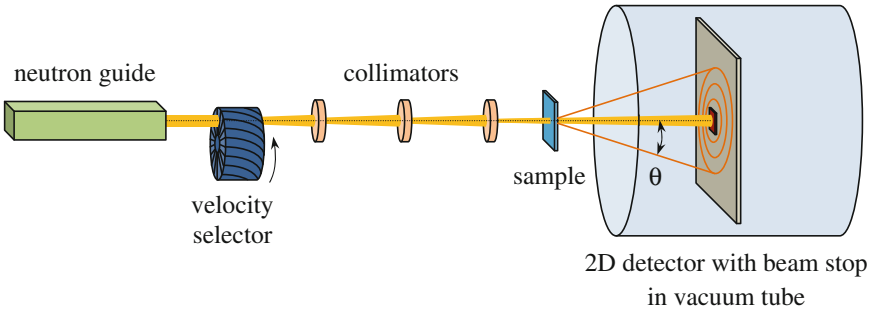


**Fig. 2.19** Schematic representation of the set-up of a SANS experiment in which one detects the intensity of the scattered neutron beam at different scattering angles θ. (Redrawn and modified from http://physics.unifr.ch/en/page/296/, 09.07.2013)

cylinder with helically curved slits which, according to its rotation speed, lets pass only neutrons of a certain narrow velocity distribution of the order of $\Delta\lambda/\lambda \approx 10$ %. This distribution can further be confined by a so-called chopper after which one adjusts the divergency and diameter of the neutron beam with a set of collimators. Finally, an aperture defines the beam size and shape directly in front of the sample. Since most of the neutrons pass the sample without deflection it is necessary to place a 'beam stop' in the center of the detector plane in order to prevent damage through the intense direct beam [78]. The sample-detector distance is variable because the detector plane can be moved back and forth in a big vacuum tube. A schematic representation with the most important elements of the instrumental set-up is shown in Fig. 2.19.

The dimensions of the detector unit directly determine which scattering angles are experimentally accessible. For example the instrument D11 at the ILL in Grenoble, which was used for this work, has a detector with an area of $96 \times 96$ cm$^2$ that can be moved to sample-detector distances from 1.2 to 39.0 m.[1] Thus, with a centered beam stop of $5 \times 5$ cm$^2$ one can detect scattering at angles between 21.80° and 0.04°. Together with the chosen wavelength of the neutron beam this defines which microstructure size range can be studied as will become obvious from the scattering theory.

### 2.5.2 Basic Scattering Theory

In the SANS experiment the distances from the neutron source to the sample and from the sample to the detector are much larger than the wavelength of the neutron

[1] http://www.ill.eu/instruments-support/instruments-groups/instruments/d11/characteristics/, 09.07.2013.

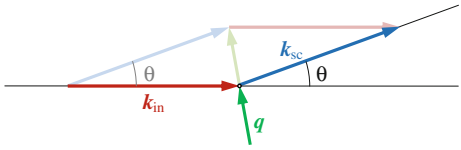


**Fig. 2.20** Illustration of the wave-vectors of an incident and an elastically scattered beam, $\boldsymbol{k}_{in}$ and $\boldsymbol{k}_{sc}$, respectively, and the momentum transfer vector $\boldsymbol{q}$ which characterizes the scattering process in the scattering angle θ

beam. Therefore one can work with the far field (or Fraunhofer) approximation which states that radiation which is emitted as spherical waves can at large distances be treated as possessing a planar wave front. This is thus true for both the incident neutron beam at the sample position and for the scattered radiation reaching the detector. Accordingly, the incident and the scattered neutrons are represented by wave-vectors, $\boldsymbol{k}_{in}$ and $\boldsymbol{k}_{sc}$, respectively, which point in the directions of the waves' propagation while their magnitude $k$ is defined by the wavelength λ

$$k = |\boldsymbol{k}| = \frac{2\pi}{\lambda}. \tag{2.38}$$

Since it is assumed that the scattering process in the SANS experiment is elastic the neutrons retain their energy and only change their direction when interacting with the sample. Therefore the incident and the scattered beam possess the same wavelength such that the magnitudes of $\boldsymbol{k}_{in}$ and $\boldsymbol{k}_{sc}$ are equal, i.e. $k_{in} = k_{sc}$. The change of the direction of propagation can be ascribed to a momentum transfer for which one defines the momentum transfer vector

$$\boldsymbol{q} \equiv \boldsymbol{k}_{sc} - \boldsymbol{k}_{in} \tag{2.39}$$

as illustrated in Fig. 2.20.

The $\boldsymbol{q}$ vector, also often referred to as the 'scattering vector', and particularly its magnitude $q$ are very important in the scattering theory. For $q$ it holds according to geometrical considerations (cp. Fig. 2.20) and using Eq. (2.38)

$$q = |\boldsymbol{q}| = 2\,k\,\sin\frac{\theta}{2} = \frac{4\pi}{\lambda}\,\sin\frac{\theta}{2} \tag{2.40}$$

where θ is the scattering angle between the incident and the scattered beam, which both possess the wavelength λ and wave-vectors of magnitude $k$. Following the examples given above, with a neutron beam of $\lambda = 10$ Å and scattering angles θ between 0.04° and 21.80° a $q$ range from $4.4 \times 10^{-4}$ to $2.4 \times 10^{-1}$ Å$^{-1}$ is covered. Through λ variations this range can further be stretched. Note that in SANS experiments one usually quotes the space-resolved scattering intensity not as a function of the scattering angle θ but as a function of $q$ which allows, e.g., to combine data measured at different wavelengths.

Constructive interference of waves, which is a prerequisite for generating a signal on the detector, occurs, according to Bragg's law, only when the path difference of two rays deflected at two sites with distance $d$ is a multiple of their wavelength λ. Accordingly it holds for scattering at a scattering angle θ

$$2\,d\,\sin\frac{\theta}{2} = n\,\lambda \tag{2.41}$$

where $n$ is an integer $\geq 1$ and $d$ the distance between two scattering centers in the sample. If the Eqs. (2.40) and (2.41) are combined one obtains (for $n = 1$) a fundamental relationship between $q$ and the length scale $d$ of the microstructure, namely

$$q = \frac{2\pi}{d}. \tag{2.42}$$

This allows to finally calculate that with a SANS experiment covering a typical $q$ range of, e.g., $4.4 \times 10^{-4}$ to $2.4 \times 10^{-1}$ $Å^{-1}$ one can probe a sample's microstructure on length scales between 1.4 μm and 2.6 nm, respectively.

### 2.5.3 Neutron Scattering

Neutrons are uncharged elementary particles with a spin of ½ and a magnetic moment of $\mu = -9.662 \times 10^{-27}$ J $T^{-1}$ [62]. Therefore, free neutrons which are irradiated on a sample interact with the atomic nuclei of the comprised atoms via the strong nuclear force [76]. Thereupon they can be scattered—if they are not adsorbed or directly transmitted, which actually happens to most of the neutrons. The likeliness for scattering depends on the type of the encountered atom and, remarkably, there are large differences for different isotopes (e.g. $^{1}H$ and $^{2}H$) and for different spin-states. One can picture that the probability for scattering is the higher the bigger the surface of an atom 'seen' by the incident neutron. Thus one assigns to each atom $i$ a 'scattering cross-section'

$$\sigma_i = 4\pi\langle|b_i|\rangle^2 \tag{2.43}$$

where $b_i$ is the atom's 'scattering length' that characterizes its interaction range [78]. Note that each atom possesses a coherent as well as an incoherent scattering length. The respective incoherent scattering cross-section gives rise to an 'internal background', which the measured SANS data is corrected for [80]. Hence all further explanations will exclusively consider the coherent scattering.

With the atoms' scattering lengths $b_i$, which are tabulated for many nuclei, one can calculate the 'scattering length density' ρ of the scattering microstructure units in the sample. The latter is an important parameter defining the amplitude of the

scattered neutron wave and thus the detected intensity. The scattering length density of, e.g., a molecule $k$ equals the sum of the scattering lengths $b_i$ of all comprised atoms $i$ divided by the volume of the molecule [78, 79]. This corresponds to

$$\rho_k = \frac{N_A \, \rho_k^0}{M_k} \sum_i b_i \tag{2.44}$$

where $N_A$ is the Avogadro constant, $M_k$ the molar mass of substance $k$ and $\rho_K^0$ its macroscopic density. In order to determine the scattering length density of a phase or a particle in which different components $k$ are mixed one can add up the individual scattering length densities $\rho_k$ weighted by the respective mole fractions $x_k$

$$\rho_{mix} = \sum_k (x_k \, \rho_k). \tag{2.45}$$

### 2.5.4 The Scattering Pattern

As mentioned previously, the detector in a SANS experiment counts how many neutrons arrive during the measuring time at different detector positions. SANS is therefore a static technique which averages out time-dependent fluctuations of the scattering signal. A scattering pattern is obtained which corresponds to the number of the scattered neutrons as a function of the scattering vector, $N(\boldsymbol{q})$. The number of detected neutrons depends on various parameters, namely (a) on the number of incident neutrons $N_{in}$, (b) on the fraction of neutrons which pass the sample without being absorbed, i.e. the sample's transmission $Tr$, (c) on the probability that an incident neutron encounters a scattering center which increases with the sample thickness $d_{sample}$, (d) on the size of the solid angle $\Omega$ within which scattering is detected, i.e. $\Delta\Omega$, and (e) last but not least on the density of the scatterers in the sample volume $V$ with the characteristic "scattering cross-sectional area ($\sigma$) per unit solid angle ($\Omega$)" [81] ($d\sigma/d\Omega$), usually referred to as 'differential scattering cross-section', [82]

$$N(\boldsymbol{q}) = N_{in} \cdot Tr \cdot d_{sample} \cdot \Delta\Omega \cdot \frac{1}{V} \frac{d\sigma(\boldsymbol{q})}{d\Omega}. \tag{2.46}$$

To evaluate the measured data one corrects for the experimental factors and considers exclusively the differential scattering cross-section per sample volume, denoted ($d\Sigma/d\Omega$), which "represents the probability of a particle of the incident beam being scattered out from the unit sample volume into the solid angle $\Delta\Omega$" [80]. One also calls ($d\Sigma/d\Omega$) the normalized 'scattering intensity' [78, 80, 82]

$$I(\boldsymbol{q}) = \frac{\mathrm{d}\Sigma(\boldsymbol{q})}{\mathrm{d}\Omega} = \frac{1}{V}\frac{\mathrm{d}\sigma(\boldsymbol{q})}{\mathrm{d}\Omega} = \frac{N(\boldsymbol{q})}{N_{\mathrm{in}}} \cdot \frac{1}{Tr \cdot d_{\mathrm{sample}} \cdot \Delta\Omega} \tag{2.47}$$

the unit of which is an inverse length. With an isotropic distribution of scattering centers in the sample the detected scattering pattern can be radially averaged which reduces $I(\boldsymbol{q})$ to $I(q)$ [76, 78].

To understand the origin of the scattering intensity $I(\boldsymbol{q})$ it is expedient to regard the scattered neutrons as waves. They emerge from all scattering centers at the positions $\boldsymbol{r}$ in the scattering volume and interfere with each other when they are scattered in the same direction, i.e. with the same momentum transfer vector $\boldsymbol{q}$. The interference leads to a neutron wave 'seen' by the detector whose amplitude $A(\boldsymbol{q})$ is directly related to the detected intensity

$$I(\boldsymbol{q}) = A(\boldsymbol{q})\, A^*(\boldsymbol{q}) = |A(\boldsymbol{q})|^2. \tag{2.48}$$

Assuming that all scattering events are independent (Born approximation) one can simply add the individual wave-functions of the scattered neutrons or rather integrate them over the whole scattering volume $V$. Accordingly, the amplitude of the detected neutron wave is [80, 82]

$$A(\boldsymbol{q}) = \int_V \rho(\boldsymbol{r})\, e^{-i\boldsymbol{q}\boldsymbol{r}}\, \mathrm{d}\boldsymbol{r} \tag{2.49}$$

where $i$ is the imaginary unit and $\rho(\boldsymbol{r})$ the scattering length density at the position $\boldsymbol{r}$. The scattering length density can be expressed as 'fluctuating' in the sample volume by $\Delta\rho(\boldsymbol{r})$ around a mean value $\bar{\rho}$ [83]

$$\rho(\boldsymbol{r}) = \bar{\rho} + \Delta\rho(\boldsymbol{r}). \tag{2.50}$$

Thus it can be shown that it is the fluctuations of the scattering length density which determine the detectable scattering intensity around the primary beam, i.e. $I(q)_{q>0}$, because it holds for the amplitudes of the neutrons which are not scattered in forward direction

$$A(\boldsymbol{q})_{q>0} = \int_V \Delta\rho(\boldsymbol{r})\, e^{-i\boldsymbol{q}\boldsymbol{r}}\, \mathrm{d}\boldsymbol{r}. \tag{2.51}$$

In other words, a scattering pattern is only observed when in the studied sample zones of different scattering length densities $\rho$ are present on the probed length scale, which simply means the sample has a microstructure with a 'scattering contrast'

$$\Delta\rho = |\rho_{\mathrm{s}} - \rho_{\mathrm{m}}| \tag{2.52}$$

where $\rho_{\mathrm{s}}$ is the scattering length density of the scatterer and $\rho_{\mathrm{m}}$ that of the surrounding matrix [76].

### 2.5.5 Solving the Scattering Problem

When the microstructure of a sample is known it is theoretically possible to compute the corresponding scattering intensity $I(q)$ by Fourier transforming its convoluted scattering length density profile which equals building the complex square of the scattered neutron waves amplitude (cp. Eq. 2.49). In principle one can also go the inverse way, Fourier transform the measured scattering intensity, deconvolute the result and estimate the system's microstructure [83]. However, since the SANS data is only measured in a limited $q$ range its Fourier transform often possesses strong termination effects. Moreover, the deconvolution is only feasible for discrete scattering particles with a simple geometry while it fails for complex systems like bicontinuous microemulsions. Hence it is often more convenient to presume a justified model for the microstructure, calculate the respective scattering function, compare it with the measured data and adjust the model if necessary. Sample characteristic parameters, like for example a particle diameter, are then yielded as the fit parameters.

If one wants to compute a system's scattering function $I(q)$ one must be aware of the different factors which contribute to the scattering intensity. This is in detail (a) the number density of the scatterers, (b) their individual shape and local scattering contrast as well as (c) their spatial correlation. Usually one distinguishes between the 'form factor' $P(q)$, which comprises the internal scattering contributions of discrete scatterers like suspended particles, and the 'structure factor' $S(q)$, which accounts for the scattering contributions due to interactions between different scatterers. In the most general case both contributions are related to each other. However, in a simplified approach these relations are neglected and the scattering intensity is calculated as product of three independent factors ('decoupling approximation') [84]

$$I(q) = n \cdot \overline{P(q)} \cdot S_{\text{eff}}(q). \tag{2.53}$$

In this equation $n$ is the number density of the scatterers, i.e. their number $N$ divided by the sample volume $V$, $\overline{P(q)}$ is the average form factor and $S_{\text{eff}}(q)$ the effective structure factor. The latter two factors will be further explained in the following.

The **average form factor** $\overline{P(q)}$ allows for the fact that the scattering particles in a sample are usually not monodisperse. Their characteristic dimension $X$ rather possesses a certain distribution around a mean value $X_0$. Thus the average form factor is calculated as [85]

$$\overline{P(q)} = \int_0^\infty P(q, X) \cdot W(X, X_0)\, \mathrm{d}X \tag{2.54}$$

where $W(X, X_0)$ is the distribution function, e.g. for a Gaussian distribution, and $P(q, X)$ is the form factor of a single particle. Form factors have been described for many different particle geometries. In general the form factor of a particle $k$ is the complex square of the amplitude $A_k(\boldsymbol{q})$ of the wave which is scattered from the particle. i.e. [85]

$$P(q) = \left\langle A_k(\mathbf{q})\, A_k^*(\mathbf{q}) \right\rangle = \left\langle |A_k(\mathbf{q})|^2 \right\rangle \tag{2.55}$$

where the brackets denote an average over all particle orientations in the sample. With this average one yields for the amplitude, instead of the three-dimensional Fourier transform in Eq. (2.51), the one-dimensional radial symmetrical form

$$A_k(q) = 4\pi\, \Delta\rho \int_0^\infty f(r)\, r^2\, \frac{\sin(qr)}{qr}\, \mathrm{d}r. \tag{2.56}$$

Here $f(r)$ is the normalized radial scattering length density distribution of the scatterer $k$ with the scattering contrast $\Delta\rho$ (cp. Eq. 2.52) and the characteristic radial scattering contrast profile $\Delta\rho(r)$

$$f(r) = \frac{\Delta\rho(r)}{\Delta\rho}. \tag{2.57}$$

Hence, the form factor of a scatterer of a certain shape can be determined based on the respective $f(r)$ function, for which many examples are found in the literature (e.g. core–shell particles [86]).

The **effective structure factor** $S_{\mathrm{eff}}(q)$ accounts for the interference of neutron waves which are scattered from different particles $k$ and $l$ and possess the amplitudes $A_k$ and $A_l$, respectively. It holds [87, 88]

$$S_{\mathrm{eff}}(q) = \frac{1}{\overline{P(q)}} \sum_k \sum_l A_k\, A_l\, S_{kl}(q) \tag{2.58}$$

where $\overline{P(q)}$ is the average form factor and $S_{kl}(q)$ the partial structure factor describing the correlation between the respective particles. To simplify the calculation of the structure factor one can, for example, assume that correlation occurs exclusively between particles of the same species $k$. If one furthermore neglects the dependence on the intraparticle scattering contributions one can replace the effective structure factor by an 'averaged structure factor' [84]

$$S_{\mathrm{av}}(q) = \sum_k x_k\, S_k(q) \tag{2.59}$$

where $x_k$ is the molar fraction of particle species $k$. Of course one must evaluate in the individual case which assumptions are reasonable. In general, $S(q)$ depends on the scatterers' interaction potential which is accounted for in the 'pair correlation function' [78]

$$g(r) = e^{-\frac{V(r)}{k_B T}} \tag{2.60}$$

where $k_B$ is the Boltzmann constant, $T$ the absolute temperature and $V(r)$ the mean field potential or the pair interaction potential for relatively dilute systems, respectively. Thus, given that the interactions in the sample are isotropic, one can write for the structure factor [78]

$$S(q) = 1 + 4\pi\, n \int_0^\infty (g(r) - 1)\, r^2\, \frac{\sin(qr)}{qr} \mathrm{d}r \tag{2.61}$$

where $n$ is the number density of scatterers. Note that the structure factor is particularly relevant in concentrated systems where the scatterers significantly interact with their neighbours such that the microstructure is locally ordered. In highly diluted systems $S(q)$ tends to unity [85].

## References


1. T. Sottmann, C. Stubenrauch, in *Microemulsions: Background, New Concepts, Applications, Perspectives*, ed. by C. Stubenrauch (Wiley, Oxford, 2009), pp. 1–83
2. T.P. Hoar, J.H. Schulman, Nature **152**, 102–103 (1943)
3. P.A. Winsor, *Solvent Properties of Amphiphilic Compounds* (Butterworths Sci. Pubs., London, 1954)
4. S.I. Ahmad, K. Shinoda, S. Friberg, J. Colloid Interface Sci. **47**, 32–37 (1974)
5. K. Shinoda, S. Friberg, Adv. Colloid Interface Sci. **4**, 281–300 (1975)
6. K. Shinoda, H. Kunieda, N. Obi, S.E. Friberg, J. Colloid Interface Sci. **80**, 304–305 (1981)
7. M. Kahlweit, J. Colloid Interface Sci. **90**, 197–202 (1982)
8. M. Kahlweit, E. Lessner, R. Strey, J. Phys. Chem. **87**, 5032–5040 (1983)
9. M. Kahlweit, E. Lessner, R. Strey, J. Phys. Chem. **88**, 1937–1944 (1984)
10. M. Kahlweit, R. Strey, Angew. Chem. **97**, 655–669 (1985)
11. K. Shinoda, M. Araki, A. Sadaghiani, A. Khan, B. Lindman, J. Phys. Chem. **95**, 989–993 (1991)
12. M. Laupheimer, S. Engelskirchen, K. Tauber, W. Kroutil, C. Stubenrauch, Tenside Surf. Det. **48**, 28–33 (2011)
13. R. Tessendorf, *Microemulsions as Templates for High Surface Area Polymers* (WiKu-Wissenschaftsverlag Dr. Stein, Köln, 2009)
14. H.D. Dörfler, A. Grosse, Prog. Colloid Polym. Sci. **101**, 113–115 (1996)
15. M.J. Lawrence, G.D. Rees, Adv. Drug Deliv. Rev. **45**, 89–121 (2000)
16. A. Lattes, I. Rico, Surf. Sci. Ser. **24**, 377–385 (1987)
17. H. Gao, J. Li, B. Han, W. Chen, J. Zhang, R. Zhang, D. Yan, Phys. Chem. Chem. Phys. **6**, 2914–2916 (2004)

18. R.F. Joubran, D.G. Cornell, N. Parris, Colloid Surf. A **80**, 153–160 (1993)
19. C.T. Lee Jr., W. Ryoo, P.G. Smith Jr., J. Arellano, D.R. Mitchell, R.J. Lagow, S.E. Webber, K.P. Johnston, J. Am. Chem. Soc. **125**, 3181–3189 (2003)
20. A.F. Forziati, J. Res. Nat. Bur. Stand. **36**, 129–136 (1946)
21. S. Burauer, T. Sachert, T. Sottmann, R. Strey, Phys. Chem. Chem. Phys. **1**, 4299–4306 (1999)
22. M. Kahlweit, R. Strey, D. Haase, P. Firman, Langmuir **4**, 785–790 (1988)
23. R. Strey, Colloid Polym. Sci. **272**, 1005–1019 (1994)
24. W. Helfrich, Z. Naturforsch. C **28**, 693–703 (1973)
25. T. Sottmann, R. Strey, J. Chem. Phys. **106**, 8606–8615 (1997)
26. L. Salomonsson, G. Stang, B. Zhmud, Tribol. Trans. **50**, 302–309 (2007)
27. P. Terech, Colloid Polym. Sci. **269**, 490–500 (1991)
28. P. Terech, R.G. Weiss, Chem. Rev. **97**, 3133–3159 (1997)
29. M. George, R. G. Weiss, in *Molecular Gels: Materials with Self-Assembled Fibrillar Networks*, ed. by R.G. Weiss, P. Terech (Springer, Dordrecht, 2006), pp. 449–551
30. G. Zhu, J.S. Dordick, Chem. Mat. **18**, 5988–5995 (2006)
31. R. G. Weiss, P. Térech, in *Molecular Gels. Materials with Self-Assembled Fibrillar Networks*, ed. by R.G. Weiss, P. Terech (Springer, Dordrecht, 2006), pp. 1–13
32. K. Nishinari, Progr.Colloid Polym. Sci. **136**, 87–94 (2009)
33. S.R. Raghavan, B.H. Cipriano, in *Molecular Gels. Materials with Self-Assembled Fibrillar Networks*, ed. by R.G. Weiss, P. Terech (Springer, Dordrecht, 2006), pp. 241–252
34. P. Terech, D. Pasquier, V. Bordas, C. Rossat, Langmuir **16**, 4485–4494 (2000)
35. J.P. Gong, in *Kobunshi Jiten (Dictionary of Polymer Science)*, ed. by A. Shoten (Society of Polymer Science, Tokyo, 2005) (in Japanese—literally cited in English in [Nis09])
36. P. H. Hermans, in *Colloid Science, Volume II: Reversible Systems*, ed. by H.R. Kruyt (Elsevier, Amsterdam, 1949), pp. 483–651
37. P. Terech, I. Furman, R.G. Weiss, J. Phys. Chem. **99**, 9558–9566 (1995)
38. P. Terech, V. Rodriguez, J.D. Barnes, G.B. McKenna, Langmuir **10**, 3406–3418 (1994)
39. M.A. Rogers, T. Pedersen, L. Quaroni, Cryst. Growth Des. **9**, 3621–3625 (2009)
40. R. Wang, X.-Y. Liu, J. Xiong, J. Li, J. Phys. Chem. B **110**, 7275–7280 (2006)
41. P. Terech, Progr. Colloid Polym. Sci. **102**, 64–70 (1996)
42. M.A. Rogers, A.G. Maragoni, Langmuir **25**, 8556–8566 (2009)
43. M. Burkhardt, S. Kinzel, M. Gradzielski, J. Colloid Interface Sci. **331**, 514–521 (2009)
44. R. Lam, L. Quaroni, T. Pederson, M.A. Rogers, Sof Matter **6**, 404–408 (2010)
45. M.A. Rogers, A.G. Marangoni, Cryst. Growth Des. **8**, 4596–4601 (2008)
46. E. Ostuni, P. Kamaras, R.G. Weiss, Angew. Chem. Int. Ed. **35**, 1324–1326 (1996)
47. K.A. Dawson, Curr. Opin. Colloid Interface Sci. **7**, 218–227 (2002)
48. D. Jordan Lloyd, in *Colloid Chemistry,* vol. 1, ed. by J. Alexander (The Chemical Catalog Co., New York, 1926), pp. 767–782
49. K. Almdal, J. Dyre, S. Hvidt, O. Kramer, Macromol. Chem. Macromol. Symp. **76**, 49–51 (1993)
50. G. Böhme, *Strömungsmechanik nicht-newtonscher Fluide* (Teubner, Stuttgart, 1981)
51. R. Brummer, *Rheology Essentials of Cosmetic and Food Emulsions* (Springer, Berlin, 2006)
52. J.W. Goodwin, R.W. Hughes, *Rheology for Chemists: An Introduction*, 2nd edn. (RCS Publishing, Cambridge, 2008)
53. M.A. Rao, *Rheology of Fluid and Semisolid Foods: Principles and Applications* 2nd edn, ed. by G.V. Barbosa-Cánovas (Springer, New York, 2007)
54. T.F. Tadros, *Rheology of Dispersions: Principles and Applications* (Wiley-VCH, Weinheim, 2010)
55. R.I. Tanner, *Engineering Rheology*, 2nd edn. (Oxford University Press, New York, 2000)
56. R. Edgeworth, B. J. Dalton, T. Parnell, Eur. J. Phys. **5**, 198–200 (1984)
57. Homepage of University of Queensland, http://smp.uq.edu.au/content/pitch-drop-experiment. Accessed 03 May 2013
58. http://en.wikipedia.org/wiki/Pitch_drop_experiment. Accessed 03 May 2013
59. E.O. Stejskal, J.E. Tanner, J. Chem. Phys. **42**, 288–292 (1965)

60. E. Hawlicka, Chem. Soc. Rev. **24**, 367–377 (1995)
61. J. Crank, *The Mathematics of Diffusion* (Oxford University Press, Oxford, 1975)
62. P.W. Atkins, *Physikalische Chemie—Dritte, korrigierte* (Wiley-VCH, Weinheim, 2002)
63. E.L. Hahn, Phys. Rev. **80**, 580–594 (1950)
64. W.S. Price, Concepts Magn. Reson. **9**, 299–336 (1997)
65. R.M. Cotts, M.J.R. Hoch, T. Sun, J.T. Markert, J. Magn. Reson. **83**, 252–266 (1989)
66. W. Heink, J. Kärger, H. Pfeifer, J. Chem. Soc. Chem. Commun. **20**, 1454–1455 (1990)
67. T. Saito, P.L. Rinaldi, J. Magn. Reson. **130**, 135–139 (1998)
68. J.E. Tanner, J. Chem. Phys. **52**, 2523–2526 (1970)
69. P. Stilbs, Prog. Nucl. Magn. Reson. Spectrosc. **19**, 1–45 (1987)
70. R. Mills, J. Phys. Chem. **77**, 685–688 (1973)
71. M.T. Clarkson, D. Beaglehole, P.T. Callaghan, Phys. Rev. Lett. **54**, 1722–1724 (1985)
72. B. Lindman, P. Stilbs, M.E. Moseley, J. Colloid Interface Sci. **83**, 569–582 (1981)
73. B. Lindman, U. Olsson, Ber. Bunsenges. Phys. Chem. **100**, 344–363 (1996)
74. P. Stilbs, M.E. Moseley, B. Lindman, J. Magn. Reson. **40**, 401–404 (1980)
75. D.M. Anderson, H. Wennerström, J. Phys. Chem. **94**, 8683–8694 (1990)
76. M. Engel, T. Spehr, B. Stühn, Bunsen-Magazin **1**, 4–15 (2011)
77. A. Guinier, Ann. Phys. Paris. **12**, 161–237 (1939)
78. I. Grillo, in *Soft Matter Characterization*, ed. by R. Borsali, R. Pecora (Springer, New-York, 2008), pp. 723–782
79. P. Schurtenberger, in *Neutrons, X-rays and Light: Scattering Methods Applied to Soft Condensed Matter*, ed. by P. Lindner, T. Zemb (Elsevier, Amsterdam, 2002), pp. 145–170
80. P. Lindner, in *Neutrons, X-rays and Light: Scattering Methods Applied to Soft Condensed Matter*, ed. by P. Lindner, T. Zemb (Elsevier, Amsterdam, 2002), pp. 23–48
81. P. N. Pusey, in *Neutrons, X-rays and Light: Scattering Methods Applied to Soft Condensed Matter*, ed. by P. Lindner, T. Zemb (Elsevier, Amsterdam, 2002), pp. 3–21
82. O. Spalla, in *Neutrons, X-rays and Light: Scattering Methods Applied to Soft Condensed Matter*, ed. by P. Lindner, T. Zemb (Elsevier, Amsterdam, 2002), pp. 49–71
83. O. Glatter, in *Neutrons, X-rays and Light: Scattering Methods Applied to Soft Condensed Matter*, ed. by P. Lindner, T. Zemb (Elsevier, Amsterdam, 2002), pp. 73–102
84. B. Weyerich, J. Brunner-Popela, O. Glatter, J. Appl. Cryst. **32**, 197–209 (1999)
85. M. Kotlarchyk, S.-H. Chen, J. Chem. Phys. **79**, 2461–2469 (1983)
86. T. Foster, J. Phys. Chem. B **115**, 10207–10217 (2011)
87. P.N. Pusey, H.M. Fijnaut, A. Vrij, J. Chem. Phys. **77**, 4270–4281 (1982)
88. P. Salgi, R. Rajagopalan, Adv. Colloid Interface Sci. **43**, 169–288 (1993)
89. T. Sottmann, R. Strey, Ber. Bunsenges. Phys. Chem. **100**, 237–241 (1996)
90. O. Holderer, N.R. de Souza, M. Monkenbusch, *The Jülich Neutron Spin-Echo Spectrometer J-NSE* (poster), http://www.jcns.info/src/POFposters/JCNS_Poster_JNSE_science_v1.pdf. Accessed 10 March 2010
91. W.S. Price, Concepts Magn. Reson. **10**, 197–237 (1998)
92. C. Stubenrauch, *Mikroemulsionen mit Alkylgucosiden aus makroskopischer und NMR-spektroskopischer Sicht* (Shaker Verlag, Aachen, 1997)

# Chapter 3
# Phase Behaviour and Rheology of Gelled Microemulsions

In order to investigate the orthogonal self-assembled character of gelled bicontinuous microemulsions the first and fundamental step was to identify under which conditions a mixture of water, *n*-decane, $C_{10}E_4$ and 12-HOA forms the desired system. Thus it was crucial to carry out phase studies. On the one hand, a microemulsion is known to be bicontinuous at its $\widetilde{T}$ temperature. There it forms one phase for surfactant mass fractions $\gamma > \widetilde{\gamma}$, while two phases are present at temperatures below the lower and above the upper microemulsion phase boundary. On the other hand, gels form below the sol-gel transition temperature, which usually increases with increasing gelator concentration as the sol-gel boundary in a gel's phase diagram reflects. Regarding the phase behaviour of a gelled microemulsion one expects to find both, microemulsion phase boundaries and a sol-gel boundary, because orthogonal self-assembled systems are supposed to retain the characteristic features of their base systems.

The microemulsion phase boundaries are the focus of Sect. 3.1. For this work they were determined with the conventional visual method and in part additionally with a specifically developed transmission method. Section 3.2 subsequently deals with the characteristic phase behaviour of the second base system, i.e. the binary gel with its sol-gel boundary. Sol-gel transition temperatures were measured with two complementary techniques, namely differential scanning calorimetry (DSC) and temperature-dependent oscillating shear rheometry. Note that the phase behaviour of the gelled microemulsion is always compared with that of the respective base system, i.e. the non-gelled microemulsion in Sect. 3.1 and the binary gel in Sect. 3.2. The phase studies yielded the appropriate parameters, i.e. composition and temperature, to form gelled, one-phase, bicontinuous microemulsions. Moreover, they revealed that the phase behaviour of the gelled microemulsion $H_2O$–*n*-decane/12-HOA–$C_{10}E_4$ indeed retains the characteristic features of its two base systems. A further characteristic property of the binary gel

M. Laupheimer, *Gelled Bicontinuous Microemulsions*,
Springer Theses, DOI: 10.1007/978-3-319-07719-2_3,

is its rheological behaviour. Thus, Sect. 3.3 proceeds with a rheometry study of the gelled bicontinuous microemulsion in comparison with the system *n*-decane/12-HOA, respectively.[1]

## 3.1 Microemulsion Phase Behaviour

An outstanding property of water–oil–non-ionic surfactant microemulsions is their high sensitivity to temperature variations. One immediately notices this when handling such a sample at different temperatures because its appearance changes from turbid to clear and vice versa. This behaviour simply reflects that at low and at high temperatures the system is phase-separated and thus forms an emulsion. At intermediate temperatures, by contrast, the microemulsion is one-phase and stays clear (cp. Sect. 2.1, Fig. 2.3). A first observation during the preparation of gelled microemulsions is that this general behaviour is maintained upon the addition of the gelator. When the gelled microemulsion samples warm up to room temperature after having been gelled in the ice bath (cp. Sect. 6.2) their turbidity decreases significantly at some point and later increases again (see Fig. 3.1). Therefore, a detailed phase study was self-evident. The samples in this study all contained equal volumes of water and oil, i.e. $\phi = 0.5$, while the mass fraction of the surfactant was varied in order to obtain $T$-$\gamma$ diagrams. Those were measured for the gelled microemulsion $H_2O$–*n*-decane/12-HOA–$C_{10}E_4$ with three different gelator concentrations, namely 1.5, 2.5 and 5.0 wt% as well as for the non-gelled base system $H_2O$–*n*-decane–$C_{10}E_4$.

### *3.1.1 Non-Gelled Base Microemulsion*

The starting point for studying the phase behaviour of gelled microemulsions was the $T$-$\gamma$ phase diagram of the non-gelled base system $H_2O$–*n*-decane–$C_{10}E_4$ ($\phi = 0.5$). the literature before [1], however, it was remeasured for the thesis at hand (using the visual method) with a focus on the one-phase region at surfactant mass fractions between $\gamma = 0.145$ and $\gamma = 0.207$ (see Fig. 3.2). Higher surfactant concentrations were not relevant because the aim of this work was to investigate one-phase microemulsions with a bicontinuous structure. These are found at temperatures in the middle of the one-phase region, i.e. at $\widetilde{T}$, for surfactant mass fractions a bit higher than $\widetilde{\gamma}$. At surfactant concentrations much higher than $\widetilde{\gamma}$ one

[1] Note that the main results of this Chapter have already been published in a peer-reviewed paper entitled "Studying orthogonal self-assembled systems: phase behaviour and rheology of gelled microemulsions" in the journal *Soft Matter* [2]. The figures are herein reproduced, in modified form, by permission of The Royal Society of Chemistry.

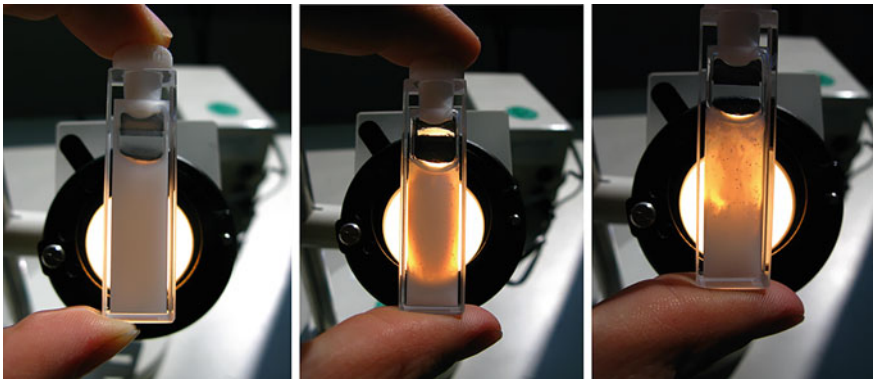

**Fig. 3.1** Photographs of a gelled microemulsion $H_2O$–*n*-decane/12-HOA–$C_{10}E_4$ ($\phi = 0.5$, $\gamma = 0.155$, $\eta = 0.015$) which becomes clearer and then turbid again (from *left* to *right*) as it warms up to room temperature after having been gelled in the ice bath

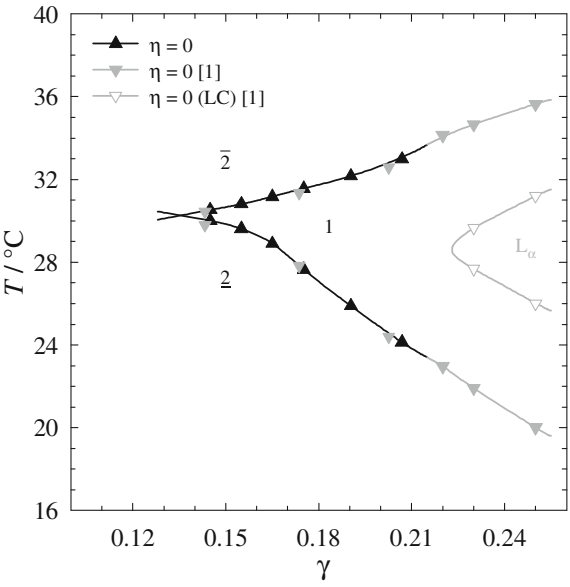


**Fig. 3.2** T-γ phase diagram of the non-gelled base microemulsion $H_2O$–*n*-decane–$C_{10}E_4$ ($\phi = 0.5$). The measured phase transition temperatures (*black*, Table A.1) are shown together with data points from Ref. [1] (*gray*, *open symbols* for the lamellar $L_\alpha$, phase) (modified from [2]—reproduced by permission of The Royal Society of Chemistry)

runs into liquid crystalline phases such as the lamellar phase reported for the microemulsion $H_2O$–*n*-decane–$C_{10}E_4$ for $\gamma > 0.222$ [1] (cp. Fig. 3.2).

In Fig. 3.2 one can see that the measured phase boundaries are in very good agreement with the data from literature [1]. The characteristic $\widetilde{X}$ point of the system $H_2O$–*n*-decane–$C_{10}E_4$ is located at $\widetilde{T} = 30.2$ °C and $\widetilde{\gamma} = 0.135$, which agrees well with the literature values of $\widetilde{T} = 30.15$ °C, $\widetilde{\gamma} = 0.132$ [1] and $\widetilde{T} = 30.15$ °C, $\widetilde{\gamma} = 0.136$ [3], respectively.

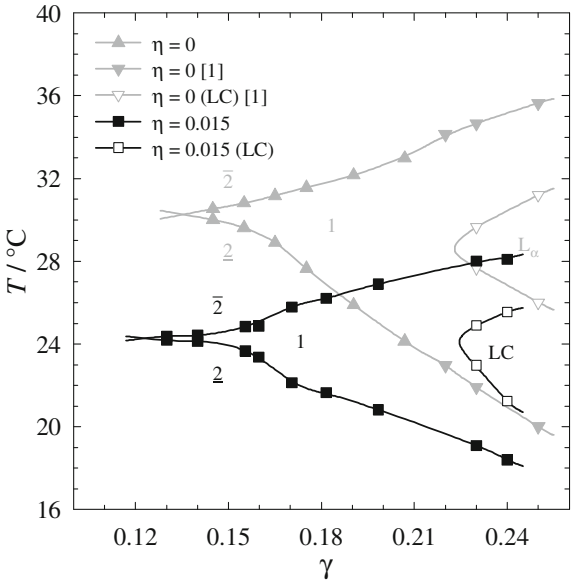


**Fig. 3.3** *T*-γ phase diagram of the gelled microemulsion $H_2O$–*n*-decane/12-HOA–$C_{10}E_4$ ($\phi = 0.5$) with 1.5 wt% gelator (*black*, Table A.2)[KJ].[2] The non-gelled base system ($\eta = 0$) is shown for comparison (*gray*, Table A.1). Transitions between the microemulsion and a liquid crystalline (LC) phase are marked with open symbols (modified from [2]—reproduced by permission of The Royal Society of Chemistry)

### 3.1.2 Gelled Microemulsion with 1.5 wt% 12-HOA

After the phase diagram of the non-gelled base microemulsion was determined the phase behaviour of the gelled microemulsion $H_2O$–*n*-decane/12-HOA–$C_{10}E_4$ was investigated. In the first step a system with 1.5 wt% of the low molecular weight organogelator 12-HOA was studied. The visually determined phase transition temperatures are shown in Fig. 3.3. Note that the gelled microemulsion also possesses a sol-gel boundary, which will be discussed in Sect. 3.2. However, as the sol-gel boundary lies well above the one-phase region it is not included in Fig. 3.3 for the sake of clarity.

One can see in Fig. 3.3 that the microemulsion phase boundaries shift to lower temperatures when 1.5 wt% 12-HOA are added to the non-gelled base system. $\widetilde{T}$ consequently decreases as well, namely by 5.9 K down to 24.3 °C. Moreover, the efficiency $\widetilde{\gamma}$ slightly increases from 0.135 in the non-gelled to 0.123 in the gelled microemulsion. In fact, these shifts are not surprising since for similar systems the

[2] Measurements carried out by Kristina Jovic during her bachelor thesis and her 'Hiwi' employment under my supervision. Note that such measurements will in the following be indicated by "KJ"

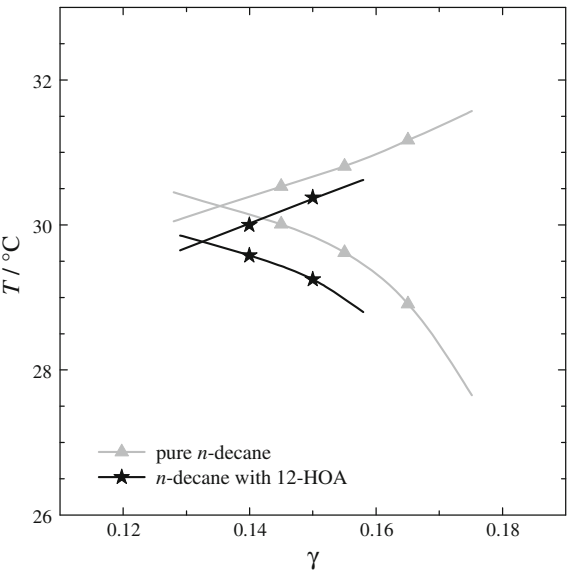


**Fig. 3.4** $T$-$\gamma$ phase diagram of a non-gelled microemulsion $H_2O$–*n*-decane/12-HOA–$C_{10}E_4$ ($\phi = 0.5$) prepared with *n*-decane which was decanted after centrifuging a binary *n*-decane/12-HOA gel with 5.0 wt% gelator (*black stars*, Table A.3).[KJ] The phase boundaries of the system with pure *n*-decane are shown for comparison (*gray triangles*, Table A.1)

same trends have been observed [4]. However, as the previously studied gelled microemulsions contained a technical grade surfactant their phase boundaries were distorted to higher temperatures at low surfactant mass fractions and the phase transition temperatures decreased particularly in this range when 12-HOA was added. The undistorted phase boundaries of the well-defined system $H_2O$–*n*-decane/12-HOA–$C_{10}E_4$, in contrast, shift rather uniformly. The reason for the temperature shifts becomes obvious when looking at the molecular structure of the gelator 12-HOA (see Fig. 2.6). Its hydrophilic carboxylic acid group in conjunction with the hydroxylated carbon chain makes up a surface active fatty acid molecule. On the one hand, such a molecule readily adsorbs at water–oil interfaces and, on the other hand, it dissolves to a certain extent monomerically in oil phases. In order to prove the monomeric solubility in *n*-decane a binary gel consisting of *n*-decane and 5.0 wt% 12-HOA was prepared and subsequently centrifuged with 3,500 rpm for about 60 min at room temperature. This procedure led to a compacted gel layer at the bottom of the test tube with a supernatant liquid layer of *n*-decane. The density of the decanted *n*-decane was measured to be 0.73018 g $cm^{-3}$ (at 20 °C) which is a bit higher than the value of 0.72994 g $cm^{-3}$ obtained for pure *n*-decane.[3] Another indication for the monomeric solubility of 12-HOA in *n*-decane is that when the decanted instead of pure *n*-decane was used to prepare a microemulsion with water and $C_{10}E_4$ phase boundaries were measured which are shifted to lower temperatures by about 0.4 K (see Fig. 3.4). This can be explained by the fact that 12-HOA as co-solvent renders the *n*-decane component more hydrophilic and improves its

[3] The density measurements were carried out with a DMA 5000 M density meter from *Anton Paar*.

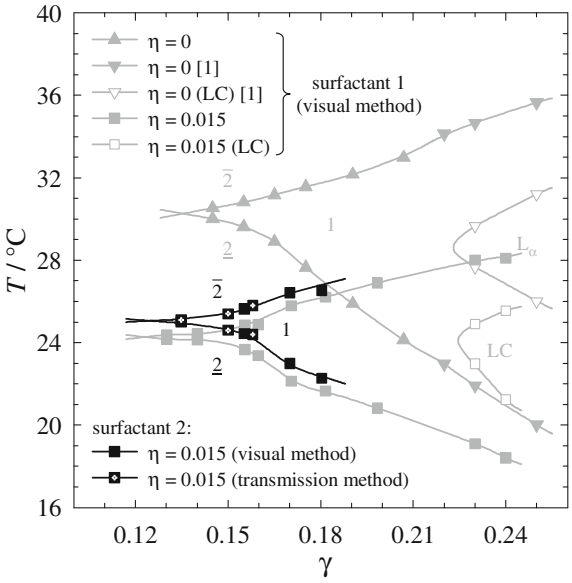


**Fig. 3.5** *T*-γ phase diagram of the gelled (η = 0.015, *squares*) and the non-gelled (η = 0, *triangles*, Table A.1) microemulsion $H_2O$–*n*-decane/12-HOA–$C_{10}E_4$ (ϕ = 0.5). Different surfactant batches were used for the gelled microemulsion which corresponds to the *gray*[KJ] (cp. Fig. 3.3, Table A.2) and the *black* (Table A.4) symbols, respectively. For one of the batches (*black*) phase transition temperatures were determined with the visual method (*plain symbols*) and with the transmission method [6] (*symbols with white crosses*[KJ])

miscibility with the non-ionic surfactant $C_{10}E_4$. Hence, the oil–surfactant miscibility gap and thus the phase boundaries of the microemulsion are decreased. In its second role, as co-surfactant, 12-HOA further adds to this effect because the adsorption of co-surfactants at the water–oil interface decreases the curvature of the surfactant monolayer in microemulsions [5]. Thus less thermal energy is needed for bending the layer and inverting its curvature, which is what formally happens at $\widetilde{T}$. Note that a flattening of the surfactant monolayer also occurs when the surfactant mass fraction is increased beyond $\widetilde{\gamma}$. This eventually results in the formation of liquid crystalline (LC) phases like the lamellar $L_\alpha$ phase located at $\gamma > 0.222$ in $H_2O$–*n*-decane–$C_{10}E_4$ [1]. In the microemulsion gelled with 1.5 wt% 12-HOA an LC phase was found at about the same surfactant concentration (see Fig. 3.3) which is hence most likely lamellar as well.

Note that in the course of the phase studies of the gelled microemulsion with 1.5 wt% gelator multiple samples were investigated. Unexpectedly, the phase transition temperatures of some samples with approximately the same surfactant mass fractions γ differed by about 0.7 K. The most likely explanation for this finding is that two different surfactant batches were used for preparing the respective samples. The phase boundaries obtained with the first surfactant batch are shown in Figs. 3.3 and 3.4. Figure 3.5 shows in comparison the somewhat higher phase

transition temperatures which were measured for the samples prepared with the second surfactant batch. One can see that the shape of the phase boundaries is the same in both cases which confirms the validity of the determined values.

It shall be highlighted at this point that while all samples prepared with the first surfactant batch were studied visually, an especially developed transmission method (cp. Sect. 6.4 and Ref. [6]) was used to measure the phase transition temperatures of some of the samples prepared with the second surfactant batch. The motivation for developing the new method was to quantify the sample turbidity by means of a UV/Vis spectrometer in order to be able to objectively assess whether one or more phases are present. With the conventional visual method (cp. Sect. 6.3) this is difficult, in particular, for gelled microemulsions which are slightly turbid in the one-phase state due to the presence of the gelator network. The distinction between a two-phase and the one-phase state thus requires instead of a simple 'turbid' versus 'clear' differentiation like for non-gelled microemulsions the differentiation between 'very turbid' and 'less turbid'. This should be facilitated on the basis of transmission values. Figure 3.5 shows that the results of the conventional visual method and those of the new transmission method are in good agreement which proves the validity of the new technique as well as the reliability of the phase boundaries obtained with the second surfactant batch.

### *3.1.3 Gelled Microemulsion with 2.5 wt% 12-HOA*

After investigating the gelled microemulsion $H_2O$–*n*-decane/12-HOA–$C_{10}E_4$ ($\phi = 0.5$) with 1.5 wt% 12-HOA, the gelator mass fraction was increased to 2.5 wt%. A visual phase study of the system with the new 12-HOA concentration yielded the phase diagram shown in Fig. 3.6. Note that again the sol-gel boundary, which will be discussed in Sect. 3.2, is not shown for the sake of clarity.

Two things are remarkable about the phase diagram of the gelled microemulsion with 2.5 wt% gelator (Fig. 3.6) compared with the one of the system with 1.5 wt% 12-HOA (Fig. 3.3), i.e. the locations of the $\widetilde{X}$ point and of the liquid crystalline (LC) phase. Regarding the $\widetilde{X}$ point it was found that in spite of the significant increase of the gelator concentration $\widetilde{T}$ is only slightly reduced, namely from 24.3 to 23.6 °C, while the efficiency is with a change from $\widetilde{\gamma} = 0.123$ to 0.121 hardly affected at all. A possible explanation for this rather unexpected observation will be discussed later in the chapter. As regards the LC phase, the latter is in the gelled microemulsions with 2.5 wt% 12-HOA shifted much closer to the $\widetilde{X}$ point than in the system with 1.5 wt% gelator. This attests that the 12-HOA molecules adsorbing at the water–oil interface have a strong rigidifying effect on the surfactant monolayer of the microemulsion. In general, the occurrence of extended LC phases in the one-phase region was little surprising because similar observations have been reported for the previously studied gelled microemulsions [4]. To learn more about the type of the LC phase a $H_2O$–*n*-decane/12-HOA–$C_{10}E_4$ ($\phi = 0.5$) sample with 2.5 wt% 12-HOA and a surfactant mass

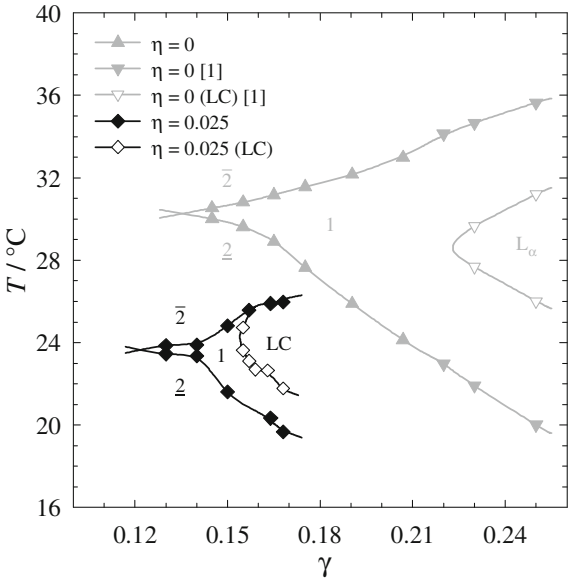


**Fig. 3.6** *T*-γ phase diagram of the gelled microemulsion $H_2O$–*n*-decane/12-HOA–$C_{10}E_4$ ($\phi = 0.5$) with 2.5 wt% gelator (*black*, Table A.5).[KJ] The non-gelled base system ($\eta = 0$) is shown for comparison (*gray*, Table A.1). Transitions between the microemulsion and a liquid crystalline (LC) phase are marked with open symbols (modified from [2]—reproduced by permission of The Royal Society of Chemistry)

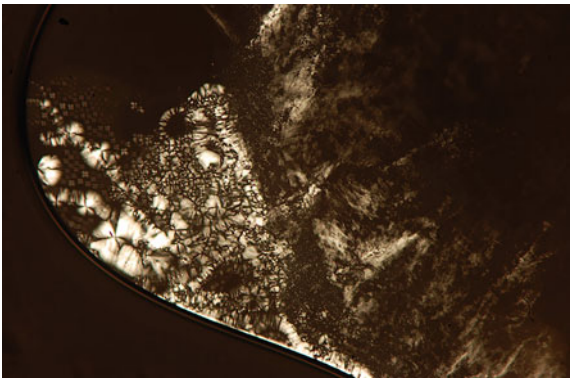

**Fig. 3.7** Picture from the polarizing microscope of a $H_2O$–*n*-decane/12-HOA–$C_{10}E_4$ ($\phi = 0.5$) sample with 2.5 wt% gelator and a surfactant mass fraction of $\gamma = 0.163$ at room temperature. The gelled part on the right reveals no characteristic pattern while some squeezed out liquid on the left shows the characteristic texture of lamellar $L_\alpha$ phases

fraction of $\gamma = 0.163$ was examined at room temperature under the polarizing microscope. In the gelled part of the sample the detection of a specific pattern was not possible, however, at the sample borders some liquid was squeezed out which

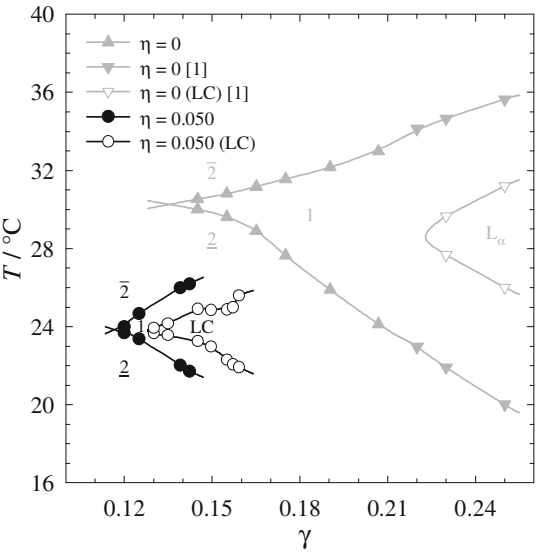


**Fig. 3.8** $T$-$\gamma$ phase diagram of the gelled microemulsion $H_2O$–*n*-decane/12-HOA–$C_{10}E_4$ ($\phi = 0.5$) with 5.0 wt% gelator (*black*, Table A.6).[KJ] The non-gelled base system ($\eta = 0$) is shown for comparison (*gray*, Table A.1). Transitions between the microemulsion and a liquid crystalline (LC) phase are marked with *open symbols* (modified from [2]—reproduced by permission of The Royal Society of Chemistry)

had a texture characteristic for $L_\alpha$ phases (see Fig. 3.7). It is thus quite likely that under the stated conditions a lamellar phase consisting of water, *n*-decane and $C_{10}E_4$ coexists with the gelator network.

### *3.1.4 Gelled Microemulsion with 5.0 wt% 12-HOA*

In a last step the gelator concentration in the system $H_2O$–*n*-decane/12-HOA–$C_{10}E_4$ was doubled from 2.5 to 5.0 wt%. The visually measured phase diagram for the respective gelled microemulsion (omitting the sol-gel boundary which will be discussed in Sect. 3.2) is shown in Fig. 3.8. Again it is mainly the expansion of the liquid crystalline phase which is changed (i.e. enlarged) in comparison to the gelled microemulsion with lower 12-HOA concentrations, while the $\widetilde{X}$ point shift upon the increase of the gelator mass fraction to 5.0 wt% is very small. One finds the efficiency slightly increased to $\widetilde{\gamma} = 0.116$ and with 23.8 °C a $\widetilde{T}$ temperature which stayed roughly constant compared to the system with 2.5 wt% gelator.

In Table 3.1 the $\widetilde{X}$ point coordinates of the gelled microemulsion $H_2O$–*n*-decane/12-HOA–$C_{10}E_4$ with all studied gelator mass fractions $\eta$ are listed for comparison. Moreover, Fig. 3.9 visualizes the trends of $\widetilde{T}$ and $\widetilde{\gamma}$ with increasing gelator concentration. It is striking that the initial addition of only 1.5 wt% 12-HOA leads to a significant shift of the $\widetilde{X}$ point, especially regarding the $\widetilde{T}$ temperature, while more than triplicating this gelator amount causes hardly any further $\widetilde{X}$ point shift. This finding implies that 12-HOA does not act as co-solvent, co-surfactant and gelling agent in equal shares for all $\eta$ values. It rather seems that

**Table 3.1** Coordinates of the $\widetilde{X}$ points of $H_2O$–*n*-decane/12-HOA–$C_{10}E_4$ microemulsions with different gelator mass fractions η at equal volumes of water and oil ($\phi = 0.5$)

| η | $\widetilde{\gamma}$ | $\widetilde{T}$ / °C |
|---|---|---|
| 0 | 0.135 | 30.2 |
| 0.015 | 0.123 | 24.3 |
| 0.025 | 0.121 | 23.6 |
| 0.050 | 0.116 | 23.8 |

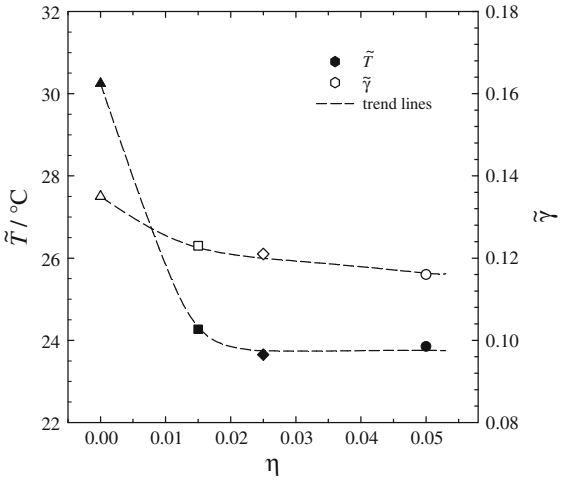


**Fig. 3.9** $\widetilde{X}$ point coordinates of the microemulsion $H_2O$–*n*-decane/12-HOA–$C_{10}E_4$, i.e. $\widetilde{T}$ (*black symbols, left axis*) and $\widetilde{\gamma}$ (*white symbols, right axis*), as function of the gelator mass fraction η (*symbols* cp. Figs. 3.2, 3.3, 3.6 and 3.8)

a certain amount of 12-HOA dissolves monomerically in *n*-decane as co-solvent and adsorbs to the water–oil interface as co-surfactant accounting for an effective change of the microemulsion composition and thus the shift of the $\widetilde{X}$ point. Additional 12-HOA, however, does not further influence the microemulsion in the described manner—the latter is obviously 'saturated' with 12-HOA—but instead strengthens the coexisting gelator network forming more and/or thicker gelator fibers which is substantiated, e.g., by the rheometry data discussed in Sect. 3.3.

At this point it is important to underline that the gelled microemulsion $H_2O$–*n*-decane/12-HOA–$C_{10}E_4$ containing 1.5, 2.5 or 5.0 wt% 12-HOA possesses the same characteristic phase behaviour as its non-gelled base system $H_2O$–*n*-decane–$C_{10}E_4$. Phase diagrams were measured with phase boundaries similar to the one of the non-gelled microemulsion; the phase transition temperatures are merely down-shifted by about 6 K and the efficiency is slightly increased. These effects, however, can be explained by the amphiphilicity of the gelator 12-HOA and do not interfere with the orthogonal self-assembled picture of gelled microemulsions. Hence, the obtained phase diagrams can be used to prepare the gelled microemulsion $H_2O$–*n*-decane/12-HOA–$C_{10}E_4$ in the one-phase, bicontinuous state in which it was investigated in this thesis.

## 3.2 Sol-Gel Transition

When the phase behaviour of a microemulsion gelled with a low molecular weight gelator is studied one must consider the phase boundaries of both base systems, i.e. those of the non-gelled microemulsion and that of the binary gel. Having discussed the phase boundaries of the microemulsion in Sect. 3.1, this chapter focuses on the sol-gel boundary which is characteristic for physical gels [9, 22, 27]. Qualitatively one observes that increasing the temperature of a physical gel leads to a transformation from a solid-like state into a liquid sol which is reversed upon cooling. This behaviour is well-known for binary gels and it was also observed for the gelled microemulsion $H_2O$–*n*-decane/12-HOA–$C_{10}E_4$ studied in this thesis. In the preparation process all components were mixed at elevated temperatures where the system is a liquid sol; subsequently gelation was induced by cooling the samples in an ice bath (cp. Sect. 6.2). The sol-gel boundary was thus crossed somewhere between 70 and 0 °C.

In the course of the phase studies sol-gel transition temperatures were determined quantitatively for both the base system *n*-decane/12-HOA and the gelled microemulsion $H_2O$–*n*-decane/12-HOA–$C_{10}E_4$ with different gelator concentrations. To be more precise, transition temperatures from the solid-like gel to the liquid sol were measured in experiments with increasing temperature. Phase studies of conventional physical gels indeed often involve heating-cooling cycles [10, 11]. However, working with temperature cycles made no sense for the gelled microemulsion investigated in this thesis because the sol-gel boundary lies in the two-phase region $\overline{2}$. Preparing a homogeneously gelled microemulsion accordingly requires a sophisticated procedure involving agitation and fast cooling (cp. Sect. 6.2) while in phase studies the temperature is changed slowly as one aims at determining the transition temperatures with high precision. Thus, it only made sense to 'melt' the gelled microemulsion for the phase studies; it would not re-form when inverting suitable measurement conditions. For the sake of comparability the binary gel was treated alike and also only studied with heating ramps. In heating-cooling cycles one often sees hysteresis effects, i.e. the transition from the gel to the sol usually occurs at higher temperatures than that from the sol to the gel [10, 11]. In this respect note that owing to the reasons given above all the sol-gel transition temperatures $T_{\text{sol-gel}}$ mentioned in this thesis refer exclusively to gel to sol transitions.

For both the gelled microemulsion and the binary gel two complementary techniques were applied for determining the sol-gel transition temperatures, namely temperature-dependent oscillating shear rheometry and differential scanning calorimetry (DSC).

### 3.2.1 Binary Gel

The $T$-η phase diagram of the base system *n*-decane/12-HOA was measured as reference for the sol-gel transition temperatures of the gelled microemulsion. For this purpose, binary gel samples with gelator mass fractions in a range from $\eta = 0.002$ to 0.050 were studied. The focus was on samples with 1.5, 2.5 and 5.0 wt% 12-HOA which are the same gelator concentrations that were used for the gelled microemulsion. Figure 3.10 shows the storage and the loss moduli, $G'$ and $G''$, measured in oscillating shear rheometry experiments at a constant frequency of 3 Hz and a shear stress of 10 Pa while the temperature was ramped up with a heating rate of 1 K $min^{-1}$.

Figure 3.10 clearly shows that at 25 °C the storage modulus $G'$ is, irrespective of the gelator concentration, considerably higher than the loss modulus $G''$ which proves the solid-like character of the gels present at this temperature [22]. The gel with the lowest 12-HOA mass fraction possesses the lowest and the one with the highest 12-HOA mass fraction the highest absolute moduli which will further be discussed in Sect. 3.3. Regarding the gel to sol transition it is the relative progression of $G'$ and $G''$ with temperature which is important. As one can see in Fig. 3.10 both $G'$ and $G''$ slightly decrease with increasing temperature. This is ascribed to a decrease of the cross-sections of the bundles of gelator fibers which are present in the gel state [27]. However, the distinct difference of $G'$ and $G''$ is maintained for a wide temperature range which demonstrates the temperature stability of the gelator network. Eventually, when the temperature approaches the sol-gel boundary, the decrease of the moduli amplifies until the storage modulus $G'$ drops below the loss modulus $G''$. At this point the gel character of the system is lost such that the corresponding temperature was taken as the sol-gel transition temperature $T_{\text{sol-gel}}$. The obtained values are $T_{\text{sol-gel}} = 59.1$ °C for the *n*-decane/12-HOA gel with 1.5 wt% gelator, $T_{\text{sol-gel}} = 67.1$ °C for the gel with 2.5 wt% and $T_{\text{sol-gel}} = 68.5$ °C for the gel with 5.0 wt% 12-HOA, respectively. Note that the temperature sweep rheometry experiments were carried out twice and the reproducibility of the sol-gel transition temperatures was ±1.0 K.

While the rheometry experiment monitors the loss of the interconnectivity and thus of the structure stability of the gelator network, DSC examines the sol-gel transition thermodynamically. With DSC one measures how much a sample cell must be heated in comparison to an empty reference cell to keep both cells at the same temperature, which is ramped up or down (here: +1 K $min^{-1}$) in the course of the measurement. Considerable differences occur when a phase transition takes place in the sample, e.g., the gel to sol transition, which is indicated by a peak in the data (see Fig. 3.11). Like it has been described in the literature [9–11], the peak maximum was taken as the sol-gel transition temperature $T_{\text{sol-gel}}$ (see Table A.8), which could be measured with an accuracy of ±1.4 K. In addition, the direction of the peak reveals that the gel to sol transition is an endothermic process (cp. Fig. 3.11) just as expected for the 'melting' of solid(-like) material. Moreover, the transition enthalpy $\Delta_{\text{sol-gel}}H$ can be determined from the peak area. Table 3.2 lists

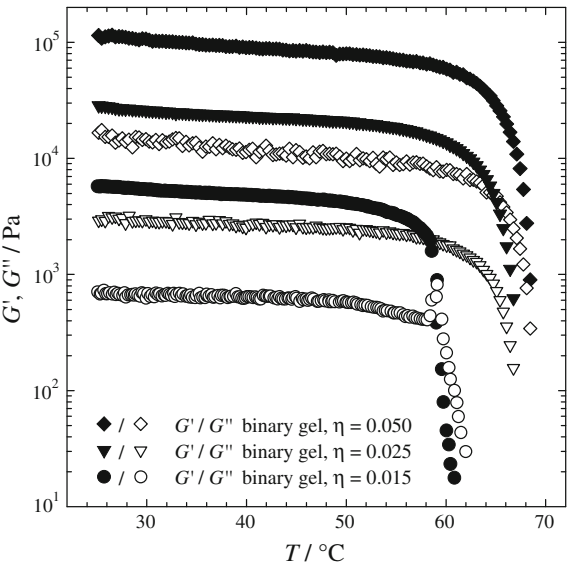


**Fig. 3.10** Storage modulus $G'$ (*filled symbols*) and loss modulus $G''$ (*open symbols*) of the binary gel *n*-decane/12-HOA with 1.5 (*circles* [2]), 2.5 (*triangles*) and 5.0 wt% (*diamonds*) gelator as a function of temperature. The data was recorded in oscillating shear rheometry experiments with $f = 3$ Hz, $\tau = 10$ Pa and a heating rate of 1 K min$^{-1}$

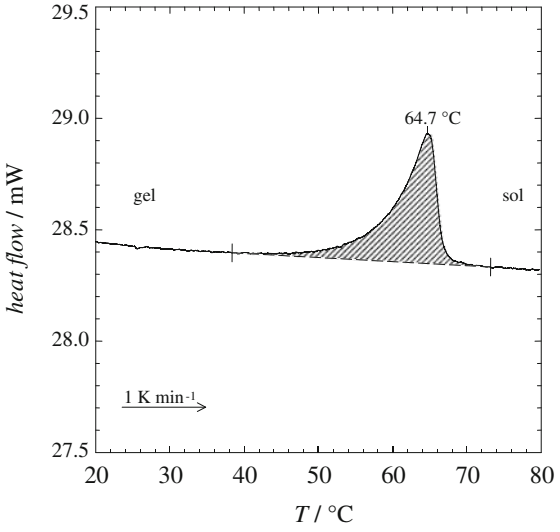


**Fig. 3.11** DSC data of a *n*-decane/12-HOA sample (31.45 mg) with $\eta = 0.037$.[KJ] The heat flow to the sample pan needed to sustain a heating rate of 1 K min$^{-1}$ is plotted versus the temperature. The peak indicates the transition from the gel to the sol and its integration (*hatched area*) yields the respective transition enthalpy

the respective values which were obtained with a reproducibility of ±0.1 J g$^{-1}$. As expected [9], $\Delta_{\text{sol-gel}}H$ increases with increasing gelator mass fraction.

In Fig. 3.12 all the $T_{\text{sol-gel}}$ values obtained for the binary gel *n*-decane/12-HOA are shown in a $T$-η phase diagram. As one can see, the sol-gel transition temperature increases with increasing gelator mass fraction which makes sense because with more 12-HOA more and/or thicker gelator fibers and thus a stronger

**Table 3.2** Sol-gel transition enthalpy $\Delta_{\text{sol-gel}}H$ of the binary gel *n*-decane/12-HOA with different gelator mass fractions η (cp. plot in Fig. 3.15)

| η | 0.002 | 0.004 | 0.008 | 0.015 | 0.020 | 0.025 | 0.037 |
|---|---|---|---|---|---|---|---|
| $\Delta_{\text{sol-gel}}H$ / J g$^{-1}$ | 0.7 | 2.0 | 2.1 | 3.7 | 3.8 | 6.6 | 7.4 |

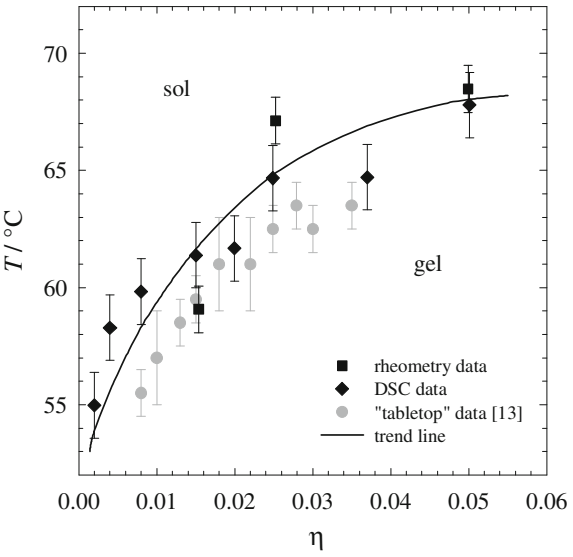


**Fig. 3.12** *T*-η phase diagram of the binary gel *n*-decane/12-HOA. The plot shows sol-gel transition temperatures determined via different methods: temperature-dependent oscillating shear rheometry (*squares*, Table A.7), differential scanning calorimetry (*diamonds*, Table A.8)[KJ] and, for comparison, a "tabletop" technique (*gray circles*) [13] (modified from [2]—reproduced by permission of The Royal Society of Chemistry)

gelator network can be built. For higher gelator concentrations the $T_{\text{sol-gel}}$ values tend to a plateau which has also been observed for 12-HOA gels with other solvents than *n*-decane [27] as well as for various other gels [9, 10, 12]. Moreover, the *T*-η diagram reveals that the results from the rheometry and the DSC measurements are in good agreement. For further comparison Fig. 3.12 shows sol-gel transition temperatures determined with a "tabletop" technique, i.e. the inversion of a test tube at different temperatures to check if the sample flows and is thus in the sol or in the gel state, respectively [13]. The present results do agree with this data even though the "tabletop" method yielded slightly lower $T_{\text{sol-gel}}$ values. This can be explained by the fact that the sol-gel transition is not a simple first-order process but rather takes place within a temperature range which is, e.g., reflected in a broad DSC peak (cp. Fig. 3.11) [9]. Thus, the samples were probably already assessed 'sol' in the "tabletop" measurements at the onset of the sol-gel transition, while the peak maximum of the DSC curves and the intersection of $G'$ and $G''$ in the rheometry measurements were reached only at higher temperatures.

### 3.2.2 Gelled Microemulsion

After studying the sol-gel boundary of the binary gel *n*-decane/12-HOA, sol-gel transition temperatures of the gelled microemulsion $H_2O$–*n*-decane/12-HOA–$C_{10}E_4$ with gelator concentrations of 1.5, 2.5 and 5.0 wt% were determined. Like for the binary gel temperature-dependent oscillating shear rheometry as well as DSC measurements were carried out for this purpose.

Figure 3.13 shows the data of the rheometry experiments. Note that the graph has the same axis scaling as Fig. 3.10, which displays the corresponding rheometry data of the binary gel. Comparing the storage and the loss moduli and their progression with temperature for the different systems one notices that at room temperature it holds $G' \gg G''$ for the gelled microemulsions with 1.5, 2.5 and 5.0 wt% 12-HOA just like for the respective binary gels. However, with increasing temperature $G'$ and $G''$ decrease "faster" for the gelled microemulsions and drop at considerably lower temperatures than for the binary gels, namely at 39.0, 41.0 and 46.6 °C with 1.5, 2.5 and 5.0 wt% gelator, respectively. Thus the gelled microemulsions have lower sol-gel transition temperatures than the binary gels while it is again the system with 1.5 wt% 12-HOA that possesses the lowest and the one with 5.0 wt% 12-HOA that possesses the highest $T_{\text{sol-gel}}$ value. Furthermore, one finds that the decrease of $G'$ and $G''$ with temperature is in fact only slightly stronger for the gelled microemulsions than for the binary gels if one exclusively regards the temperature ranges

$$T_{\text{sol-gel}} - 10\,\text{K} \lesssim T < T_{\text{sol-gel}}.$$

One must keep in mind that the system $H_2O$–*n*-decane/12-HOA–$C_{10}E_4$ is much more complex than a binary gel. Thus there are multiple composition parameters which might influence the sol-gel transition temperature. However, within the scope of this thesis the water-to-oil volume ratio was always kept constant at 1:1 ($\phi = 0.5$) which means besides the gelator mass fraction $\eta$ only the surfactant mass fraction $\gamma$ was sometimes varied. With a view on the one-phase bicontinuous regions of the differently gelled systems the focus was indeed on just a few $\gamma$ values rather than on $\gamma$ variations. Accordingly, the sol-gel transition temperature of the gelled microemulsion was rheometrically determined for only one surfactant mass fraction per gelator concentration, namely for $\gamma = 0.150$ with 1.5 and 2.5 wt% 12-HOA and for $\gamma = 0.123$ with 5.0 wt% 12-HOA (Fig. 3.13). These surfactant mass fractions are slightly higher than the respective $\widetilde{\gamma}$ values (cp. Table 3.1) such that the gelled microemulsions are one-phase and bicontinuous at the $\widetilde{T}$ temperatures where further measurements, e.g., rheometry (cp. Sect. 3.3), were carried out. With the temperature-dependent rheometry measurements it was now proved that the systems are indeed completely gelled under these conditions, which was, in fact, the main objective of measuring the sol-gel transition temperatures. The DSC measurements confirmed this result yielding sol-gel transition temperatures of the gelled microemulsion $H_2O$–*n*-decane/12-HOA–$C_{10}E_4$ which

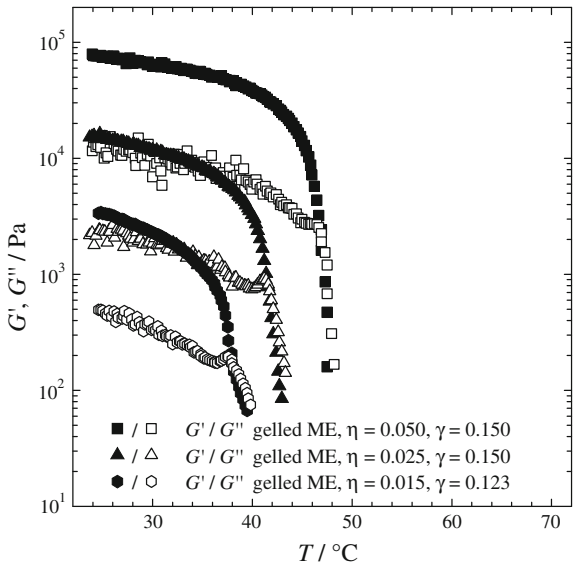


**Fig. 3.13** Storage modulus $G'$ (*filled symbols*) and loss modulus $G''$ (*open symbols*) of the gelled microemulsion $H_2O$–*n*-decane/12-HOA–$C_{10}E_4$ with 1.5 (*hexagons*), 2.5 (*triangles*) and 5.0 wt% (*squares*) gelator as a function of temperature. The data was recorded in oscillating shear rheometry experiments with $f = 3$ Hz, $\tau = 2$ Pa for $\eta = 0.015$, $\tau = 5$ Pa for $\eta = 0.025$ and $\tau = 20$ Pa for $\eta = 0.050$, respectively, and a heating rate of 1 K $min^{-1}$. The scaling of the axis is the same as for the binary gel in Fig. 3.10 (modified from [2]—reproduced by permission of The Royal Society of Chemistry)

lie considerably above the upper microemulsion phase boundary and thus in the $\overline{2}$ region. This is illustrated in Fig. 3.14 for the system with 1.5 and 2.5 wt% gelator, for which samples with three different surfactant mass fractions were investigated with DSC. *T*-γ phase diagrams are shown which comprise both the microemulsion phase boundaries discussed in Sect. 3.1 and the determined sol-gel transition temperatures. Note that no trend is observed for $T_{\text{sol-gel}}$ if one varies γ. In a previous study in which the sol-gel boundaries of gelled microemulsions with technical-grade surfactants were investigated over a wider γ range the sol-gel transition temperatures were found to decrease with increasing γ [14].

As mentioned above, with DSC one not only obtains sol-gel transition temperatures but also thermodynamical information like the sol-gel transition enthalpy $\Delta_{\text{sol-gel}}H$. Figure 3.15 shows that the latter increases for the gelled microemulsion with increasing gelator concentration just as it is the case for the binary gel. Furthermore, one can see that transforming a gelled microemulsion to the sol state requires on average about 1.5 J $g^{-1}$ less energy than melting the respective binary gel. Note that the plot shows data for gelled microemulsions with different surfactant mass fractions γ. However, like for the sol-gel transition temperatures no distinct relation between $\Delta_{\text{sol-gel}}H$ and γ is observable. The sol-gel transition

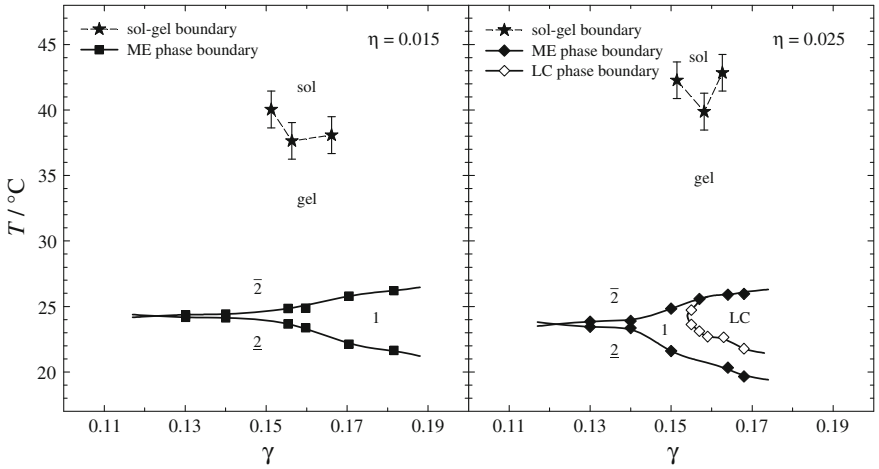


**Fig. 3.14** $T$-γ phase diagrams of the gelled microemulsion $H_2O$–*n*-decane/12-HOA–$C_{10}E_4$ with 1.5 (*left*, Table A.2) and 2.5 wt% (*right*, Table A.5) gelator. The stars mark the sol-gel transition temperatures determined by DSC measurements (Table A.10), while the squares and the diamonds mark the phase boundaries of the microemulsion (*filled symbols*) and a liquid crystalline (LC) phase (*open symbols*), respectively[KJ]

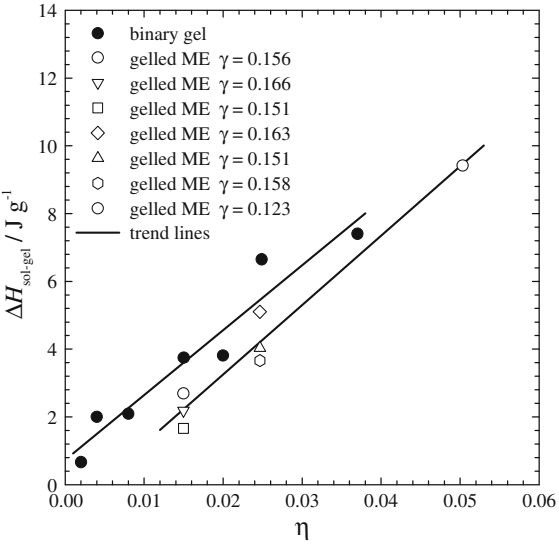


**Fig. 3.15** Sol-gel transition enthalpy of the binary gel *n*-decane/12-HOA (*filled symbols*, Table 3.2) and the gelled microemulsion $H_2O$–*n*-decane/12-HOA–$C_{10}E_4$ (*open symbols*, Table A.10) versus the gelator mass fraction η

enthalpy values for the different surfactant mass fractions scatter around the linear trend line just as much as the values of the binary gel without any surfactant do.

In order to compare the results of the temperature-dependent oscillating shear rheometry measurements and of DSC for the different systems the determined sol-gel transition temperatures are presented in a bar diagram (Fig. 3.16). To assure

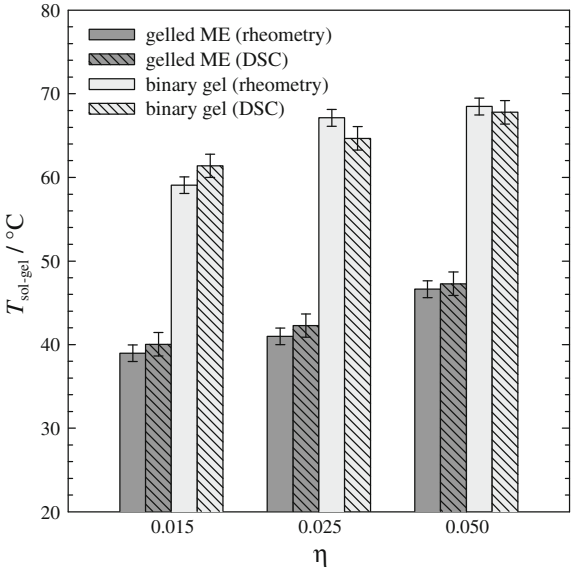


**Fig. 3.16** Sol-gel transition temperatures determined via rheometry (*plain bars*) and DSC (*dashed bars*)[KJ] for the binary gel *n*-decane/12-HOA (*light gray*, Tables A.7 and A.8) and the gelled microemulsion $H_2O$–*n*-decane/12-HOA–$C_{10}E_4$ (*dark gray*, Tables A.9 and A.10) with different gelator mass fractions η. The surfactant mass fractions in the microemulsions were $\gamma = 0.150$ (rheometry) and $\gamma = 0.151$ (DSC) for 1.5 and 2.5 wt% 12-HOA and $\gamma = 0.123$ (rheometry and DSC) for 5.0 wt% 12-HOA (modified from [2]—reproduced by permission of The Royal Society of Chemistry)

comparability, the diagram includes exclusively the DSC results of those gelled microemulsions whose surfactant mass fraction is close or identical to that of the samples studied via rheometry, i.e. the ones with $\gamma = 0.151$ for 1.5 and 2.5 wt% gelator (rheometry: $\gamma = 0.150$). For 5.0 wt% gelator only samples with $\gamma = 0.123$ were studied with both methods. One can see that the $T_{sol\text{-}gel}$ values determined via rheometry and DSC are in good agreement. In most cases the transition temperatures from DSC are slightly higher than those from the rheometry measurements. This can be due to the fact that rheometry detects the loss of the gelator network's stability, i.e. when the connections between the gelator fibers break, while DSC yields the 'melting point' of the gelator network. It is thus reasonable that the rheometry parameters already change at lower temperatures where the non-permanent junction zones (hydrogen bonds) [15] in the network break while the DSC peak maximum is reached at higher temperatures when the permanent junction zones (crystalline) [15] and the crystalline gelator fibers melt.

What one can also see in Fig. 3.16 is that the sol-gel transition temperature of the gelled microemulsion increases with increasing gelator mass fraction as is the case for the binary gel. A mathematical expression which describes this behaviour, i.e. which relates the sol-gel transition temperature to the gelator concentration,

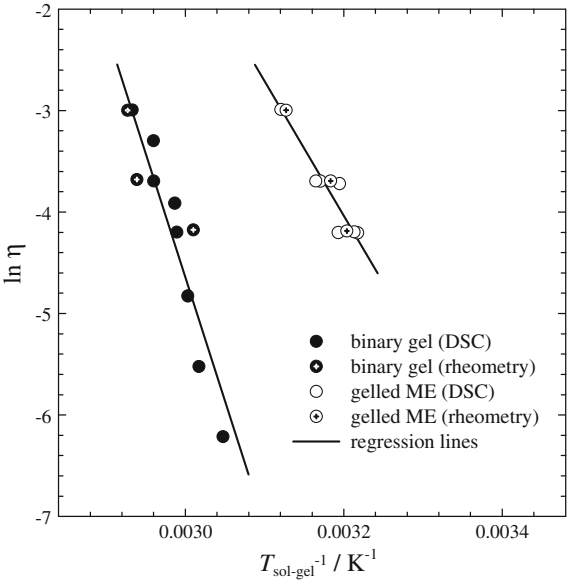


**Fig. 3.17** Plot of ln η versus $T_{sol\text{-}gel}^{-1}$ according to Eq. (3.1) for the binary gel *n*-decane/12-HOA (*black*, Tables A.7 and A.8) and the gelled microemulsion $H_2O$–*n*-decane/12-HOA–$C_{10}E_4$ (*white*, Tables A.9 and A.10). The data was obtained from DSC (*plain symbols*)[KJ] and rheometry (*dotted symbols*) measurements. The gelled microemulsions had different surfactant mass fractions γ as specified in the respective tables

has been developed by Eldridge and Ferry for gelatin gels [16]. Based on the assumption that the cross-linking of the gelator network is governed by dimerization processes of the biopolymer chains they derived an equation of the form [9]

$$\ln c = \frac{\Delta H}{R\, T_{sol-gel}} + constant \tag{3.1}$$

in which $c$ is the concentration of the gelator, $R$ the universal gas constant, $T_{sol\text{-}gel}$ the absolute gel to sol transition temperature and $\Delta H$ the enthalpy associated to the cross-linking process. According to this equation, which has been applied to various physical gels [10, 17, 18, 22], the plot of ln $c$ versus $T_{sol\text{-}gel}^{-1}$ should be linear. This is roughly found for both the binary gel *n*-decane/12-HOA and the gelled microemulsion $H_2O$–*n*-decane/12-HOA–$C_{10}E_4$ as can be seen in Fig. 3.17, where the natural logarithm of the gelator mass fraction η is plotted versus the inverse absolute sol-gel transition temperatures which were determined in the DSC and rheometry measurements. Note that the gelator mass fraction is used in this plot instead of a molar concentration; however, this does not change the general trend of the data. From the slopes of the regression lines which are $-2.44 \times 10^4$ K for the binary gel and $-1.33 \times 10^4$ K for the gelled microemulsion one can calculate $\Delta H$ values of $-203$ and $-110$ kJ mol$^{-1}$, respectively. These values mean that breaking one mole of cross-links [16] in the gelator network of the binary gel requires almost twice as much energy as breaking the same number of cross-links in the gelled microemulsion. This suggests that the cross-links in the gelled microemulsions are weaker than in the binary gel which could mean that the

ratio of permanent to non-permanent junction zones differs in the two systems. Moreover it is pretty likely that the solvent in the gel, i.e. the *n*-decane or the microemulsion, respectively, has an influence on the strength of the interactions in the junction zones. In particular the hydrogen bonds in the non-permanent junction zones could be disturbed by the water within the microemulsion.

Another approach is to interpret the gel to sol transition as a melting or dissolution of crystals [9]. In this case the equation to relate the sol-gel transition temperature $T_{\text{sol-gel}}$ to the gelator concentration $c$ is expressed as [9]

$$\ln c = -\frac{\Delta_{\text{melt}}H}{R}\left(\frac{1}{T_{\text{sol}-\text{gel}}} - \frac{1}{T_{\text{melt}}}\right) \tag{3.2}$$

where $R$ is the universal gas constant, $\Delta_{\text{melt}}H$ the enthalpy of fusion of the gelator and $T_{\text{melt}}$ the gelator's melting temperature, respectively. According to this equation the melting temperature of 12-HOA can be calculated from the intercepts of the regression lines in Fig. 3.17. One yields 83 °C in the case of the binary gel and 72 °C in the case of the gelled microemulsion which is indeed both close to the 12-HOA melting temperature of 74–76 °C specified by the supplier *Sigma-Aldrich*.[4] This shows that it is justified to use the crystal melting approach for the 12-HOA gels which makes sense with respect to the crystallinity of the gelator fibers and of the permanent junction zones [22].

To sum up, the results of this chapter demonstrate that the gelled microemulsion $H_2O$–*n*-decane/12-HOA–$C_{10}E_4$ possesses a sol-gel boundary just like its binary base system *n*-decane/12-HOA. Temperature-dependent oscillating shear rheometry and DSC measurements revealed in good agreement that the sol-gel transition temperature of both systems increases with increasing gelator concentration which, according to the DSC data, is also true for the sol-gel transition enthalpy. The general phase behaviour of the 12-HOA gel is thus not changed when "the solvent is replaced by a microemulsion". This reveals that the binary gel and the gelled microemulsion are physical gels of the same type which further confirms the orthogonal self-assembled character of the gelled microemulsion. The change of the solvent, however, does influence the strength of the gelator network which is a common phenomenon [8, 12, 20]. The sol-gel transition temperatures of the studied gelled microemulsions are about 20 K below those of the respective binary gels and also lower sol-gel transition enthalpies were measured. Furthermore, a lower cross-linking enthalpy was determined according to a mathematical model [16] in case of the gelled microemulsion compared to the binary gel. Hence the gelled microemulsion is a 'weaker' 12-HOA gel than its binary base system. The gelled microemulsion's surfactant mass fraction showed no significant influence on the sol-gel transition temperature. Regarding the gelator concentration it was proved that 5.0, 2.5 wt% and even 1.5 wt% 12-HOA are enough to gel the microemulsion's one-phase region—the sol-gel boundary is located more that

[4] http://www.sigmaaldrich.com/catalog/product/aldrich/219967, 12.04.2013.

10 K above the upper microemulsion phase boundary in all three cases. Hence, it was confirmed that the subsequent investigations on the one-phase bicontinuous microemulsions were carried out on completely gelled systems.

## 3.3 Rheology of Gelled Bicontinuous Microemulsions

After the phase studies had revealed the microemulsion phases boundaries and the sol-gel boundary of the system $H_2O$–*n*-decane/12-HOA–$C_{10}E_4$ with different gelator concentrations (see Sects. 3.1 and 3.2, respectively) it was known (a) at which temperatures ($\widetilde{T}$) and compositions ($\gamma > \widetilde{\gamma}$) the system is in the one-phase bicontinuous region and (b) that this region is indeed completely gelled. Moreover, striking similarities to the phase behaviour of the gelled microemulsion's base systems, i.e. the non-gelled microemulsion $H_2O$–*n*-decane–$C_{10}E_4$ and the binary gel *n*-decane/12-HOA, were seen which indicated the orthogonal self-assembled character of $H_2O$–*n*-decane/12-HOA–$C_{10}E_4$. To substantiate that the gelled microemulsion is orthogonal self-assembled in its bicontinuous state, which is the main goal of this thesis, selected samples were prepared according to the gained knowledge and studied with different methods (cp. Sects. 3.3–4.3). In this chapter the results of oscillating shear rheometry experiments are discussed which bear information about the viscoelasticity of the gelled bicontinuous microemulsion. Viscoelastic behaviour is typical for gels as they combine properties of viscous liquids and elastic solids [21]. Hence, the binary gel *n*-decane/12-HOA was studied as reference system.

### *3.3.1 Binary Gel*

At first, rheometry measurements were carried out on the binary gel *n*-decane/12-HOA with 1.5, 2.5 and 5.0 wt% gelator which served as reference for the respective gelled bicontinuous microemulsions. Just like the gelled microemulsions, which were to be investigated in the bicontinuous state and thus at their $\widetilde{T}$ temperatures, the binary gels were studied exclusively at one single temperature. In principle, there was no specific requirement regarding the measuring temperature of a binary gel but to lie below the sol-gel boundary. However, it was reasonable to study the base systems and the gelled bicontinuous microemulsions at comparable temperatures thus "room temperature" $T = 25.0$ °C, which is close to the gelled microemulsions' $\widetilde{T}$ temperatures (cp. Table 3.1), was used for all binary gels.

An interesting observation was made when the samples were placed in the rheometer gap, i.e. when the upper plate was lowered onto the gels. While common gels are squeezed out of the gap completely unaltered by this mechanical

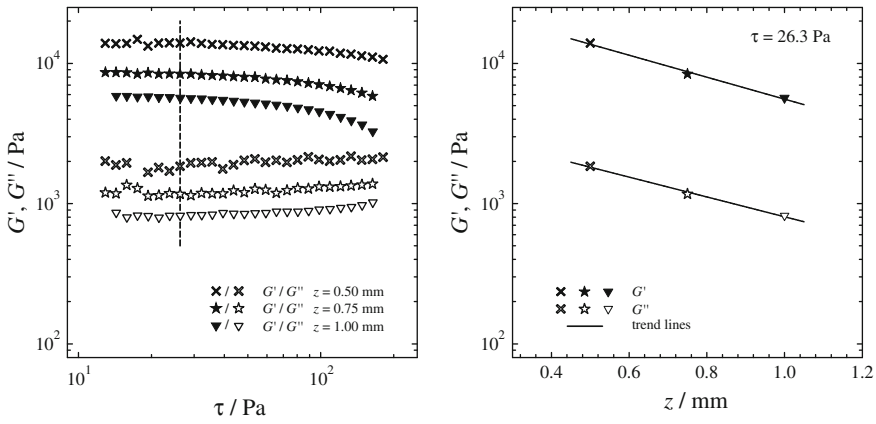


**Fig. 3.18** Storage modulus $G'$ (*filled symbols*) and loss modulus $G''$ (*open symbols*) of a *n*-decane/12-HOA sample with 2.5 wt% 12-HOA measured at 25.0 °C with oscillating shear rheometry at a constant frequency of 3 Hz and varied shear stress τ (*left*). The gap width was successively decreased from $z = 1.00$ (*triangles*) to 0.75 (*stars*) and 0.50 mm (*crosses*) which leads to an exponential increase of $G'$ and $G''$ as it is shown on the *right* for $\tau = 26.3$ Pa (*dashed line in the left diagram*, Table A.11) (modified from [2]—reprodu Royal Society of Chemistry)

treatment the 12-HOA gels expel liquid; thus obviously only the solvent is squeezed out. Accordingly, the gelator fraction of a sample between the plates must increase with decreasing gap size and indeed this could be evidenced through a series of stress sweep measurements. A binary gel with 2.5 wt% 12-HOA was studied for this purpose at gap widths $z$ of 1.00 mm, 0.75 mm and subsequently 0.50 mm with a constant frequency of 3 Hz in a shear stress range of about 13–180 Pa (Fig. 3.18, left). The determined storage and loss moduli, $G'$ and $G''$, are the higher the smaller the gap width—an exponential relationship was found (cp. Fig. 3.18, right). Thus the more solvent has been squeezed out the stronger is the investigated gel which is what one expects for an amplified gelator fraction in the sample. (Indeed, analogical results will shortly be presented for gels prepared with different gelator mass fractions.) The described behaviour of the 12-HOA gel is not reversible, i.e. re-increasing the rheometer gap width neither led to a reabsorption of the squeezed out solvent nor to a recovery of the initial $G'$ and $G''$ values. Thus the 12-HOA network obviously broke under the mechanical compression. Furthermore, the described experiment revealed that it was important to work with a gap size which matched the applied amount of sample such that alterations of the sample composition due to solvent loss were minimized. However, solvent loss in any case occurs as a function of time because of evaporation at the lateral surface of the sample in the gap. Thus the gap width $z$ should be preferably small. Considering these issues a gap width of $z = 1.00$ mm was identified as appropriate measuring parameter for the rheometry experiments described in the following. Note that choosing a suitable gap width was only

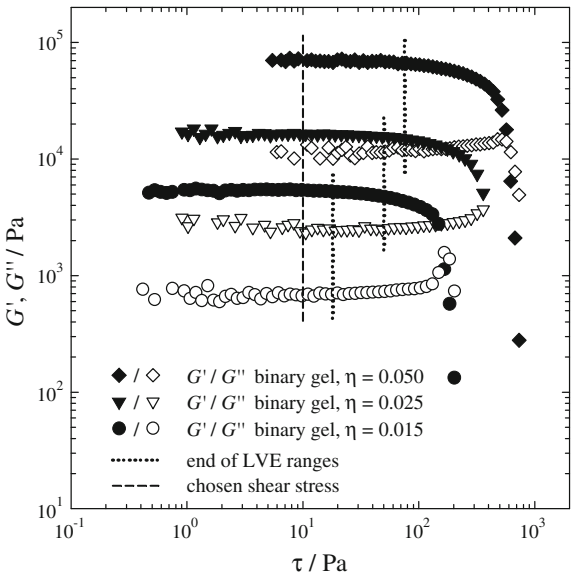


**Fig. 3.19** Storage modulus $G'$ (*filled symbols*) and loss modulus $G''$ (*open symbols*) of the binary gel *n*-decane/12-HOA with 1.5 (*circles*), 2.5 (*triangles*) and 5.0 wt% (*diamonds*) 12-HOA measured at 25.0 °C with oscillating shear rheometry at a constant frequency of 3 Hz and varied shear stress τ. The *dotted lines* indicate the ends of the LVE regions and the *dashed line* marks the shear stress $\tau = 10$ Pa which was used for the subsequent frequency sweep measurements (modified from [2]—reproduced by permission of The Royal Society of Chemistry)

possible since a plate–plate assembly, not a plate–cone assembly, was used as measuring system.

In order to determine the rheological properties of gels without damaging their microstructure it is important to work with shear stresses which are not too high but within the LVE region. Hence this region was initially located for the system *n*-decane/12-HOA with each gelator concentration (1.5, 2.5 and 5.0 wt%) in a stress-sweep measurement in which the storage modulus $G'$ and the loss modulus $G''$ were determined at a constant frequency of 3 Hz in a suitable shear stress range (see Fig. 3.19). The general progression of $G'$ and $G''$ with increasing shear stress τ is the same for all 12-HOA gels. Upon very small stresses the gels do not produce a strain response which is sufficiently strong to be measured accurately. Thus $G'$ and especially $G''$ scatter strongly for very small τ values (data not shown in Fig. 3.19). This scattering ceases with increasing τ and $G'$ and $G''$ remain virtually constant until the end of the LVE region. There the storage modulus begins to fall while the loss modulus starts to increase. At very high shear stresses the moduli $G'$ and $G''$ converge and then both drop which indicates the breakdown of the gels' microstructure.

The extension of the LVE region varies for different gelator mass fraction in the *n*-decane/12-HOA gel. It roughly stretches up to 18 Pa with 1.5 wt%, to 50 Pa

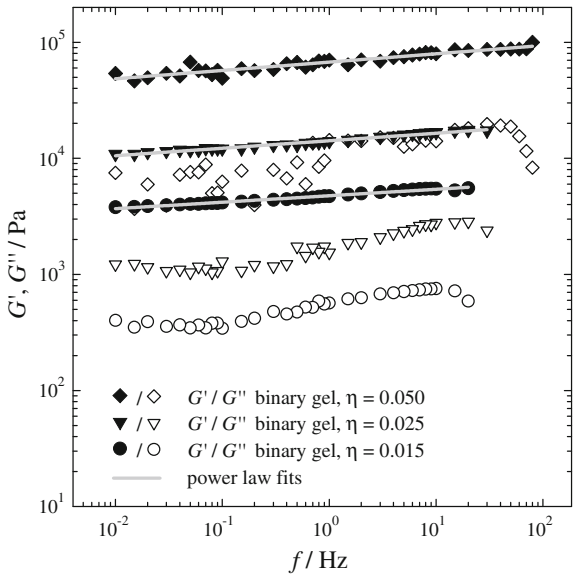


**Fig. 3.20** Storage modulus $G'$ (*filled symbols*) and loss modulus $G''$ (*open symbols*) of the binary gel *n*-decane/12-HOA with 1.5 (*circles*), 2.5 (*triangles*) and 5.0 wt% (*diamonds*) 12-HOA measured at 25.0 °C with oscillating shear rheometry at a constant shear stress of 10 Pa and varied frequency *f*. The *gray lines* are fits according to Eq. (3.3), the fit parameters are given in Table 3.3 (modified from [2]—reproduced by permission of The Royal Society of Chemistry)

with 2.5 wt% and to 75 Pa with 5.0 wt% gelator while meaningful $G'$ and $G''$ values could be measured above shear stresses of about 1, 3 and 6 Pa, respectively. The enlargement of the LVE region with increasing 12-HOA concentration indicates that the binary gel is the stronger the more gelator is involved. This is directly confirmed by the fact that the absolute $G'$ and $G''$ values also increase with increasing gelator concentration. In this respect the stress sweeps, which were well reproducible (about 2 % variation of $G'$ and $G''$ in repeated measurements), allow a first assessment of a studied sample. For the subsequently carried out frequency sweep measurements a shear stress of 10 Pa was chosen for all binary gels.

Figure 3.20 shows the storage and loss moduli $G'$ and $G''$ of the binary gel *n*-decane/12-HOA with 1.5, 2.5 and 5.0 wt% gelator for different frequencies in a range from 0.01 to about 80 Hz. The displayed data are the mean values of four measurements per sample the average standard deviation of which is $\leq$ 12 % for $G'$ and $\leq$ 33 % for $G''$ (cp. Table 6.3, the deviation increases with the gelator concentration since $G'$ and $G''$ scatter at 10 Pa the most for 5.0 wt% 12-HOA, cp. Fig. 3.19). For all gelator concentrations it holds that the storage modulus $G'$ is considerably larger than the loss modulus $G''$; on average about 6 to 9 times which corresponds to loss factors tan δ (cp. Eq. (2.23)) of 0.15–0.11 (see Table 3.3). This rheologic behaviour is characteristic for strong gels or 'soft solids', for which $G'$

**Table 3.3** Fit parameters κ and $G'_0$ of Eq. (3.3), storage modulus $G'$ and loss modulus $G''$ at 1 Hz (mean values of four measurements with $\tau = 10$ Pa) and loss factor tan δ (average values over the investigated frequency ranges) for the binary gel *n*-decane/12-HOA with different gelator mass fractions η

| η | κ | $G'_0$ / Pa | $G'$(1 Hz) / Pa | $G''$(1 Hz) / Pa | tan δ |
|---|---|---|---|---|---|
| 0.015 | 0.06 | $4.8 \times 10^3$ | $4.7 \times 10^3$ | $5.7 \times 10^2$ | 0.11 |
| 0.025 | 0.06 | $1.4 \times 10^4$ | $1.4 \times 10^4$ | $1.5 \times 10^3$ | 0.12 |
| 0.050 | 0.07 | $6.7 \times 10^4$ | $7.0 \times 10^4$ | $1.4 \times 10^4$ | 0.15 |

and $G''$ only slightly depend on the frequency [21]. The latter is especially true for the storage modulus $G'$ to which a power law equation of the type

$$G' = G'_0 f^{\kappa} \tag{3.3}$$

could be fitted. In Table 3.3, which lists the respective fit parameters $G'_0$ and κ, one can see that the exponent of the frequency is indeed close to zero ($\kappa << 0.1$) for all gelator concentrations. Very similar patterns of $G'$ and $G''$ versus frequency as the ones measured for the *n*-decane/12-HOA gels (Fig. 3.20) have been reported for 12-HOA gels with other solvents, such as nitrobenzene [19] and *n*-dodecane [27]. Terech et al. referred to a respective diagram as "typical rheogram of a HSA [= 12-HOA] organogel" [27] and, in the case of the dodecane gel, determined for $G'$ also a power law fit with a frequency exponent of 0.06 [27]. For the 12-HOA gels described in the literature [19, 27] just as for the systems discussed here the absolute values of $G'$ and $G''$ differ for different solvents and for varying gelator concentration. The $G'$ and $G''$ moduli which were measured for *n*-decane/12-HOA with 1.5, 2.5 and 5.0 wt% gelator at a frequency of 1 Hz range from $4.7 \times 10^3$ to $7.0 \times 10^4$ Pa and from $5.7 \times 10^2$ to $1.4 \times 10^4$ Pa, respectively (see Table 3.3). Note that $G'$(1 Hz) corresponds to the fit parameter $G'_0$ for which good agreement is found.

### 3.3.2 Gelled Bicontinuous Microemulsion

In order to study the viscoelasticity of gelled microemulsions in their one-phase bicontinuous state $H_2O$–*n*-decane/12-HOA–$C_{10}E_4$ samples were prepared based on the knowledge gained in the microemulsion phase studies (cp. Sect. 3.1). Besides equal volumes of water and oil ($\phi = 0.5$) surfactant mass fractions were used which are somewhat higher than $\widetilde{\gamma}$ (cp. Table 3.1), namely $\gamma = 0.150$ with 1.5 and 2.5 wt% 12-HOA but only $\gamma = 0.123$ with 5.0 wt% gelator due to the presence of the LC phase. To ensure bicontinuity each system was probed at its $\widetilde{T}$ temperature (cp. Table 3.1); thus the measuring temperatures were 24.3, 23.6 and 23.8 °C for the gelled microemulsion with 1.5, 2.5 and 5.0 wt% gelator, respectively. Note that the temperature-dependent rheometry measurements used to

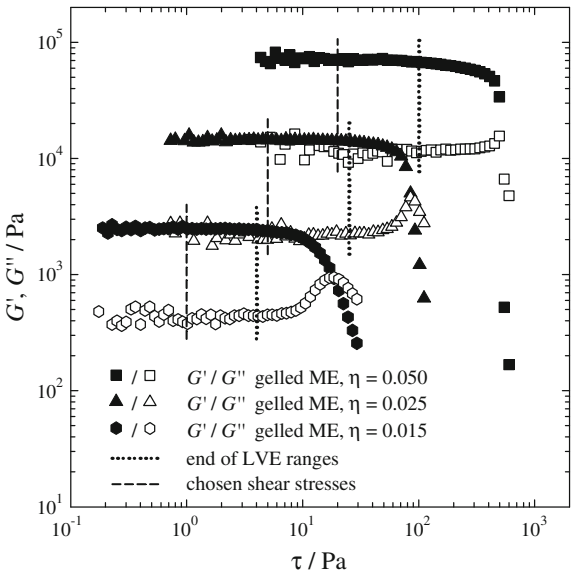


**Fig. 3.21** Storage modulus $G'$ (*filled symbols*) and loss modulus $G''$ (*open symbols*) measured with oscillating shear rheometry at 3 Hz and varied shear stress $\tau$ for the gelled bicontinuous microemulsion $H_2O$–*n*-decane/12-HOA–$C_{10}E_4$ ($\phi = 0.5$) with 1.5 (*hexagons*, $\gamma = 0.150$), 2.5 (*triangles*, $\gamma = 0.150$) and 5.0 wt% (*squares*, $\gamma = 0.123$) 12-HOA at the respective $\tilde{T}$ temperatures 24.3, 23.6 and 23.8 °C. The *dotted lines* indicate the ends of the LVE regions and the *dashed lines* the shear stresses 2, 5 and 20 Pa which were used for the subsequent frequency sweep measurements (modified from [2]—reproduced by permission of The Royal Society of Chemistry)

determine the sol-gel boundary (cp. Sect. 3.2) showed that small temperature variations (1–2 K) around room temperature hardly affected the storage and the loss modulus neither of the binary gels (cp. Fig. 3.10) nor of the gelled microemulsions (cp. Fig. 3.13). Hence it is justifiable to compare in the following the rheometry results of the differently gelled microemulsions with each other and also with those of the binary gel, in spite of the different temperatures which were used for the measurements.

Just like for the binary gel, the first step was to identify the LVE region of the gelled bicontinuous microemulsion $H_2O$–*n*-decane/12-HOA–$C_{10}E_4$ with 1.5, 2.5 and 5.0 wt% 12-HOA. Hence stress sweep measurements were carried out at a frequency of 3 Hz which yielded the storage and the loss moduli of the systems at different shear stresses $\tau$ (Fig. 3.21). One can see that the general trends in the data are the same as those found for the binary gel (cp. Fig. 3.19). $G'$ and $G''$ increase with increasing gelator concentration and they are frequency independent for low shear stresses until the end of the LVE region where they drop for high shear stresses. However, in the case of the gelled bicontinuous microemulsion the extension of the LVE region varies much stronger with the gelator concentration

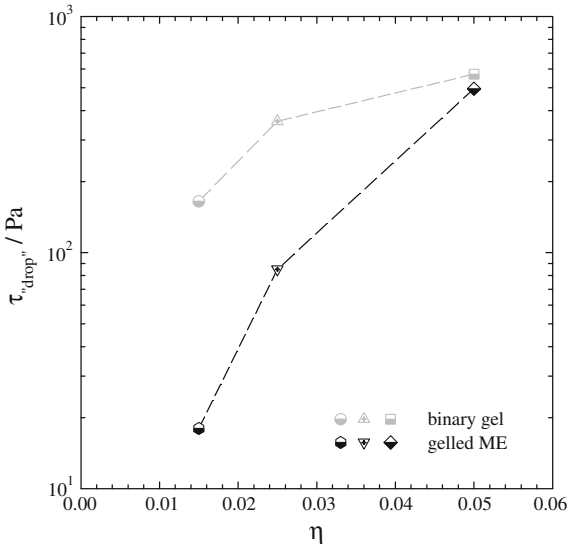


**Fig. 3.22** Semi-logarithmic plot of the shear stress $\tau_{\text{"drop"}}$ which causes a breakdown of the gelator network (intersection of $G'$ and $G''$) versus the gelator mass fraction η (Table A.12). The *black symbols* represent the values of the gelled bicontinuous microemulsion $H_2O$–*n*-decane/12-HOA–$C_{10}E_4$ and the *gray symbols* those of the binary base system *n*-decane/12-HOA, respectively. The *dashed lines* guide the eye

than in the case of the binary base system. The LVE region ends at 4 Pa for the gelled bicontinuous microemulsion with 1.5 wt%, at 25 Pa with 2.5 wt% and at 100 Pa with 5.0 wt% 12-HOA. Meaningful values for the two moduli are obtained above shear stresses of about 0.2, 0.7 and 5 Pa, respectively. From these values it is obvious that the frequency sweeps could not be performed with the same shear stress for all three gelator concentrations. Thus τ values about one order of magnitude below those at the ends of the LVE regions were used, namely 2 Pa for the gelled bicontinuous microemulsion with 1.5 wt%, 5 Pa with 2.5 wt% and 20 Pa with 5.0 wt% gelator.

The extension of the LVE region and particularly the shear stress $\tau_{\text{"drop"}}$ for which $G'$ and $G''$ drop, i.e. the stress which causes a breakdown of the gel's microstructure, give an idea about the stability of the gelator network in the studied system. To compare the latter for the gelled bicontinuous microemulsion and the binary gel the respective $\tau_{\text{"drop"}}$ values are plotted in Fig. 3.22 versus the gelator mass fraction η. Note that since it is difficult to state at which point exactly $G'$ and $G''$ drop, the shear stress for which $G'$ and $G''$ intersect was taken as $\tau_{\text{"drop"}}$. One can see that $\tau_{\text{"drop"}}$, just like the extension of the LVE region, increases in greater steps with the 12-HOA concentration in the case of the gelled bicontinuous microemulsion than in the case of the binary gel. However, the absolute $\tau_{\text{"drop"}}$ values are lower for the gelled bicontinuous microemulsion than for the binary base system. This shows that less stress is needed to break down the 12-HOA network

in a bicontinuous microemulsion than in *n*-decane which means that the stabilizing network junctions must be weaker in the gelled bicontinuous microemulsions than in the binary gels. Note that this observation confirms what was found when studying the sol-gel boundary. The latter was considerably lower for the gelled microemulsions compared to the binary gels (cp. Fig. 3.16). Furthermore, the DSC measurements revealed lower sol-gel transition enthalpies for the gelled microemulsions and that less energy is needed to break cross-links in the gelator network of a gelled microemulsion than in the gelator network of a binary gel (cp. Sect. 3.2).

With the determined shear stresses in the LVE region frequency sweep measurements were carried out on the gelled bicontinuous microemulsion. Figure 3.23 shows the storage and the loss moduli obtained with the different gelator mass fractions in a frequency range from 0.01 to about 80 Hz. The plotted values are the average of four ($\eta = 0.015$), six ($\eta = 0.025$) and three ($\eta = 0.050$) measurements with average standard deviations of $\leq$8 % for $G'$ and $\leq$26 % for $G''$ (cp. Table 6.3). It is obvious that there are close analogies to the results obtained with the binary gels (cp. Fig. 3.20). Irrespective of the gelator concentration the storage modulus $G'$ is considerably bigger than the loss modulus $G''$ which indicates that the gelled bicontinuous microemulsions are also strong, solid-like gels. This manifests in loss factors tan $\delta$ (cp. Eq. (2.23)) which are much smaller than one, namely in the range of 0.13–0.16 (see Table 3.4). Furthermore, the storage modulus $G'$ can be fitted to a power law (Eq. (3.3)) as was the case for the binary base system. The obtained frequency exponents $\kappa$ are 0.07 for all gelator mass fractions and thus close to zero (see Table 3.4) which shows that for gelled bicontinuous microemulsions $G'$ is also hardly frequency-dependent. Looking at the absolute values of the storage and the loss modulus of the gelled bicontinuous microemulsion one finds, as expected and already seen in the stress sweep measurements, an increase with increasing gelator concentration. At a frequency of 1 Hz $G'$ ranges from $2.8 \times 10^3$ to $6.3 \times 10^4$ Pa and $G''$ from $3.5 \times 10^2$ to $9.1 \times 10^3$ Pa, respectively (cp. Table 3.4).

The magnitudes of the storage and the loss modulus in the gelled bicontinuous microemulsions are almost the same as those in the binary gels with the respective gelator concentrations. In a similar study of gelled microemulsions, by contrast, a considerable decrease of $G'$ and $G''$ compared to the respective binary gels has been reported [23]. However, in this study the gelator mass fraction of the gelled microemulsions referred to the oil phase, not to the entire system, and was thus on overall much lower than in the corresponding binary gels. Moreover, additives (monomer and cross-linker) and a technical-grade surfactant were used the effects of which on the gelator network were not investigated. In the well-defined system $H_2O$–*n*-decane/12-HOA–$C_{10}E_4$ of this thesis this is not the case. The similarity of $G'$ and $G''$ between the gelled bicontinuous microemulsion and the binary gel *n*-decane/12-HOA is still interesting since different stress durabilities and sol-gel transition temperatures were found for the systems. Terech et al. reported analogical results, namely different sol-gel transition temperatures but the same storage moduli for *n*-dodecane/12-HOA and toluene/12-HOA gels [27]. They

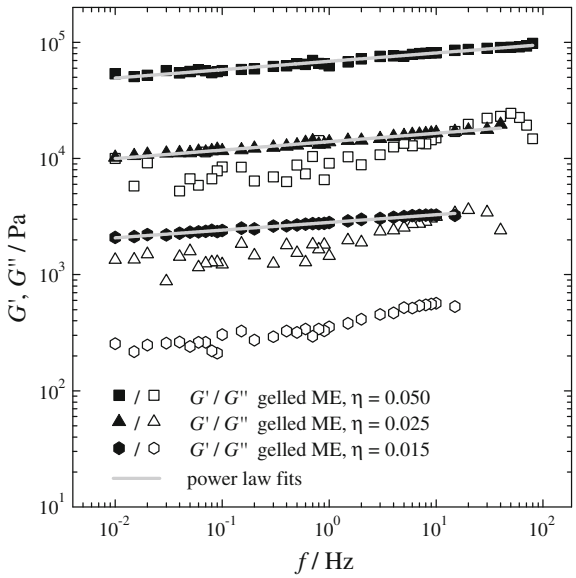


**Fig. 3.23** Storage modulus $G'$ (*filled symbols*) and loss modulus $G''$ (*open symbols*) of the gelled bicontinuous microemulsion $H_2O$–*n*-decane/12-HOA–$C_{10}E_4$ ($\phi = 0.5$) with 1.5 (*hexagons*, $\gamma = 0.150$), 2.5 (*triangles*, $\gamma = 0.150$) and 5.0 wt% (*squares*, $\gamma = 0.123$) 12-HOA. The oscillating shear rheometry measurements were carried out at constant shear stresses of 2, 5 and 20 Pa and the $\widetilde{T}$ temperatures 24.3, 23.6 and 23.8 °C for $\eta = 0.015$, 0.025 and 0.050, respectively. The *gray lines* are fits according to Eq. (3.3), the fit parameters are given in Table 3.4 (modified from [2]—reproduced by permission of The Royal Society of Chemistry)

**Table 3.4** Fit parameters $\kappa$ and $G'_0$ of Eq. (3.3), storage modulus $G'$ and loss modulus $G''$ at 1 Hz (mean values of 4, 3 and 6 measurements with 2, 5 and 20 Pa for 1.5, 2.5 and 5.0 wt% gelator, respectively) and loss factor tan $\delta$ (average values over the investigated frequency ranges) for the gelled bicontinuous microemulsion $H_2O$–*n*-decane/12-HOA–$C_{10}E_4$ ($\phi = 0.5$) with different gelator mass fractions $\eta$ and the surfactant mass fractions $\gamma$

| $\eta$ | $\gamma$ | $\kappa$ | $G'_0$ / Pa | $G'$(1 Hz) / Pa | $G''$(1 Hz) / Pa | tan $\delta$ |
|---|---|---|---|---|---|---|
| 0.015 | 0.150 | 0.07 | $2.8 \times 10^3$ | $2.8 \times 10^3$ | $3.5 \times 10^2$ | 0.13 |
| 0.025 | 0.150 | 0.07 | $1.4 \times 10^4$ | $1.4 \times 10^4$ | $1.4 \times 10^3$ | 0.14 |
| 0.050 | 0.123 | 0.07 | $6.9 \times 10^4$ | $6.3 \times 10^4$ | $9.1 \times 10^3$ | 0.16 |

explained their observations by a substantial influence of the solvent on the gelator network. Accordingly, one can interpret the results of this thesis such that the gelled bicontinuous microemulsion is a physical gel of the same type as its binary base system *n*-decane/12-HOA—just the solvent has been exchanged.

The second base system of the gelled bicontinuous microemulsion, i.e. the non-gelled bicontinuous microemulsion, is a low viscous Newtonian liquid with $G'$ and $G''$ values orders of magnitude below those seen for the solid-like 12-HOA gels [23]. Accordingly, this system is not expected to significantly influence the

rheological behaviour of the gelled bicontinuous microemulsion and was therefore not studied here. Studying the rheology of both base systems of an orthogonal self-assembled system only makes sense if the two base systems possess similar storage and loss moduli as it is, e.g., the case for a gelled aqueous solution of worm-like micelles. Due to the entanglement of the worm-like micelles the aqueous solution is highly viscous just like the second base system, i.e. the binary hydrogel [24]. Hence the rheological properties of the gelled micellar solution are influenced by both base systems (in degrees determined by the surfactant to gelator ratio) [24], while in the case of the gelled bicontinuous microemulsions the binary gel is clearly dominating.

A comparison of the storage and loss moduli of the studied gelled bicontinuous microemulsions and binary gels (Fig. 3.20 vs. 3.23) reveals that $G'$ and $G''$ are almost identical for both systems with 5.0 and 2.5 wt% gelator. However, with 1.5 wt% 12-HOA the moduli of the gelled bicontinuous microemulsion are on average 1.6 times lower than those of the binary base system. A possible explanation for this finding is the fact that 12-HOA, which is a surface active molecule, not only self-assembles to form gelator fibers in the bicontinuous microemulsion but also adsorbs at the large water–oil interface as was clearly evidenced by the phase boundary shifts observed in the microemulsion phase studies (cp. Sect. 3.1). (Note that monomeric solubility of 12-HOA in *n*-decane occurs in the gelled bicontinuous microemulsion as well as in the binary gel.) As a consequence, a reduced amount of 12-HOA is available in the gelled bicontinuous microemulsion for forming the gelator network, which is thus weaker than in the binary gel. However, assuming that not a proportion but a fix number of 12-HOA molecules adsorb at the interface the weakening effect is noticed in particular when the total gelator concentration is small, i.e. here with 1.5 wt% 12-HOA. With 2.5 and 5.0 wt% 12-HOA the network-forming gelator amount seems to be effectively the same in the gelled bicontinuous microemulsion and in the binary gel which explains why the systems' rheological responses are so similar at these gelator concentrations.

Figure 3.24 shows the storage and the loss moduli of the gelled bicontinuous microemulsion and of the binary gel measured at 1 Hz versus the gelator mass fraction $\eta$. One can see that the data points follow linear trend lines in the double logarithmic plot. For the storage modulus $G'$, which is particularly characteristic for the elastic properties and the strength of solid-like gels [25], the trend has been described by a power law [27]

$$G' \sim \eta^{\psi}. \tag{3.4}$$

From a fit to the data points one obtains exponents of $\psi = 2.25$ for the binary gel *n*-decane/12-HOA and $\psi = 2.56$ for the gelled bicontinuous microemulsion $H_2O$–*n*-decane/12-HOA–$C_{10}E_4$ while an exponent of 2.22 has been reported for a binary 12-HOA gel with *n*-dodecane as solvent [27]. For a theoretical model of a network formed by rigid chains which are permanently and rigidly connected to each other the respective exponent is two [26]. Considering that the obtained fit

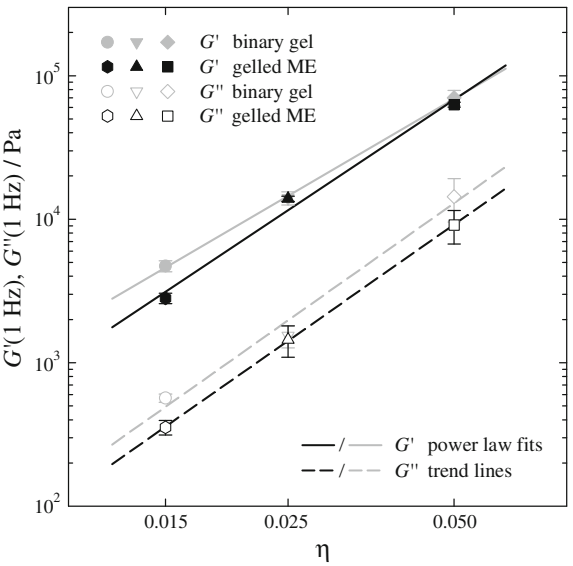


**Fig. 3.24** Double logarithmic plot of the storage modulus $G'$ (*filled symbols*) and the loss modulus $G''$ (*open symbols*) determined in oscillation measurements at 1 Hz for the gelled bicontinuous microemulsion $H_2O$–*n*-decane/12-HOA–$C_{10}E_4$ (*black*, Table 3.3) and the binary gel *n*-decane/12-HOA (*gray*, Table 3.4) versus the gelator mass fraction η. The *solid lines* are fits according to Eq. (3.4) and the *dashed lines* are respective trend lines

parameters are based on only three data points they can roughly be seen as close to 2 which suggests a stabilization of the gelator network in the studied gels by rigid knots [7, 27]. This indeed makes sense as 12-HOA gels do possess 'permanent', i.e. crystalline, junction zones [15].

Summing up, the rheological properties of the studied gelled bicontinuous microemulsions are strikingly congruent with those of the respective binary gels. Identical qualitative behaviour was observed in all rheometry measurements and with 2.5 and 5.0 wt% 12-HOA the storage and the loss moduli are even quantitatively the same for both systems. These results show that $H_2O$–*n*-decane/12-HOA–$C_{10}E_4$ is an orthogonal self-assembled system which maintains the rheological characteristics of its base system *n*-decane/12-HOA.

## References

1. C. Stubenrauch, C. Frank, R. Strey, D. Burgemeister, C. Schmidt, Langmuir **18**, 5027–5030 (2002)
2. M. Laupheimer, K. Jovic, F.E. Antunes, M.M.M. da Graça, C. Stubenrauch, Soft Matter **9**, 3661–3670 (2013)
3. S. Burauer, T. Sachert, T. Sottmann, R. Strey, Phys. Chem. Chem. Phys. **1**, 4299–4306 (1999)
4. C. Stubenrauch, R. Tessendorf, R. Strey, I. Lynch, K.A. Dawson, Langmuir **23**, 7730–7737 (2007)
5. M.H.G.M. Penders, R. Strey, J. Phys. Chem. **99**, 10313–10318 (1995)
6. M. Laupheimer, C. Stubenrauch, Tenside Surf. Det. **51**, 17–25 (2014)
7. P. Terech, S. Friol, Tetrahedron **63**, 7366–7374 (2007)
8. P. Terech, V. Rodriguez, J.D. Barnes, G.B. McKenna, Langmuir **10**, 3406–3418 (1994)

9. S.R. Raghavan, B.H. Cipriano, in *Molecular Gels. Materials with Self-Assembled Fibrillar Networks*, ed. by R.G. Weiss, P. Terech (Springer, Dordrecht, 2006), pp. 241–252
10. M. Núñez-Santiago, A. Tecante, Carbohydr. Polym. **69**, 763–773 (2007)
11. M. Tomšič, F. Prossnigg, O. Glatter, J. Colloid Interface Sci. **322**, 41–50 (2008)
12. M. George, R.G. Weiss, in: *Molecular Gels. Materials with Self-Assembled Fibrillar Networks*, ed. by R.G. Weiss, P. Terech (Springer, Dordrecht, 2006), pp. 449–551
13. R. Tessendorf, unpublished work
14. R. Tessendorf, *Microemulsions as Templates for High Surface Area Polymers* (WiKu-Wissenschaftsverlag Dr. Stein, Köln, 2009)
15. M.A. Rogers, T. Pedersen, L. Quaroni, Cryst. Growth Des. **9**, 3621–3625 (2009)
16. J.E. Eldridge, J.D. Ferry, J. Phys. Chem. **58**, 992–995 (1954)
17. K. Murata, M. Aoki, T. Suzuki, T. Harada, H. Kawabata, T. Komori, F. Ohseto, K. Ueda, S. Shinkai, J. Am. Chem. Soc. **116**, 6664–6676 (1994)
18. N. Amanokura, K. Yoza, H. Shinmori, S. Shinkai, D.N. Reinhoudt, J. Chem. Soc. Perkin Trans. **2**, 2585–2591 (1998)
19. P. Terech, C. Rossat, F. Volino, J. Colloid Interface Sci. **227**, 363–370 (2000)
20. S. Bhattacharya, A. Pal, J. Phys. Chem. B **112**, 4918–4927 (2008)
21. K. Nishinari, Progr. Colloid Polym. Sci. **136**, 87–94 (2009)
22. P. Terech, R.G. Weiss, Chem. Rev. **97**, 3133–3159 (1997)
23. M. Magno, R. Tessendorf, B. Medronho, M.M.M. da Graça, C. Stubenrauch, Soft Matter **5**, 4763–4772 (2009)
24. A.M. Brizard, M.C.A. Stuart, J.H. van Esch, Faraday Discuss. **143**, 345–357 (2009)
25. M. Burkhardt, S. Kinzel, M. Gradzielski, J. Colloid Interface Sci. **331**, 514–521 (2009)
26. J.L. Jones, C.M. Marques, J. Phys. France **51**, 1113–1127 (1990)
27. P. Terech, D. Pasquier, V. Bordas, C. Rossat, Langmuir **16**, 4485–4494 (2000)

# Chapter 4
# Microstructure of Gelled Bicontinuous Microemulsions

To verify the orthogonal self-assembled character of gelled bicontinuous microemulsions it is important to study not only their phase behaviour and rheological properties (see Sect. 4.3) but also their microstructure. In orthogonal self-assembled systems the microstructures of the base systems are maintained and coexist with each other. Thus in case of gelled bicontinuous microemulsions one expects bicontinuous microemulsion domains to coexist with a three-dimensional gelator network. In order to prove this assumption for the system $H_2O$–*n*-decane/12-HOA–$C_{10}E_4$ the microstructure was investigated with different methods. Those methods were also applied to the base systems, i.e. the non-gelled bicontinuous microemulsion $H_2O$–*n*-decane–$C_{10}E_4$ and the binary gel *n*-decane/12-HOA, to be able to disclose the structural similarities. First, the gelled and the non-gelled microemulsion were studied with $^1$H-NMR self-diffusion measurements. Those revealed that the microemulsion domains are indeed bicontinuous at the $\widetilde{T}$ temperature, irrespective of the presence of the gelator network (Sect. 4.1). The coexistence of the bicontinuous microemulsion with the network of 12-HOA fibers was subsequently demonstrated with small angle neutron scattering (SANS, Sect. 4.2) and freeze-fracture transmission electron microscopy (FFEM, Sect. 4.3). The scattering curves of the gelled bicontinuous microemulsion comprise the characteristic scattering patterns of both base systems and the FFEM pictures visualize the coexisting microstructures.

## 4.1 NMR Self-Diffusion Measurements

The phase studies in Sect. 3.1 revealed that the gelled system $H_2O$–*n*-decane/12-HOA–$C_{10}E_4$ possesses qualitatively the same phase behaviour, namely phase boundaries of the same shape, as the non-gelled base microemulsion $H_2O$–*n*-decane–$C_{10}E_4$. This suggests that also the microstructure is similar in the two systems, i.e. that the system $H_2O$–*n*-decane/12-HOA–$C_{10}E_4$ is also able to form a microemulsion with a surfactant monolayer between water and oil domains

M. Laupheimer, *Gelled Bicontinuous Microemulsions*,
Springer Theses, DOI: 10.1007/978-3-319-07719-2_4,

which changes its curvature as a function of temperature. The here discussed Fourier transform pulsed-gradient spin-echo (FT-PGSE) $^1$H-NMR measurements give experimental evidence for this assumption and verify the bicontinuity at the $\widetilde{T}$ temperature. They were performed with a gelled $H_2O$–*n*-decane/12-HOA–$C_{10}E_4$ ($\phi = 0.5$) sample with 1.5 wt% gelator at a surfactant mass fraction of $\gamma = 0.170$ as well as, for comparison, with the non-gelled $H_2O$–*n*-decane–$C_{10}E_4$ ($\phi = 0.5$) microemulsion at the same $\gamma$. Both microemulsions were studied at various temperatures within their one-phase regions.

### 4.1.1 Preliminary Measurements

To be able to assign the different signals in the Fourier transformed spectra of the PGSE experiments to the components of the microemulsion preliminary $^1$H-NMR measurements without a magnetic field gradient were carried out in the NMR service lab for samples of the individual substances (Fig. 4.1, left). The water protons give rise to a sharp singular signal at 4.8 ppm while the signals of all other substances are further upfield. The spectrum of the surfactant $C_{10}E_4$ comprises a multiplet around 3.5 ppm which is from the oxyethylene head group, while the signals at 1.5, 1.2 and 0.8 ppm are from the decyl chain and its methyl end group, respectively. The oil *n*-decane also possesses signals in the high-field region, namely at 1.3 ppm from the $–CH_2–$ and at 0.9 ppm from the $–CH_3$ end groups. In the gelator spectrum there is a signal at 3.6 ppm from the proton on C-atom 12 which carries the OH-group, the triplet at 2.3 ppm is from the two protons neighbouring the carboxylic acid group, the signals at 1.6, 1.4 and 1.3 ppm are from the $–CH_2–$ groups within the alkyl chain and the signal at 0.9 ppm is from the methyl end group. The OH-signal is very broad and thus not visible in the spectrum.

Besides the components' chemical shifts one needs to know the self-diffusion coefficients of pure water and *n*-decane, $D_{0,H_2O}$ and $D_{0,n\text{-decane}}$, in the relevant temperature region to be able to calculate the relative self-diffusion coefficients $D_{rel}$ according to Eq. (2.34). For water a Speedy-Angell power law equation describing the temperature-dependence of the self-diffusion coefficient has been reported in the literature [1]

$$D_{0,H_2O} = 1.635 \times 10^{-8}\,\mathrm{m^2\,s^{-1}} \left( \frac{T}{215.05\,\mathrm{K}} - 1 \right)^{2.063}. \tag{4.1}$$

Thus this equation was used to calculate $D_{0,H_2O}$ for the temperatures at which the microemulsions were studied. For *n*-decane no equivalent equation was found in the literature. Therefore, $D_{0,n\text{-decane}}$ was measured in FT-PGSE experiments for several temperatures in a range from 21.3 to 34.8 °C (see Fig. 4.1, right). One

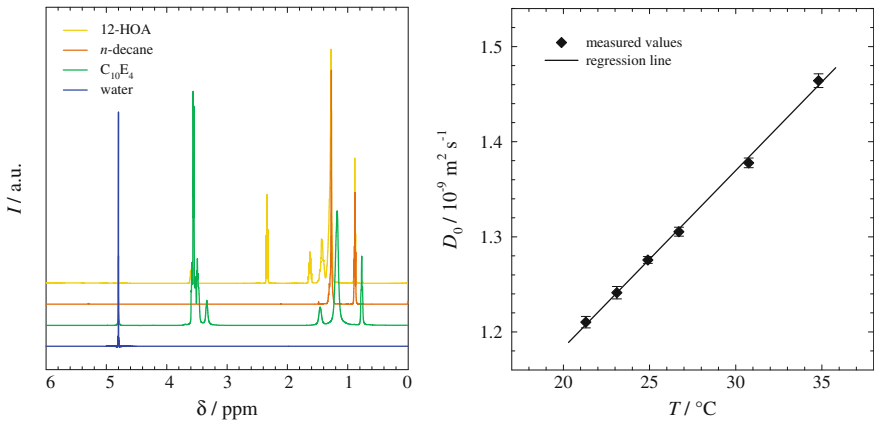


**Fig. 4.1** (*Left*) $^1$H-NMR spectra of the individual microemulsion components, namely water (*blue*), the surfactant $C_{10}E_4$ (*green*), *n*-decane (*orange*) and the gelator 12-HOA (*yellow*) (The $^1$H-NMR spectra of the single components were measured in the NMR service lab on a 500 MHz narrow-bore spectrometer. The preparation of the samples is specified in the Experimental Methods (Sect. 6.7)). (*right*) Self-diffusion coefficient $D_0$ of pure *n*-decane for different temperatures (Table A.13) and regression line according to Eq. (4.2)

observes that $D_{0,n\text{-decane}}$ increases linearly with temperature and a linear regression yields

$$D_{0,n-\text{decane}} = 1.863 \times 10^{-11}\,\text{m}^2\,\text{s}^{-1}\,^\circ\text{C}^{-1} \cdot T + 8.108 \times 10^{-10}\,\text{m}^2\,\text{s}^{-1} \qquad (4.2)$$

according to which $D_{0,n\text{-decane}}$ was calculated for the relevant temperatures.

### *4.1.2 Non-Gelled Base Microemulsion*

The characteristic temperature-dependant change of the relative self-diffusion coefficients $D_{\text{rel}}$ of water and oil in a microemulsion was first studied with the base system $H_2O$–*n*-decane–$C_{10}E_4$ ($\phi = 0.5$, $\gamma = 0.170$). Figure 4.2 (left) shows the respective $^1$H-NMR spectrum which possesses signals at 4.8, 3.7, 1.4 and 0.9 ppm. A comparison with Fig. 4.1 (left) reveals that the signal at 4.8 ppm can be attributed to water and the one at 3.7 ppm to the surfactant. At 1.4 and 0.9 ppm, however, the signals of the surfactant and of *n*-decane overlap. This also becomes apparent in the decays of the signals in the FT-PGSE experiment, i.e. when one plots the echo attenuation according to Eq. (2.33) semi-logarithmically versus $k = \{\gamma^2_{\text{g,pr.}}\, g^2\, \delta^2\, (\Delta - \delta/3)\}$ (Fig. 4.2, right). One can see that the data points of the signals at 4.8 and 3.7 ppm follow linear trend lines the negative slopes of which are the self-diffusion coefficients $D$ of water and $C_{10}E_4$. However, for the

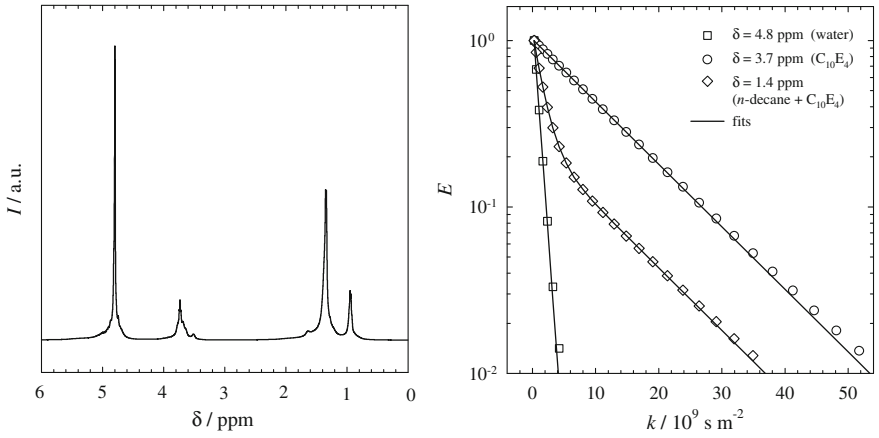


**Fig. 4.2** (*Left*) $^1$H-NMR spectrum of the non-gelled microemulsion $H_2O$–*n*-decane–$C_{10}E_4$ ($\phi = 0.5$, $\gamma = 0.170$). (*Right*) Echo attenuations $E$ of the signals at 4.8, 3.7 and 1.4 ppm plotted semi-logarithmically versus $k = \{\gamma^2_{g,pr.}\, g^2\, \delta^2\, (\Delta - \delta/3)\}$. The data was recorded at 29.0 °C in a FT-PGSE experiment with a diffusion time of $\Delta = 150$ ms and magnetic field gradient pulses of duration $\delta = 1$ ms and increasing strength $g$

signal at 1.4 ppm one finds a biexponential decay the second part of which is parallel to the decay of the surfactant signal at 3.7 ppm. When the data points are fitted it is possible to deconvolute the contributions of *n*-decane and the surfactant, respectively, as $D_{C_{10}E_4}$ is known.

The slopes of the curves in Fig. 4.2 (right) reveal the different self-diffusion coefficients of the microemulsion components. The water decay is the steepest which reflects that the water molecules self-diffuse faster than the other microemulsion components. Water possesses self-diffusion coefficients in the range of $1.2 \times 10^{-9}$ m$^2$ s$^{-1}$, while for *n*-decane values around $6.5 \times 10^{-10}$ m$^2$ s$^{-1}$ and for the surfactant around $9.0 \times 10^{-11}$ m$^2$ s$^{-1}$ were determined. These differences can partly be ascribed to the different sizes and molecular weights of the molecules. However, studying the temperature-dependence of the self-diffusion coefficients, it becomes obvious that the change of the microemulsion's microstructure has a considerable influence on the evolution of the $D$ values. Without an effect of the microstructure one would expect the self-diffusion coefficients to increase with increasing temperature as it is the case for pure *n*-decane (cp. Fig. 4.1, right). $D_{H_2O}$, in contrast, decreases from the lower to the upper phase boundary of the studied microemulsion sample (see Fig. 4.3, right) because the microstructure changes from water-continuous to oil-continuous. Note that within the narrow one-phase region studied here the microemulsion is always bicontinuous and does not change its microstructure from oil-in-water droplets to water-in-oil droplets. However, the curvature of the surfactant layer changes and one can clearly monitor that this change is attended by an increasing obstruction for the self-diffusing water molecules. Since the effect on the self-diffusion of the *n*-decane molecules is

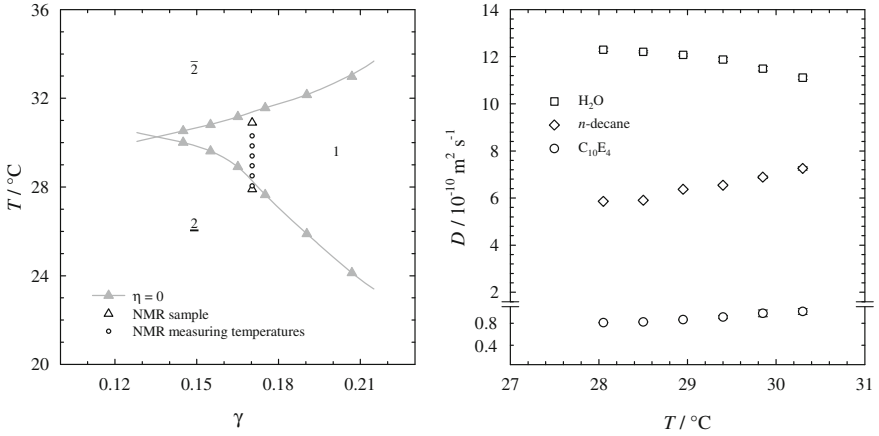


**Fig. 4.3** (*Left*) $T$-$\gamma$ phase diagram of the non-gelled microemulsion $H_2O$–*n*-decane–$C_{10}E_4$ ($\phi = 0.5$, Table A.1). The *white triangles* mark the phase boundaries of the NMR sample with $\gamma = 0.170$ and the *circles* the temperatures where PGSE NMR measurements were carried out. (*Right*) Determined self-diffusion coefficients $D$ for water (*squares*), *n*-decane (*diamonds*) and the surfactant $C_{10}E_4$ (*circles*) in the microemulsion plotted versus temperature (Table A.14)

opposed one finds for $D_{n\text{-decane}}$, respectively, values which increase with temperature (see Fig. 4.3, right). It is important to be aware that the increase of $D_{n\text{-decane}}$ is amplified by the temperature-induced acceleration of self-diffusion. When it comes to the self-diffusion of the surfactant the temperature effect is even dominating. As mentioned in Sect. 2.4, $D_{C_{10}E_4}$ theoretically possesses a maximum for zero mean curvature of the water–oil interface it resides in, i.e. in the middle of the one-phase region [2, 3]. However, Fig. 4.3 (right) instead shows a constant increase of $D_{C_{10}E_4}$ with temperature which means that the temperature-induced acceleration of the surfactant self-diffusion overcompensates the effects of the structural changes in the narrow temperature window of the study. It shall furthermore be mentioned that the restriction of the surfactant's self-diffusion to the two dimensions of the $C_{10}E_4$ monolayer (if one neglects the monomeric solubility in the bulk phases) explains why $D_{C_{10}E_4}$ is about an order of magnitude lower than $D_{H_2O}$ and $D_{n\text{-decanae}}$.

Note that $D_{C_{10}E_4}$ was determined in this study particularly because it was required to deconvolute from the superimposed high-field $^1$H-NMR signals the self-diffusion coefficient $D_{n\text{-decanae}}$ of the oil component. The latter as well as $D_{H_2O}$ were in the next step normalized in order to eliminate the structure-unspecific temperature effects. For this purpose the Eqs. (4.1) and (4.2) were used to calculate $D_{0,H_2O}$ and $D_{0,n\text{-decane}}$, respectively, before the relative self-diffusion coefficients were computed according to Eq. (2.34). The resulting $D_{rel,H_2O}$ and $D_{rel,n\text{-decane}}$ values reflect exclusively the effects coming from the changes of the microemulsion's microstructure. When they are plotted versus the temperature (see Fig. 4.4) one finds an intersection of the two trend lines at 29.1 °C which is the middle

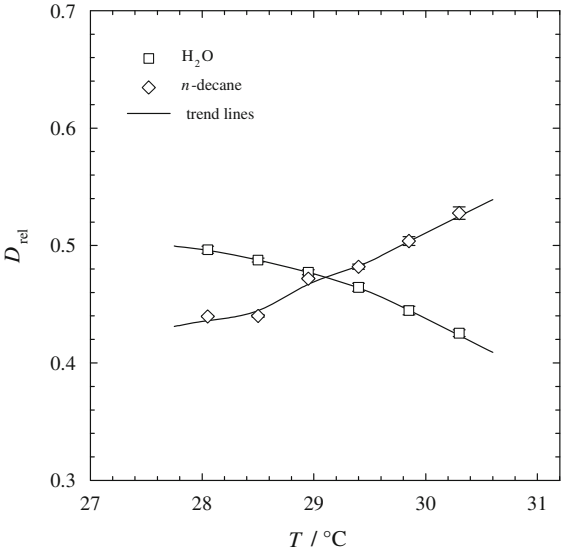


**Fig. 4.4** Relative self-diffusion coefficients $D_{rel}$ of water (*squares*) and *n*-decane (*diamonds*) in the one-phase region of the non-gelled microemulsion $H_2O$–*n*-decane–$C_{10}E_4$ ($\phi = 0.5$, $\gamma = 0.170$) plotted versus temperature (Table A.15)

of the one-phase region. At this temperature the microemulsion is bicontinuous which allows both water and *n*-decane to self-diffuse with the same relative velocities. The $D_{rel}$ value at the intersection is 0.47 while $\overline{0.6}$ is theoretically predicted for a perfect bicontinuous system with an interfacial layer of zero mean curvature [2]. However, values somewhat below $\overline{0.6}$ have been reported in several cases [4–7]. This was attributed to structural defects, mainly local tubular connections between surfactant monolayers, due to which the mean curvature of the interfacial layer deviates from zero [2, 5, 8].

### *4.1.3 Gelled Microemulsion*

To verify the bicontinuity of the microemulsion in the presence of the gelator network a $H_2O$–*n*-decane/12-HOA–$C_{10}E_4$ ($\phi = 0.5$) sample with a surfactant mass fraction of $\gamma = 0.170$ and a gelator mass fraction of 1.5 wt% was studied with the FT-PGSE NMR method. In the $^1$H-NMR spectrum one finds signals at 4.8, 3.7, 1.3 and 0.9 ppm (see Fig. 4.5, left). As is the case for the non-gelled microemulsion (cp. Fig. 4.2, left) the signals at $\delta = 4.8$ and $\delta = 3.7$ ppm can be assigned to water and the ethylene oxide head group of $C_{10}E_4$, respectively, while at 1.3 and 0.9 ppm one finds the superimposed signals of the alkyl protons of $C_{10}E_4$ and *n*-decane. Especially the high-field signals might also comprise small contributions from the gelator 12-HOA. However, the concentration of the latter in the mixture is very low and even at around 2.3 ppm where 12-HOA possesses a signal which would not overlap with any other (cp. Fig. 4.1, left) no signal is seen

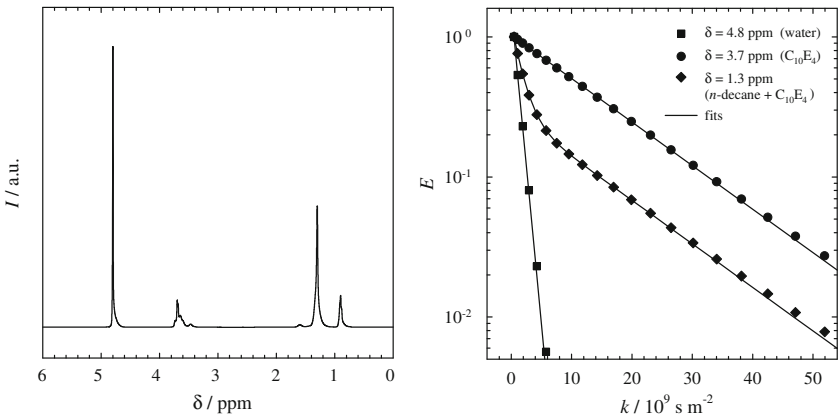


**Fig. 4.5** (*Left*) $^1$H-NMR spectrum of the gelled microemulsion $H_2O$–*n*-decane/12-HOA–$C_{10}E_4$ with 1.5 wt% gelator ($\phi = 0.5$, $\gamma = 0.170$). (*Right*) Echo attenuations $E$ of the signals at 4.8, 3.7 and 1.3 ppm plotted semi-logarithmically versus $k = \{\gamma_{g,pr.}^2\, g^2\, \delta^2\, (\Delta - \delta/3)\}$. The data was recorded at 24.5 °C in a FT-PGSE experiment with a diffusion time of $\Delta = 30$ ms and magnetic field gradient pulses of duration $\delta = 1$ ms and increasing strength $g$

in the spectrum of the gelled microemulsion. Moreover, most of the gelator molecules are assembled in crystalline gelator fibers and thus immobile, which means that the gelator is "invisible" in the FT-PGSE study.

The plot of the echo signal decays in Fig. 4.5 (right) reveals the same trends as for the non-gelled base microemulsion. The self-diffusion of the water molecules is the fastest while the surfactant $C_{10}E_4$ possesses the smallest of the measured self-diffusion coefficients. As regards the absolute values one finds in the gelled microemulsion self-diffusion coefficients of water, *n*-decane and the surfactant which are of the same orders of magnitude but somewhat smaller than in the non-gelled base system (see Fig. 4.6, right, vs. Fig. 4.3, right). This is due to the fact that the gelator shifts the microemulsion phase boundaries to lower temperatures (cp. Fig. 4.6, left, vs. Fig. 4.3, left, and Sect. 3.1) where the self-diffusion of all molecules is reduced. Still, just as in the non-gelled case, the self-diffusion coefficient of water in the microemulsion decreases with temperature while $D_{n\text{-decane}}$ and $D_{C_{10}E_4}$ increase from the lower to the upper phase boundary of the system (albeit only slightly in case of the surfactant). The explanations for these trends are the same as those given above for the non-gelled base system.

Figure 4.7 shows the plot of the relative self-diffusion coefficients of water and *n*-decane in the gelled microemulsion versus temperature. What is conspicuous is that the error bars, especially of the water self-diffusion coefficients, are bigger than in the case of the non-gelled microemulsion (cp. Fig. 4.4). This could be due to the different sample preparation in the NMR tubes (cp. Sect. 6.7) owing to which one possibly sees small convection effects in the gelled microemulsion. However, since the $D_{H_2O}$ values determined in different measurements only vary by $\leq$8 % these effects are not changing the general trend. As is the case for the

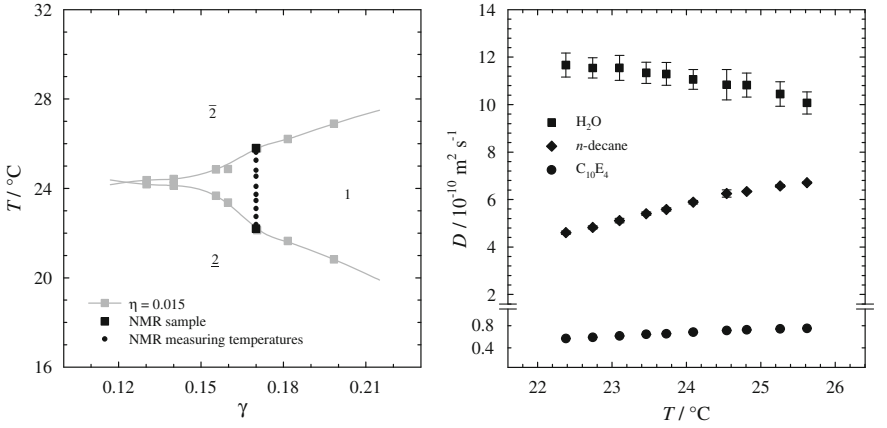


**Fig. 4.6** (*Left*) $T$-$\gamma$ phase diagram of the gelled microemulsion $H_2O$–*n*-decane/12-HOA–$C_{10}E_4$ with 1.5 wt% 12-HOA ($\phi = 0.5$, Table A.2).[KJ] The *black squares* mark the phase boundaries of the NMR sample with $\gamma = 0.170$ and the *circles* the temperatures where PGSE NMR measurements were carried out. (*Right*) Determined self-diffusion coefficients $D$ for water (*squares*), *n*-decane (*diamonds*) and the surfactant $C_{10}E_4$ (*circles*) in the gelled microemulsion plotted versus temperature (Table A.16)

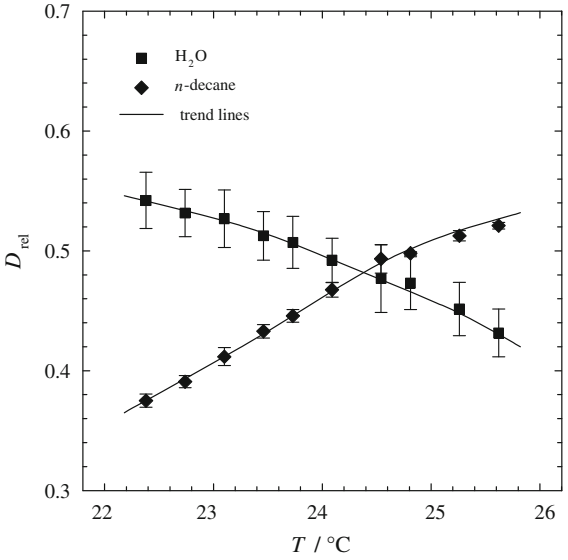


**Fig. 4.7** Relative self-diffusion coefficients $D_{rel}$ of water (*squares*) and *n*-decane (*diamonds*) in the one-phase region of the gelled microemulsion $H_2O$–*n*-decane/12-HOA–$C_{10}E_4$ with 1.5 wt% 12-HOA ($\phi = 0.5$, $\gamma = 0.170$) plotted versus temperature (Table A.17)

non-gelled system $D_{rel,H_2O}$ decreases and $D_{rel,n\text{-decanae}}$ increases when the one-phase region is crossed from the lower to the upper phase boundary. Hence one can infer that in the gelled system $H_2O$–*n*-decane/12-HOA–$C_{10}E_4$ an identical microstructure change takes place as in the non-gelled base microemulsion,

namely the bending of the surfactant layer which separates water and oil domains. The two trend lines of the $D_{\mathrm{rel},H_2O}$ and the $D_{\mathrm{rel},n\text{-decanae}}$ values intersect and indicate the bicontinuity of the microemulsion structure at about 24.3 °C which corresponds to the $\widetilde{T}$ temperature of the system (cp. Table 3.1). Like for the non-gelled microemulsion $D_{\mathrm{rel}}$ at the intersection is smaller than the theoretical value, namely about 0.48 instead of $\overline{0.6}$. For a gelled microemulsion in a previous study the intersection of $D_{\mathrm{rel,water}}$ and $D_{\mathrm{rel,oil}}$ was at about 0.33 [9, 10]. In both the previous and the present study the values of $D_{H_2O}$ were not corrected for hydration. As some of the water molecules form a hydration shell around the surfactant head groups and thus self-diffuse with a reduced velocity (that of the surfactant molecules) one should in principle consider only the self-diffusion coefficient of the free water molecules, $D_{H_2O,\mathrm{free}}$, for the calculation of $D_{\mathrm{rel},H_2O,\mathrm{free}}$. $D_{H_2O,\mathrm{free}}$ could be extracted from

$$D_{H_2O} = f_{\mathrm{hyd.}} D_{H_2O,\mathrm{hyd.}} + (1 - f_{\mathrm{hyd.}}) D_{H_2O,\mathrm{free}} = f_{\mathrm{hyd.}} D_{C_{10}E_4} + (1 - f_{\mathrm{hyd.}}) D_{H_2O,\mathrm{free}} \tag{4.3}$$

where $f_{\mathrm{hyd.}}$ is the fraction of water molecules in the hydration shells possessing the self-diffusion coefficient $D_{H_2O,\mathrm{hyd.}}$ (which equals the measured value $D_{C_{10}E_4}$) while $D_{H_2O}$ is the self-diffusion coefficient measured for water. $D_{H_2O,\mathrm{free}}$ is a little bigger than $D_{H_2O}$ thus $D_{\mathrm{rel},H_2O}$ would increase a bit leading to slightly increased values of $D_{\mathrm{rel}}$ and $T$ at the intersection point. However, the overall picture would not change if this correction was used because the described effect is very small (see [11] for further details).

Summing up, the FT-PGSE NMR study revealed that the gelled system $H_2O$–*n*-decane/12-HOA–$C_{10}E_4$ not only possesses phase boundaries with a shape typical for microemulsions but has indeed the respective microstructure which changes as a function of temperature. At the temperature $\widetilde{T}$ the relative self-diffusion coefficients of water and *n*-decane are equal which is evidence for the gelled microemulsion's bicontinuity. The close analogy of the $D_{\mathrm{rel}}$ versus $T$ plots of the gelled microemulsion and its non-gelled base system furthermore show that the microemulsion microstructure is generally unaffected by the presence of the gelator network.

## 4.2 Small Angle Neutron Scattering

After it was proved by the FT-PGSE NMR measurements that the system $H_2O$–*n*-decane/12-HOA–$C_{10}E_4$ indeed possesses bicontinuous microemulsion domains at the $\widetilde{T}$ temperature the next step was to evidence that these domains coexist in the gelled bicontinuous microemulsion with a network of gelator fibers. Therefore small angle neutron scattering (SANS) experiments were carried out on the instrument D11 of the ILL in Grenoble, France, which yielded scattering data in a

$q$ range from $5.2 \times 10^{-1}$ Å$^{-1}$ down to $7.0 \times 10^{-4}$ Å$^{-1}$. This data bears information about the microstructure on length scales between 1.2 nm and 0.9 μm. However, as the dimensions of the gelator network presumably extend further into the micrometer range the SANS measurements were complemented with 'very small angle neutron scattering' (V-SANS) measurements performed on the KWS-3 of the FRM II in Garching near Munich, Germany. Those covered a $q$ range down to $1.2 \times 10^{-4}$ Å$^{-1}$ allowing to study microstructures up to a size of 5.1 μm.

### *4.2.1 Conception of the SANS Study*

Just like any other study in this thesis, the SANS study did not only include samples of the gelled bicontinuous microemulsion $H_2O$–*n*-decane/12-HOA–$C_{10}E_4$ but also samples of the relevant base systems. Thus the obtained data can directly be compared with that of, in this case, both the non-gelled bicontinuous microemulsion $H_2O$–*n*-decane–$C_{10}E_4$ and the binary gel *n*-decane/12-HOA. The concentration of 12-HOA in the gelled microemulsion as well as in the binary gel was 1.5, 2.5 and 5.0 wt%. The surfactant mass fraction was held constant at $\gamma = 0.150$ in the non-gelled and in all gelled microemulsions ($\phi = 0.5$), i.e. is somewhat above the systems' $\widetilde{\gamma}$ values (cp. Table 3.1). Moreover, the scattering contrast, which is essential in SANS studies, was carefully adjusted by selectively deuterating different sample components. This is possible since the coherent scattering lengths of hydrogen and deuterium differ significantly with $b(^1\text{H}) = -3.7 \times 10^{-13}$ cm and $b(^2\text{H}) = +6.7 \times 10^{-13}$ cm [12]. In SANS studies of microemulsions one usually adjusts the so-called 'bulk contrast' by using heavy water ($D_2O$) as the aqueous component while the oil component and the surfactant are non-deuterated. Alternatively one uses deuterated aqueous and oil components and a non-deuterated surfactant which yields the so-called 'film contrast'. Both bulk and film contrast samples were prepared to elucidate the microstructure of the gelled bicontinuous microemulsion. Additionally, the 'inverse bulk contrast' was adjusted in the case of the non-gelled microemulsion for which deuterated oil was used instead of $D_2O$. To make sure that the microemulsion samples were in "pure" film or bulk contrast, i.e. to avoid scattering length density differences between the two microemulsion components which were (non-)deuterated, 'contrast matching' was performed. For this purpose small amounts of deuterated solvent were added to the technically non-deuterated bulk component in the cases of the bulk contrast (cp. Table 4.1). The scattering length density of the respective component thus changed, according to Eq. (2.45), and could be matched to that of the surfactant. In the case of the film contrast the scattering length densities of the two deuterated bulk components had to be matched for which d22-*n*-decane was mixed with 2.1 wt% non-deuterated *n*-decane. Note that the surfactant $C_{10}E_4$ possesses a monomeric solubility in the oil which was accounted for in the performed contrast matching (it was assumed that the *n*-decane subphase contains 2.1 wt% $C_{10}E_4$ [13]). The scattering length densities before and after contrast matching are given in Fig. 4.8. It is obvious that without

**Table 4.1** Compositions of the water and the oil components in the contrast-matched microemulsion SANS samples

| Contrast | Water component | | Oil component | |
|---|---|---|---|---|
| | $H_2O$ / wt% | $D_2O$ / wt% | *n*-decane / wt% | d22-*n*-decane / wt% |
| Bulk | 0 | 100.0 | 90.4 | 9.6 |
| Film | 0 | 100.0 | 2.1 | 97.9 |
| Inverse bulk | 89.4 | 10.6 | 0 | 100.0 |

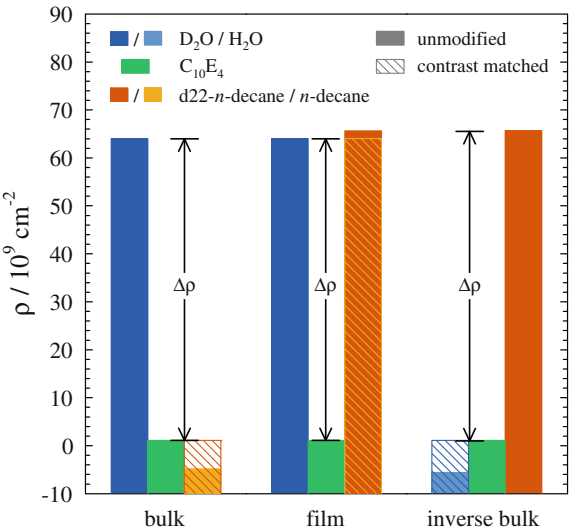


**Fig. 4.8** Scattering length densities ρ of the water component (*blue*), the surfactant (*green*) and the oil component (*orange*) in the bulk, film and inverse bulk contrast microemulsion SANS samples (Table A.18). The *plain bars* display the scattering length densities of the pure substances and the *dashed bars* those of the contrast matched components after the addition of some deuterated or non-deuterated solvent, respectively (cp. Table 4.1). The *arrows* mark the adjusted scattering contrasts Δρ

contrast matching the microemulsion samples would possess different scattering contrasts, which would contribute to the scattering function $I(q)$. Therefore the interpretation of $I(q)$ would be much more intricate which was prevented by the performed contrast matching. The binary gel was prepared with fully deuterated *n*-decane and non-deuterated gelator; hence there was no need (nor possibility) for contrast matching. Non-deuterated gelator was furthermore used in all gelled microemulsion samples.

Besides deciding on appropriate sample compositions it was crucial for the SANS study to chose suitable measuring temperatures for the different microemulsion samples. Since the aim was to investigate the microemulsions in their bicontinuous state the measurements were to be carried out at the respective phase

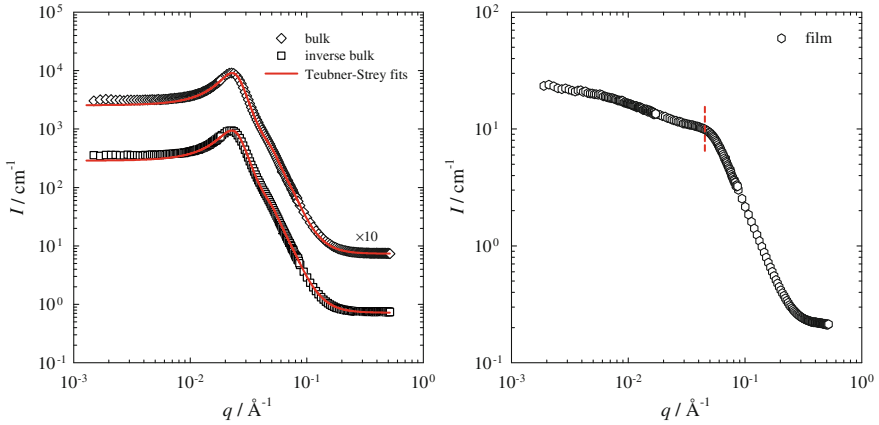


**Fig. 4.9** SANS data ($\lambda = 6$ Å) of the non-gelled bicontinuous microemulsion $H_2O$–*n*-decane–$C_{10}E_4$ ($\phi = 0.5$, $\gamma = 0.150$) in bulk (28.3 °C, *diamonds*) and inverse bulk (30.4 °C, *squares*) contrast (*left*) as well as in film contrast (28.3 °C, *right*). The bulk contrast curves were fitted with the Teubner-Strey formula (Eq. 4.4) taking into account multiple scattering (*solid red lines*). The characteristic shoulder of the film contrast curve is located at a $q$ value twice as high as that of the bulk curves' maxima (*dashed red line*)

inversion temperatures. However, the $\widetilde{T}$ temperatures listed in Table 3.1 were not applicable because phase boundaries of a microemulsion shift when deuterated components are used (the use of $D_2O$ instead of $H_2O$, e.g. lowers the phase boundaries by about 2 K) [14]. Hence the phase boundaries of all microemulsion SANS samples were determined and the respective midpoints were used as measuring temperatures (cp. Table 6.4). For the binary gels no specific measuring temperatures were required, thus values around room temperature were set.

### *4.2.2 Non-Gelled Bicontinuous Microemulsion*

To be able to judge whether the addition of gelator changes the microstructure of a bicontinuous microemulsion, it was important to first investigate the non-gelled bicontinuous microemulsion $H_2O$–*n*-decane–$C_{10}E_4$ ($\phi = 0.5$, $\gamma = 0.150$) as reference system. Contrast matched bulk, inverse bulk and film samples were prepared for this purpose. They were studied exclusively with SANS at a neutron wavelength of 6 Å, not with V-SANS, since a non-gelled bicontinuous microemulsion scatters with constant intensity at very low $q$ values. The obtained scattering curves are shown in Fig. 4.9.

For all three different contrasts, scattering curves were measured which are typical for bicontinuous microemulsions. Both bulk contrast curves show a characteristic peak which is slightly sharper in the 'normal' than in the inverse bulk contrast and possesses a maximum at $q_{max} = 2.3 \times 10^{-2}$ Å$^{-1}$. The film contrast

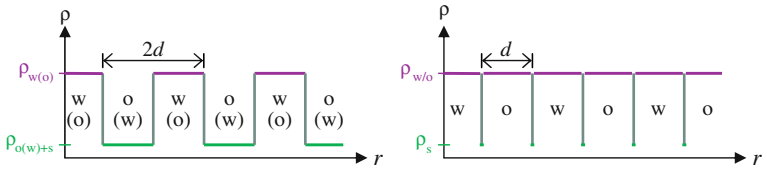


**Fig. 4.10** Scattering length density profile $\rho(r)$ of a bicontinuous microemulsion with alternating water (w) and oil (o) domains of size $d$ in (inverse) bulk (*left*) and in film (*right*) contrast. The thickness of the surfactant (s) layer is neglected

curve is of distinctly lower intensity and features instead of the peak a characteristic shoulder at $q_{\text{shoulder}} = 2q_{\max} = 4.6 \times 10^{-2}$ Å$^{-1}$. The values $q_{\max}$ and $q_{\text{shoulder}}$ directly correlate with the microstructural dimensions of the studied system, i.e. the domain size of the bicontinuous microemulsion. The doubling of the characteristic $q$ value indicates that the microstructural unit which is 'seen' in film contrast is only half as large as the one observed in bulk contrast (cp. Eq. (2.42)). Indeed this is perfectly in line with theory. The repetition distance in the scattering length density profile of a bicontinuous microemulsion in film contrast equals the domain size $d$ while it is $2d$ in the case of a bulk contrast sample (see Fig. 4.10).

What is disregarded in the schematic representations of the scattering length density profiles in Fig. 4.10 is that the alternation of water and oil domains in a bicontinuous microemulsion is locally quasi-periodic, however, not over an infinite distance. Since the system possesses no long-range order the periodicity of the $\rho(r)$ pattern is sooner or later lost. A model for bicontinuous microemulsions in bulk contrast which takes these effects into account has been developed by Teubner and Strey. They introduced two parameters, namely $d_{\text{TS}}$ which characterizes the local quasi-periodicity (and equals thus twice the microemulsion domain size $d$) and the correlation length $\xi_{\text{TS}}$ which describes over which distance the quasi-periodicity is lost. The respective Teubner-Strey formula describing the scattering intensity with an incoherent background scattering $I_{\text{bg}}$ is [15]

$$I(q) = \frac{8\pi c_2 \langle \eta^2 \rangle / \xi_{\text{TS}}}{a_2 + c_1 q^2 + c_2 q^4} + I_{\text{bg}} \tag{4.4}$$

with the contrast factor

$$\langle \eta^2 \rangle = \phi_{\text{d}}(1 - \phi_{\text{d}})(\Delta\rho^2) \tag{4.5}$$

where $\phi_{\text{d}}$ is the volume fraction of the deuterated component in the system and $\Delta\rho$ is the scattering contrast. Furthermore, $a_2$, $c_1$ and $c_2$ are coefficients which relate to the characteristic length scales by

$$d_{TS} = 2\pi\left(\frac{1}{2}\left(\frac{a_2}{c_2}\right)^{0.5} - \left(\frac{c_1}{4c_2}\right)\right)^{-0.5} \tag{4.6}$$

and

$$\xi_{TS} = \left(\frac{1}{2}\left(\frac{a_2}{c_2}\right)^{0.5} + \left(\frac{c_1}{4c_1}\right)\right)^{-0.5}. \tag{4.7}$$

The scattering data of the bicontinuous microemulsion $H_2O$–*n*-decane–$C_{10}E_4$ in both the bulk and the inverse bulk contrast could be fitted with the Teubner-Strey formula (cp. Fig. 4.9, left). However, to obtain accurate fits some double and triple scattering had to be taken into account, i.e. 2.60 % double and 0.25 % triple scattering in the 'normal' bulk and 2.40 % double and 0.20 % triple scattering in the inverse bulk contrast, respectively. The fits yielded $d_{TS}$ values of 263 ± 1 Å in the 'normal' and 264 ± 1 Å in the inverse bulk contrast. With this almost quantitative agreement the domain size of the bicontinuous microemulsion is in both cases $d = 132 \pm 1$ Å. The correlation length $\xi_{TS}$, in contrast, differs slightly; it is 148 ± 3 Å in the 'normal' and 141 ± 3 Å in the inverse bulk contrast indicating that the microstructure in the inverse bulk contrast sample is a little less ordered. This is in accordance with the slightly higher fraction of multiple scattering in the 'normal' compared to the inverse bulk contrast sample. An explanation for the different degrees of order is that deuterium has a "structuring effect" which is particularly strong for $D_2O$ that was used for the 'normal' bulk contrast but much weaker in the case of deuterated oil which is comprised in the inverse bulk contrast sample. An additional parameter that affects the described order discrepancy is the measuring temperature. The latter was 28.3 °C in case of the 'normal' and 30.4 °C in case of the inverse bulk contrast. Since structural fluctuations increase with increasing temperature it is reasonable that $\xi_{TS}$ and thus the range of the bicontinuous microemulsion's quasi-periodicity are smaller in the inverse than in the 'normal' bulk contrast.

### *4.2.3 Binary Gel*

In addition to the non-gelled bicontinuous microemulsion also the second base system, i.e. the binary gel *n*-decane/12-HOA, was investigated separately via SANS. For this purpose gel samples with 1.5, 2.5 and 5.0 wt% non-deuterated 12-HOA in fully deuterated d22-*n*-decane were prepared. Figure 4.11 shows on the left the scattering data obtained with SANS measurements at the two neutron wavelengths 6 and 13 Å. On the right Fig. 4.11 displays the 6 Å-data combined with the results from the V-SANS measurements. All measurements were carried

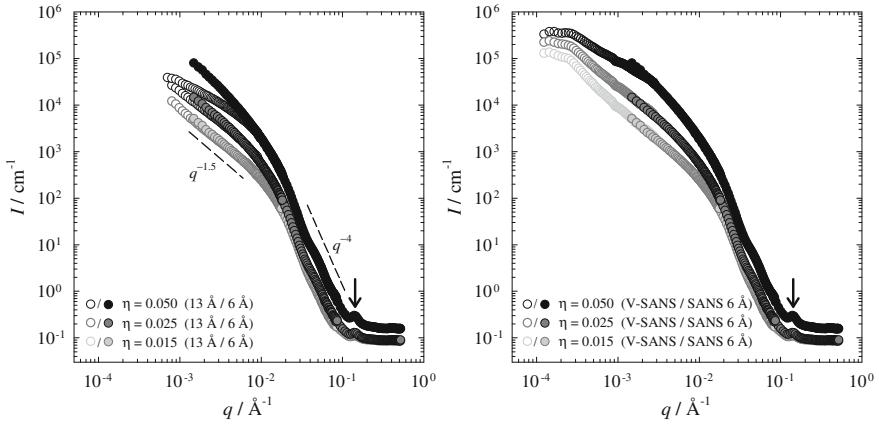


**Fig. 4.11** SANS data of the binary gel d22-*n*-decane/12-HOA with 1.5 (*light gray*), 2.5 (*dark gray*) and 5.0 wt% (*black*) gelator. Data measured with SANS at neutron wavelengths of $\lambda = 6$ Å (*filled symbols*) and $\lambda = 13$ Å (*open symbols*, *left*) at 22.7, 21.9 and 23.8 °C, respectively, as well as V-SANS data measured at 22.5 °C (*open symbols*, *right*) are shown. The *arrow* points at the Bragg diffraction peak of the crystal lattice within the 12-HOA fibers and junction zones [17–19]

out around room temperature. However, specific measuring temperatures were not required for the binary gels.

Comparing the data measured at the two different wavelengths (Fig. 4.11, left) one finds that in particular for the sample containing 5.0 wt% gelator the intensity of the 13 Å-data is lower than that of the 6 Å-data. Furthermore the slopes of the 6 Å-data and the 13 Å-data are considerably different which is a strong indication for multiple scattering at $\lambda = 13$ Å [16]. The occurrence of multiple scattering is reflected by decreasing sample transmissions with increasing wavelength. While a transmission decrease from 88 to 76 % for the gel with 1.5 wt% 12-HOA has no great impact, the effect is stronger with 2.5 wt% gelator where the transmission decreases from 86 to 64 % and severe in the 5.0 wt% 12-HOA gel in which the transmission drops from 71 to 28 %. Since the interpretation of data with multiple scattering is very complicated the 13 Å-data was neglected in the further data analysis. As regards the V-SANS data shown in Fig. 4.11 (right) a quite good overlap with the 6 Å-data from the SANS measurements was obtained at $7 \times 10^{-4}$ Å$^{-1} \lesssim q \lesssim 3 \times 10^{-3}$ Å$^{-1}$—at least for the gels with 1.5 and 2.5 wt% gelator. The data of the 5.0 wt% 12-HOA gel admittedly show considerable discrepancies which is probably because the V-SANS measurements were also carried out using a high wavelength of $\lambda = 12.8$ Å and thus come with the just described transmission and multiple scattering issue. Still, it is another issue which makes the V-SANS data rather suspicious and led to its exclusion from the further data analysis. Note that for *all* investigated samples—not only for the three binary gels—the changeover from a plateau in the very low $q$ regime to an intensity decrease was observed at $q \approx 2.5 \times 10^{-4}$ Å$^{-1}$. In general, scattering curves possess a plateau of constant intensity in the very low $q$ range, which is known as

the 'Guinier regime', and the $q$ range where this plateau is left relates to the largest dimension of the microstructure in the sample (e.g. to the rod length in case of rods). The obtained V-SANS data thus implies that this dimension is identical in *all* studied systems which is, in fact, very unlikely. Hence the changeover is most probably an instrumental artefact. One must assume that the scattering curves increase further for $q$ values below $q \approx 2.5 \times 10^{-4}$ Å$^{-1}$ which implies that the length of the gelator fibers is at least about 2.5 µm.

Turning to the discussion of the 6 Å-data from the SANS measurements, a first observation is that the scattering intensity increases with increasing gelator mass fraction while the SANS curves are qualitatively similar for all gels. This indicates an increased number of scattering events in the gels with high gelator concentrations which is reasonable assuming that more gelator fibers are present. Nevertheless, the comparatively high intensity of the gel with 5.0 wt% 12-HOA is conspicuous which becomes obvious comparing the level of the incoherent background scattering in the different samples. The latter is caused by protonated components, i.e. in the case of the binary gel predominantly by the non-deuterated gelator. Accordingly, it is expected that the intensity of the background scattering scales with the gelator mass fraction. Given that the background intensity increases by $\sim$2 % from 1.5 to 2.5 wt% gelator, an increase by $\sim$6 % would be expected from 1.5 to 5.0 wt% 12-HOA while a $\sim$84 % increase was observed. Hence, note that for a reasonable quantitative data analysis, which will be presented below, the data of the 5.0 wt% 12-HOA gel had to be corrected by a factor of 0.577.

Looking at the different $q$ regions one can identify distinct scattering patterns which characterize the structure of the gelator network on different length scales. Firstly, at high $q$ values one finds a small peak at $\sim$0.14 Å$^{-1}$ (marked by an arrow in Fig. 4.11). According to Terech et al. who saw the same peak for 12-HOA gels in toluene, dodecane and nitrobenzene, this is the (001) Bragg reflection of the monoclinic $P2_1/a$ crystal lattice within the 12-HOA fibers and junction zones [17–19]. In this crystal structure the 12-HOA molecules are paired via their carboxylic acid groups [18] and, indeed, the $q$ value of the peak corresponds to $d = 45$ Å (cp. Eq. (2.42)) which is approximately twice the length of a 12-HOA molecule [17]. Secondly, in a $q$ range of roughly $10^{-1}$ Å$^{-1}$ to $2 \times 10^{-2}$ Å$^{-1}$ the gels' scattering curves follow a $q^{-4}$ decay which is characteristic for the 'Porod region'. In this region the scattering pattern is caused by the abrupt change of the scattering length density at interfaces within the sample [20]. The scattering in this region is therefore characteristic for the cross-section of the gelator fibers. Finally, at $q$ values below $\sim 2 \times 10^{-2}$ Å$^{-1}$, the scattering pattern is determined by the "longitudinal properties" of the 12-HOA fibers in the gelator network, such as their stiffness and length. The SANS curves are here not as steep as in the Porod region but seem to be the steeper the higher the gelator concentration. To explain this behaviour a suitable model for the gelator network had to be found.

The model which was first considered for describing the experimental SANS data of the binary gels is the worm-like chain model of Kratky and Porod [21, 22]. This model is widely used for polymer-like and worm-like micelles [23–29] the SANS curves of which look very similar to those obtained for the 12-HOA gels. Originally

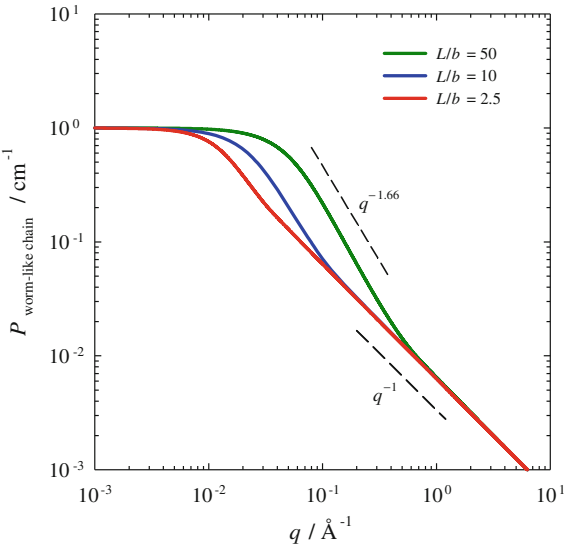


**Fig. 4.12** Form factor of worm-like chains with different $L/b$ ratios, computed according to Eq. (4.8) with "method 2" described in Ref. [30]

the model was developed for semi-flexible polymers which are treated as semi-flexible cylinders with a contour length $L$ and a Kuhn length $b$. The latter is defined as twice the persistence length and represents thus a measure for the cylinders' flexibility. Pedersen and Schurtenberger determined based on Monte Carlo simulations numerical approximations for the form factor of such worm-like chains with and without excluded volume effects [30]. Those expressions are of the general form

$$P_{\text{worm-like chain}}(q, L, b) = cP_{\text{chain}}(q, L, b) + (1 - c)P_{\text{rod}}(q, L) \tag{4.8}$$

where $c$ is an exponential 'cross-over function' and $P_{\text{chain}}$ and $P_{\text{rod}}$ are the form factors of a flexible chain and of a stiff rod, respectively. The form factor of a stiff cylindrical rod possess a characteristic $q^{-1}$ decay in the low $q$ range while that of a flexible chain in a good solvent is proportional to $q^{-1.66}$ (or to $q^{-2}$ in a theta-solvent) in the respective $q$ range [31]. For semi-flexible worm-like chains which locally behave as stiff rods and over wider distances as flexible chains one finds, going from higher to lower $q$ values, a changeover from a $q^{-1}$ to a $q^{-1.66}$ regime, respectively, and eventually a changeover to the flat Guinier regime (cp. Fig. 4.12). According to the description given above, the location of the changeover to the Guinier regime is determined by the contour length $L$ while the Kuhn length $b$ determines where one finds the changeover between $q^{-1}$ and $q^{-1.66}$. For stiff chains, which possess a small $L/b$ ratio, both changeovers are close-by such that the respective scattering curves exhibit an extended $q^{-1}$ and just a narrow $q^{-1.66}$ regime. For very flexible chains with a high $L/b$ ratio the situation is opposite and the $q^{-1.66}$ regime extends up to high $q$ values, i.e. in the extreme case up to the Porod regime determined by the chain's cross-section (note that the latter is not included in Fig. 4.12).

Comparing the calculated curves in Fig. 4.12 with the SANS curves of the binary gel *n*-decane/12-HOA in Fig. 4.11 it becomes obvious that applying the worm-like chain model one would have to assume pretty small Kuhn lengths in order to model the measured data. The latter show a $q^{-1.5}$ decay in the low $q$ range, a distinct $q^{-1}$ regime is not perceived. The deviation of $q^{-1.5}$ from $q^{-1.66}$ could possibly be explained by a broad distribution of different Kuhn lengths within the samples which would smear the changeover between the $q^{-1}$ and the $q^{-1.66}$ regime. However, in any case the Kuhn lengths would be close to the dimension of the fiber cross-section and way smaller than the fiber length (notably, the latter is so big that it cannot even be determined from the reliable SANS data because the Guinier regime is not reached in the covered $q$ range). As explained above, such short Kuhn lengths would mean that the gelator fibers were very flexible which, however, is quite unlikely regarding their crystallinity (cp. Bragg peak in Fig. 4.11) and also regarding the FFEM pictures which will be presented in Sect. 4.3. Consequently, another model had to be found to analyze the SANS data of the binary gels.

The second model which was tested describes the gelator network as a combination of "free" gelator fibers and gelator fiber nodes which account for independent scattering contributions $I_{\text{fibers}}$ and $I_{\text{nodes}}$, respectively [18]. These contributions add up to the total scattering intensity of the gel

$$I_{\text{gel}}(q) = I_{\text{fibers}} + I_{\text{nodes}} \tag{4.9}$$

which is detected in the SANS experiment. According to Eq. (2.53) both $I_{\text{fibers}}$ and $I_{\text{nodes}}$ are products of the number density $n$, the average form factor $\overline{P(q)}$ and the effective structure factor $S_{\text{eff}}(q)$ of the fibers and nodes, respectively. Assuming for simplicity that for both scatterers, i.e. the "free" fibers and the nodes, $S_{\text{eff,sc}}(q) = 1$, it holds

$$I_{\text{sc}} = \frac{N_{\text{sc}}}{V} \cdot \overline{P_{\text{sc}}} \tag{4.10}$$

where $V$ is the sample volume and $N_{\text{sc}}$ is absolute number of scatterers. $\overline{P_{\text{sc}}}$ is the average form factor given in Eq. (2.54) which allows for a distribution $W(X, X_0)$ of a scatterer's characteristic dimension $X$ around a mean value $X_0$. A convenient distribution function is given by Gauss

$$W(X, X_0) = \frac{1}{\sigma_X \sqrt{2\pi}} e^{-\frac{(X-X_0)^2}{2\sigma_X^2}} \tag{4.11}$$

where $\sigma_X$ (the curve's half width at half height) is a measure of the polydispersity. To calculate the average form factor $\overline{P_{\text{sc}}}$ one needs the form factor $P_{\text{sc}}$ of a single scatterer. The latter depends on the geometry of the scatterer, hence at this point specific shapes must be presumed for the gelator fibers and nodes in order to deduce their scattering functions. According to Terech et al. [18] a reasonable

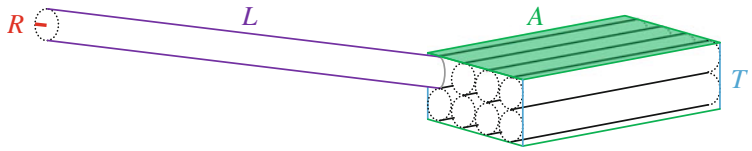


**Fig. 4.13** Schematic representation of cylindrical fibers of cross-sectional radius $R$ and a lamellar node of area $A$ and thickness $T$ in a gelator network according to the presented model. Note that all fibers extend beyond the node as "free" gelator fibers of length $L$ until they are incorporated in the next node

approach is to treat the gelator fibers as cylindrical rods and the nodes as lamellae, which can be pictured as stacked layers of parallelly arranged fibers (see Fig. 4.13). As will be shown, this combination allows the modeling of scattering curves which in the low $q$ range are proportional to about $q^{-1.5}$, just like the data measured for the investigated gels.

The form factor of a cylindrical rod, i.e. the gelator fiber, with a length $L$ and a circular cross-section of radius $R$ is [32]

$$P_{\text{fiber}} = \frac{L\pi}{q} \cdot P_{\text{fcs}}(R) \tag{4.12}$$

where

$$P_{\text{fcs}}(R) = \left(\frac{R\ 2\pi\ \Delta\rho\ \mathrm{J}_1(qR)}{q}\right)^2 \tag{4.13}$$

is the form factor of the fiber cross-section. $\Delta\rho$ is the scattering length density difference between the gelator fiber and the solvent, i.e. the scattering contrast, and $\mathrm{J}_1$ is the first order Bessel function. The form factor of a lamellar node with an area $A$ and the thickness $T$ is [32]

$$P_{\text{node}} = \frac{A\ 2\pi}{q^2} \cdot P_{\text{nth}}(T) \tag{4.14}$$

with

$$P_{\text{nth}}(T) = \left(\frac{2\ \Delta\rho}{q}\ \sin(\frac{qT}{2})\right)^2 \tag{4.15}$$

being the form factor for the node thickness and $\Delta\rho$ again the scattering contrast. Assuming that the fiber radii $R$ in the sample are distributed around a mean radius $R_0$ and the lamellae thicknesses $T$ around a mean value $T_0$ one inserts the Eqs. (4.12) and (4.14) in Eq. (2.54) to calculate the average form factor.

Inserting the latter in Eq. (4.10) one obtains for the scattering intensities from the $N_{\text{fibers}}$ gelator fibers and the $N_{\text{nodes}}$ nodes

$$I_{\text{fibers}} = \frac{N_{\text{fibers}}}{V} \int_{R=0}^{\infty} \frac{L\pi}{q} \cdot P_{\text{fcs}}(R) \cdot W(R, R_0)\ \mathrm{d}R \tag{4.16}$$

and

$$I_{\text{nodes}} = \frac{N_{\text{nodes}}}{V} \int_{T=0}^{\infty} \frac{A2\pi}{q^2} \cdot P_{\text{nth}}(T) \cdot W(T, T_0)\ \mathrm{d}T, \tag{4.17}$$

respectively. Note that the scattering intensity from the fibers $I_{\text{fibers}}$ is proportional to $q^{-1}$ in the low $q$ range, which corresponds to length scales much bigger than the fiber cross-section. The scattering function $I_{\text{nodes}}$, in turn, is proportional to $q^{-2}$ at low $q$ values where the scattering is independent of the node thickness. Hence, with comparable dimensions of the fiber cross-section and the node thickness one can yield with Eq. (4.9) a scattering curve for the gel which possesses a $q^{-1.5}$ behaviour in the low $q$ regime, just as experimentally observed for the binary gels.

Aiming to fit the measured scattering curves using Eq. (4.9) another aspect was considered. Since the obtained (reliable) scattering data does not extend down to the Guinier regime it was not possible to determine a reasonable value for the length $L$ of the gelator fibers nor for the area $A$ of the lamellar nodes. These two parameters influence the scattering functions $I_{\text{fibers}}$ and $I_{\text{nodes}}$ in the same way as the numbers of the scatterers $N_{\text{fibers}}$ and $N_{\text{nodes}}$, respectively. For example, a few long fibers yield the same scattering intensity as many short fibers. Accordingly, it made no sense to use $N_{\text{fibers}}$ and $L$ as individual fit parameters—which is equally true for $N_{\text{nodes}}$ and $A$. To overcome this issue the following route was developed. One can imagine that the gelator molecules in the sample make up fibers the total length of which is $L_{\text{total}}$. For this length it holds

$$L_{\text{total}} = L_{\text{fibers}} + L_{\text{nodes}} \tag{4.18}$$

where $L_{\text{fibers}}$ is the length obtained by lining up all "free" gelator fibers and $L_{\text{nodes}}$ is obtained adding up the lengths of all the fibers involved in nodes. Introducing the parameter $f$ as the length fraction of the "free" gelator fibers in the sample

$$f = \frac{L_{\text{fibers}}}{L_{\text{total}}} \tag{4.19}$$

the length $L_{\text{fibers}}$, which is nothing but the product of the number of fibers $N_{\text{fibers}}$ and their individual length $L$, can be written as

$$L_{\text{fibers}} = N_{\text{fibers}} \cdot L = f \cdot L_{\text{total}}. \tag{4.20}$$

If a circular fiber cross-section of radius $R$ is assumed it is possible to estimate $L_{\text{total}}$ by dividing the total fiber volume $V_{\text{fibers}}$ generated by the gelator molecules by the fiber cross-sectional area, i.e.

$$L_{\text{total}} = \frac{V_{\text{fibers}}}{\pi R^2}. \tag{4.21}$$

Assuming, furthermore, that the gelator fibers are monoclinic crystals, as indicated by the Bragg peak (cp. Fig. 4.11), one obtains the space requirements per gelator molecule in the fiber from the monoclinic elementary cell which possesses a volume of $V_{\text{cell}} = 1897.3$ Å$^3$ and contains four 12-HOA molecules, i.e. $N_{\text{cell}} = 4$ [33]. It thus holds

$$V_{\text{fibers}} = \frac{m_{12-\text{HOA}}}{M_{12-\text{HOA}}} \cdot (1 - g) \cdot N_{\text{A}} \cdot \frac{V_{\text{cell}}}{N_{\text{cell}}} \tag{4.22}$$

where $m_{12\text{-HOA}}$ is the mass of the gelator in the sample and $M_{12\text{-HOA}} = 300.48$ g mol$^{-1}$ its molar mass, respectively. The parameter $g$ is introduced as the mole fraction of monomerically dissolved gelator, which is not involved in forming gelator fibers, and $N_{\text{A}}$ is the Avogadro constant. Using the Eqs. (4.20) and (4.21) to express the length $L$ of one gelator fiber as

$$L = \frac{f \cdot L_{\text{total}}}{N_{\text{fibers}}} = \frac{f}{N_{\text{fibers}}} \cdot \frac{V_{\text{fibers}}(g)}{\pi R^2}. \tag{4.23}$$

Eqation (4.16) for the scattering intensity $I_{\text{fibers}}$ is finally obtained in the form

$$I_{\text{fibers}} = f \frac{V_{\text{fibers}}(g)}{V} \int_{R=0}^{\infty} \frac{1}{R^2 q} \cdot P_{\text{fcs}}(R) \cdot W(R, R_0)\ \mathrm{d}R. \tag{4.16a}$$

One can see that $I_{\text{fibers}}$ is, as intended, no longer dependent on the absolute number of gelator fibers $N_{\text{fibers}}$ nor on their individual length $L$ but instead on the length fraction $f$ of "free" gelator fibers in the sample as well as on the mole fraction $g$ of monomerically dissolved gelator. Hence, $f$ and $g$ are used as fit parameters besides the mean fiber radius $R_0$ and its distribution coefficient $\sigma_{\text{R}}$.

In order to substitute the number of nodes $N_{\text{nodes}}$ and their individual area $A$ in Eq. (4.17) one uses for the total scattering area

$$A_{\text{nodes}} = N_{\text{nodes}} \cdot A. \tag{4.24}$$

This total area can be calculated from the length of all gelator fibers in nodes, $L_{\text{nodes}}$, divided by the number of fiber layers per node, $N_{\text{layers}}$, multiplied with the

width $2R$ of one gelator fiber. The number of layers $N_{\text{layers}}$ is just the thickness $T$ of the nodes divided by the gelator fiber width $2R$ such that one yields with Eq. (4.24) for the area per gelator node

$$A = \frac{A_{\text{nodes}}}{N_{\text{nodes}}} = \frac{1}{N_{\text{nodes}}} \cdot \frac{L_{\text{nodes}}}{N_{\text{layers}}} \cdot 2R = \frac{4R^2 L_{\text{nodes}}}{N_{\text{nodes}} T}. \tag{4.25}$$

Using the Eqs. (4.18), (4.19) and (4.21) the length of all fibers in nodes can furthermore be expressed as

$$L_{\text{nodes}} = (1-f) \cdot L_{\text{total}} = (1-f) \cdot \frac{V_{\text{fibers}}(g)}{\pi R^2}. \tag{4.26}$$

Finally, Eq. (4.26) is inserted in (4.25) and the latter in Eq. (4.17) yielding

$$I_{\text{nodes}} = (1-f) \frac{V_{\text{fibers}}(g)}{V} \int_{T=0}^{\infty} \frac{8}{Tq^2} \cdot P_{\text{nth}}(T) \cdot W(T, T_0)\, \mathrm{d}T. \tag{4.17a}$$

The absolute number of nodes $N_{\text{nodes}}$ and their individual area $A$ are thus eliminated from $I_{\text{nodes}}$ which now also depends on $f$ and $g$ as well as on the mean node thickness $T_0$ and its distribution coefficient $\sigma_T$. This eventually opened up the way to analyze the measured SANS data of the binary gels with a set of reasonable fit parameters.

The modeled scattering intensity of the gel according to Eq. (4.9) with (4.16a) and (4.17a) does not include any background scattering. Hence the background intensity $I_{\text{bg}}$ was subtracted from the measured SANS data of the binary gels *n*-decane/12-HOA. As explained above, the data measured for the gel with 5.0 wt% 12-HOA was corrected by a factor of 0.577. The scattering contrast in all binary gels was obtained according to Eq. (2.52) from the difference between the scattering length density of the protonated gelator 12-HOA and that of the solvent d22-*n*-decane as $\Delta\rho = 6.58 \times 10^{10}$ cm$^{-2}$. The sample volume was always $V =$ 610 µl while the masses of 12-HOA in the samples were $m_{\text{12-HOA}} = 0.0079$ g in the gel with 1.5 wt% gelator, $m_{\text{12-HOA}} = 0.0135$ g in the gel with 2.5 wt% gelator and $m_{\text{12-HOA}} = 0.0272$ g in the gel with 5.0 wt% gelator, respectively. Figure 4.14 shows the obtained fit curves together with the measured SANS data and Table 4.2 lists the fit parameters.

The good agreement of the calculated fit curves and the measured SANS data in Fig. 4.14 shows that the gel model based on cylindrical fibers and lamellar nodes is indeed suitable for describing the studied 12-HOA gels. Furthermore, several trends of the fit parameters (cp. Table 4.2) substantiate the model.

Firstly, the length fraction of "free" gelator fibers $f$ decreases with increasing gelator mass fraction $\eta$ in the sample which means that at high gelator concentrations more gelator fibers are involved in forming nodes. This implies a strengthening of the gelator network which is perfectly in line with the increasing sol-gel

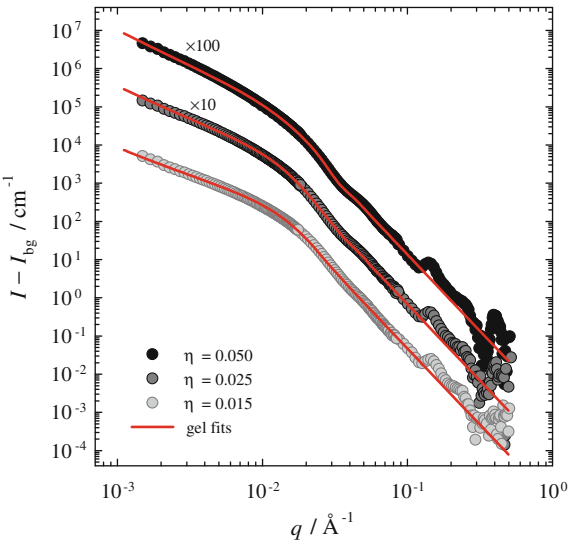


**Fig. 4.14** SANS data (λ = 6 Å) of the binary gel d22-*n*-decane/12-HOA with 1.5 (22.7 °C, *light gray*), 2.5 (21.9 °C, *dark gray*) and 5.0 wt% (23.8 °C, corrected by a factor of 0.577, *black*) gelator. The *red lines* are fits according to Eq. (4.9) with (4.16a) and (4.17a). The fit parameters are given in Table 4.2

**Table 4.2** Fit parameters used for the gel fits according to Eq. (4.9) which are shown in Fig. 4.14

| η | $R_0$ / Å | $\sigma_R$ / Å | $T_0$ / Å | $\sigma_T$ / Å | $f$ | $g$ |
|---|---|---|---|---|---|---|
| 0.015 | 106 | 40 | 310 | 29 | 0.94 ± 0.02 | 0.39 ± 0.05 |
| 0.025 | 118 | 35 | 325 | 31 | 0.83 ± 0.05 | 0.32 ± 0.07 |
| 0.050 | 111 | 29 | 350 | 50 | 0.75 ± 0.07 | 0.30 ± 0.08 |

Note that the accuracy of the mean fiber radius $R_0$, the mean thickness of the nodes $T_0$ and their distribution coefficients $\sigma_R$ and $\sigma_T$, respectively, is rather uncertain (see text for details) and thus not specified here. $f$ is the length fraction of "free" gelator fibers according to Eq. (4.19) and $g$ is the mole fraction of monomerically dissolved gelator

temperatures which were measured for increasing gelator concentrations in the *n*-decane/12-HOA gel (cp. Sect. 3.2) as well as with the increase of the storage and the loss moduli (cp. Sect. 3.3), respectively. Secondly, one finds an increase of the mean node thickness $T_0$ with increasing 12-HOA mass fraction in the gel which certainly also adds to the stability of the gelator network. Using the mean radius $R_0$ of the gelator fibers, which shows no distinct dependence on the gelator concentration, one can calculate that the nodes in the investigated gels consist on average of 1.4 to 1.6 fiber layers. In other words, the junction zones in the gels are usually single or double layers of aligned gelator fibers which means that the thickness of the gelator nodes is very similar to the gelator fibers' cross-sectional dimension. Accordingly, the Porod regime, where the scattering intensity is proportional to $q^{-4}$, is in the same

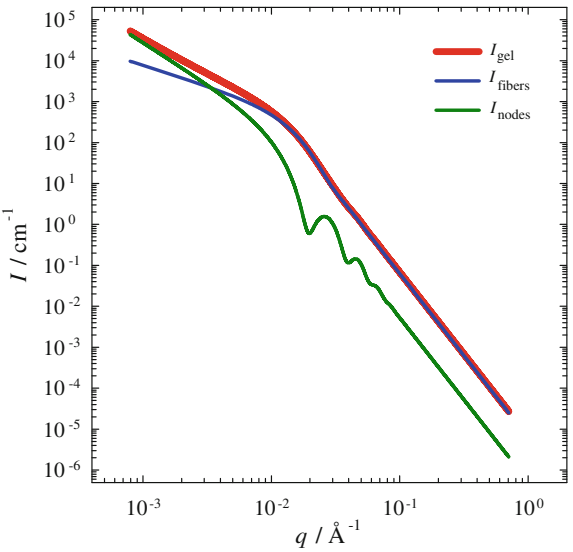


**Fig. 4.15** Fit curve of the binary gel with 2.5 wt% 12-HOA (*red line*) which, according to Eq. (4.9), is the sum of the scattering contribution from the "free" fibers in the gelator network, given by Eq. (4.16a), (*blue line*) and the scattering contribution from the gelator fibers in nodes, given by Eq. (4.17a), (*green line*)

$q$ range for both scattering functions $I_{\text{fibers}}$ and $I_{\text{nodes}}$. Figure 4.15 illustrates this for the fit curve of the *n*-decane/12-HOA gel with 2.5 wt% gelator for which the individual scattering contributions are shown. One can see that $I_{\text{fibers}}$ dominates in the high $q$ range while the influence of $I_{\text{nodes}}$ is stronger at lower $q$ values. In the Porod regime both scattering curves possess oscillations correlated with the fiber radius $R_0$ and the node thickness $T_0$, respectively, which are more or less smeared due to the parameter's polydispersity reflected by the distribution coefficients $\sigma_R$ and $\sigma_T$. Note that it is difficult to determine unambiguous values for these coefficients, in particular for $\sigma_T$ because $I_{\text{nodes}}$ is in the Porod regime about one order of magnitude lower than $I_{\text{fibers}}$. Moreover, the relatively large number of six fit parameters enables different parameter combinations to influence the fit curve. For example, increasing the mean node thickness $T_0$ shifts the $I_{\text{nodes}}$ curve to the lower $q$ range and at the same time increases its overall influence in $I_{\text{gel}}$. The influence of $I_{\text{nodes}}$ on $I_{\text{gel}}$, however, also depends on the fraction of "free" gelator fibers $f$. Thus, the simultaneous determination of all fit parameters yields values the accuracy of which is uncertain which is why no specific errors are given in Table 4.2 for $R_0$, $T_0$, $\sigma_R$ and $\sigma_T$. One must also keep in mind that the applied model includes several assumptions. For example, the gelator fibers are treated as monoclinic crystals which is not necessarily true as it has been stated in the literature that the crystalline packing of the gelator molecules within the fibers differs from the packing in a neat gelator crystal [34, 35]. However, even if the absolute values of the fit parameters are not very precise still strikingly reasonable trends were observed. This is substantiated when finally turning to the parameter $g$ which was introduced as the mole fraction of gelator molecules monomerically dissolved in the solvent of the gel. If one uses $g$ to calculate the concentration of monomerically dissolved 12-HOA in the sample volume $V = 610$ µl by

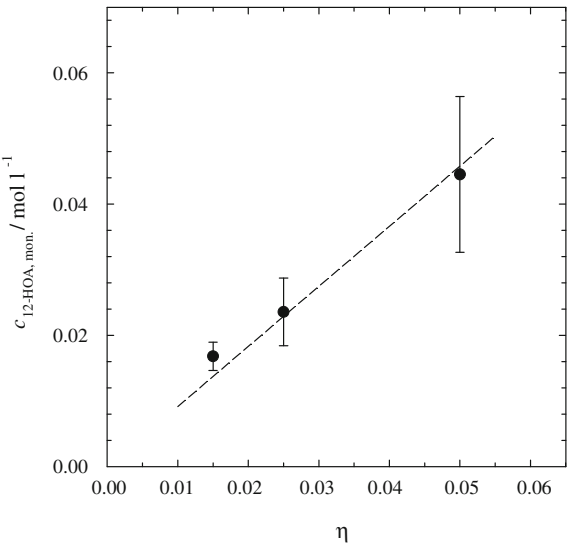


**Fig. 4.16** Concentration of monomerically dissolved gelator in the binary gel *n*-decane/12-HOA with different gelator mass fractions η (Table A.19). The *dashed line* is a linear trend line through the origin

$$c_{12-\text{HOA,mon.}} = \frac{m_{12-\text{HOA}} \cdot g}{M_{12-\text{HOA}} \cdot V} \tag{4.27}$$

where $m_{12\text{-HOA}}$ is the mass of the gelator in the sample and $M_{12\text{-HOA}} = 300.48$ g mol$^{-1}$ its molar mass, respectively, one finds a linear increase of $c_{12\text{-HOA,mon.}}$ with the gelator mass fraction η (see Fig. 4.16). This indicates there is a constant partition coefficient in the gel for 12-HOA molecules assembled to gelator fibers and monomers dissolved in *n*-decane.

### *4.2.4 Gelled Bicontinuous Microemulsion*

After investigating the two base systems, the gelled bicontinuous microemulsion $H_2O$ –*n*-decane/12-HOA–$C_{10}E_4$ ($\phi = 0.5$) was studied by SANS. The surfactant mass fraction in the system was $\gamma = 0.150$ like in the non-gelled bicontinuous microemulsion while the gelator concentrations were 1.5, 2.5 and 5.0 wt% like in the binary gel to ensure comparability. Samples in bulk as well as in film contrast were prepared for all 12-HOA concentrations and investigated by both SANS and V-SANS at temperatures in the middle of the one-phase region (cp. Table 6.4). In Fig. 4.17 the SANS data obtained at neutron wavelengths of $\lambda = 6$ Å and $\lambda = 13$ Å as well as the V-SANS data are shown. As discussed for the binary gel, the intensity of the 13 Å-data is lower than that of the 6 Å-data reflecting a decrease of the sample transmission due to multiple scattering, which is more pronounced in the bulk than in the film contrast samples (cp. Fig. 4.17, top). Moreover, the V-SANS data shows the same suspicious turnover to a plateau in the

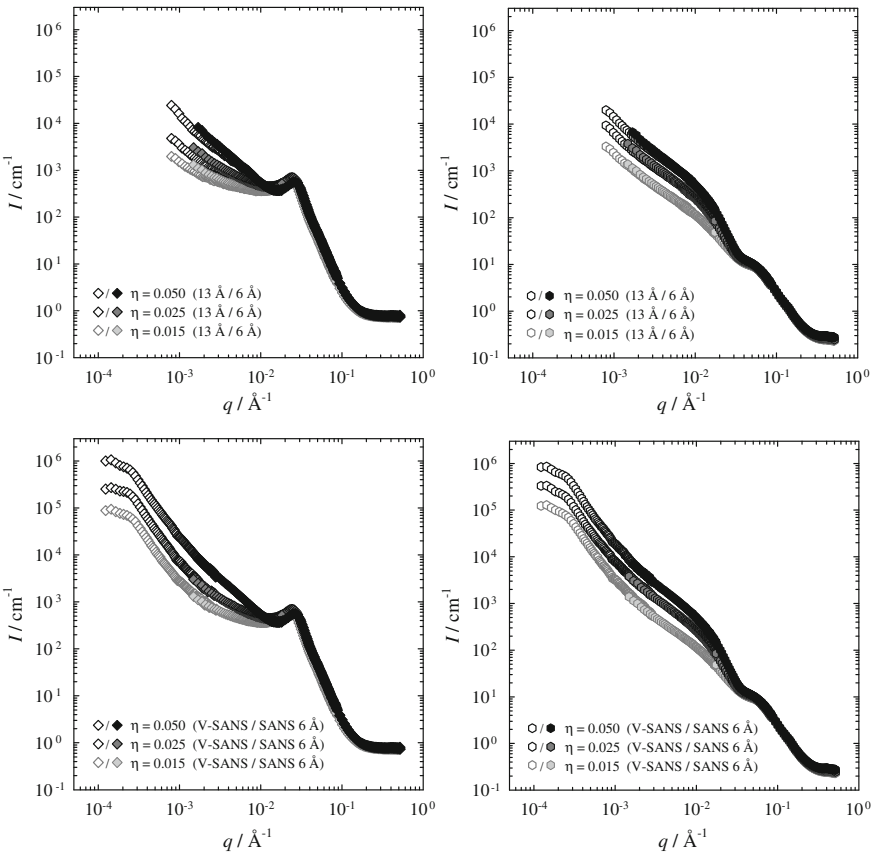


**Fig. 4.17** SANS data of the gelled bicontinuous microemulsion $H_2O$–*n*-decane/12-HOA–$C_{10}E_4$ ($\phi = 0.5$, $\gamma = 0.150$) with 1.5 (*light gray*), 2.5 (*dark gray*) and 5.0 wt% (*black*) gelator in bulk (*left*) and in film (*right*) contrast. Data measured with SANS at neutron wavelengths of $\lambda = 6$ Å (*filled symbols*) and $\lambda = 13$ Å (*open symbols*, *top*) as well as V-SANS data (*open symbols*, *bottom*) are shown. The measuring temperatures are given in Table 6.4

low $q$ region at $q \approx 2.5 \times 10^{-4}$ Å$^{-1}$ as it is the case for the binary gels (cp. Fig. 4.17, bottom). Consequently, the data analysis for the gelled bicontinuous microemulsions also concentrated on the 6 Å-data. For the system with 2.5 wt% 12-HOA this data is shown in Fig. 4.18 along with the respective data of the relevant base systems, i.e. the binary gel with 2.5 wt% 12-HOA and the non-gelled bicontinuous microemulsion.

Looking at the SANS curves of the gelled bicontinuous microemulsions one immediately recognizes that they comprise scattering contributions both from bicontinuous microemulsion domains and a gelator network. In the high $q$ range, where the gelator network scatters only weakly, the scattering from the bicontinuous microemulsion dominates. Thus, the characteristic microemulsion peak is

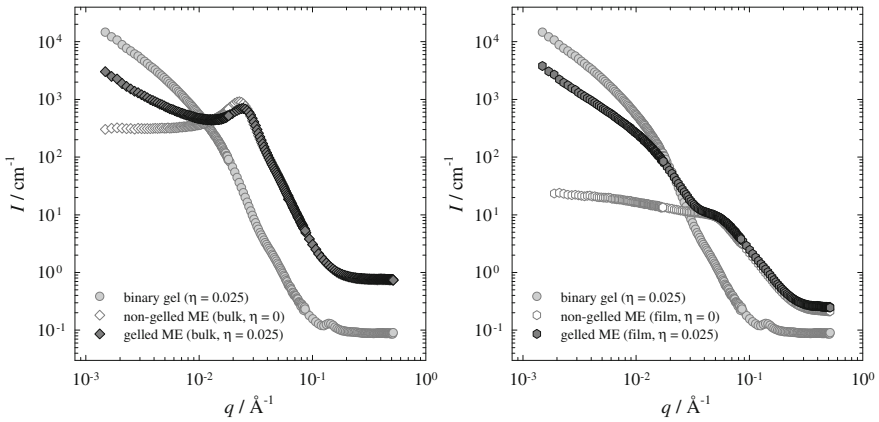


**Fig. 4.18** SANS data ($\lambda = 6$ Å) of the gelled bicontinuous microemulsion $H_2O$–*n*-decane/12-HOA–$C_{10}E_4$ ($\phi = 0.5$, $\gamma = 0.150$) with 2.5 wt% gelator (*dark gray symbols*) in bulk (*left*, *diamonds*) and in film (*right*, *hexagons*) contrast. The scattering curves of the base systems, i.e. the binary gel *n*-decane/12-HOA with 2.5 wt% gelator (*light gray circles*) and the non-gelled bicontinuous microemulsion $H_2O$–*n*-decane–$C_{10}E_4$ ($\phi = 0.5$, $\gamma = 0.150$, *white symbols*), are shown for comparison. All measuring temperatures are given in Table 6.4

clearly visible in the SANS curves of the gelled bicontinuous microemulsions in bulk contrast at $q_{max} \approx 2.5 \times 10^{-2}$ Å$^{-1}$ while the curves of the samples in film contrast correspondingly feature the shoulder typical for bicontinuous microemulsions at $q_{shoulder} \approx 5.0 \times 10^{-2}$ Å$^{-1}$. Going to lower $q$ values one finds for the gelled bicontinuous microemulsions a strong increase of the scattering intensity which does not occur for the non-gelled bicontinuous microemulsion but for the binary *n*-decane/12-HOA gels. Hence, this proves the presence of the gelator network in the gelled bicontinuous microemulsions.

Note that the increase of the scattering intensity in the low $q$ range is not the only evidence for the presence of crystalline 12-HOA fibers and junction zones in the gelled bicontinuous microemulsions. Subtracting from the scattering curves that of the non-gelled bicontinuous microemulsion in bulk or film contrast, respectively, (see Fig. 4.19) one uncovers at $q \approx 0.14$ Å$^{-1}$ the Bragg diffraction peak from the crystal lattice within the fibers and nodes, which is also seen in the SANS curves of the binary gels (cp. Fig. 4.11). Moreover, even a second Bragg peak at $q \approx 0.40$ Å$^{-1}$ is found which is hardly noticeable in the scattering curves of the binary gels but has indeed been described in a SAXS study of 12-HOA gels [17]. (Note that Fig. 4.19 does not show data of the gelled microemulsion with 1.5 wt% 12-HOA in bulk contrast since in the latter the Bragg peaks are buried in the noisy background. The data of the binary gel is shown for comparison without any subtraction).

The described observations strongly suggest that the SANS curves of the gelled bicontinuous microemulsions are the sum of scattering contributions from a bicontinuous microemulsion and from a 12-HOA gel. However, adding up

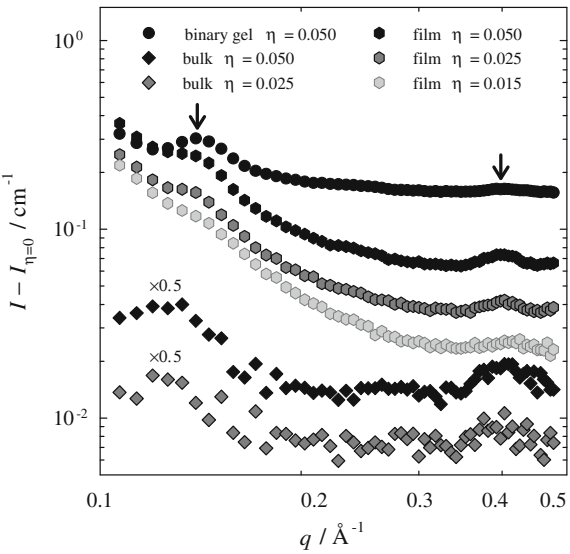


**Fig. 4.19** SANS data of the gelled bicontinuous microemulsion in bulk (*diamonds*) and film (*hexagons*) contrast from which the scattering of the respective non-gelled bicontinuous microemulsions was subtracted. The data of the binary gel d22-*n*-decane/12-HOA with 5.0 wt% gelator (*black circles*) is shown for comparison. The positions of the Bragg peaks are marked by the *arrows*

scattering curves of the two base systems does not directly yield the scattering curve of the respective gelled bicontinuous microemulsion as one can see in Fig. 4.18. This is not surprising because the solvent around the gelator network is no longer *n*-decane but a bicontinuous microemulsion to which 12-HOA was added, in turn. Also the results of the other techniques employed in this work show that the bicontinuous microemulsion and the gelator network in a gelled bicontinuous microemulsion are not identical to the base systems (cp., e.g. the shifts of the microemulsion phase boundaries and of the sol-gel transition temperatures discussed in Sects. 3.1 and 3.2, respectively). Hence, in the SANS data of the gelled bicontinuous microemulsion one finds corresponding alterations with varying gelator mass fraction.

A close look on the microemulsion peak in the SANS data of the bicontinuous microemulsion samples in bulk contrast shows that the peak maximum shifts slightly to higher $q_{max}$ values and lower intensities with increasing 12-HOA concentration while at the same time the peak broadens a bit. This indicates that the microemulsion domain size decreases which makes sense assuming an increase of monomerically dissolved 12-HOA, which adsorbs to the water–oil interface and acts as co-surfactant. To quantify the described effect the SANS curves of the gelled bicontinuous microemulsions in bulk contrast were fitted with the Teubner-Strey formula (Eq. (4.4)). Note that the scattering contribution from the gelator network in the relevant $q$ range is about one order of magnitude lower than that of the bicontinuous microemulsion domains (cp. Fig. 4.18). Hence its influence can be neglected within this $q$ regime. Figure 4.20 (left) shows the measured data together with the Teubner-Strey fits and Table 4.3 lists the respective fit parameters.

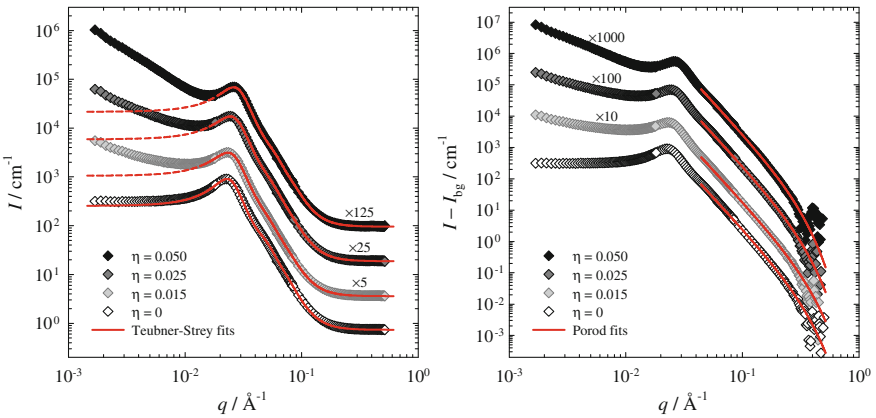


**Fig. 4.20** SANS curves of the bicontinuous microemulsions $H_2O$–*n*-decane/12-HOA–$C_{10}E_4$ ($\phi = 0.5$, $\gamma = 0.150$) in bulk contrast without gelator (28.3 °C, *white*) as well as gelled with 1.5 (23.7 °C, *light gray*), 2.5 (23.3 °C, *dark gray*) and 5.0 wt% (21.9 °C, *black*) 12-HOA. The *red lines* are fits with the Teubner-Strey formula (Eq. (4.4) taking into account multiple scattering, *left*) and with the Porod formula for diffuse interfaces (Eq. (4.28), *right*), respectively. The fit parameters are given in Table 4.3

**Table 4.3** Parameters used for the Teubner-Strey fits, according to Eq. (4.4), and the Porod fits, according to Eq. (4.28), which are shown in Fig. 4.2

| η | Teubner-Strey fit | | | | | Porod fit | |
|---|---|---|---|---|---|---|---|
| | $\xi_{TS}$ / Å | $d_{TS}$ / Å | $d$ / Å | Double sc. / % | Triple sc. / % | $S/V$ / $10^{-2}$ Å$^{-1}$ | $t$ / Å |
| 0 | 148 ± 3 | 263 ± 1 | 132 ± 1 | 2.60 | 0.25 | 1.05 ± 0.03 | 3.1 ± 0.1 |
| 0.015 | 128 ± 3 | 256 ± 1 | 128 ± 1 | 1.60 | 0.17 | 0.77 ± 0.03 | 2.9 ± 0.1 |
| 0.025 | 122 ± 3 | 244 ± 1 | 122 ± 1 | 1.80 | 0.15 | 1.08 ± 0.03 | 3.2 ± 0.1 |
| 0.050 | 120 ± 3 | 229 ± 1 | 115 ± 1 | 1.90 | 0.20 | 1.15 ± 0.03 | 3.5 ± 0.1 |

Figure 4.20 (left) shows that the measured SANS curves of the gelled bicontinuous microemulsions in bulk contrast are well described by the Teubner-Strey formula down to $q$ values of $\sim 1.5 \times 10^{-2}$ Å$^{-1}$. To obtain quantitative fits in the high $q$ range some double and triple scattering was included just as in case of the non-gelled bicontinuous microemulsion, which is shown in Fig. 4.20 for comparison. As expected one finds a decrease of the microemulsion domain size $d$ with increasing gelator concentration in the system (cp. Table 4.3). As mentioned before, this can be ascribed to the adsorption of 12-HOA molecules at the water–oil interface in the bicontinuous microemulsion which goes along with an increase of the internal interface. The internal interface per volume $S/V$ can be determined from the high $q$ part of the scattering data using the following equation for the Porod regime in a system with diffuse interfaces [36]

$$\lim_{q\to\infty} I(q) = \frac{2\pi(\Delta\rho)^2}{q^4} \cdot \frac{S}{V} \cdot e^{-q^2t^2} + I_{bg}. \tag{4.28}$$

Here $\Delta\rho$ is the scattering contrast, which is for the bulk contrast samples $6.29 \times 10^{10}$ cm$^{-2}$ (cp. Table A.18), $t$ is a parameter accounting for the diffusivity of the amphiphilic film due to which there is no sharp scattering length density change at the interface and $I_{bg}$ is the intensity of the incoherent background scattering. Figure 4.20 (right) shows the respective fits to the SANS data of the bicontinuous microemulsions in bulk contrast (from which the incoherent background was subtracted). Looking at Table 4.3 one sees indeed an increase of $S/V$ from 1.5 to 5.0 wt% gelator in the gelled bicontinuous microemulsion. However, the comparatively high $S/V$ value of the non-gelled bicontinuous microemulsion is unexpected. The most likely explanation for it is that the multiple scattering in the non-gelled sample was distinctly higher than in the gelled systems, which particularly affects the high $q$ range used for the Porod fit. If one calculates with the Teubner-Strey Equation (4.4) a scattering curve without multiple scattering based on the $\xi_{TS}$ and the $d_{TS}$ value determined for the non-gelled bicontinuous microemulsion a subsequent Porod fit yields a much smaller surface to volume ratio of only $S/V = 0.39 \times 10^{-2}$ Å$^{-1}$. This illustrates the sensitivity of the Porod fit for diffuse interfaces. Finally, high multiple scattering reflects a comparatively high order of the microstructure. And indeed, the ratio of the correlation length $\xi_{TS}$ to $d_{TS}$ is 0.56 for the non-gelled bicontinuous microemulsion and decreases to 0.50, 0.50 and 0.52 for the gelled bicontinuous microemulsion with 1.5, 2.5 and 5.0 wt% 12-HOA, respectively. This means that the quasi-periodicity of the bicontinuous microemulsion is in the gelled systems sooner lost than in the non-gelled case, which is possibly due to a disturbing effect of the present gelator fibers. The slightly higher order with 5.0 wt% than with 1.5 and 2.5 wt% 12-HOA could be an indication for an approaching lamellar phase. However, the shape of the measured SANS curves shows that all gelled microemulsions, each of which was prepared at $\gamma = 0.150$, are still bicontinuous (even though the system with 5.0 wt% gelator was predicted to be liquid crystalline according to the phase diagram presented in Fig. 3.8).

In the next step the scattering in the low $q$ range was analyzed. Here the SANS curves of the gelled bicontinuous microemulsions are dominated by the scattering from the gelator network. In Fig. 4.18 one can see that with equal amounts of surfactant in the sample a lower scattering intensity is detected at low $q$ values for a gelled bicontinuous microemulsion than for a binary gel. This can be due to less or smaller fibers and junction zones in the gelator network when the latter is in the bicontinuous microemulsion instead of in pure *n*-decane. Remember that the scattering intensity of the binary gel *n*-decane/12-HOA, especially in the low $q$ range, is determined by the gelator concentration in the system (cp. Fig. 4.11). Hence it seems that in the gelled bicontinuous microemulsions a smaller fraction of the comprised 12-HOA is involved in forming the gelator network than is the case in the binary gels which, in turn, implies an increase of gelator monomers in the solvent of the gel. In order to verify these assumptions the fit model which was

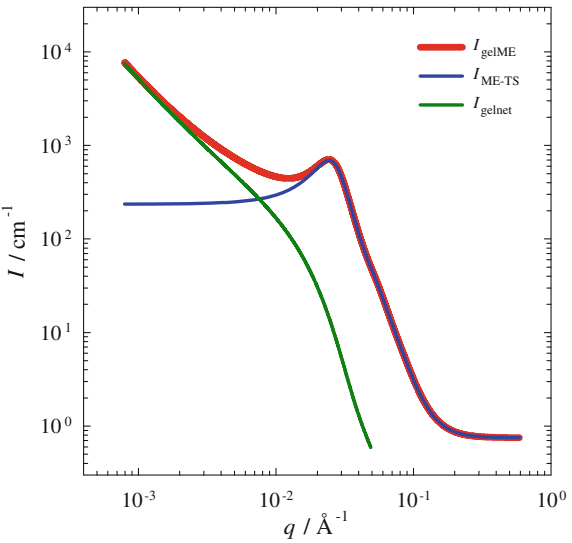


**Fig. 4.21** Fit curve of the gelled bicontinuous microemulsion in bulk contrast with 2.5 wt% 12-HOA (*red line*) which, according to Eq. (4.29), is the sum of the scattering from the bicontinuous microemulsion domains (see Eq. (4.4), *blue line*) and the scattering from the gelator network (see Eq. (4.9), *green line*)

developed for the binary gel is used. Following the idea that the scattering from a gelled bicontinuous microemulsion is the sum of the scattering contributions from the gelator network and from the bicontinuous microemulsion domains the equation

$$I_{\text{gelME}}(q) = I_{\text{gelnet}}(q) + I_{\text{ME-TS}}(q) \tag{4.29}$$

is used to describe the scattering function of a gelled bicontinuous microemulsion in bulk contrast over the full $q$ range. Therein $I_{\text{gelnet}}$ is the scattering intensity according to Eq. (4.9) which models the gelator network as cylindrical fibers and lamellar nodes. $I_{\text{ME-TS}}$, in turn, is the microemulsion scattering intensity according to the Teubner-Strey formula given in Eq. (4.4). Note that in principle one should sum up the amplitudes of the neutron waves scattered from the bicontinuous microemulsion domains and from the gelator network and square the result to obtain $I_{\text{gelME}}$ (cp. Eq. (2.48)). Equation (4.29) would then comprise an additional cross-term which, however, was neglected for the sake of simplicity.

The parameters which were previously determined for the Teubner-Strey fit (cp. Table 4.3) were used and not further touched when the scattering data of the gelled bicontinuous microemulsions in bulk contrast were fitted to Eq. (4.29). Just as the binary gels, all gelled bicontinuous microemulsions had a volume of $V = 610$ µl. The masses of 12-HOA in the bulk contrast samples were 0.0087, 0.0148 and 0.0299 g for 1.5, 2.5 and 5.0 wt% gelator, respectively. The scattering contrast was calculated according to Eq. (2.52) as difference between the scattering length density of the 12-HOA in the gelator fibers and that of the surrounding bulk contrast microemulsion, which was computed for each sample according to Eq. (2.45). Hence $\Delta\rho$ values of $\sim 5.7 \times 10^{10}$ cm$^{-2}$ were obtained. Figure 4.21 shows for the

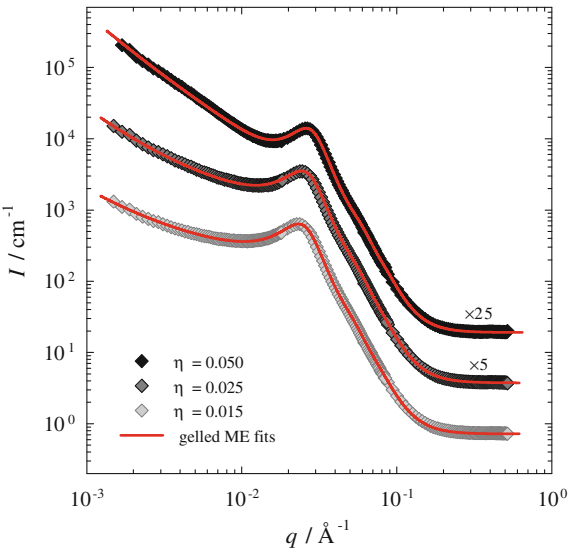


**Fig. 4.22** SANS curves of the gelled bicontinuous microemulsions $H_2O$–*n*-decane/12-HOA–$C_{10}E_4$ ($\phi = 0.5$, $\gamma = 0.150$) in bulk contrast with 1.5 (23.7 °C, *light gray*), 2.5 (23.3 °C, *dark gray*) and 5.0 wt% (21.9 °C, *black*) gelator. The *red lines* are fits according to Eq. (4.29). The fit parameters are given in Table 4.4

gelled bicontinuous microemulsion in bulk contrast with 2.5 wt% 12-HOA the determined fit curve according to Eq. (4.29) together with the two comprised scattering functions $I_{\text{ME-TS}}$ and $I_{\text{gelnet}}$. Figure 4.22 shows for all investigated gelator concentrations the fit curves besides the measured SANS data. The fit parameters are listed in Table 4.4.

The good superposition of the calculated scattering curves and the measured SANS data in Fig. 4.22 shows that Eq. (4.29) is well applicable for modeling the scattering of gelled bicontinuous microemulsions in bulk contrast. Moreover, the fit parameters listed in Table 4.4 show very reasonable trends. For example, the length fraction of "free" gelator fibers $f$ is the smaller the higher the gelator concentration in the system, which reflects an increase of the gelator network stability due to more junction zones. This is exactly the same observation as was made for the binary gel with varying gelator mass fraction. However, in general slightly higher $f$ values were determined for the gelled bicontinuous microemulsions than for the binary gels (cp. Table 4.2). This is consistent with the determined sol-gel transition temperatures and the rheometry results (cp. Sects. 3.2 and 3.3, respectively) which substantiate a more stable gelator network in the binary gels than in the respective gelled bicontinuous microemulsions. Note that a significant increase of the mean fiber radius $R_0$ with increasing gelator mass fraction was seen for the gelled bicontinuous microemulsion which was not the case for the binary gels. Thus, the strength of the gelator network depends stronger on the gelator concentration in the gelled bicontinuous microemulsions than in the binary gels. Along with the increase of the gelator fiber radius goes an increase of the gelator node thickness $T_0$ such that the average number of fiber layers in the nodes stays constant at about 1.5, which was also found for the binary gels. Note that the accuracy of the fit parameters $R_0$ and $T_0$, and especially that of the distribution

**Table 4.4** Parameters used in $I_{gel}$ according to Eq. (4.9) for the fits of the SANS data of the gelled bicontinuous microemulsions in bulk contrast according to Eq. (4.29), which are shown in Fig. 4.22

| η | $R_0$ / Å | $\sigma_R$ / Å | $T_0$ / Å | $\sigma_T$ / Å | $f$ | $g$ |
|---|---|---|---|---|---|---|
| 0.015 | 86 | 32 | 255 | 24 | 0.98 ± 0.02 | 0.67 ± 0.05 |
| 0.025 | 94 | 37 | 275 | 28 | 0.94 ± 0.04 | 0.69 ± 0.07 |
| 0.050 | 110 | 28 | 335 | 27 | 0.82 ± 0.05 | 0.75 ± 0.08 |

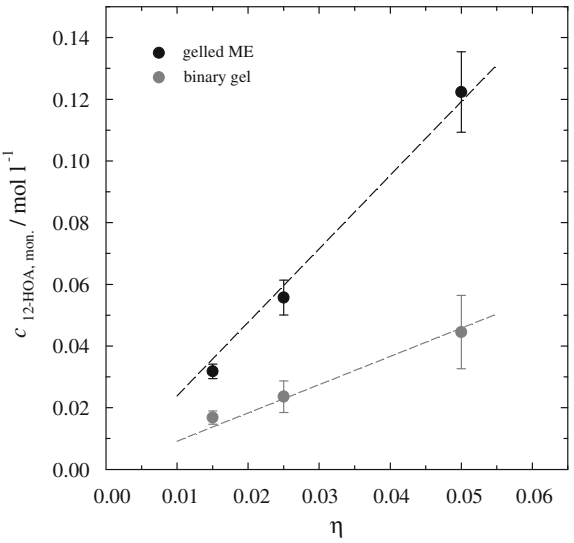


**Fig. 4.23** Concentration of monomerically dissolved gelator in the gelled bicontinuous microemulsion $H_2O$–*n*-decane/12-HOA–$C_{10}E_4$ ($\phi = 0.5$, $\gamma = 0.150$, *black*) at different gelator mass fractions η (Table A.19). The values of the binary gel *n*-decane/12-HOA (*gray*) are shown for comparison. The *dashed lines* are linear trend lines through the origin

coefficients $\sigma_R$ and $\sigma_T$, is equally uncertain as for the binary gels. Indeed, on top of the above discussed difficulties to find an unambiguous set of fit parameters the contribution $I_{gelnet}$ of the gelator network is in the Porod regime much smaller than the contribution $I_{ME\text{-}TS}$ of the bicontinuous microemulsion domains (cp. Fig. 4.21). Hence, the parameters of the binary gels were chosen as starting point for fitting the SANS curves of the gelled bicontinuous microemulsions. Subsequently, the parameters were modified until the calculated curves described well the intensity decay in the low $q$ range, which is, just as the Porod regime, also distinctly dependent on $R_0$ and $T_0$. Finally, turning to the parameter $g$ which was introduced as the mole fraction of monomerically dissolved gelator one finds values which are considerably larger than those determined for the binary gels. This means in the gelled bicontinuous microemulsions a much smaller fraction of 12-HOA is involved in forming gelator fibers than is the case in the binary gels. Accordingly, the concentration of 12-HOA monomers (calculated with Eq. (4.27)) is distinctly higher, and increases stronger with the gelator mass fraction, if the solvent around the gelator network is a bicontinuous microemulsion and not pure *n*-decane (see Fig. 4.23). The hypothesis that a relatively high percentage of the 12-HOA within

the gelled bicontinuous microemulsions does not form gelator fibers is hence corroborated. In fact, it makes sense that many 12-HOA molecules reside monomerically in the microemulsion because there they can not only dissolve in *n*-decane but also adsorb at the water–oil interface. Again, this behaviour accounts for the observed reduction of the domain size as well as for the down shift of the phase boundaries (cp. Sect. 3.1).

To sum up, the SANS study clearly confirms that the gelled bicontinuous microemulsion $H_2O$–*n*-decane/12-HOA–$C_{10}E_4$ consists of bicontinuous microemulsion domains and a gelator network. This was seen in film as well as in bulk contrast samples. The scattering curves of the latter were quantitatively analyzed using the Porod and the Teubner-Strey formula. Adding to the latter a scattering function which was initially developed for the binary gel *n*-decane/12-HOA the 6 Å-SANS data of the gelled bicontinuous microemulsions in bulk contrast could be fitted over the full $q$ range. The main fit parameters were the mean radius $R_0$ of the gelator fibers, the mean thickness $T_0$ of the gelator fiber nodes, the length fraction $f$ of "free" gelator fibers, i.e. fibers which are not involved in nodes, and the mole fraction $g$ of monomerically dissolved gelator. Even though these parameters could not be determined with a very high precision strikingly reasonable trends were observed. These trends are in good agreement with the results of several other techniques employed in this thesis and indicate that the stability of the gelator network increases with increasing gelator mass fraction in the system. Compared to the binary gel, the stability increase is lower for the gelled bicontinuous microemulsion which correlates with an increased concentration of 12-HOA molecules which do not form gelator fibers.

## 4.3 Electron Microscopy

Finally, freeze-fracture transmission electron microscopy (FFEM) pictures were taken in order to manifest the coexistence of the bicontinuous microemulsion domains with gelator fibers in gelled bicontinuous microemulsions. FFEM allows to image nanometer-sized microstructures of soft matter systems. However, one must be aware that—other than e.g. SANS—FFEM is an indirect and destructive method. Before one yields pictures of a sample, a 'replica' of the latter must be produced in numerous intricate steps. These involve rapid sample freezing and fracturing for which it is evident that only local "snap-shots" of the microstructure are captured. 'Shadowing' the fractured surface with platinum vapour and subsequently depositing a carbon layer on top one obtains an ultrathin film, the replica, which is finally inspected under the transmission electron microscope. For the thesis at hand FFEM pictures of the two base systems, i.e. the non-gelled bicontinuous microemulsion ($\phi = 0.5$, $\gamma = 0.170$) and the binary gel ($\eta = 0.015$), as well as of the gelled bicontinuous microemulsion ($\phi = 0.5$, $\gamma = 0.170$) with 1.5 wt% gelator were taken.

### 4.3.1 Non-Gelled Bicontinuous Microemulsion

The non-gelled base microemulsion $H_2O$–*n*-decane–$C_{10}E_4$ ($\phi = 0.5$, $\gamma = 0.170$) was equilibrated in its bicontinuous state, i.e. in the middle of the phase boundaries at 29.7 °C (cp. Fig. 3.2), from where it was rapidly frozen to 'cryofix' and then replicate its microstructure. One of the obtained FFEM pictures is shown in Fig. 4.24.

On the FFEM picture one can see the bicontinuous microstructure of the microemulsion. The neighbouring water and oil domains fracture differently for which one obtains the characteristic shadowing pattern in the replicas. The seen microemulsion domains have on average a diameter of 60 ± 10 nm. This is about 4.5 times bigger than what was found with the SANS measurements ($d = 132$ Å). Admittedly, a deviation of this magnitude cannot be attributed to the fact that the surfactant mass fraction in the FFEM sample was 2 wt% bigger than in the SANS sample, though it is known that the microemulsion domains are the bigger the further $\gamma$ exceeds $\widetilde{\gamma}$ [14]. One must rather assume that structural changes occurred in the replica preparation procedure. It is quite likely that the cooling rate achieved in the freezing step was too low such that the sample started to phase separate. Hence, the frozen microemulsion did not possess the same microstructure as in its non-frozen initial state. In the SANS measurements, by contrast, the samples were studied non-invasively. Thus the domain size $d = 132$ Å, which was in fact determined independently for a bicontinuous microemulsion in 'normal' and one in inverse bulk contrast and is furthermore consistent with the SANS curve of a third film contrast sample, seems more reliable than the FFEM results. To validate this argument the domain size in the bicontinuous microemulsion is calculated according to the equation [14]

$$d = 7.16 \frac{v_{\text{surfactant}}}{a_{\text{surfactant}}} \frac{\phi(1-\phi)}{\phi_{\text{surf.,int.}}} \tag{4.30}$$

where $\phi$ is the oil volume fraction according to Eq. (2.2) and $v_{\text{surfactant}}$ and $a_{\text{surfactant}}$ are the volume of a surfactant molecule and the area it occupies in the surfactant monolayer at the water–oil interface, respectively. For $\phi_{\text{surf.,int.}}$ it holds

$$\phi_{\text{surf.,int.}} = \frac{V_{\text{surf.,int.}}}{V_{\text{water}} + V_{\text{oil}} + V_{\text{surfactant}}} \tag{4.31}$$

where $V_{\text{surf.,int.}}$ is the volume of surfactant adsorbed at the water–oil interface while $V_{\text{water}}$, $V_{\text{oil}}$ and $V_{\text{surfactant}}$ are the total volumes of water, oil and surfactant within the sample mixture. The latter three values are known since they relate to the masses of the compounds via their densities. However, $V_{C_{10}E_4,\text{int.}}$ must be estimated for which it is assumed (like for contrast matching the SANS samples, cp. Sect. 4.2) that the *n*-decane subphase in the studied microemulsion contains 2.1 wt% manometrically dissolved $C_{10}E_4$ [13]. The $\phi_{C_{10}E_4,\text{int.}}$ value in a

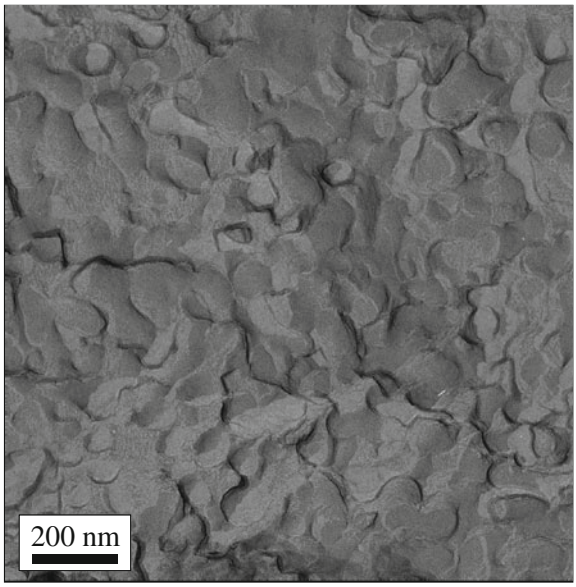


**Fig. 4.24** FFEM picture of the non-gelled bicontinuous microemulsion $H_2O$–*n*-decane–$C_{10}E_4$ ($\phi = 0.5$, $\gamma = 0.170$) frozen from 29.7 °C (picture taken by Natalie Preisig)

bicontinuous microemulsion with $\gamma = 0.170$ and $\phi = 0.5$ is hence 0.149. Using furthermore the literature values $V_{C_{10}E_4}$ = 579 Å$^3$ and $a_{C_{10}E_4} = 53.9$ Å$^2$ [37] one obtains for the theoretical domain size of the studied FFEM sample $d = 129$ Å which is obviously much closer to the SANS (132 Å) than to the FFEM (60 nm) results. Therefore, the absolute dimensions of the microemulsion domains in the FFEM pictures do not reflect the real domain size even though the bicontinuous microstructure is nicely pictured.

### *4.3.2 Binary Gel*

Secondly, the binary gel *n*-decane/12-HOA was investigated. A sample with a gelator concentration of 1.5 wt% was prepared and "shock-frozen" from room temperature. In Fig. 4.25 several of the obtained FFEM pictures are shown. In these pictures the 12-HOA gelator fibers are readily visible. As expected one can see elongated strands which are obviously twisted. The diameter of the imaged individual fibers is on average 27 ± 6 nm. This fits quite well to the SANS results according to which the diameter of the fibers is about 21.2 nm. In the literature fiber widths between 10 and 100 nm have been reported for 12-HOA gels with various different solvents (benzene, carbon tetrachloride, chloroform, acetone, ethanol, soybean oil) [38, 39]. Regarding the length of the gelator fibers the obtained FFEM pictures are equally non-specific as the SANS data. At some points on the pictures the fibers seem to descend from the fractured surface into the sample volume, in other places they appear broken (e.g. Fig. 4.25, bottom left).

In addition one finds gelator fibers which span an entire FFEM picture (e.g. Fig. 4.25, top left), thus these are at least ∼3.3 μm long. The fiber diameter can in any case be regarded as the more characteristic quantity for a specific gel because, according to literature [40], the length of gelator fibers often varies considerably, while the cross-sectional dimensions do not. Looking at the different FFEM pictures in Fig. 4.25 one notices that in some places single gelator fibers cross above or underneath one another (e.g. middle left), while in other spots there are fiber bundles in which the gelator strands are in contact over extended distances and mostly arranged in parallel (e.g. top right). These fiber bundles can be seen as the transient junction zones of the gelator network, which confirms that treating the latter as lamellar nodes in the fit model for the SANS data is justified. Permanent junction zones, i.e. one gelator fiber branching into two, cannot unambiguously be identified on the shown FFEM pictures and thus seem to be comparatively rare.

Note that many of the FFEM pictures of the binary gel show a great number of gelator fibers, in fact, way more than one would expect for a gelator mass fraction of only 1.5 wt% (e.g. Fig. 4.25, middle left). Other pictures, by contrast, display hardly any gelator fibers or merely a few small fiber pieces (e.g. Fig. 4.25, bottom right). Remember in this regard that with the FFEM technique only tiny sections of a sample are imaged one of which is not necessarily representative for the entire sample volume. Based on the distinctly diverging frequency of gelator fibers in the different FFEM pictures one can conclude that the density of the gelator network is uneven throughout the sample volume. This, in turn, precludes any designation of the gelator fraction in a 12-HOA gel sample based on FFEM pictures. A possible explanation for the uneven distribution of the gelator fibers is that when the sol is cooled for gelling temperature gradients in the sample cause an uneven distribution of gelator fiber nuclei. Artefacts coming from the replica preparation, however, can also not fully be ruled out. A feature of the FFEM pictures which originates from the replica preparation procedure is the observation that the gelator fibers appear as elevations in some pictures, while one perceives their imprint in others. Fracturing the frozen samples naturally yields inverse fractured surfaces with gelator fibers adhering or missing, which is reflected by the prepared replicas. Note in this context that the shadowing with platinum vapour generates dark metal accumulations in front and light shadows in the back of surface elevations, while the appearance of surface cavities is opposite.

A special notice deserves at this point the twist of the gelator fibers for which an average pitch of 155 ± 35 nm was measured. For 12-HOA gels with carbon tetrachloride and benzene as solvents pitch values of 320 and 480 nm, respectively, have been estimated based on studies of the circular dichroism [41]. Quite intuitively the twist is related to the chirality of the 12-HOA molecule but it is, in fact, remarkable that all fibers in each FFEM picture possess the same handedness. This implies that all gelator fibers in the studied *n*-decane/12-HOA gel are made up of one enantiomer of 12-HOA because, naturally, if a helix is formed of a pure D-compound and another one of a pure L-compound they are just mirrored. Actually, no enantiopure 12-HOA had been ordered for the work at hand. Nevertheless, it is possible that a substance with an excess of one enantiomer was

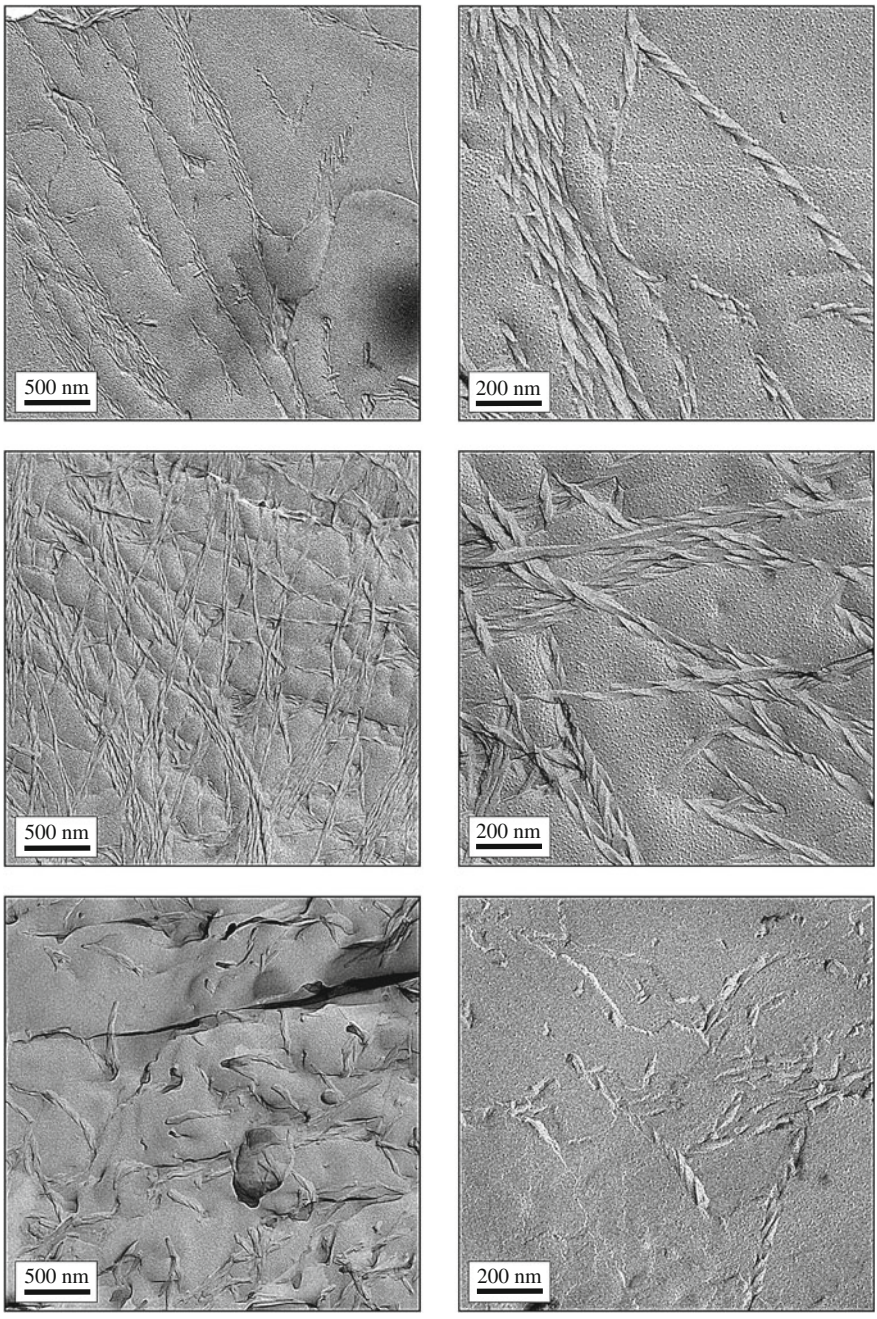


**Fig. 4.25** FFEM pictures of the binary gel *n*-decane/12-HOA with 1.5 wt% gelator frozen from room temperature (pictures taken by Natalie Preisig)

delivered. A plausible explanation is that a way to produce 12-HOA is the hydrogenation of naturally occurring ricinoleic acid which yields 12-HOA in its D-configuration [42]. In order to verify the assumption that the used 12-HOA is not a racemic mixture its melting point was measured.[1] The obtained value of 79.5 ± 0.5 °C is close to 79.8 °C which has been reported for purified D-12-HOA while a value of 76.2 °C was reported for DL-12-HOA [42]. Hence, it is quite likely that the gelator purchased for this work comprises predominantly one enantiomer of 12-HOA which is in excellent accordance with literature stating that gels are only formed by enantiopure 12-HOA but not by the racemat [38, 42]. The D-form of 12-HOA has been found to self-assemble to left-handed helices while right-handed fibers are obtained with L-12-HOA regardless of the used solvent [38]. Since the twist of the gelator fibers in the imaged *n*-decane/12-HOA gel could be characterized as left-handed it is concluded that a high enantiomeric excess of D-12-HOA was present in the used gelator.

### 4.3.3 Gelled Bicontinuous Microemulsion

After taking FFEM pictures of both a bicontinuous microemulsion and a binary 12-HOA gel the respective gelled bicontinuous microemulsion $H_2O$–*n*-decane/12-HOA–$C_{10}E_4$ ($\phi = 0.5$) was studied. The investigated sample contained a surfactant mass fraction of $\gamma = 0.170$ and 1.5 wt% of the gelator. According to the determined phase boundaries the system was equilibrated in its bicontinuous state at 24.0 °C (cp. Fig. 3.3) from where it was subsequently "shock-frozen". Figure 4.26 shows several of the obtained FFEM pictures. One can see that the microstructural features identified in the FFEM pictures of the two base systems are combined in the case of the gelled bicontinuous microemulsion. One finds twisted gelator fibers besides the bicontinuous domains of the microemulsion. However, on some of the pictures only a bicontinuous microemulsion or only gelator fibers are seen (cp. Fig. 4.26, bottom). This strongly suggests that the replica preparation procedure requires further improvement. In the top and middle pictures of Fig. 4.26 the contour of the gelator fibers within the bicontinuous microemulsion is less clear than in the pictures of the binary gel (cp. Fig. 4.25). The fibers appear covered by the microemulsion which could explain why a comparatively large fiber thickness of on average 46 ± 9 nm was measured (pitch 190 ± 50 nm). With SANS, by contrast, a gelator fiber diameter of about 17.2 nm was determined for a gelled bicontinuous microemulsion sample with 1.5 wt% 12-HOA. The imaged bicontinuous microemulsion domains are on average 53 ± 14 nm in size which is again distinctly larger than the domain size obtained from the SANS measurements ($d = 128$ Å). As explained above for the

[1] The measurement of the melting point was carried out in a Thiele tube SMP-20 from *Büchi* with a heating rate of 0.2 K $min^{-1}$.

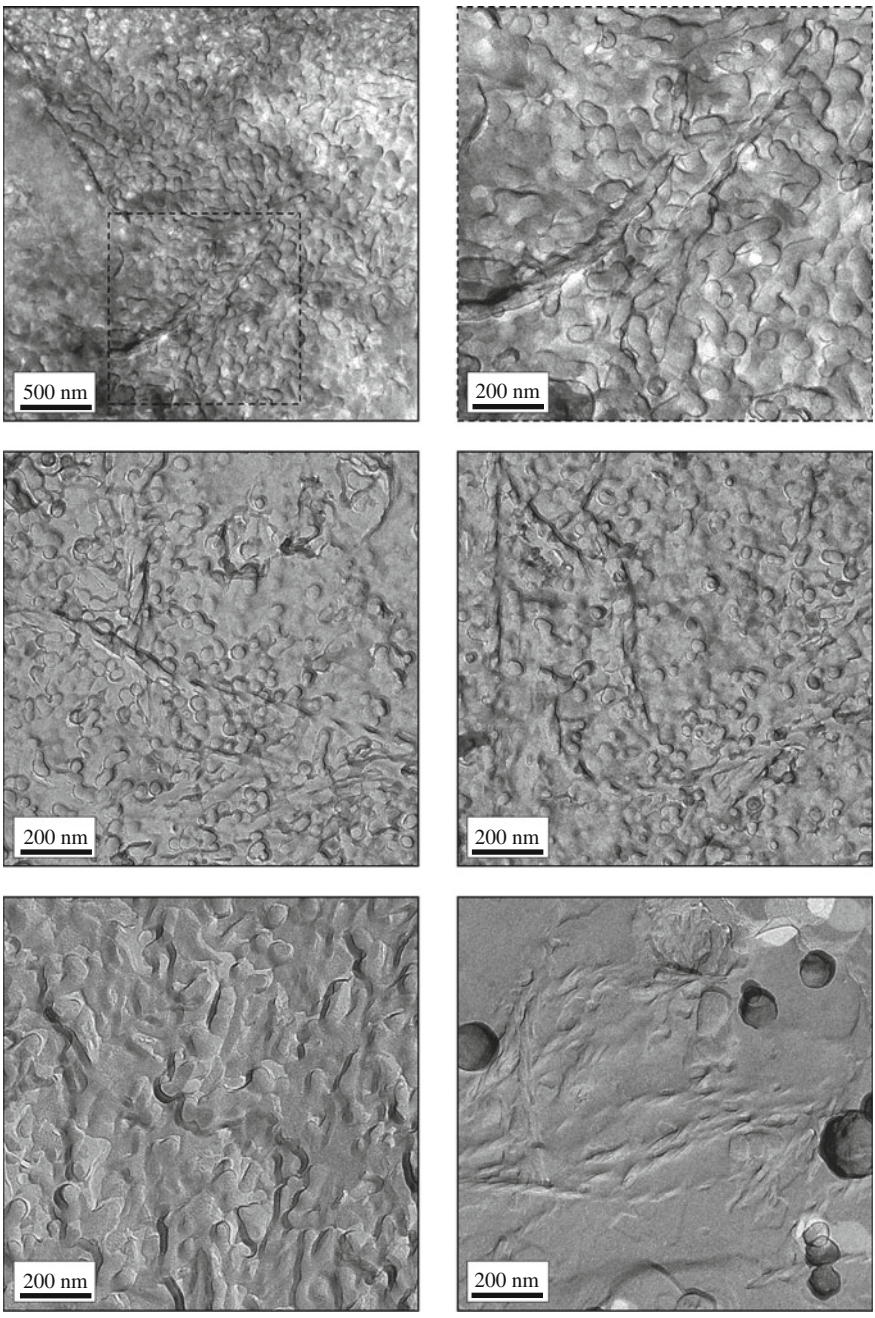


**Fig. 4.26** FFEM pictures of the gelled bicontinuous microemulsion $H_2O$–*n*-decane/12-HOA–$C_{10}E_4$ ($\phi = 0.5$, $\gamma = 0.170$) with 1.5 wt% gelator frozen from 24.0 °C (pictures taken by Natalie Preisig)

**Table 4.5** FFEM and SANS results for the gelled bicontinuous microemulsion $H_2O$–*n*-decane/12-HOA–$C_{10}E_4$ ($\phi = 0.5$, $\eta = 0.015$, FFEM: $\gamma = 0.170$, SANS: $\gamma = 0.150$), the non-gelled bicontinuous microemulsion $H_2O$–*n*-decane–$C_{10}E_4$ ($\phi = 0.5$, FFEM: $\gamma = 0.170$, SANS: $\gamma = 0.150$) and the binary gel *n*-decane/12-HOA ($\eta = 0.015$)

| | ME domain size $d$ / nm | | Gelator fiber thickness / nm | | Fiber pitch / nm |
|---|---|---|---|---|---|
| | FFEM | SANS | FFEM | SANS | FFEM |
| Non-gelled bicontinuous ME | 60 ± 10 | 13.2 ± 0.1 | – | – | – |
| Binary gel | – | – | 27 ± 6 | ~21.2 | 155 ± 35 |
| Gelled bicontinuous ME | 53 ± 14 | 12.8 ± 0.1 | 46 ± 9 | ~17.2 | 190 ± 50 |

non-gelled bicontinuous microemulsion, a too low cooling rate in the cyro-fixation step is one probable cause. An overview of the microstructural dimensions determined from the FFEM pictures and the SANS measurements is given in Table 4.5.

At this point it must be underlined that in the FFEM pictures the bicontinuous microemulsion domains are observed all around the gelator fibers where in the binary gel there is just the plain surface of the oil. Though the sizes of the imaged microstructures are unexpectedly big, this confirms that the gelled bicontinuous microemulsion can be seen as a gel in which the solvent has been replaced by a bicontinuous microemulsion or, respectively, as a bicontinuous microemulsion throughout which a gelator network is spun. The demonstration of the orthogonal self-assembly of gelled bicontinuous microemulsions is hence complemented by a visual proof.

## References


1. M. Holz, S.R. Heil, A. Sacco, Phys. Chem. Chem. Phys. **2**, 4740–4742 (2000)
2. D.M. Anderson, H. Wennerström, J. Phys. Chem. **94**, 8683–8694 (1990)
3. B. Lindman, U. Olsson, Ber. Bunsenges. Phys. Chem. **100**, 344–363 (1996)
4. J.O. Carnali, A. Ceglie, B. Lindman, K. Shinoda, Langmuir **2**, 417–423 (1986)
5. U. Olsson, K. Nagai, H. Wennerström, J. Phys. Chem. **92**, 6675–6679 (1988)
6. K. Shinoda, M. Araki, A. Sadaghiani, A. Khan, B. Lindman, J. Phys. Chem. **95**, 989–993 (1991)
7. C. Stubenrauch, *Mikroemulsionen mit Alkylglucosiden aus makroskopischer und NMR-spektroskopischer Sicht* (Shaker Verlag, Aachen, 1997)
8. B. Lindman, K. Shinoda, M. Jonströmer, A. Shinohara, J. Phys. Chem. **92**, 4702–4706 (1988)
9. C. Stubenrauch, R. Tessendorf, A. Salvati, D. Topgaard, T. Sottmann, R. Strey, I. Lynch, Langmuir **24**, 8473–8482 (2008)
10. R. Tessendorf, *Microemulsions as Templates for High Surface Area Polymers* (WiKu-Wissenschaftsverlag Dr. Stein, Köln, 2009)
11. C. Stubenrauch, G.H. Findenegg, Langmuir **14**, 6005–6012 (1998)
12. A.-J. Dianoux, G. Lander (eds.), *Neutron Data Booklet* (OCP Science Imprint, Grenoble, 2003)
13. S. Burauer, T. Sachert, T. Sottmann, R. Strey, Phys. Chem. Chem. Phys. **1**, 4299–4306 (1999)
14. T. Sottmann, R. Strey, S.-H. Chen, J. Chem. Phys. **106**, 6483–6491 (1997)

15. M. Teubner, R. Strey, J. Chem. Phys. **87**, 3195–3200 (1987)
16. P. Lindner, in *Neutrons, X-rays and Light: Scattering Methods Applied to Soft Condensed Matter*, ed. by P. Lindner, T. Zemb (Elsevier, Amsterdam, 2002), pp. 23–48
17. P. Terech, Colloid Polym. Sci. **269**, 490–500 (1991)
18. P. Terech, V. Rodriguez, J.D. Barnes, G.B. McKenna, Langmuir **10**, 3406–3418 (1994)
19. P. Terech, D. Pasquier, V. Bordas, C. Rossat, Langmuir **16**, 4485–4494 (2000)
20. G. Porod, in *Small Angle X-Ray Scattering*, ed. by O. Glatter, O. Kratky (Academic Press, New York, 1982), pp. 17–51
21. R.G. Kirste, R.C. Oberthür, in *Small Angle X-Ray Scattering*, ed. by O. Glatter, O. Kratky (Academic Press, London, 1982), pp. 387–431
22. O. Kratky, G. Porod, Rec. Trav. Chim. Pays-Bas **68**, 1106–1122 (1949)
23. M. Bergström, J.S. Pedersen, Phys. Chem. Chem. Phys. **1**, 4437–4446 (1999)
24. J.-F. Berret, in *Molecular Gels. Materials with Self-Assembled Fibrillar Networks*, ed. by R.G. Weiss, P. Terech. (Springer, Dordrecht, 2006), pp. 667–720
25. V.M. Garamus, J.S. Pedersen, H. Kawasaki, H. Maeda, Langmuir **16**, 6431–6437 (2000)
26. G. Jerke, J.S. Pedersen, S.U. Egelhaaf, P. Schurtenberger, Phys. Rev. E **56**, 5772–5788 (1997)
27. D. Madenci, A. Salonen, P. Schurtenberger, J.S. Pedersen, S.U. Egelhaaf, Phys. Chem. Chem. Phys. **13**, 3171–3178 (2011)
28. J.S. Pedersen, L. Cannavacciuolo, P. Schurtenberger, in *Giant Micelles, Properties and Applications*, ed. by R. Zana, E.W. Kaler. Surface Science Series, vol. 140 (CRC Press, Boca Raton, 2007), pp. 179–222
29. A. Stradner, O. Glatter, P. Schurtenberger, Langmuir **16**, 5354–5364 (2000)
30. J.S. Pedersen, P. Schurtenberger, Macromolecules **29**, 7602–7612 (1996)
31. P. Schurtenberger, in *Neutrons, X-rays and Light: Scattering Methods Applied to Soft Condensed Matter*, ed. by P. Lindner, T. Zemb (Elsevier, Amsterdam, 2002), pp. 259–298
32. O. Glatter, in *Neutrons, X-rays and Light: Scattering Methods Applied to Soft Condensed Matter*, ed. by P. Lindner, T. Zemb (Elsevier, Amsterdam, 2002), pp. 73–102
33. T. Kuwahara, H. Nagase, T. Endo, H. Ueda, M. Nakagaki, Chem. Lett. **62**, 435–436 (1996)
34. E. Ostuni, P. Kamaras, R.G. Weiss, Angew. Chem. Int. Ed. **35**, 1324–1326 (1996)
35. P. Terech, I. Furman, R.G. Weiss, J. Phys. Chem. **99**, 9558–9566 (1995)
36. R. Strey, J. Winkler, L. Magid, J. Phys. Chem. **95**, 7502–7507 (1991)
37. T. Sottmann, *Mikroemulsionen: Eigenschaften von internen Grenzflächen* (Cuvillier Verlag, Göttingen, 1997)
38. T. Tachibana, H. Kambar, Bull. Chem. Soc. Jpn **42**, 3422–3424 (1969)
39. T. Tamura, T. Suetake, T. Ohkubo, K. Ohbu, J. Am. Oil Chem. Soc. **71**, 857–861 (1994)
40. P. Terech, R.G. Weiss, Chem. Rev. **97**, 3133–3159 (1997)
41. T. Tachibana, T. Mori, K. Hori, Bull. Chem. Soc. Jpn **53**, 1714–1719 (1980)
42. T. Sakurai, Y. Masuda, H. Sato, A. Yamagishi, H. Kawaji, T. Atake, K. Hori, Bull. Chem. Soc. Jpn **83**, 145–150 (2010)

# Chapter 5
# Conclusions and Outlook

The thesis at hand presents a comprehensive study of the characteristic properties and microstructure of the system $H_2O$–*n*-decane/12-HOA–$C_{10}E_4$ which was confirmed to be a gelled bicontinuous microemulsion at appropriate compositions and temperatures. This had been assumed due to the fact that water, *n*-decane and the non-ionic surfactant $C_{10}E_4$ have long been known to form low viscous microemulsions [1, 2], while 12-HOA is a low molecular weight organogelator which is able to gel various organic solvents but has also shown to gel microemulsions [3–6]. Hence, the question arose as to how bicontinuous microemulsion domains and a gelator network coexist in such a gelled system. Is a bicontinuous microstructure still formed when a gelator is added to a microemulsion? And does 12-HOA self-assemble to the same kind of gelator network within a bicontinuous microemulsion as within an ordinary oil? A preliminary study [6] indicated that this is indeed the case, which led to the hypothesis that gelled bicontinuous microemulsions are so-called orthogonal self-assembled systems. Orthogonal self-assembly means that two components which individually form self-assembled structures still do this in the same way when they are combined in one system. Accordingly, the objective was to compare characteristic properties and the microstructure of two 'base systems', namely the non-gelled bicontinuous microemulsion $H_2O$–*n*-decane–$C_{10}E_4$ and the binary organogel *n*-decane/12-HOA, with those of $H_2O$–*n*-decane/12-HOA–$C_{10}E_4$ which was chosen as model system for a supposedly orthogonal self-assembled gelled bicontinuous microemulsion (Fig. 5.1, top left).

Firstly, a phase study was carried out (cp. Sect. 3.1) in which *T*-$\gamma$ diagrams of the gelled system $H_2O$–*n*-decane/12-HOA–$C_{10}E_4$ ($\phi = 0.5$) with 1.5, 2.5 and 5.0 wt% 12-HOA as well as of the non-gelled base microemulsion were measured. Note that besides the conventional visual method for phase studies using a thermostated water basin also a newly developed technique based on temperature-dependent transmission measurements with a UV/V is spectrometer [7] was employed. The results show that in the presence of the gelator the same typical phase boundaries exist as in the non-gelled microemulsion $H_2O$–*n*-decane–$C_{10}E_4$ (see Fig. 5.1, top right). This was a first evidence that the system under investigation is indeed a gelled

M. Laupheimer, *Gelled Bicontinuous Microemulsions*,
Springer Theses, DOI: 10.1007/978-3-319-07719-2_5,

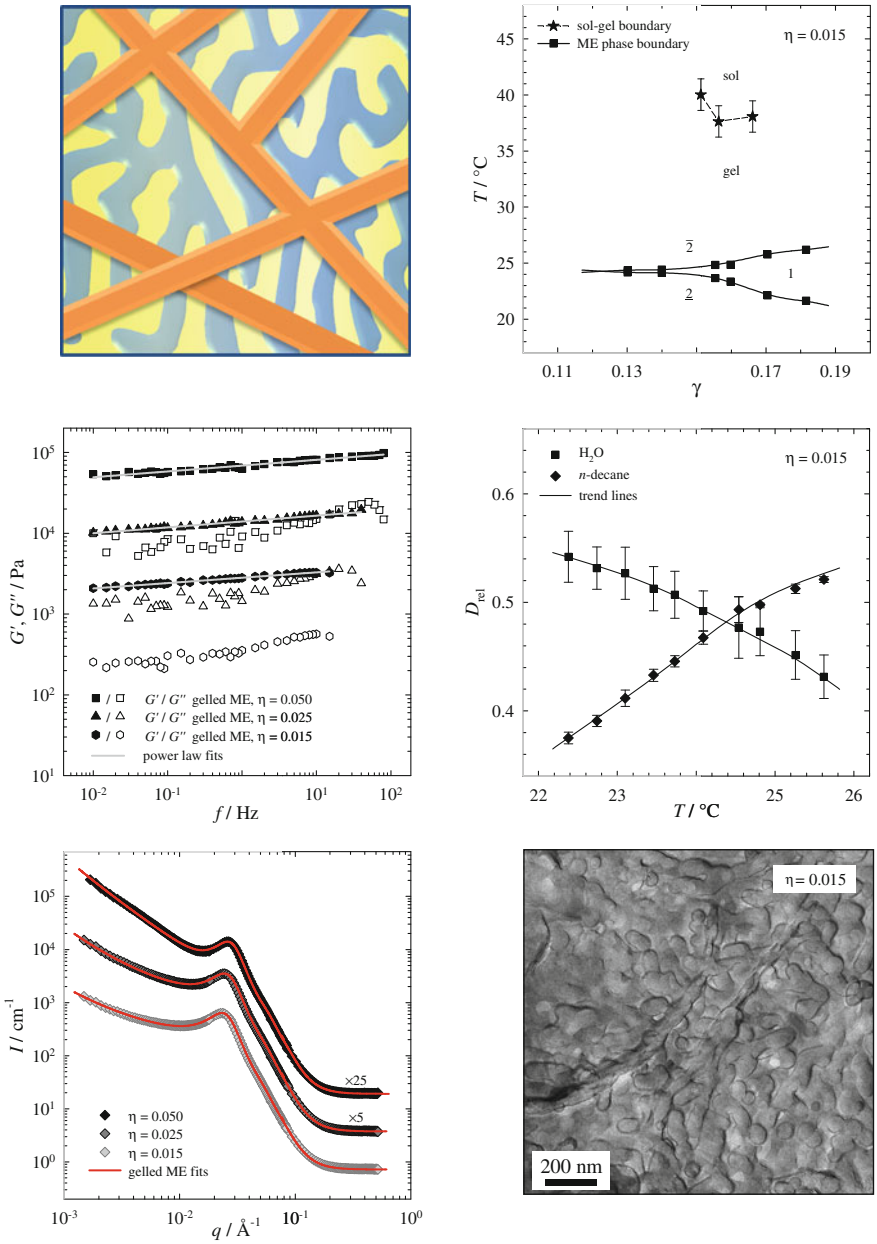


**Fig. 5.1** Schematic drawing of a gelled bicontinuous microemulsion (*top left*) and results for the investigated system $H_2O$–*n*-decane/12-HOA–$C_{10}E_4$ ($\phi = 0.5$): phase diagram[KJ] (*top right*); storage and loss moduli from oscillating shear rheometry (*middle left*); relative self-diffusion coefficients for water and oil from FT-PGSE $^1$H-NMR (*middle right*); fitted SANS curves of bulk contrast samples (*bottom left*) and a FFEM picture (by Natalie Preisig, *bottom right*)

microemulsion. Moreover, the phase boundaries allowed to specify at which temperature the microstructure is bicontinuous. Bicontinuity is found in a microemulsion at the $\widetilde{T}$ temperature which determines, together with the surfactant mass fraction $\widetilde{\gamma}$, the characteristic $\widetilde{X}$ point of the system. When 12-HOA is added to the non-gelled base microemulsion $H_2O$–*n*-decane–$C_{10}E_4$ the $\widetilde{X}$ point shifts from $\widetilde{T} = 30.2$ °C and $\widetilde{\gamma} = 0.135$ down to $\widetilde{T}$ temperatures of 24.3, 23.6 and 23.8 °C with 1.5, 2.5 and 5.0 wt% gelator as well as to slightly higher efficiencies $\widetilde{\gamma}$ of 0.123, 0.121 and 0.116, respectively. In the same time a liquid crystalline phase extends further and further to the $\widetilde{X}$ point. An explanation for these observations is that the gelator 12-HOA is a surface active molecule which can adsorb at the water–oil interface of a microemulsion and thus changes the properties of the surfactant layer. The shift of the microemulsion phase boundaries was the first indication that a certain part of the component 12-HOA in the system $H_2O$–*n*-decane/12-HOA–$C_{10}E_4$ is not involved in forming gelator fibers but resides monomerically in the microemulsion. The results of the subsequently employed techniques corroborated this finding repeatedly.

Secondly, the focus was on the gel phase behaviour (cp. Sect. 3.2), i.e. on the sol-gel transition temperatures which were determined with DSC and with temperature-dependent oscillating shear rheometry measurements. With both methods it was found that for equal gelator mass fractions the sol-gel transition temperature of the gelled microemulsion $H_2O$–*n*-decane/12-HOA–$C_{10}E_4$ is about 20 K below that of the binary gel *n*-decane/12-HOA. This reflects that the gelator network is weaker when the surrounding solvent is a microemulsion instead of pure *n*-decane. Thermodynamical parameters like the sol-gel transition enthalpies obtained from the DSC measurements support this conclusion, which is furthermore consistent with the assumption of a higher concentration of gelator monomers in the microemulsion than in *n*-decane. It is natural that 12-HOA molecules which reside in the solvent of the gel lack for the formation and stabilization of the gelator network. The observed weakening effect is thus not surprising. Fundamental changes of the gel behaviour upon the "exchange of the solvent", however, were not encountered in the described measurements, nor in any of the subsequently carried out investigations. Note that the decreased sol-gel transition temperatures still lie more than 10 K above the upper microemulsion phase boundary which was shown for $H_2O$–*n*-decane/12-HOA–$C_{10}E_4$ with 1.5 (see Fig. 5.1, top right), 2.5 and 5.0 wt% 12-HOA. Hence, when those systems were further studied as gelled bicontinuous microemulsions in their one-phase state proper gelation was assured.

Thirdly, oscillating shear rheometry measurements were carried out (cp. Sect. 3.3) to determine the storage and the loss modulus of the gelled bicontinuous microemulsion and the binary gel. The shear stress-dependence of the moduli allowed to evaluate the linear viscoelastic (LVE) range of the different systems. As expected for a stronger gelator network, the LVE range extends to higher shear stresses for the binary gel than for the gelled bicontinuous microemulsion. However, the differences between the two systems decrease with increasing gelator concentration. Subsequently, the storage and the loss modulus were investigated as a function of the shear frequency for

which shear stresses within the respective LVE ranges were applied. The results show that both moduli are hardly frequency-dependent, neither in the gelled bicontinuous microemulsion $H_2O$–*n*-decane/12-HOA–$C_{10}E_4$ (see Fig. 5.1, middle left) nor in the binary gel *n*-decane/12-HOA with 1.5, 2.5 or 5.0 wt% gelator. This finding attests that gelled bicontinuous microemulsions are strong, solid-like gels, just like their base system.

Fourthly, the relative self-diffusion coefficients of water and *n*-decane were determined via FT-PGSE $^1$H-NMR measurements (cp. Sect. 4.1) at different temperatures within the one-phase region of a gelled microemulsion with 1.5 wt% 12-HOA (see Fig. 5.1, middle right). It was shown that the water in the system self-diffuses the slower the higher the temperature while the opposite is true for *n*-decane. This reflects the gradual change of the microemulsion's microstructure, i.e. of the curvature of the surfactant layer which bends around oil at low and around water at high temperatures. At an intermediate temperature the relative self-diffusion coefficients of water and *n*-decane are equal which proves that the gelled microemulsion $H_2O$–*n*-decane/12-HOA–$C_{10}E_4$ is indeed bicontinuous in the middle of its one-phase region. Exactly the same trends were observed for the non-gelled base microemulsion $H_2O$–*n*-decane–$C_{10}E_4$. Hence, the properties of the latter—just like those of the binary gel—are not changed significantly in the gelled bicontinuous microemulsion.

Fifthly, small angle neutron scattering (SANS) experiments were carried out (cp. Sect. 4.2) which demonstrate the coexistence of the bicontinuous microemulsion domains and a gelator network in gelled bicontinuous microemulsions. The system $H_2O$–*n*-decane/12-HOA–$C_{10}E_4$ was investigated with 1.5, 2.5 and 5.0 wt% 12-HOA in bulk as well as in film contrast using SANS and V-SANS measurements so that scattering data in a $q$ range between $5.2 \times 10^{-1}$ and $1.2 \times 10^{-4}$ Å$^{-1}$ were obtained. The data clearly show features of both the microemulsion domains and the gelator network. While the V-SANS data was excluded from a quantitative data analysis, full fits of the data collected in the SANS measurements at a neutron wavelength of 6 Å were accomplished for the gelled bicontinuous microemulsions in bulk contrast (see Fig. 5.1, bottom left). For these fits the scattering function of bulk contrast bicontinuous microemulsions according to Teubner and Strey was added to a scattering function which was also used to interpret the scattering data of the binary gel. The gelator network was treated for the calculation of this scattering function as consisting of cylindrical rods with a circular cross-section and lamellar nodes. While the rods model the "free" gelator fibers in the network the nodes are pictured as stacked layers of parallelly arranged fibers which constitute the network junction zones. Since the fitted SANS data does not comprise the Guinier regime in the low $q$ range neither the gelator fiber length nor the node area or the absolute numbers of these scatterers were extractable. Therefore the length fraction of "free" gelator fibers and the mole fraction of monomerically dissolved gelator were introduced as meaningful fit parameters instead. The fit results are perfectly in line with the conclusions from the previous studies. They confirm that in a gelled bicontinuous microemulsion the concentration of 12-HOA molecules which reside in the solvent instead of forming gelator fibers is considerably higher than within a

binary gel. The associated weakening of the gelator network is, particularly for low gelator concentrations, reflected in thinner gelator fibers in the gelled bicontinuous microemulsions than in the binary gels. At high gelator concentrations one recognizes that, moreover, in the gelled bicontinuous microemulsions smaller length fractions of the fibers are involved in stabilizing nodes than is the case in the binary gels. As regards the bicontinuous microemulsion a decrease of the domain size and a slight reduction of the order of the microstructure were found upon gelation.

Finally, FFEM pictures were taken (cp. Sect. 4.3) which image coexisting bicontinuous microemulsion domains and twisted gelator fibers within the system $H_2O$–*n*-decane/12-HOA–$C_{10}E_4$ with 1.5 wt% gelator (see Fig. 5.1, bottom right). The measured microemulsion domain size and diameter of the gelator fibers are admittedly distinctly bigger than what was expected according to the SANS study. However, the FFEM pictures still provide a visual proof for the orthogonal self-assembly of gelled bicontinuous microemulsions.

In summary, the results presented in this thesis show in striking consistence that in the system $H_2O$–*n*-decane/12-HOA–$C_{10}E_4$ the gelator molecules form a network which is surrounded by a bicontinuous microemulsion. Both microstructures self-assemble in parallel and do, in principle, not influence each other. The observed deviations between the gelled bicontinuous microemulsion $H_2O$–*n*-decane/12-HOA–$C_{10}E_4$ and its base systems, the non-gelled bicontinuous microemulsion $H_2O$–*n*-decane–$C_{10}E_4$ and the binary gel *n*-decane/12-HOA, are due to the amphiphilic character of 12-HOA. The latter causes gelator molecules to adsorb at the water–oil interface in the presence of the microemulsion instead of forming gelator fibers. Hence, it is strictly speaking a bicontinuous microemulsion consisting of water, *n*-decane, $C_{10}E_4$ and the co-surfactant 12-HOA which coexists with the gelator network, or constitutes the solvent in the 12-HOA gel, respectively. One could thus, following to the used nomenclature, also name the system "{$H_2O$–*n*-decane–$C_{10}E_4$/12-HOA}/12-HOA". In any case, the fact that the bicontinuous microemulsion and the gelator network form simultaneously and coexist with each other proves that gelled bicontinuous microemulsions are orthogonal self-assembled systems. These were in this regard for the first time studied in the work at hand using a set of complementary physico-chemical methods.

The studies carried out for this thesis raised several points which deserve further investigation. For example, the phase studies could be refined by examining more samples in a wider composition range and with a particular focus on the liquid crystalline region. With regard to the rheological properties of the gelled bicontinuous microemulsions it would be interesting to compare the results obtained with oscillating shear rheometry to values from a non-invasive microrheological method, namely diffusing wave spectroscopy (DWS). The latter is a dynamic light scattering technique which allows determining the storage and the loss modulus in a very large frequency range without mechanical interaction with the sample [8]. Furthermore, static small angle light scattering (SALS) measurements could be used to reliably extend the scattering data collected in the SANS

study to lower $q$ values. However, other than in SANS, the scattering contrast cannot be adjusted by selective deuteration in SALS. Hence, an alternative approach is to repeat the SANS measurements at wide sample detector distances with a high neutron wavelength taking precautions against multiple scattering. Promising possibilities are to reduce the sample thickness, which, however, complicates the sample preparation, or to attenuate the scattering contrast by a higher deuteration of the technically non-deuterated solvent(s) in the gelled bicontinuous microemulsion. In any case rather long measuring times will be necessary. To improve the accuracy of the fit parameters in the quantitative analysis of the scattering data it would be useful to work with automatic fitting algorithms. Concerning the FFEM pictures it is advisable to explore superior techniques for the replica preparation of gelled bicontinuous microemulsions. In particular faster sample freezing and better fractioning have promise to image the domains of the bicontinuous microemulsion in their unaltered, original size and show more clearly the coexisting structures in the gelled bicontinuous microemulsion.

Besides refining the investigation of the model system $H_2O$–*n*-decane/12-HOA–$C_{10}E_4$ it is also expedient to alter the latter and transfer the gained knowledge. Aiming at a gelled bicontinuous microemulsion in which the gelator network is not weakened and the microstructure of the microemulsion not changed in comparison to the respective base systems it is advisable to seek after a gelator which is not amphiphilic and hence does not partition between the microemulsion and the gelator network. However, finding a gelator suitable for a certain solvent, like a microemulsion, is not an easy task since a gel is only formed when a sensitive balance between solubility and insolubility of the gelator in the liquid is given [9, 10]. Another approach might thus be to regard a non-gelled bicontinuous microemulsion saturated with gelator monomers as one of the base systems. With a view to potential applications of gelled bicontinuous microemulsions the choice of the used substances is particularly important. Since one crucial criterion is economy the first step would be to use a technical-grade surfactant instead of a pure one. Moreover, it can be inevitable to restrict the composition of the gelled bicontinuous microemulsion to hazard-free compounds if it is to be used in a cosmetical or pharmaceutical product. For example, for dermal or transdermal drug delivery it is desirable to administer microemulsions in a high viscous instead of in liquid form [11]. Hence in this context it is definitely beneficial that this work demonstrated that gelled bicontinuous microemulsions retain their unique properties albeit gelation.

## References

1. S. Burauer, T. Sachert, T. Sottmann, R. Strey, Phys. Chem. Chem. Phys. **1**, 4299–4306 (1999)
2. C. Stubenrauch, C. Frank, R. Strey, D. Burgemeister, C. Schmidt, Langmuir **18**, 5027–5030 (2002)
3. C. Stubenrauch, R. Tessendorf, R. Strey, I. Lynch, K.A. Dawson, Langmuir **23**, 7730–7737 (2007)

4. C. Stubenrauch, R. Tessendorf, A. Salvati, D. Topgaard, T. Sottmann, R. Strey, I. Lynch, Langmuir **24**, 8473–8482 (2008)
5. M. Magno, R. Tessendorf, B. Medronho, M. da Graça Martins Miguel, C. Stubenrauch, Soft Matter **5**, 4763–4772 (2009)
6. R. Tessendorf, *Microemulsions as Templates for High Surface Area Polymers* (WiKu-Wissenschaftsverlag Dr. Stein, Köln, 2009)
7. M. Laupheimer, C. Stubenrauch, Tenside Surf. Det. **51**, 17–25 (2014)
8. T.G. Mason, H. Gang, D.A. Weitz, J. Opt. Soc. Am. A **14**, 139–149 (1997)
9. M. George, R.G. Weiss, in *Molecular Gels. Materials with Self-Assembled Fibrillar Networks*, ed. by R.G. Weiss, P. Terech (Springer, Dordrecht, 2006), pp. 449–551
10. G. Zhu, J.S. Dordick, Chem. Mat. **18**, 5988–5995 (2006)
11. S. Heuschkel, A. Goebel, R.H.H. Neubert, J. Pharm. Sci. **97**, 603–631 (2008)

# Chapter 6
# Experimental Methods

## 6.1 Chemicals

All chemicals listed in Table 6.1 were used as received.

## 6.2 Sample Preparation

Three different kinds of samples were prepared for this work, namely non-gelled microemulsions of the type $H_2O$–*n*-decane–$C_{10}E_4$, gelled microemulsions of the type $H_2O$–*n*-decane/12-HOA–$C_{10}E_4$ and binary organogels *n*-decane/12-HOA. All chemicals besides the bidistilled water were purchased and used as received (cp. Table 6.1). The samples were weighted into glass vessels suitable for the respective experiment. Note that all microemulsions were prepared with equal volumes of water and *n*-decane, i.e. $\phi = 0.5$, which was ensured by using Eppendorf pipettes for transferring the liquids.

In general, all components of a sample were added to the vessel which was then tightly sealed. Mixing the components in the non-gelled microemulsions was accomplish by shaking the vessels. However, when a sample contained the gelator 12-HOA, which was added as solid, the latter first had to be molten. For this purpose the vessel was placed in a water bath at about 70 °C for several minutes. Subsequently, all components were mixed by shaking the vessel before the sample was put into an ice bath for gelation. This procedure was quite simple for the binary gels; however, preparing a homogeneously gelled microemulsion was more intricate. Since the sol-gel transition of all studied $H_2O$–*n*-decane/12-HOA–$C_{10}E_4$ samples takes place within the two-phase region $\overline{2}$ (cp. Sects. 3.1 and 3.2) it was important to disperse the excess water phase throughout the whole sample volume before the systems gelified. For this purpose the heated vessel with a microemulsion in the two-phase sol state was shaken and rotated until a uniform white emulsion was obtained. Then the sample had to be quickly transferred into the ice bath for gelation. Afterwards a microscopy lamp (*Gerhardt* Belani) was used to

M. Laupheimer, *Gelled Bicontinuous Microemulsions*,
Springer Theses, DOI: 10.1007/978-3-319-07719-2_6,

**Table 6.1** Used chemicals

| Name | Abbreviation | Supplier | Purity |
|---|---|---|---|
| Water | $H_2O$ | | Bidistilled |
| Deuterium oxide | $D_2O$ | Aldrich | 99.98 ± 0.01 atom% D |
| *n*-decane | | Aldrich | 99 + % |
| d22-*n*-decane | | Isotec | 99 atom% D |
| Tetraethylene glycol monodecyl ether | $C_{10}E_4$ | Fluka | ≥97.0 % |
| | | Aldrich | ~97 % |
| 12-Hydroxyoctadecanoic acid | 12-HOA | Aldrich | 99 % |
| Cyclohexane | | Merck | p.a. |

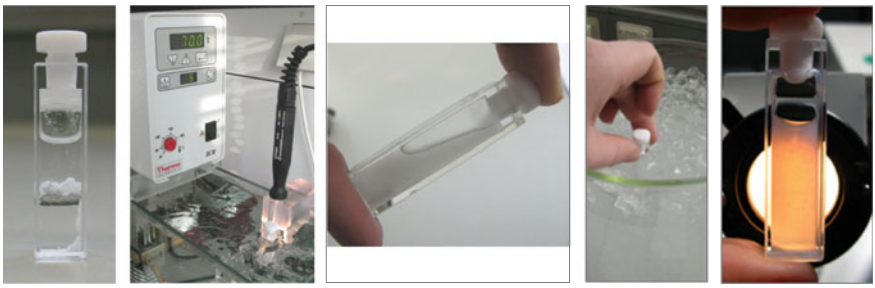

**Fig. 6.1** Preparation of a gelled microemulsion sample. From *left* to *right* cuvette with all components; heating of the sample in the water bath; mixing the sample in the sol state; gelling the sample in the ice bath; check of the gelled sample's homogeneity

check the homogeneity of the gelled microemulsion. When the gelling procedure had been successful one observed an evenly turbid sample without considerably darker or lighter spots; otherwise the gelling procedure was repeated (Fig. 6.1).

## 6.3 Visual Phase Studies

In order to visually determine the phase transition temperatures of the microemulsion samples they had to be inspected at different temperatures. The non-gelled microemulsions were prepared in scaled test tubes for this purpose, while cuvettes with a sample layer thickness of 1 mm (*Hellma* 404.000-QX) were used for the gelled microemulsions. By means of home-built sample holders the vessels were fixed in a water-filled glass basin, which was equipped with a DC30 thermostat from *Thermo Scientific*. The latter allowed to adjust the water temperature in steps of ±0.1 K, however, a thermometer with an accuracy of ±0.01 K (*Greisinger* GMH 375 with probe GTF 401) was used for temperature control close to the sample holder. To be able to stir the non-gelled microemulsions a magnetic stirrer (*Heidolph* MR Hei-Mix L) was placed under the basin and the test

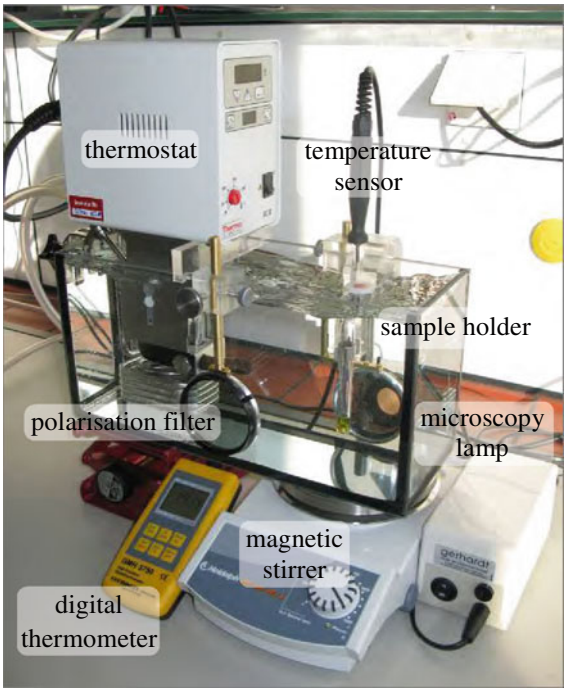


**Fig. 6.2** Experimental set-up for visually determining microemulsion phase boundaries

tubes were equipped with magnetic stirring bars. Thus turbid emulsions were generated when a sample was phase-separated which is, in fact, the criterion to differentiate between a two- (or more-) phase and the one-phase state. To facilitate the turbidity assessment a microscopy lamp (*Gerhardt* Belani) illuminated the samples from the back. Additionally, two crossed polarising filters (*hama* Pol circular) could be placed in the front and at the back of the basin to identify anisotropic (e.g. liquid crystalline) phases. A photograph of the experimental set-up is shown in Fig. 6.2.

An initial fast temperature scan helped to roughly locate the phase boundaries of a microemulsion. Subsequently, the lower ($T_{\underline{2}-1}$) and the upper ($T_{1-\overline{2}}$) phase transition temperature were precisely identified by crossing them with temperature steps of 0.1 K in the direction from the two-phase to the one-phase region. This direction was important to avoid the nucleation process initiating the phase separation when one moves from the one-phase to the two-phase region, which can be kinetically delayed and cause an inaccurate determination of the phase transition temperature. The non-gelled microemulsions were stirred during the measurement and identified as one phase when they were clear. Any slight turbidity coming from emulsification of the phase-separated sample indicated the two-phase state. The gelled microemulsions, in contrast, were not completely clear in the one-phase state but slightly turbid due to the presence of the gelator network. In fact, the turbidity increased with increasing gelator content. However, fortunately a significantly stronger turbidity was observed for gelled two-phase compared to gelled

one-phase microemulsions. Stirring the gelled samples was neither possible nor necessary because the high viscosity effectively impeded macroscopic phase separation. After each temperature step the sample was given enough time to equilibrate, which took longer for the gelled than for the non-gelled microemulsions. The phase transition temperatures were identified with a precision of $\pm 0.2$ K. Note that most of the measurements of the gelled microemulsion samples were carried out by Kristina Jovic during her bachelor thesis and her 'Hiwi' employment under my supervision, which is indicated by "KJ" where the respective data is shown. Once several samples with different surfactant mass fractions $\gamma$ had been investigated, the data points were plotted in a $T$-$\gamma$ diagram and the microemulsion phase boundaries were interpolated. Furthermore, an extrapolation to the characteristic $\widetilde{X}$ point was possible if the $\gamma$ values of the studied mixtures were close to $\widetilde{\gamma}$, i.e. when the difference between the determined transition temperatures was small.

## 6.4 Transmission-Based Phase Studies

The transmission-based determination of phase boundaries follows the same principle as the conventional visual method described in the previous Sect. 6.3. Two-phase samples form turbid emulsions while one-phase samples are clear or, in the case of gelled microemulsions, at least significantly clearer. The crucial question is how to detect and assess the turbidity of a sample. In the visual method this happens with the eye of the experimenter. However, visual turbidity perception is only qualitative. Another experimenter might therefore assess a sample differently and identify slightly shifted phase transition temperatures, especially under changed lighting conditions. To eliminate such ambiguities it is necessary to quantify the sample turbidity for which a specific method was developed in the course of this thesis. The idea is to measure the transmission of a microemulsion at different temperatures by means of a UV/Vis spectrometer and to deduce from the data whether the sample consists of one phase or of two phases. In general, high transmission values correspond to the clear one-phase state while low transmission indicates the turbid two-phase situation. Of course, 'high' and 'low' are not judged based on absolute transmission values but in comparison with each other. Note that the developed transmission method is described in detail in a paper entitled "Transmission measurements as tool to study phase transitions of liquid mixtures" in the peer-reviewed journal *Tenside Surfactants Detergents* [1]. Here just the key information is given. The transmission method was used in the work at hand to determine phase transition temperatures of a gelled bicontinuous microemulsion with 1.5 wt% gelator. The respective raw data was collected by Kristina Jovic during her bachelor thesis and her 'Hiwi' employment under my supervision which is indicated by "KJ" where the results are shown.

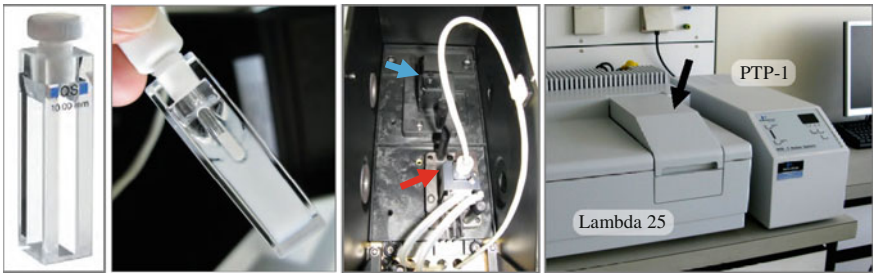


**Fig. 6.3** Equipment for the transmission-based phase studies. From *left* to *right Hellma* 114F-QS cuvette, cuvette with gelled microemulsion sample and plugged-in temperature sensor; sample in the measuring cell (*red arrow*), the reference position in the back is empty (*blue arrow*); UV/Vis spectrometer Lambda 25 and PTP-1 Peltier system from *PerkinElmer*, the arrow points at the measuring cell.[1]

### 6.4.1 Measurement Set-Up

The transmission measurements were carried out with a Lambda 25 UV/Vis spectrometer with the accessory PTP-1 Peltier system from *PerkinElmer*. The latter allowed to thermostat the cell holder in steps of ±0.1 K. However, the actual sample temperature was measured by a joined temperature sensor (accuracy ±0.1 K) which was put through the opening of the cuvette right into the sample. To fit the measuring cell the cuvettes had to have outer dimensions of 12.5 × 12.5 $mm^2$. Hence, *Hellma* 114F-QS cuvettes, which feature sample layer thicknesses of 4 mm in one and of 10 mm in the other direction, were used for the gelled microemulsion. All the equipment is shown in Fig. 6.3. To control the measurements a computer with the *PerkinElmer* software UVWinLab as well as a customized version of TempLab was used.

### 6.4.2 Measurement Routine

Before any measurement was carried out the transmission was set to 100 % by the "Autozero" function for which the cell holders in both the measuring and the reference position were empty. There was no need to calibrate the system to any specific reference sample because the focus was on relative rather than on absolute transmission values. Thus the reference position stayed unoccupied during all transmission measurements. For the determination of an appropriate wavelength for carrying out the phase studies spectra of the microemulsion were recorded with

[1] (http://www.hellma-analytics.com/kuevetten/136/de/pg_id,41$g_id,22$item_id,116/fluoreszenzmessungen.html#116,14.03.2013)

UVWinLab. For this purpose the temperature was manually set to appropriate values and the whole accessible wavelength range, i.e. $\lambda = 190$–$1100$ nm, was scanned.

Subsequently, TempLab was used to run transmission measurements with an automatic step-wise temperature variation. The wavelength was held constant at the previously determined value in this measurements and the size of the temperature steps $\Delta T$ and their length $\Delta t$ were set to values of $\Delta T = 0.1$ K and $\Delta t = 20$ min, respectively. Furthermore, a start and an end temperature above and below the phase boundary in question were defined. Note that the lower phase transition temperature was studied with increasing temperature, i.e. with steps of $\Delta T = +0.1$ K, while $\Delta T = -0.1$ K was used for the upper phase boundary in order to perform two-phase to one-phase transitions, respectively. In the course of a measurement the software recorded every 20 s the current time, the transmission and the temperature of the sample.

### 6.4.3 Wavelength and Sample Layer Thickness

To be able to identify the number of phases of a microemulsion based on its transmission it is necessary that the transmission differs significantly when the sample is in the one-phase and in the two-phase state. As the transmission depends on the wavelength as well as on the sample layer thickness $d_{\text{sample}}$, spectra of a gelled microemulsion ($\phi = 0.5$, $\eta = 0.015$, $\gamma = 0.144$) were recorded in the two-phase state $\underline{2}$ ($d_{\text{sample}} = 4$ mm), in the one-phase state ($d_{\text{sample}} = 4$ and 10 mm) and in the two-phase state $\overline{2}$ ($d_{\text{sample}} = 4$ mm), i.e. at 23.5, 25.0 and 26.5 °C, respectively (Fig. 6.4).

One sees in Fig. 6.4 (right) that the transmission is close to 0 % over the whole wavelength range $\lambda = 190$–$1100$ nm when the microemulsion is in the two-phase state. When it is in the one-phase state, in contrast, the transmission increases with increasing wavelength. Therefore the biggest transmission difference between the two situations is reached at $\lambda = 1100$ nm. However, as this is at the very edge of the spectrometer's capabilities, $\lambda = 1050$ nm was used for the subsequent phase studies. Furthermore, the sample layer thickness $d_{\text{sample}}$ had to be considered in order to maximize the transmission difference and thus facilitate the identification of a sample's state based on the measured transmission. As the transmission in the one-phase state is significantly lower with $d_{\text{sample}} = 10$ mm than with $d_{\text{sample}} = 4$ mm (see Fig. 6.4, right) the phase studies were carried out with a sample layer thickness of $d_{\text{sample}} = 4$ mm.

### 6.4.4 Data Evaluation

For data evaluation all transmission values and sample temperatures recorded during a measurement were firstly plotted versus the time. Figure 6.5 (left) shows the time slot of such a plot in which the lower phase transition temperature of a

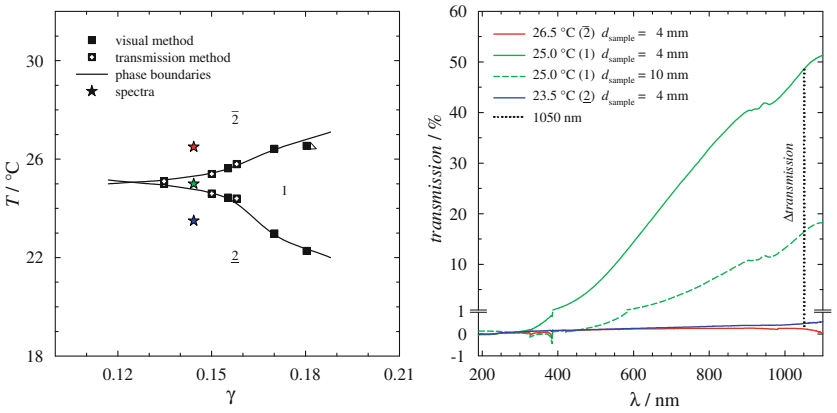


**Fig. 6.4** (*Left*) $T$-$\gamma$ phase diagram of the gelled microemulsion $H_2O$–*n*-decane/12-HOA–$C_{10}E_4$ ($\phi = 0.5$, $\eta = 0.015$, Table A.4) with 'the second surfactant' (cp. Fig. 3.5). The phase boundaries were measured with the visual (*plain symbols*) and the transmission [1] (*symbols with white crosses*[KJ]) method. The stars mark at which temperatures (*same colors*) the spectra (*right*, taken from [1], © Carl Hanser Verlag, München, and modified) of a sample with $\gamma = 0.144$ were recorded. The sample layer thicknesses were $d_{sample} = 4$ mm (*solid lines*) and $d_{sample} = 10$ mm (*dashed line*). The wavelength $\lambda = 1050$ nm (*dotted line*) where the transmission difference was nearly maximum was chosen for the phase studies

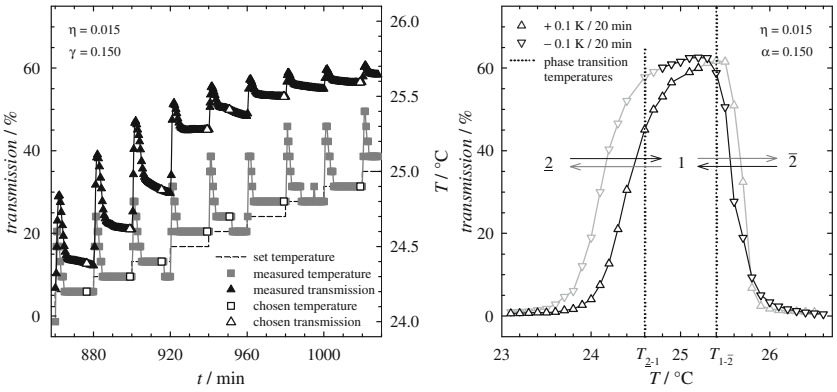


**Fig. 6.5** Transmission data ($\gamma = 1050$, $d_{sample} = 4$ mm) of the gelled microemulsion $H_2O$–*n*-decane/12-HOA–$C_{10}E_4$ ($\phi = 0.5$, $\eta = 0.015$, $\gamma = 0.150$). (*Left*) Transmission (*triangles*) and temperature (*squares*) versus time at temperatures around the lower phase boundary; heating steps are +0.1 K every 20 min (*dashed line*). Plotting the equilibrium transmission values versus the corresponding temperatures (*open symbols*) one obtains the transmission versus temperature profile (*right*). Results for cooling steps (*inverse triangles*) are shown for comparison. $T_{\underline{2}\text{-}1} = 24.6$ °C and $T_{1-\overline{2}} = 25.4$ °C (*dotted lines*) were identified as phase transition temperatures (cp. Fig. 3.5 and Fig. 6.4, *left*; taken from [1], © Carl Hanser Verlag, München)

gelled microemulsion ($\phi = 0.5$, $\gamma = 0.150$, $\eta = 0.015$) is passed. The temperature was increased during the measurement by $\Delta T = +0.1$ K every 20 min but the actual sample temperature did not exactly follow these settings. An overheating effect was observed which caused the temperature to first rise up by about 0.6 K instead of only 0.1 K, after which it took some time until a constant temperature was reached. Note that some temperatures were skipped, *e.g.* $T = 24.5$ °C at 920 min $\lesssim t \lesssim$ 940 min in Fig. 6.5 (left) for which no data points were recorded. To evaluate which transmission the sample possesses at the different temperatures time intervals of constant temperature were identified. During these time intervals the sample equilibrated and, ideally, a constant transmission value was reached before the temperature changed.

The equilibrium transmission values were identified and subsequently plotted versus the respective temperatures to yield the transmission versus temperature profile of the sample (Fig. 6.5, right). This profile shows, as expected, high transmission values at medium temperatures for the clear one-phase sample while the transmission is close to 0 % at low and high temperatures where the microemulsion is in its two-phase state. Interestingly there is no flat transmission plateau in the gelled microemulsion's one-phase region as one expects from theory and which was observed for non-gelled microemulsions [1]. The transmission of the gelled microemulsion rather increases with increasing temperature in this range, which is seen both for measurements with heating and with cooling steps (see Fig. 6.5, right) as well as with prolonged temperature steps of up to $\Delta t = 52$ min [1]. Hence, it was not possible to identify the gelled microemulsions' phase transition temperatures in the same way as for non-gelled microemulsions where one assigns $T_{\underline{2}-1}$ and $T_{1-\overline{2}}$ to the sharp kinks at the edges of the one-phase plateau [1]. Instead, the plot of the 'raw data' versus temperature (e.g. Fig. 6.5, left) was used to identify the phase boundaries of gelled microemulsions. The one-phase region was assumed to be reached at the first temperature where the transmission ($\gg 0$ %) does not constantly change during the equilibration time $\Delta t$ but quickly becomes constant. For the microemulsion sample with $\eta = 0.015$ and $\gamma = 0.150$ this is the case at 24.6 °C (see Fig. 6.5) which is thus the lower phase transition temperature $T_{\underline{2}-1}$ (cp. Figs. 3.5 and 6.4, left). Note that even if both the lower and the upper phase boundary were crossed in the course of a transmission measurement, it was exclusively the two-phase to one-phase transition which was evaluated to obtain the respective phase transition temperature because of the reasons discussed in Sect. 6.3. The validity of the transmission method was proved by measuring with it the phase boundaries of non-gelled microemulsions and comparing the results to those of a conventional visual phase study [1]. Almost the same values were obtained with both methods. Furthermore, it is shown in this work that also for a gelled microemulsion the phase transition temperatures measured with the transmission and with the visual method are in very good agreement (see Figs. 3.5 and 6.4, left). The phase transition temperatures determined with the transmission method have an accuracy of $\pm 0.2$ K, just as those determined visually.

## 6.5 Differential Scanning Calorimetry

Differential scanning calorimetry (DSC) is a thermal characterisation technique which was used to determine the sol-gel transition temperatures $T_{\text{sol-gel}}$ and the sol-gel transition enthalpies $\Delta_{\text{sol-gel}}H$ of the binary gel and the gelled microemulsion with different compositions. The measurements were carried out by Kristina Jovic during her bachelor thesis and her 'Hiwi' employment under my supervision (which is indicated by "KJ" where the respective data is shown) on a differential scanning calorimeter DSC 4000 from *PerkinElmer* (Fig. 6.6, left). The latter is a single-furnace instrument working on the principle of heat flux. It measures and compares the heat flow rates to a sample and an empty reference cell while the temperature of both cells is changed simultaneously. Sealed aluminium pans (B016-9321 from *PerkinElmer*) were used as cells. They were filled with 25–37 mg of sample which was weighted in on a KC BA 100 balance from *Sartorius* with a precision of ±0.001 mg. (About 0.4 g of the samples was prepared beforehand in small glass vessels as described in Sect. 6.2.) The pans were placed in the furnace of the instrument (Fig. 6.6, right) through which nitrogen flowed as purge gas with a flow rate of 20.0 ml $\text{min}^{-1}$.

The applied temperature program consisted of three segments. Firstly, the temperature was held constant at 10 °C for 1 min. Secondly, the temperature was ramped up with a heating rate of 1.00 K $\text{min}^{-1}$ from 10 to 80 °C where it was, thirdly, held constant again for 1 min. Note that exclusively heating ramps but no heating-cooling cycles were performed for the reasons explained in Sect. 3.2. All measurements were controlled via the computer software Pyris™ from *PerkinElmer* which was also used for the data analysis. The temperature of the peak maximum in a recorded heat flow versus temperature curve was taken as the sol-gel transition temperature (according to Ref. [ 2–4]) while the area under the peak yielded the sol-gel transition enthalpy (cp. Fig. 3.12). The errors for replicating the measurements were $\Delta T_{\text{sol-gel}} = \pm 1.4$ K and $\Delta(\Delta_{\text{sol-gel}}H) = \pm 0.1$ J $\text{g}^{-1}$.

Note that the calorimeter was calibrated to the melting points of indium (156.60 °C) and zinc (419.47 °C). However, it was confirmed that this calibration was also valid in the temperature range of the sol-gel transitions of the investigated 12-HOA gels by measuring the melting point of cyclohexane. Indeed, the deviation of the determined cyclohexane melting temperature (6.64 °C) to the literature value (6.72 °C [5]) is much smaller than $\Delta T_{\text{sol-gel}}$.

## 6.6 Oscillating Shear Rheometry

Oscillating shear rheometry experiments were carried out in this thesis to study the viscoelastic properties of gelled bicontinuous microemulsions and binary gels with different gelator concentrations and, furthermore, to investigate the sol-gel transition temperatures of the gelled systems. For these purposes the storage modulus

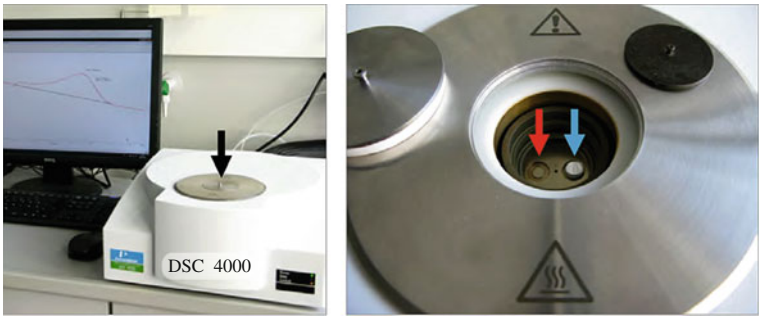


**Fig. 6.6** Differential scanning calorimeter DSC 4000 from *PerkinElmer* (*left*) and its open furnace (*black arrow*) with an aluminium pan on the reference position (*blue arrow*) besides the unoccupied measuring position (*red arrow*) (*right*)

$G'$ and the loss modulus $G''$ were determined with a stress-controlled shear rheometer, namely a StressTech rheometer from *Rheologica Instruments* (a Physica MCR 501 rheometer from *Anton Paar* was used to measure the sol-gel transition temperatures of the binary gel with 2.5 and 5.0 wt% gelator). As measuring geometry a plate–plate assembly was used. The upper (moving) plate had a diameter of 2.5 cm. The lower (stationary) plate could be thermostated via a Peltier element with a precision of ±0.1 K. The rheometer was connected to a computer and controlled via the specific software StressTech from *Rheologica Instruments* (RheoPlus from *Anton Paar*, respectively).

To carry out a measurement the upper plate was attached to the instrument after which the rheometer was initialized, i.e. the zero gap width position was determined for the new measuring assembly. Then the desired measuring temperature, which was the $\widetilde{T}$ temperature for the gelled microemulsions, (see Table 6.2) was set and the upper plate was raised by a few centimeters in order to apply the sample. The latter was prepared in a glass vessel which, in case of the gelled microemulsions, was placed on the thermostated rheometer plate for some time until the system was one-phase. Then the sample was transferred to the plate with a spatula ($\sim$0.7 g). Afterwards the upper plate was lowered to the measuring position (usually gap width $z = 1.00$ cm) and the sample was given 30 min to equilibrate at the measuring temperature.

Three different types of oscillating shear rheometry measurements were performed, namely stress sweeps, frequency sweeps and temperature sweeps. In all of them the storage modulus $G'$ and the loss modulus $G''$ were determined, however, different parameters were varied and held constant, respectively.

In the **oscillation stress sweeps**, which served primarily to locate the end of a system's LVE region, the shear stress was increased in typically 60 logarithmical steps in a range adjusted to the studied sample (roughly between $10^{-1}$ and $10^{3}$ Pa). The oscillation frequency was constant at 3 Hz and the temperature at the $T_{\text{rheo}}$ value stated in Table 6.2. All stress sweep measurements were repeated at least

**Table 6.2** Measuring temperatures $T_{rheo}$ for the stress and the frequency sweep measurements and shear stresses $\tau_{freq.sweep}$ used for the latter in case of the binary gels *n*-decane/12-HOA and the gelled microemulsions $H_2O$–*n*-decane/12-HOA–$C_{10}E_4$ ($\phi = 0.5$) with the gelator mass fractions $\eta$ and the surfactant mass fractions $\gamma$

| Sample | $\eta$ | $\gamma$ | $T_{rheo}$ / °C | $\tau_{freq.sweep}$ / Pa |
|---|---|---|---|---|
| Binary gel | 0.015 | – | 25.0 | 10 |
| Binary gel | 0.025 | – | 25.0 | 10 |
| Binary gel | 0.050 | – | 25.0 | 10 |
| Gelled ME | 0.015 | 0.150 | 24.3 | 2 |
| Gelled ME | 0.025 | 0.150 | 23.6 | 5 |
| Gelled ME | 0.050 | 0.123 | 23.8 | 20 |

**Table 6.3** Repetitions of oscillation frequency sweeps and obtained average standard deviations of the storage modulus $G'$ and the loss modulus $G''$ for the binary gels *n*-decane/12-HOA and the gelled microemulsions $H_2O$–*n*-decane/12-HOA–$C_{10}E_4$ ($\phi = 0.5$) with the gelator mass fractions $\eta$ and the surfactant mass fractions $\gamma$

| Sample | $\eta$ | $\gamma$ | Frequency sweep repetitions | Average standard deviation of | |
|---|---|---|---|---|---|
| | | | | $G'$ / % | $G''$ / % |
| Binary gel | 0.015 | – | 4 | 9 | 7 |
| Binary gel | 0.025 | – | 4 | 10 | 18 |
| Binary gel | 0.050 | – | 4 | 12 | 33 |
| Gelled ME | 0.015 | 0.150 | 4 | 8 | 12 |
| Gelled ME | 0.025 | 0.150 | 6 | 4 | 24 |
| Gelled ME | 0.050 | 0.123 | 3 | 4 | 24 |

twice for which a good reproducibility, i.e. only about 2 % variation of both $G'$ and $G''$, was found.

The **oscillation frequency sweeps** were carried out at the same temperatures $T_{rheo}$ as the stress sweeps but with a constant shear stress $\tau_{freq.sweep}$ within the LVE region of the respective sample (see Table 6.2). The frequency was varied in up to 40 steps between 80 and 0.01 Hz. The measurements were repeated three to six times for the different systems for which different average standard deviations of $G'$ and $G''$ were obtained (see Table 6.3).

The **oscillation temperature sweeps** were used to investigate the sol-gel transition temperatures of the binary gels and the gelled microemulsions. For this purpose the frequency was set to 3 Hz and the shear stress to the same value as for the frequency sweeps, i.e. $\tau_{freq.sweep}$ (see Table 6.2). The measurements were started at the temperature $T_{rheo}$ (see Table 6.2) which was then ramped up with a heating rate of 1 K $min^{-1}$. The software collected data every 20 s until the measurements were stopped after the dropdown of $G'$ and $G''$ which indicated the transition from the solid-like gel to the liquid sol. The temperature sweeps were carried out with two samples for each system in which the sol-gel transition temperature could be determined with a reproducibility of $\pm 1.0$ K.

## 6.7 FT-PGSE $^1$H-NMR Self-Diffusion Measurements

The Fourier transform pulsed-gradient spin-echo (FT-PGSE) $^1$H-NMR measurements were carried out on a *Bruker* AVANCE III/400 spectrometer with the widebore diffusion probe DIFF/30 which is equipped with a *Bruker* BCU II –80/60 temperature unit. For operating the system, setting up experiments as well as processing the data the *Bruker* software TopSpin 3.0 was used.

### *6.7.1 Sample Preparation*

To study the samples in the NMR spectrometer they had to be filled into 5 mm NMR tubes. However, preliminary experiments revealed that in low viscous liquids like *n*-decane convective flow occurs within these tubes, especially at elevated temperatures. Convective flow is a result of temperature gradients inside the sample and causes an increase of the self-diffusion coefficients with increasing diffusion times $\Delta$ which is a common problem for PGSE NMR measurements (e.g. [6–8]). To ensure that self-diffusion is the only transport mechanism inside the sample tube it is recommended to reduce the sample diameter [7]. For this purpose the *n*-decane (a mixture of 80 vol% deuterated and 20 vol% protonated oil) was filled into a glass capillary of 1.2 mm inner diameter ($\sim$4.5 cm filling height) which was placed inside a 5 mm NMR tube (ST500-8 from *Norell*). The capillary was wrapped with Teflon tape at the top and the bottom to keep it aligned in the middle of the NMR tube. In the case of the non-gelled microemulsion the sample diameter was reduced by putting empty capillaries into the 5 mm tube which contained the microemulsion sample ($\sim$2.0 cm filling height). Both strategies successfully suppressed convection. As high viscosity also inhibits convective flow, the gelled microemulsion was measured in a 5 mm tube without reducing the sample diameter ($\sim$3.5 cm filling height).

The non-gelled microemulsion was prepared in an ordinary test tube from which it was transferred to a pre-thermostated NMR tube in its one-phase state. The components of the gelled microemulsion were directly weighted into an NMR tube which was then sealed before it was heated up to melt the gelator and to homogenize the sample (cp. description of the procedure in Sect. 6.2). The phase boundaries of both microemulsion samples were determined visually in a water basin before the NMR measurements were carried out. For the non-gelled sample $T_{\underline{2}-1} = 27.9$ °C and $T_{1-\overline{2}} = 30.9$ °C were found while the phase transition temperatures of the gelled microemulsion sample were $T_{\underline{2}-1} = 22.2$ °C and $T_{1-\overline{2}} = 25.8$ °C.

For the preliminary measurements of the single components (cp. Fig. 4.1, left) in the NMR service lab the samples were the following. The gelator 12-HOA was dissolved in deuterated chloroform ($CDCl_3$) which yielded a non-gelled solution to which some tetramethylsilane (TMS) was added as standard. The *n*-decane was mixed with deuterated dichloromethane ($CD_2Cl_2$) and some TMS. The water

sample consisted of $D_2O$. For the surfactant sample 16.8 wt% $C_{10}E_4$ were dissolved in $D_2O$. While the surfactant sample was measured at 10 °C, i.e. below the miscibility gap, all other measurements were carried out at room temperature.

### 6.7.2 FT-PGSE $^1$H-NMR Measurements

All FT-PGSE $^1$H-NMR measurements were carried out using the stimulated spin-echo sequence which is theoretically described in Sect. 2.4. However, other than depicted in Fig. 2.17, the applied magnetic field gradient pulses were not rectangular but of sinusoidal shape. This is advantageous, for example, regarding the minimization of disturbing eddy current effects which arise when the magnetic field strength is rapidly changed. Indeed, the effect of the gradient pulses remains practically unaltered if their shape is changed [9]. Merely the length of the pulses has to be adjusted: to achieve an 'effective duration' of $\delta$ a half-sine shaped gradient pulse must have the length ($\pi/2\ \delta$). In this case integration over a fictive rectangular pulse of length $\delta$ yields the same area than integration over the real pulse. In the performed experiments magnetic field gradient pulses of the effective duration $\delta = 1$ ms were applied. Each experiment consisted of a series of 32 consecutive scans in which the gradient strength $g$ was successively increased up to a predetermined value $g_{max}$. The $g_{max}$ value was chosen such that it caused a complete disappearance of the measured spin echo signals. For each temperature measurements with two different diffusion times, namely $\Delta = 30$ and 150 ms, were carried out. This allowed checking the occurrence of convection.

When a new sample was inserted into the spectrometer the system was shimmed to optimize the homogeneity of the constant magnetic field and the receiver gain was set to a convenient value. Moreover, in order to record a proper signal, matching and tuning were performed using the wobbling routine every time a new temperature was reached. At each temperature the sample was equilibrated for 10 min before a measurement was started.

Even though a new temperature was quickly reached and subsequently held constant by the temperature unit of the instrument the 'translation' of the set-temperature to the actual temperature of the sample was quite difficult. Since a direct measurement of the temperature inside the spectrometer is not possible due to the strong magnet the gelled microemulsion sample itself was used as 'temperature sensor'. It was measured over an extended temperature range and visually examined at each temperature. From a clearly visible turbidity change it was obvious that the system changed from the one-phase to the two-phase state between $T_{set} = 24.8$ °C and $T_{set} = 25.2$ °C as well as between $T_{set} = 28.8$ °C and $T_{set} = 29.2$ °C. These observations were accompanied by a broadening of the NMR signals from the one-phase to the two-phase regions. Accordingly, set-temperatures of 25.0 and 29.0 °C corresponded to the previously determined phase transition temperatures 22.2 and 25.8 °C which leads to

$$T = 0.9\, T_{\text{set}} - 0.3\ ^{\circ}\text{C} \tag{6.1}$$

as equation for the temperature calibration. The temperature error is thus ±0.2 °C in the temperature range of the gelled microemulsion and somewhat bigger outside this range.

### 6.7.3 Data Evaluation

After the measurements the recorded series of successively attenuated FID echo signals were Fourier transformed into the frequency domain using the *Bruker* software TopSpin 3.0. The subsequent data treatment, which included baseline and phase correction as well as peak picking and the calculation of the self-diffusion coefficients, was accomplished using a MATLAB routine. The reported self-diffusion coefficients are the mean values of usually three measurements carried out at one temperature. The variation of the parameters $g_{\max}$ and $\Delta$ within these measurements had hardly any effect on the obtained self-diffusion coefficients all of which deviate from the mean values by $\leq$8 % (usually even $\leq$3 %). This proves the absence of convective flow as the obtained $D$ values are independent of the diffusion time $\Delta$. The chemical shifts in the NMR spectra were referenced to the water signal, which was set to a value of $\delta = 4.8$ ppm, or to the TMS signal with $\delta = 0$ ppm, respectively.

## 6.8 Small Angle Neutron Scattering

The small angle neutron scattering (SANS) experiments were carried out on the instrument D11 at the Institute Laue-Langevin (ILL) in Grenoble, France, and the very small angle neutron scattering (V-SANS) experiments on the KWS-3 at the Research Neutron Source Heinz-Maier Leibnitz (FRM II) in Garching near Munich, Germany.

### 6.8.1 Samples

The gelled bicontinuous microemulsions, non-gelled bicontinuous microemulsions and binary gels were measured in *Hellma* 404.000-QX quartz glass cuvettes in which the sample thickness is 1 mm. All gelled samples were directly prepared in these cuvettes (610 µl, cp. procedure in Sect. 6.2) while the non-gelled microemulsions were prepared in test tubes (920 µl) and transferred to thermostated cuvettes in their one-phase state just before the measurement. Note that the

**Table 6.4** SANS (V-SANS) measuring temperatures of the bicontinuous microemulsion $H_2O$–*n*-decane/12-HOA–$C_{10}E_4$ in different scattering contrasts and in the binary gel d22-*n*-decane/12-HOA with different gelator mass fractions η

| Contrast | $\eta = 0$ | $\eta = 0.015$ | $\eta = 0.025$ | $\eta = 0.050$ |
|---|---|---|---|---|
| Bulk | 28.3 | 23.7 (24.1) | 23.3 (23.6) | 21.9 (22.0) |
| Inverse bulk | 30.4 | – | – | – |
| Film | 28.3 | 22.7 (23.5) | 22.5 (22.6) | 21.8 (21.9) |
| Binary gel | – | 22.7 (22.5) | 21.9 (22.5) | 23.8 (22.5) |

mixtures of deuterated and non-deuterated water and *n*-decane required for contrast matching (cp. Table 4.1) were prepared in advance as stock solutions, which were then weighted in as the water or oil component, respectively. After the preparation the phase boundaries of all microemulsion samples were determined visually in a water basin and later re-checked at the neutron scattering facilities to chose appropriate measuring temperatures in the middle of the one-phase region. Since the V-SANS measurements of the gelled samples were carried out three months after the SANS measurements the sample compositions possibly changed a little due to evaporation in spite of the sealing of the cuvettes. However, if some solvent evaporated this affected mostly the border areas of the sample volume of the gels not the center where the neutron beam hit the sample. Still the measuring temperatures were adjusted a bit and in any case the sample in the thermostated SANS cell was visually inspected directly before a measurement was started to make sure that the microemulsion was in the one-phase state. Table 6.4 lists the used measuring temperatures.

### *6.8.2 SANS Measurements at the D11*

To record at the D11 SANS curves for a $q$ range from 7.0 $10^{-4}$ to 5.2 $10^{-1}$ $Å^{-1}$ each sample was measured with four different instrument configurations, namely with a neutron wavelength λ of 6 Å at sample-detector distances $d_{s\text{-}d}$ of 1.2, 8.0 and 39.0 m as well as with $\lambda = 13$ Å at $d_{s\text{-}d} = 39.0$ m. The collimator-sample distance was set to 8.0 m at $d_{s\text{-}d} = 1.2$ m, to 28.0 m at $d_{s\text{-}d} = 8.0$ m and to 40.5 m at $d_{s\text{-}d} = 39.0$ m. Moreover, transmission measurements were carried out for each wavelength for which the distances between both sample and detector and sample and collimator were 8.0 m with $\lambda = 6$ Å and 4.0 m with $\lambda = 13$ Å, respectively. Prior to all measurements proper positions for the beam stop in front of the detector area had to be determined for every sample-detector distance and wavelength because the neutron beam is exposed to gravity on its way to the detector. In fact, the beam center was recorded in short 'empty beam' measurements for each configuration to later be able to radially average around it. In order not to damage the sensitive detector with the direct beam an attenuator was used in the empty beam measurements, just like in the transmission measurements which

were also carried out with short measuring times, i.e. 120 s for $\lambda = 6$ Å and 150 s for $\lambda = 13$ Å. For the other measurements measuring times between about one and forty minutes were chosen such that in total a minimum of two million counts were accumulated on the detector area. This took the shorter the stronger the scattering of the respective sample; strong scattering was especially obtained at low sample-detector distances and, e.g., microemulsions in film contrast scattered weaker than those in bulk contrast. For absolute calibration it was necessary to additionally measure the scattering of an empty and a water-filled cuvette in all used instrument configurations as well as the incoherent background for which the neutron beam was blocked with a piece of cadmium. The absolute scattering intensity could then be calculated by [10]

$$I(q) = \frac{I_{\text{sample}} - I_{\text{bg}} - \frac{Tr_{\text{sample}}}{Tr_{\text{ec}}}\left(I_{\text{ec}} - I_{\text{bg}}\right)}{I_{\text{H}_2\text{O}} - I_{\text{bg}} - \frac{Tr_{\text{H}_2\text{O}}}{Tr_{\text{ec,H}_2\text{O}}}\left(I_{\text{ec,H}_2\text{O}} - I_{\text{bg}}\right)} \cdot \frac{Tr_{\text{H}_2\text{O}}\, d_{\text{H}_2\text{O}}}{Tr_{\text{sample}}\, d_{\text{sample}}} \cdot \frac{\mathrm{d}\Sigma(\text{H}_2\text{O})}{\mathrm{d}\Omega} \tag{6.2}$$

where $I$ denotes the detected intensity, $Tr$ the transmission, $d$ the layer thickness, bg the background and ec the empty cell. Furthermore $\mathrm{d}\Sigma(\text{H}_2\text{O})/\mathrm{d}\Omega$ is the scattering cross-section of water on the instrument D11 which is known. The absolute calibration was part of the raw data processing, which was performed with the software LAMP from ILL. It also included steps like masking the area around the beam center and radially averaging the two-dimensionally detected data and took into account the dead time of the detector. The $\lambda = 6$ Å-datasets from the different sample-detector distances overlap with scale factors of 0.605 for the data of $d_{\text{s-d}} = 8.0$ m and 1.050 for the data of $d_{\text{s-d}} = 39.0$ m. The data collected at $d_{\text{s-d}} = 39.0$ and $\lambda = 13$ Å were adjusted to those measured at $\lambda = 6$ Å without absolute calibration.

### 6.8.3 V-SANS Measurements at the KWS-3

Other than the D11 which is a pinhole SANS instrument the KWS-3 runs on the focusing mirror principle such that V-SANS measurements in a very low $q$ range are possible. For the present work scattering data was collected in a $q$ range from $1.2\ 10^{-4}$ to $2.8\ 10^{-3}$ Å$^{-1}$ for which a neutron wave-length of 12.8 Å, a sample-detector distance of 9.35 m and sample-collimator distance of 10 m were used. Besides the scattering measurement one transmission measurement was performed per sample. To calibrate the scattering data to the absolute scale normalization was performed with respect to an empty beam measurement. Additionally, the scattering of an empty cuvette was measured as well as the incoherent background scattering, for which the neutron beam was blocked with a piece of boron carbide. The data treatment was carried out using the software QtiKWS from the FRM II.

## 6.9 Electron Microscopy

In order to study the gelled and non-gelled bicontinuous microemulsion as well as the binary gel with a transmission electron microscope, which operates under vacuum, it was necessary to generate replicas of the samples which endure these experimental conditions. For this purpose the sample under investigation was equilibrated at the environmental condition of interest and then rapidly frozen to capture a snapshot of the sample's microstructure ('cryofixation'). Subsequently the frozen sample was fractured which yielded an uneven fractured surface exposing the different microstructural units in the sample. This surface was replicated for which platinum was vapour deposited on it from a certain depositing angle. The elevations on the fractured surface casted metal-free shadows in this procedure, which is therefore also called 'shadowing'. Thus, areas of different metal concentration evolved which created the contrast in the FFEM pictures. To stabilize the replicas they were coated with a thin carbon layer before they were washed, dried and looked at under a transmission electron microscope Tecnai $G^2$ Sphera from *FEI*. Note that preparing replicas and operating the electron microscope are sophisticated tasks which require long training and a lot of experience. Therefore the FFEM pictures were taken by Dr. Natalie Preisig who is an expert in the field.

### *6.9.1 Cryofixation of the Non-Gelled Bicontinuous Microemulsion*

For electron microscopy 3.5 ml of the non-gelled microemulsion $H_2O$–*n*-decane–$C_{10}E_4$ ($\phi = 0.5$, $\gamma = 0.170$) were prepared whereupon the phase boundaries were checked visually in a water basin. Then the microemulsion was in its one-phase state transferred to a special glass apparatus in which it was thermostated at 29.7 °C, i.e. in the middle of the phase boundaries where the microstructure is bicontinuous. Subsequently tweezers which clamped a "sandwich" of two copper grids between two copper plates were placed in the microemulsion for about 30–40 min such that the liquid had time to completely wet the sandwich. Afterwards mechanics were released that catapulted the tweezers with the microemulsion-soaked sandwich into a container of liquid ethane with a temperature of −183 °C which "shock-froze" the microemulsion.

### *6.9.2 Cryofixation of the Gelled Samples*

The gelled samples for electron microscopy were prepared with a volume of 1.0 ml in short glass test tubes according to the procedure described in Sect. 6.2. After checking the phase boundaries the gelled microemulsion $H_2O$–*n*-decane/12-HOA–$C_{10}E_4$ ($\phi = 0.5, \eta = 0.015, \gamma = 0.170$) was thermostated in a water bath at 24.0 °C.

To collect a small volume for freezing two copper plates with centered cavities were glued on the arms of tweezers, which were then pierced into the gelled bicontinuous microemulsion and closed. After checking that the copper sandwich was properly filled with the gel the tweezers were put back into the thermostated sample volume for about 10 min. The binary gel *n*-decane/12-HOA ($\eta = 0.015$), in contrast, was kept at room temperature. With the help of a spatula and a scalpel a small piece was taken out and placed between two copper plates which were then clamped between tweezers. In both cases the tweezers with the sample sandwich were manually transferred as quickly as possible into liquid ethane (note that the gelled bicontinuous microemulsion did not experience serious temperature changes on this way since the room temperature was close to 24 °C).

### 6.9.3 Fracturing and Shadowing of the Frozen Samples

After freezing in liquid ethane the samples were transferred to a container with liquid nitrogen at −196 °C. Therein the sandwiches were fractured in the middle by applying mechanical force with the help of a scalpel and tweezers. It was important that a fractured surface was obtained in this procedure. When just one copper plate cracked off the sample shadowing it would not yield a usable replica, thus such samples had to be discarded. The samples which fractured properly were, still under liquid nitrogen, fixed on a specimen holder which was covered with a metal plate and then clamped to a manipulator. With the latter the holder with the frozen samples was quickly transferred into the vacuum chamber of the Freeze Fracture and Etching System BAF060 from *Leica*. The specimen stage therein had been cooled down to −150 °C. After locking in, the cover plate of the specimen holder was removed and the samples were sputtered with evaporated platinum at an angle of 45° until an approximately 2 nm thick metal layer was deposited. Subsequently, carbon was vapour deposited on top of that from a 90° angle creating a stabilizing layer with a thickness of about 20 nm.

### 6.9.4 Cleaning and Inspecting the Replicas

After the deposition of the carbon layer the samples were soundly replicated and could be locked out of the BAF060. Now the replicas had to be cleaned from the thawing samples for which they were immersed in acetone or *n*-decane on a spot plate. In the solvent the replicas detached from the sample residues, however, several washing cycles were necessary to properly clean the replicas. Hence, the most part of the solvent was removed and replaced by fresh solvent about 3–4 times. Eventually each floating replica was fished up on a fine copper grid held by a pair of tweezers. The tweezers with the replica on the grid were then immersed

into warm *n*-decane for further cleaning. After a final cleaning step in acetone the grids with the replicas were allowed to dry and could then be inspected under the transmission electron microscope. The latter was operated at 200 kV and controlled via the software Tecnai from *FEI*. Pictures were taken from different parts of the replicas with magnifications between 5,000- and 50,000-fold.

## References

1. M. Laupheimer, C. Stubenrauch, Tenside Surf. Det. **51**, 17–25 (2014)
2. S.R. Raghavan, B.H. Cipriano, in *Molecular Gels Materials with Self-Assembled Fibrillar Networks*, eds by R.G. Weiss, P. Terech (Springer, Dordrecht 2006), p. 241–252
3. M. Núñez-Santiago, A. Tecante, Carbohydr. Polym. **69**, 763–773 (2007)
4. M. Tomšič, F. Prossnigg, O. Glatter, J. Colloid Interface Sci. **322**, 41–50 (2008)
5. R.H. Stokes, R.P. Tomlins, J. Chem. Thermodyn. **6**, 379–386 (1974)
6. W.J. Goux, L.A. Verkruyse, S.J. Salter, J. Magn. Reson. **88**, 609–614 (1990)
7. N. Hedin, T.Y. Yu, I. Furó, Langmuir **16**, 7548–7550 (2000)
8. H. Kato, T. Saito, M. Nabeshima, K. Shimada, S. Kinugasa, J. Magn. Reson. **180**, 266–273 (2006)
9. W.S. Price, P.W. Kuchel, J. Magn. Reson. **94**, 133–139 (1991)
10. P. Lindner, in *Neutrons, X-rays and Light: Scattering Methods Applied to Soft Condensed Matter*, eds. by P. Lindner, T. Zemb, (Elsevier, Amsterdam 2002), p. 23–48

# Appendix

Tables A.1, A.2, A.3, A.4, A.5, A.6, A.7, A.8, A.9, A.10, A.11, A.12, A.13, A.14, A.15, A.16, A.17, A.18 and A.19.

**Table A.1** Phase transition temperatures of the non-gelled base microemulsion $H_2O$–*n*-decane–$C_{10}E_4$ ($\phi = 0.5$) [1]

| $\gamma$ | $T_{\underline{2}-1}$ /°C | $T_{1-\overline{2}}$ /°C |
|---|---|---|
| 0.145 | 30.01 | 30.53 |
| 0.155 | 29.62 | 30.81 |
| 0.165 | 28.91 | 31.17 |
| 0.175 | 27.65 | 31.57 |
| 0.190 | 25.89 | 32.16 |
| 0.207 | 24.13 | 32.98 |

The phase diagram is shown in Figs. 3.2, 3.3, 3.4, 3.5, 3.6, 3.8 and 4.3 (left)

**Table A.2** Phase transition temperatures of the microemulsion $H_2O$–*n*-decane/12-HOA–$C_{10}E_4$ ($\phi = 0.5$) with 1.5 wt% gelator (measured by Kristina Jovic) [1]

| $\gamma$ | $T_{\underline{2}-1}$ /°C | $T_{1-\overline{2}}$ /°C | $T_{1-LC}$ /°C | $T_{LC-1}$ /°C |
|---|---|---|---|---|
| 0.130 | 24.18 | 24.37 | | |
| 0.140 | 24.13 | 24.42 | | |
| 0.155 | 23.67 | 24.85 | | |
| 0.160 | 23.37 | 24.87 | | |
| 0.170 | 22.13 | 25.79 | | |
| 0.182 | 21.65 | 26.21 | | |
| 0.198 | 20.82 | 26.90 | | |
| 0.230 | 19.09 | 28.01 | 22.98 | 24.90 |
| 0.240 | 18.40 | 28.10 | 21.24 | 25.55 |

The phase diagram is shown in Figs. 3.3, 3.5, 3.14 (left), 4.6 (left) and 5.1 (top right)

M. Laupheimer, *Gelled Bicontinuous Microemulsions*,
Springer Theses, DOI: 10.1007/978-3-319-07719-2,

**Table A.3** Phase transition temperatures of the microemulsion $H_2O$–*n*-decane–$C_{10}E_4$ ($\phi = 0.5$) prepared with *n*-decane decanted from a centrifuged *n*-decane/12-HOA gel ($\eta = 0.050$) (measured by Kristina Jovic) [1]

| $\gamma$ | $T_{\underline{2}-1}$ /°C | $T_{1-\bar{2}}$ /°C |
|---|---|---|
| 0.140 | 29.58 | 30.00 |
| 0.150 | 29.25 | 30.38 |

The phase diagram is shown in Fig. 3.4

**Table A.4** Phase transition temperatures of the microemulsion $H_2O$–*n*-decane/12-HOA–$C_{10}E_4$ ($\phi = 0.5$) with 1.5 wt% gelator which was prepared with a different surfactant batch

| $\gamma$ | $T_{\underline{2}-1}$ /°C | $T_{1-\bar{2}}$ /°C |
|---|---|---|
| 0.135 | 25.00[a] | 25.10[a] |
| 0.150 | 24.60[a] | 25.40[a] |
| 0.155 | 24.44 | 25.63 |
| 0.158 | 24.40[a] | 25.80[a] |
| 0.170 | 22.98 | 26.42 |
| 0.180 | 22.27 | 26.54 |

The phase diagram is shown in Figs. 3.5 and 6.4 (left)
[a]Measured with the transmission method [2] by Kristina Jovic

**Table A.5** Phase transition temperatures of the microemulsion $H_2O$–*n*-decane/12-HOA–$C_{10}E_4$ ($\phi = 0.5$) with 2.5 wt% gelator (measured by Kristina Jovic) [1]

| $\gamma$ | $T_{\underline{2}-1}$ /°C | $T_{1-\bar{2}}$ /°C | $T_{1-LC}$ /°C | $T_{LC-1}$ /°C |
|---|---|---|---|---|
| 0.130 | 23.45 | 23.85 | | |
| 0.140 | 23.36 | 23.89 | | |
| 0.150 | 21.60 | 24.83 | | |
| 0.155 | | | 23.62 | 24.73 |
| 0.157 | | 25.58 | 23.11 | |
| 0.159 | | | 22.70 | |
| 0.163 | | | 22.65 | |
| 0.164 | 20.33 | 25.90 | | |
| 0.168 | 19.66 | 25.96 | 21.78 | |

The phase diagram is shown in Figs. 3.6 and 3.14 (right)

**Table A.6** Phase transition temperatures of the microemulsion $H_2O$–*n*-decane/12-HOA–$C_{10}E_4$ ($\phi = 0.5$) with 5.0 wt% gelator (measured by Kristina Jovic) [1]

| $\gamma$ | $T_{\underline{2}-1}$ /°C | $T_{1-\overline{2}}$ /°C | $T_{1-LC}$ /°C | $T_{LC-1}$ /°C |
|---|---|---|---|---|
| 0.120 | 23.68 | 24.01 | | |
| 0.125 | 23.37 | 24.67 | | |
| 0.130 | | | 23.67 | 23.94 |
| 0.135 | | | 23.57 | 24.17 |
| 0.139 | 22.04 | 25.99 | | |
| 0.142 | 21.71 | 26.18 | | |
| 0.145 | | | 23.26 | 24.91 |
| 0.150 | | | 22.98 | 24.86 |
| 0.155 | | | 22.31 | 24.88 |
| 0.157 | | | 22.07 | 25.00 |
| 0.159 | | | 21.93 | 25.60 |

The phase diagram is shown in Fig. 3.8

**Table A.7** Sol-gel transition temperatures of the binary gel *n*-decane/12-HOA determined with temperature-dependent oscillating shear rheometry (3 Hz, 10 Pa, 1 K $min^{-1}$; cp. Fig. 3.10)

| $\eta$ | $T_{sol\text{-}gel}$ /°C | Ref. |
|---|---|---|
| 0.015 | 59.1 | [1] |
| 0.025 | 67.1 | |
| 0.050 | 68.5 | |

The data is shown in Figs. 3.12 and 3.16 as well as, converted to ln $\eta$ and $T^{-1}$ in $K^{-1}$, in Fig. 3.17

**Table A.8** Sol-gel transition temperatures of the binary gel *n*-decane/12-HOA determined from DSC measurements carried out by Kristina Jovic

| $\eta$ | $T_{sol\text{-}gel}$ /°C | Ref. |
|---|---|---|
| 0.002 | 55.0 | |
| 0.004 | 58.3 | |
| 0.008 | 59.8 | |
| 0.015 | 61.4 | [2] |
| 0.020 | 61.7 | |
| 0.025 | 64.7 | [2] |
| 0.037[a] | 64.7 | |
| 0.050 | 67.8 | [2] |

The data is shown in Figs. 3.12 and 3.16 as well as, converted to ln $\eta$ and $T^{-1}$ in $K^{-1}$, in Fig. 3.17

[a] The raw data of this measurement is shown in Fig. 3.11

**Table A.9** Sol-gel transition temperatures of the gelled microemulsion $H_2O$–*n*-decane/12-HOA–$C_{10}E_4$ ($\phi = 0.5$) determined with temperature-dependent oscillating shear rheometry (3 Hz, 2 Pa for $\eta = 0.015$, 5 Pa for $\eta = 0.025$, 20 Pa for $\eta = 0.050$, 1 K $min^{-1}$; cp. Fig. 3.13) [2]

| $\eta$ | $\gamma$ | $T_{sol\text{-}gel}$ /°C |
|---|---|---|
| 0.015 | 0.150 | 39.0 |
| 0.025 | 0.150 | 41.0 |
| 0.050 | 0.123 | 46.6 |

The data is shown in Fig. 3.16 as well as, converted to ln $\eta$ and $T^{-1}$ in $K^{-1}$, in Fig. 3.17

**Table A.10** DSC data of the gelled microemulsion $H_2O$–*n*-decane/12-HOA–$C_{10}E_4$ ($\phi = 0.5$) (measurements carried out by Kristina Jovic)

| $\eta$ | $\gamma$ | $T_{sol\text{-}gel}$ /°C | $\Delta_{sol\text{-}gel} H$ /J $g^{-1}$ | Ref. |
|---|---|---|---|---|
| 0.015 | 0.151 | 40.0[a] | 1.7 | |
| 0.015 | 0.156 | 37.6 | 2.7 | |
| 0.015 | 0.166 | 38.1 | 2.2 | |
| 0.025 | 0.151 | 42.3[a] | 4.0 | [1] |
| 0.024 | 0.158 | 39.9 | 3.7 | |
| 0.025 | 0.163 | 42.8 | 5.1 | |
| 0.050 | 0.123 | 47.3[a] | 9.4 | [1] |

The sol-gel transition temperatures are shown in Fig. 3.14 and the marked ([a]) values in Fig. 3.16. Figure 3.17 shows the data converted to ln $\eta$ and $T_{sol\text{-}gel}^{-1}$ in $K^{-1}$. The sol-gel transition enthalpy is shown in Fig. 3.15

**Table A.11** Storage modulus $G'$ and loss modulus $G''$ of the binary system *n*-decane/12-HOA with 2.5 wt% gelator measured at 25.0 °C in oscillating shear rheometry measurements with a frequency of 3 Hz at shear stress of $\tau = 26.3$ Pa for successively decreasing rheometer gap width $z$

| $z$ /mm | $G'$ /Pa | $G''$ /Pa |
|---|---|---|
| 1.00 | $5.7 \times 10^3$ | $8.2 \times 10^2$ |
| 0.75 | $8.4 \times 10^3$ | $1.2 \times 10^3$ |
| 0.50 | $1.4 \times 10^4$ | $1.8 \times 10^3$ |

The data is shown in Fig. 3.18 (right) [1]

**Table A.12** Shear stresses $\tau_{\text{“drop”}}$ for which the storage modulus $G'$ and the loss modulus $G''$ of the binary gel *n*-decane/12-HOA and the gelled bicontinuous microemulsion $H_2O$–*n*-decane/12-HOA–$C_{10}E_4$ with the gelator mass fractions $\eta$ intersect in oscillation stress sweep measurements with a frequency of 3 Hz

| $\eta$ | $\tau_{\text{“drop”}}$ /Pa | |
|---|---|---|
| | Binary gel | Gelled bicontinuous ME |
| 0.015 | 165 | 18 |
| 0.025 | 360 | 85 |
| 0.050 | 570 | 495 |

The data is shown in Fig. 3.22

**Table A.13** Self-diffusion coefficient $D_0$ of pure *n*-decane for different temperatures

| $T$ /°C | $D_0$ /$10^{-9}$ m$^2$ s$^{-1}$ |
|---|---|
| 21.3 | 1.21 |
| 23.1 | 1.24 |
| 24.9 | 1.28 |
| 26.7 | 1.31 |
| 30.8 | 1.38 |
| 34.8 | 1.46 |

The data is shown in Fig. 4.1 (right)

**Table A.14** Self-diffusion coefficients $D$ for water, *n*-decane and the surfactant $C_{10}E_4$ in the non-gelled microemulsion $H_2O$–*n*-decane–$C_{10}E_4$ ($\phi = 0.5$, $\gamma = 0.170$) for different temperatures within the one-phase region

| $T$ /°C | $D_{H_2O}$ /$10^{-9}$ m$^2$ s$^{-1}$ | $D_{n\text{-decane}}$ /$10^{-10}$ m$^2$ s$^{-1}$ | $D_{C_{10}E_4}$ /$10^{-11}$ m$^2$ s$^{-1}$ |
|---|---|---|---|
| 28.1 | 1.23 | 5.86 | 8.08 |
| 28.5 | 1.22 | 5.90 | 8.22 |
| 29.0 | 1.21 | 6.37 | 8.63 |
| 29.4 | 1.19 | 6.55 | 9.10 |
| 29.9 | 1.15 | 6.89 | 9.79 |
| 30.3 | 1.11 | 7.26 | 10.12 |

The data is plotted in Fig. 4.3 (right)

**Table A.15** Self-diffusion coefficients $D_0$ for pure water and pure *n*-decane calculated according to Eqs. (4.1) [3] and (4.2), respectively, as well as relative self-diffusion coefficients $D_{rel}$ according to Eq. (2.34) for water and *n*-decane in the non-gelled microemulsion $H_2O$–*n*-decane–$C_{10}E_4$ ($\phi = 0.5$, $\gamma = 0.170$) for different temperatures within the one-phase region

| $T$ /°C | $D_{0,H_2O}$ /$10^{-9}$ m$^2$ s$^{-1}$ | $D_{0,n\text{-decane}}$ /$10^{-9}$ m$^2$ s$^{-1}$ | $D_{rel,H_2O}$ /m$^2$ s$^{-1}$ | $D_{rel,n\text{-decane}}$ /m$^2$ s$^{-1}$ |
|---|---|---|---|---|
| 28.1 | 2.48 | 1.33 | 0.496 | 0.440 |
| 28.5 | 2.50 | 1.34 | 0.488 | 0.440 |
| 29.0 | 2.53 | 1.35 | 0.477 | 0.472 |
| 29.4 | 2.56 | 1.36 | 0.464 | 0.482 |
| 29.9 | 2.58 | 1.37 | 0.445 | 0.504 |
| 30.3 | 2.61 | 1.38 | 0.425 | 0.528 |

The $D_{rel}$ values are plotted in Fig. 4.4

**Table A.16** Self-diffusion coefficients $D$ for water, *n*-decane and the surfactant $C_{10}E_4$ in the gelled microemulsion $H_2O$–*n*-decane/12-HOA–$C_{10}E_4$ with 1.5 wt% gelator ($\phi = 0.5$, $\gamma = 0.170$) for different temperatures within the one-phase region

| $T$ /°C | $D_{H_2O}$ /$10^{-9}$ m$^2$ s$^{-1}$ | $D_{n\text{-decane}}$ /$10^{-10}$ m$^2$ s$^{-1}$ | $D_{C_{10}E_4}$ /$10^{-11}$ m$^2$ s$^{-1}$ |
|---|---|---|---|
| 22.4 | 1.17 | 4.60 | 5.67 |
| 22.7 | 1.15 | 4.82 | 5.91 |
| 23.1 | 1.16 | 5.11 | 6.14 |
| 23.5 | 1.13 | 5.40 | 6.42 |
| 23.7 | 1.13 | 5.58 | 6.53 |
| 24.1 | 1.11 | 5.89 | 6.81 |
| 24.5 | 1.08 | 6.26 | 7.13 |
| 24.8 | 1.08 | 6.34 | 7.23 |
| 25.3 | 1.04 | 6.57 | 7.40 |
| 25.6 | 1.01 | 6.71 | 7.52 |

The data is plotted in Fig. 4.6 (right)

**Table A.17** Self-diffusion coefficients $D_0$ for pure water and pure *n*-decane calculated according to Eqs. (4.1) [3] and (4.2), respectively, as well as relative self-diffusion coefficients $D_{rel}$ according to Eq. (2.34) for water and *n*-decane in the gelled microemulsion $H_2O$–*n*-decane/12-HOA–$C_{10}E_4$ with 1.5 wt% gelator ($\phi = 0.5$, $\gamma = 0.170$) for different temperatures within the one-phase region

| $T$ /°C | $D_{0,H_2O}$ /$10^{-9}$ m$^2$ s$^{-1}$ | $D_{0,n\text{-decane}}$ /$10^{-9}$ m$^2$ s$^{-1}$ | $D_{rel,H_2O}$ /m$^2$ s$^{-1}$ | $D_{rel,n\text{-decane}}$ /m$^2$ s$^{-1}$ |
|---|---|---|---|---|
| 22.4 | 2.15 | 1.23 | 0.542 | 0.375 |
| 22.7 | 2.17 | 1.23 | 0.532 | 0.391 |
| 23.1 | 2.19 | 1.24 | 0.527 | 0.412 |
| 23.5 | 2.21 | 1.25 | 0.513 | 0.433 |
| 23.7 | 2.23 | 1.25 | 0.507 | 0.446 |
| 24.1 | 2.25 | 1.26 | 0.492 | 0.467 |
| 24.5 | 2.27 | 1.27 | 0.477 | 0.493 |
| 24.8 | 2.29 | 1.27 | 0.473 | 0.498 |
| 25.3 | 2.31 | 1.28 | 0.451 | 0.513 |
| 25.6 | 2.33 | 1.29 | 0.431 | 0.521 |

The $D_{rel}$ values are plotted in Figs. 4.7 and 5.1 (middle right)

**Table A.18** Scattering length densities ρ of the water phase, the surfactant $C_{10}E_4$ and the oil phase of the microemulsion SANS samples in bulk, film and inverse bulk contrast

| Contrast | ρ /$10^9$ cm$^{-2}$ | | | Δρ /$10^9$ cm$^{-2}$ |
|---|---|---|---|---|
| | Water phase | Surfactant | Oil phase | |
| Bulk | 64.0[a] | 1.1[b] | –4.8[a] → 1.1 | 62.9 |
| Film | 64.0[a] | 1.1[b] | 65.6[b] → 64.0 | 62.9 |
| Inverse bulk | –5.6[a] → 1.1 | 1.1[a] | 65.7[b] | 64.6 |

Contrast matching according to Table 4.1 changed the values as indicated by the "→". The data is shown in Fig. 4.8

[a] fully deuterated

[b] fully non-deuterated

**Table A.19** Concentration of monomerically dissolved gelator in the binary gel *n*-decane/12-HOA and in the gelled bicontinuous microemulsion $H_2O$–*n*-decane/12-HOA–$C_{10}E_4$ ($\phi = 0.5$, $\gamma = 0.150$) with different gelator mass fractions $\eta$

| $\eta$ | Binary gel | | Gelled microemulsion | |
|---|---|---|---|---|
| | $c_{12\text{-HOA,mon.}}$ / mol $l^{-1}$ | $\Delta c_{12\text{-HOA,mon.}}$ / mol $l^{-1}$ | $c_{12\text{-HOA,mon.}}$ / mol $l^{-1}$ | $\Delta c_{12\text{-HOA,mon.}}$ / mol $l^{-1}$ |
| 0.015 | 0.017 | 0.002 | 0.032 | 0.002 |
| 0.025 | 0.024 | 0.005 | 0.056 | 0.006 |
| 0.050 | 0.045 | 0.012 | 0.122 | 0.013 |

The data is shown in Figs. 4.16 and 4.23

## References

1. M. Holz, S.R. Heil, A. Sacco, Phys. Chem. Chem. Phys **2**, 4740–4742 (2000)
2. M. Laupheimer, K. Jovic, F.E. Antunes, M. da Graça Martins Miguel, C. Stubenrauch, Soft Matter **9**, 3661–3670 (2013)
3. M. Laupheimer, C. Stubenrauch, Tenside Surf. Det **51**, 17–25 (2014)